The University Of Sheffield.

Modelling and Identification of Interaction Effects for Stability Analysis in LVDC Power Networks

A thesis submitted for the degree of Doctor of Philosophy

Department of Electronic and Electrical Engineering

Faculty of Engineering

The University of Sheffield

Nickolay Nesterov

June-2020

Abstract

Power electronic converters play a vital role in the transition towards low voltage (LV)DC distributed power systems (DPSs) with the proliferation of renewables and end-use electrification. These systems are prone to oscillations from small disturbances due to interactions occurring between sources and loads — power electronic converters, with their tight regulation, introduce a negative impedance characteristic that may destabilize poorly damped oscillatory modes of the network. Recent evidence of the existence of modal interactions that may occur between loads gives rise to additional complexity in dynamic behaviour. As DPSs are subject to many inherent uncertainties and a wide range of operating conditions, different interaction phenomena may influence the small-signal dynamics in a nonlinear manner. Hence, with highly uncertain systems, extrapolating behaviour based on ideal and nominal models can lead to serious qualitative errors.

The thesis focuses on the modelling and small-signal analysis of LVDC DPSs with uncertainties arising from parameter variability. A new automated tool, SymMIAL, is developed to help synthesise high-fidelity state-space system models based on a modular approach. Symbolic linearisation is performed to ensure models represent small-signal dynamics over all possible operating points. Probabilistic variance-based sensitivity analysis (VBSA) is proposed to quantify the influence of parameters and their interactions over the full-range of uncertainties.

Using this novel methodology and newly developed modelling tools, the impact of uncertain parameters on the small-signal dynamics of LVDC DPSs can now be comprehensively investigated. A test DC power system was constructed featuring two parallel filter-converter subsystems fed from a common point through a resistive line. For the first time, an apparent dichotomy in the effect of source-side line resistance is revealed through small-signal sensitivity analysis — line resistance is shown to contribute to both positive and negative damping to filter modes, depending on precise operating conditions.

To resolve this contention, linear mode coupling theory is applied to system state-space models. Contribution of line resistance to damping of modes is quantified and apportioned to different interaction phenomena. Positive damping occurs through source-load interaction; negative damping occurs through modal interaction. Analytical results based on theoretical models are validated against measured data from experimental hardware LVDC DPSs and simulations.

Acknowledgements

First and foremost, I would like to thank my advisor, Dr. Milijana Odavic, for her continuous professional and personal support over the years, which have been undoubtedly some of the most difficult times in my life. It would never have been possible to undertake the research successfully without her understanding, unwavering guidance, and patience. She has given me ample opportunities to pursue my own research interests, while still teaching me a level of scientific rigour—often absent in the engineering discipline—that will forever stay with me for which I am eternally grateful.

A sincere appreciation to all the academic, research, and support staff with the Electrical Machines and Drives Group, in particular Prof. Dave Stone for his past guidance, and the late Mr. Laurence Obodo for his assistance in the lab. I am also extremely grateful to the Department for its financial support and many opportunities for development. Thank you to Dr. George Konstantopoulos for allowing the use of the Control and Power Systems Lab for my experimental work. I am especially thankful to all the friends I have met along the way who have kept me sane—you know who you are.

I owe everything to my parents: thank you for your love and the countless opportunities you have given me in life. Even though sixteen thousand kilometres and nine and a half hours separates us, it feels like I am still home with your support: day or night, wherever I go and with whatever I do. And to my sister, Dasha – you have helped me all my life and continue to remind me that there is more to life than work.

Lastly, but not least, to my wife Nelufer. You have been an amazing friend and partner, supporting me day-after-day, through highs and lows, and without your belief in me, I doubt I could have finished my thesis.

Nickolay Nesterov

Sheffield, June 2020

Table of Contents

Table of Contents ..... **i**
List of Figures ..... **v**
List of Tables ..... **xi**
Nomenclature ..... **xiii**
1 Introduction **1**
1.1 Transformation of Modern Electrical Power Systems 2
1.1.1 Addressing energy sustainability in the 21st Century 2
1.1.2 Distributed Power Systems (DPS): a paradigm shift towards decentralisation 5
1.1.3 The case for Low-Voltage Direct-Current (LVDC) DPS 8
1.2 Challenges for LVDC Distributed Power Systems 9
1.2.1 Power system instability: a background 10
1.2.2 Interactions influencing small-signal stability 16
1.2.3 System modelling and stability analysis techniques 20
1.2.4 Identification of interactions in the presence of uncertainties 24
1.3 Research Aims and Objectives 26
1.4 Main Contributions and Outline of the Thesis 28
2 Preliminaries on Interaction Phenomena in LVDC Distributed Power Systems **33**
2.2 Introduction 34
2.3 Source-load Interactions 35
2.3.1 Negative input impedance characteristic of downstream constant power loads (CPLs) 38
2.3.2 Output impedance characteristics of poorly damped resonant upstream networks 41

2.3.3 Instability caused by interaction between a poorly damped source-side filter and a CPL 43
2.4 Small-signal Modelling and Stability Analysis of LVDC DPSs 46
2.4.1 Frequency domain techniques and impedance-based stability criteria 47
2.4.2 State-space techniques and modal decomposition 50
2.5 Modal (Resonance) Interactions 55
2.5.1 Nonlinear behaviour of eigenvalues 55
2.5.2 Modelling of coupled subsystems 56
2.6 Summary 62
3 Modelling Framework for Small-signal Stability Analysis of LVDC Distributed Power Systems 63
3.1 Introduction 64
3.2 Modular Modelling of DC Power Systems 65
3.2.1 Nonlinear state-space system model 65
3.2.2 System as a network of subsystems 66
3.2.3 Linearising and extracting transfer functions 67
3.3 Subsystem Component Models 69
3.3.1 Passive network components 69
3.3.2 Active components: PWM DC-to-DC power converters 73
3.3.3 Feedback controllers 78
3.4 SymMIAL: A MATLAB Toolbox for Symbolic Model Interconnection and Linearisation 80
3.4.1 Purpose and overview 80
3.4.2 Program implementation 80
3.5 Example: Application to a Single Active Load System 87
3.6 Summary 91
4 Design and Verification of Power System Models: Experimental Hardware and Simulation 93
4.1 Introduction 94
4.2 Input Filter Instability with an Active Load based on Synchronous Buck Converter under Voltage-mode Control 94
4.2.1 System overview 95

4.2.2 Description and design of experimental hardware 96
4.2.3 Experimental setup and test regime 102
4.2.4 Stability analysis and experimental results 106
4.3 Summary 111
5 Influence of Parametric Uncertainties and their Interactions on Small-signal Stability based on Variance-based Sensitivity Analysis 112
5.1 Introduction 113
5.1.1 Background 114
5.2 Variance-based Sensitivity Analysis (VBSA) 116
5.2.1 Analysis of Variance 116
5.2.2 Sensitivity Indices 120
5.2.3 Estimation of Sensitivity Indices through Probabilistic Sampling 122
5.3 Application of VBSA for Small-Signal Analysis of LVDC DPSs 125
5.4 Parallel-Connected Input Filters with CPLs fed by an Uncertain Distribution Line: A Case Study 127
5.4.1 Aim 127
5.4.2 System overview 127
5.4.3 Identification of Interaction Effects using VBSA 132
5.4.4 Investigation of the effect of source-side resistance via modal analysis 134
5.4.5 Validation of predicted behaviour using time-domain simulation 136
5.4.6 Conclusions from the case study 139
5.5 Summary 139
6 Analysis of Mode Coupling Between Parallel-connected Input Filters with Constant Power Loads 141
6.1 Introduction 142
6.1.1 Background 143
6.2 Mode Tracking and the Decoupled State-space Model 144
6.2.1 Mode tracking under parameter variation 144
6.2.2 Decoupled State-Matrix Model 149
6.3 Mode Coupling Between Parallel-connected Input Filters with Constant Power Loads 151
6.3.1 System Overview 151

6.3.2 Detailed model description with active loads 152
6.3.3 Simplified model description with ideal CPLs 153
6.4 Small-signal Stability Analysis of the LVDC DPS Affected by Mode Coupling 156
6.4.1 Effect of filter parameter changes on mode coupling and small-signal stability 156
6.4.2 Effect of source-side line resistance variability on mode coupling and small-signal stability 160
6.5 Experimental Results 164
6.6 Summary 170
7 Conclusion 171
7.1 Thesis Summary 171
7.2 Research Outcomes 172
7.2.1 Original contributions 173
7.3 Suggestions for Future Research 174
References 179
Appendix A – Source Code Blocks for the SymMIAL Toolbox 191
Appendix B – Component Parameter Measurement and Estimation 211

List of Figures

FIGURE 1.1 Sankey diagram of UK energy flows showing the transformation of primary energy resources to end-use sectors (all units in TWh). (Data from the Digest of UK Energy Statistics 2018 [8].) 4

FIGURE 1.2 Overview of the structure of conventional large-scale centralised power system (CPS) with electrical grid based on interconnected transmission and distribution networks. 5

FIGURE 1.3 Example of AC and DC DPS architectures and microgrids. 6

FIGURE 1.4 (a) Power supply topology as a CPS: single converter supplying multiple outputs to individual loads; **(b)** Power supply topology as a DPS: power distribution through an intermediate bus V_{bus} supplying multiple point-of-load converters. 7

FIGURE 1.5 Circuit representation of a DC system with source and load subsystem. 17

FIGURE 1.6 Circuit representation of a DC system with modal coupled subsystems. A coupling factor σ influences energy exchange between subsystem A and B. 18

FIGURE 1.7 An overview of modelling and stability analysis methods used for power electronics-based LVDC DPSs. Those highlighted in blue are within the scope of this thesis. 21

FIGURE 1.8 An overview of several methods used for sensitivity analysis. Methods that are highlighted in blue are within the scope of this thesis. 24

FIGURE 2.1 An example LVDC distributed power system. The source-load interfaces (*IF-1* to *IF-5*) are subject to impedance interactions. 36

FIGURE 2.2 Cascaded two-stage power system with source-load interaction due to source-side output impedance $Z_S(s)$ and load-side input impedance $Z_L(s)$. 37

FIGURE 2.3 The negative incremental impedance characteristic ($\Delta R_{CPL}<0$) of an ideal CPL. 38

FIGURE 2.4 Circuit diagrams of an **(a)** ideal CPL; and its **(b)** linearised equivalent. 38

FIGURE 2.5 Input impedance of different output regulated converters, $Z_{in,2}(s)$, $Z_{in,3}(s)$, $Z_{in,4}(s)$, and that of an ideal CPL, $Z_{in,1}(s)$. The region in red indicates the frequencies at which input has a negative incremental resistance. 40

FIGURE 2.6 Circuit diagram of an 2nd-order LC filter with DCR (R_L). 41

FIGURE 2.7 Output impedance of low-pass LC input filters, $Z_{out,1}(s)$, $Z_{out,2}(s)$, $Z_{out,3}(s)$, at different damping ratios, $\zeta = \{0.01, 0.1, 0.707\}$ at $f_0 = 1\text{kHz}$. 42

FIGURE 2.8 Simplified circuit diagram of a cascaded system with source-side output impedance $Z_S(s)$ and load-side input impedance $Z_L(s)$. 43

FIGURE 2.9 Bode plot representation of the Middlebrook stability criterion showing conditions for source-side output impedance $Z_S(s)$ (input filter) and load-side input impedance $Z_L(s)$ (CPL)..... 45

FIGURE 2.10 A two-port network model: (a) circuit level representation, (b) frequency domain block diagram..... 47

FIGURE 2.11 Frequency domain block diagram of cascaded two-port models. 48

FIGURE 2.12 The Middlebrook Stability Criterion [36] represented on the complex plane. Valid stability region lies within the unit circle offset by a suitable gain margin (GM), $|T_{OL}(s) \leq 1/GM|$. 49

FIGURE 2.13 System of two uncoupled subsystems described dynamics of two independent states, $dx_1/dt=A_1x_1$ and $dx_2/dt=A_2x_2$. 56

FIGURE 2.14 System as two coupled subsystems showing state variable dependence on coupling factors (σ), $dx/dt=Ax+\sigma x$..... 58

FIGURE 2.15 Trajectory of the eigenvalues of the coupled system, as a parameter $\rho 1$ is varied from -5 to 5 in steps of +0.0005. 61

FIGURE 3.1 Block diagram representation of a time-invariant, MIMO nonlinear state-space model. 66

FIGURE 3.2 Block diagram representation of a full-order DC power system, made up of an interconnection of many smaller subsystems. 68

FIGURE 3.3 Two-port representation of a passive distribution network. 70

FIGURE 3.4 Circuit representation of a passive distribution network, $v_{in}(t)$ and $i_{out}(t)$ selected as independent model input variables. 70

FIGURE 3.5 Circuit diagram of an LC filter with parasitic resistances. 71

FIGURE 3.6 Circuit diagram of a one-port subsystem in time domain and s-domain..... 72

FIGURE 3.7 Circuit representation of a switch-mode DC-to-DC converter with averaged power stage dynamics..... 74

FIGURE 3.8 Circuit diagram of a synchronous buck converter. 75

FIGURE 3.9 The two subcircuits of the synchronous buck converter at different switching state: **(a)** $q(t) = 0$, **(b)** $q(t) = 1$ 76

FIGURE 3.10 General block representation of a linear controller in state-space form. 78

FIGURE 3.11 Circuit diagram of a *type-III* analogue compensator. 78

FIGURE 3.12 Program flow showing steps for generating a full system model from subsystems 81

FIGURE 3.13 Circuit model of a single load based on a tightly regulated buck converter with an input filter and type-III compensator. 87

FIGURE 3.14 Block diagram representation of the single load system in Figure 3.13 88

FIGURE 4.1 Block diagram of the experimental cascaded LVDC power system. 95

FIGURE 4.2 Test-bench of the experimental cascaded power system. 96

FIGURE 4.3 Synchronous buck converter power stage used for active loads. 98

FIGURE 4.4 Bode plots of buck converter plant model (duty cycle-to-output voltage), 5kHz compensator, and open-loop transfer function showing gain and phase margins. 100

FIGURE 4.5 3P3Z control implementation as a 3rd-order digital IIR filter with Direct Form Type-I realization 101

FIGURE 4.6 Circuit diagram of the experimental LVDC power system featuring an input LC filter and voltage-mode controlled buck converter. 102

FIGURE 4.7 Input impedance $Z_{in}(s)$ of the model of the experimental closed-loop converter with 5kHz control loop bandwidth. 105

FIGURE 4.8 The critical eigenvalue plot from the system model with 5kHz bandwidth, stepwise variation of V_{ref} from 24V to 33V in 1V increments. 106

FIGURE 4.9 Measured waveforms from experimental system with a 5kHz bandwidth showing an onset of instability following a small step change in V_{ref}. 107

FIGURE 4.10 The critical eigenvalue plot from the system model with 1kHz bandwidth, stepwise variation of V_{ref} from 24V to 33V in 1V increments. 108

FIGURE 4.11 Measured waveforms from experimental system with a 1KHz bandwidth showing an onset of instability following a small step change in V_{ref}. 108

FIGURE 4.12 The critical eigenvalue plot from the system model with 100Hz bandwidth, stepwise variation of V_{ref} from 24V to 33V in 1V increments. 109

FIGURE 4.13 Measured waveforms of experimental system with a 100Hz bandwidth showing no overshoot following a large step change in V_{ref} (0 to 31V). 109

FIGURE 4.14 Experimental waveforms of the input filter voltage and current, showing an oscillation period of 1.56ms (641Hz). 110

FIGURE 4.15 Bode plot of the input and output impedances of the experimental system under nominal operating conditions showing near instability 110

FIGURE 5.1 Studied LVDC DPS with multiple active loads fed by a non-ideal (resistive) line..... 128

FIGURE 5.2 Circuit diagram of a single active load..... 128

FIGURE 5.3 Estimation of VBSA sensitivity indices under *Case A*. 133

FIGURE 5.4 Estimation of VBSA sensitivity indices under *Case B*. 133

FIGURE 5.5 Effects of 30% parameter uncertainty in C_{F2} and L_{F2} on the derivative sensitivity of the critical eigenvalue to R_{line} perturbations (for *Case 1*). All other parameters remain nominal. 135

FIGURE 5.6 Critical eigenvalue sensitivity to R_{line} changes vs. capacitance C_{F2} (cross-section of Figure 5.5 at fixed inductance value $L_{F2} = 2.2\text{mF}$) 135

FIGURE 5.7 Region 2, time domain simulations showing the effect on V_{bus} under: **(a)** decreasing R_{line}, **(b)** increasing R_{line}..... 137

FIGURE 5.8 Region 1, time domain simulations showing the effect on V_{bus} under: **(a)** decreasing R_{line}, **(b)** increasing R_{line}..... 138

FIGURE 6.1 Possible eigenvalue (λ_1, λ_2) trajectories when varying a single parameter..... 145

FIGURE 6.2 Eigenvalue mode tracking via participation factor analysis. 148

FIGURE 6.3 Block diagram overview of the LVDC power system with two parallel-connected filter-load subsystems on the same distribution bus fed by a resistive line 151

FIGURE 6.4 Comparison of the input impedance Bode diagrams of the detailed model (based on active loads with controller dynamics) and simplified model (based on ideal CPLs). 152

FIGURE 6.5 Ideal circuit model of the system in Figure 6.3. 153

FIGURE 6.6 Trajectory of eigenvalues '*Mode 1'* and '*Mode 2*' over varying resonant frequency of *filter 1* ($3850 < \omega_{n,F1} < 7150$ rad/s). Filter damping ratios held constant ($\zeta_{F1} = \zeta_{F2} = 0.0028$)*;* $R_{line} = 0.25\Omega$. 157

FIGURE 6.7 Trajectory of participation factors '*State* $V_{C,F1}$ to *Mode 1'* and '*State* $V_{C,F2}$ to *Mode 1*' over varying resonant frequency of *filter 1* ($3850 < \omega_{n,F1} < 7150$ rad/s). Filter damping ratios held constant ($\zeta_{F1} = \zeta_{F2} = 0.0028$)*;* $R_{line} = 0.25\Omega$. 157

FIGURE 6.8 Trajectory of eigenvalues '*Mode 1'* and '*Mode 2*' over varying resonant frequency of *filter 1* ($3850 < \omega_{n,F1} < 7150$ rad/s). Filter damping ratios, $\zeta_{F1}=0.0028$, $\zeta_{F2}=0.0038$; $R_{line} = 0.25\Omega$. 159

FIGURE 6.9 Trajectory of participation factors '*State* $V_{C,F1}$ to *Mode 1'* and '*State* $V_{C,F2}$ to *Mode 1*' over varying resonant frequency of *filter 1* ($3850 < \omega_{n,F1} < 7150$ rad/s). Filter damping ratios, $\zeta_{F1}=0.0028$, $\zeta_{F2}=0.0038$; $R_{line} = 0.25\Omega$..... 159

FIGURE 6.10 System minimum damping ratio (ζ_{min}) as a function of the resonant frequency of filter 1 ($3850 < \omega_{n,F1} < 7150$ rad/s) at different values of line resistance $R_{line} = \{0,0.1,0.25,0.5\}$. 162

FIGURE 6.11 Sensitivity of minimum damping ratio (ζ_{min}) to R_{line} perturbations as a function of the resonant frequency of filter 1 ($3850 < \omega_{n,F1} < 7150$ rad/s) at different values of line resistance $R_{line} = \{0,0.1,0.25,0.5\}$. 163

FIGURE 6.12 Input impedance of the system under different R_{line} values. 163

FIGURE 6.13 Power stability boundaries at different values of R_{line} values: (a) System 1; (b) System 2. 165

FIGURE 6.14 Test-bench of the experimental two-parallel connected cascaded power system. 166

FIGURE 6.15 Filter waveforms of active loads in parallel connected to a resistive distribution line after increasing line resistance from 0.25Ω to 0.5Ω showing unstable oscillations. Operation under closely matched input filters (*System 1*). 167

FIGURE 6.16 Zoomed snapshot of oscillations in Figure 6.15 indicating a coupling between filters and exchange of energy (i.e., as voltage of F_1 rises, the voltage in F_1 falls)..... 168

FIGURE 6.17 Filter waveforms of active loads in parallel connected to a resistive distribution line after decreasing line resistance from 0.25Ω to 0.17Ω showing unstable oscillations. Operation under closely matched input filters (*System 1*). 168

FIGURE 6.18 Filter waveforms of active loads in parallel connected to a resistive distribution line after decreasing line resistance from 0.25Ω to 0.1Ω. Unstable oscillations only occur in a single filter. Operation under well-separated input filters (*System 2*)..... 169

FIGURE 7.1 Frequency domain feedback with two parallel loads, $Y_{in,1}(s)$ and $Y_{in,2}(s)$, reshaped by source-side resistance, $R_S(s)$..... 176

FIGURE B.1 (a) Output impedance Z_{out} low-pass filter design using frequency response data of individual elements Z_L, Z_{C1}, Z_{C2}, **(b)** Representation of the combined frequency response for Z_{out} (where source input V_{in} replaced by a short circuit)..... 212

FIGURE B.2 Frequency sweep measurement settings, LCR Meter *Hioki IM3533-01*..... 212

FIGURE B.3 Output impedance Z_{out} of input filter 1 based on parameter measurements. 213

FIGURE B.4 Output impedance Z_{out} of input filter 2 based on parameter measurements. 213

FIGURE B.5 Filter model used to fit experimental *FRD* (impedance data) for parameter estimation. 214

FIGURE B.6 Example process for parameter estimation by fitting to a greybox plant model using experimentally measured *FRD* 216

FIGURE B.7 Variable resistor model used in test-bench experiments with parameter values given in Table B.4 217

List of Tables

TABLE 4.1 Parameters of the experimental system. 103
TABLE 4.2 Values of the 3P3Z controller variables at different bandwidths. 103
TABLE 4.3 Controller parameters in continuous-time domain form used for small-signal stability analysis. 104
TABLE 5.1 Fixed system parameters 130
TABLE 5.2 Uncertain parameters 131
TABLE 5.3 Case A and Case B values for input filter (*F2*) of active load 2 131
TABLE 5.4 Simulation scenarios under operation in Region 1 and Region 2. 136
TABLE 6.1 System parameters of the reduced-order circuit model 155
TABLE 6.2 Mode tracking based on dominant states 156
TABLE 6.3 Summary of damping and sensitivity under different values of R_{line}. 161
TABLE 6.4 Measured filter parameters in the experimental system 165
TABLE A.1 SymMIAL code repository summary 191
TABLE B.1 Parameters for different filter designs 215
TABLE B.2 Filter designs (*F1-II* to *F1-VIII*) by auxiliary capacitor(s) selection 215
TABLE B.3 Auxiliary capacitor values and part numbers 215
TABLE B.4 Rheostat (*Ohmite RJSR50E*) resistance–position values, experimentally measured. 218

Nomenclature

List of Acronyms and Abbreviations

LV	Low voltage
AC	Alternating current
CPL	Constant power load
DC	Direct current
DG	Distributed generation
DER	Distributed energy resources
PWM	Pulse-width modulation
PE	Power electronic(s)
3p3z	3-Pole/3-Zero compensator
AL	Active load
MC	Monte Carlo (MC) experiments
SSR	Subsynchronous resonance
MIMO	Multiple-input multiple-output
SISO	Single-input single-output
PID	Proportional–integral–derivative controller
SMPS	Switch-mode power supply
OAT	One-at-a-time
FRD	Frequency response data
CPS	Centralised power system
DPS	Distributed power system

List of Acronyms and Abbreviations (continued)

FRA	Frequency response analysis
LTI	Linear time invariant
POL	Point-of-load (converter)
OL	Open-loop
CL	Closed-loop
TF	Transfer function
DCR	DC resistance
$R_{DS(on)}$	Drain-source on-state resistance
ESR	Equivalent series resistance
VBSA	Variance-based Sensitivity Analysis
SSA	State-space averaging
CCM	Continuous conduction mode
SA	Sensitivity analysis
GSA	Global SA
HDMR	High Dimensional Model Representation
ANOVA	Analysis of variance

Chapter 1

Introduction

Decarbonisation of energy systems is at the forefront in the fight against the growing threat of climate change, rising global energy demands, and emerging risks to energy security. To limit the use of conventional fossil fuels, modern electrical power systems are integrated with localised small-scale power generators based on renewable energy sources [1]. Likewise, more efficient energy use at the consumer-end is being achieved with the electrification of multiple sectors including industry, residential, and transport [1], [2]. These changes, made possible by the technological innovations in power electronic converters, are radically altering the composition of power networks from both the supply-side and load-side. As a consequence of these now highly distributed technologies, the conventional paradigm of top-down centralised power systems (CPS) is shifting towards one based on distributed power systems (DPS) comprising of localised generators and loads with various power electronic-based interfaces [3]. Furthermore, the use of low-voltage direct current (LVDC) distribution systems are gaining considerable interest owing to their numerous benefits of increased efficiency, utility, and ease of control compared to traditional AC-based systems [4], [5]. However, the widespread adoption of LVDC DPSs is predicated on their reliable operation. Ensuring stability is increasingly challenged due to poor power network damping, complex nonlinear behaviour of power electronic-based interfaces, and the potential interactions that may occur between various power system components. This is further complicated by the wide range of operating

conditions and uncertainties that traditional power system modelling and analysis techniques often neglect.

This chapter introduces the research topic, provides context, and defines the scope of the thesis. Section 1.1 establishes the present-day transition towards power electronics dominated DPS and the potential for wider adoption of LVDC DPSs. Section 1.2 sets out the main factors impacting the stability of these systems and the challenge in modelling and small-signal stability analysis considering parametric uncertainties. Here, the current research gaps are introduced to the reader. Subsequently, Section 1.3 defines the central research aims and lists the central objectives of the research. Finally, Section 1.4 outlines the contents and original contributions of each of the chapters.

1.1 Transformation of Modern Electrical Power Systems

The development and operation of energy systems are increasingly required to address challenges concerning environmental sustainability, energy demands, and security of the energy supply. A brief overview of this is discussed (Section 1.1.1) which explain subsequent developments relating to electrical power systems: the growth of renewable energy generation and increased electrification enabled by power electronic converters. The widespread adoption of these new technologies calls for more efficient and versatile designs for modern power networks—DPS are introduced as an alternative to conventional top-down CPS (Section 1.1.2). In particular, LVDC DPS are emerging as a promising solution for an increasing number of applications (Section 1.1.3).

1.1.1 Addressing energy sustainability in the 21st Century

Energy systems are vital for modern society. Our ability to harness energy drives the development and the prosperity of societies through activities in areas such as agriculture, industry, transport, information technology, and the built environment.

Ultimately, progress in these areas is directly linked to human development and people's quality of life. It is projected that global energy demand from all primary sources will grow approximately by 27% from 2018 to 2040 (~163,000 to 207,000 TWh), with

demand coming primarily from population growth, urbanisation in developing nations, and rising incomes [6]. At present, the energy demand from domestic, industrial and services sectors is expected to be met with traditional sources such as natural gas and coal. Similarly, energy demand from the transport sector will be met with liquid fuels such as petroleum. This, however, comes at a profound cost to the environment, placing our future prosperity at risk.

The adverse environmental impact of fossil fuels has been a focus of global concern for many decades. Rising temperatures and sea levels with an increased frequency of extreme weather events are forecasted which may lead to scarcity of food and water, loss of housing and livelihoods, mass migration, ultimately leading to lower global standards of living. To address these climate risks, a widespread international effort has focused on introducing sustainable policies that limit anthropogenic greenhouse gas emissions, in particular carbon dioxide. Although conventional fuels have enabled past growth, future development must prioritise sustainability through alternative energy sources and improved in energy conversion, distribution, and energy use. The modern concept of sustainable development was initially proposed in 1987 in the Brundtland Report, titled *Our Common Future*, as '*development that meets the needs of the present without compromising the ability of future generations to meet their own needs'* [7].

Following the publication of the Brundtland Report, there has been an increased political imperative to adopt policies for future sustainability relating to economic, social and the environmental factors globally [7]. International agreements to mitigate climate change through targeted reductions in greenhouse gas emissions have been established, most notably the *United Nations Framework Convention on Climate Change (1992),* the *Kyoto Protocol (1997)*, and the *Paris Agreement (2015).*

The introduction of sustainability policies has caused energy systems of today to have drastically different requirements compared to those of the 20th century. The evolving trade-offs between cost, greenhouse gas emissions, and energy security have an impact on our existing systems of production, conversion, and consumption of energy. Such processes are likely to be dominated by electrical systems in the future. As such, improvements to power generation capacity, low-carbon technologies, efficiency, and design of electrical power networks present opportunities towards achieving sustainability.

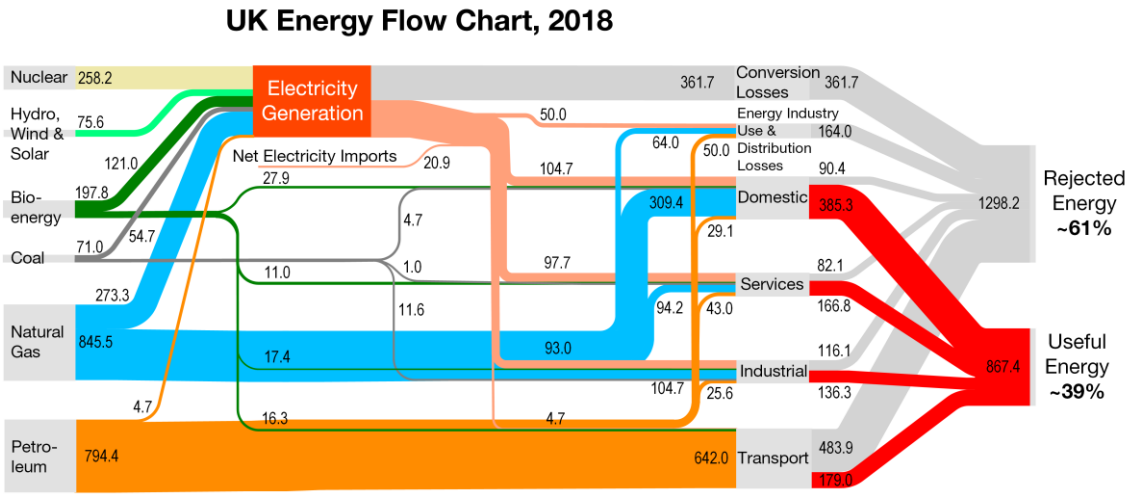

FIGURE 1.1 Sankey diagram of UK energy flows showing the transformation of primary energy resources to end-use sectors (all units in TWh). (Data from the Digest of UK Energy Statistics 2018 [8].)

The United Kingdom is a representative example of a developed economy that is actively reducing its primary energy dependence away from conventional fuels. The annual energy flows of the UK (2018) are depicted in Figure 1.1, showing the primary energy resources directed towards different sectors for end-use. The overwhelming majority of primary energy demand is currently met by fossil fuels, mostly petroleum and natural gas. The transportation sector is the largest consumer of these fuels, with automotive vehicles accounting for the majority, followed by aerospace and marine, while rail has for the most part already electrified. Within the domestic sector, fossil fuel consumption is used principally for household heating. Achieving sustainability will be achieved in no small part from the decarbonisation of heat and transport.

Electrification of these end-uses is a key strategy towards limiting greenhouse gas emissions. However, full electrification in sectors presently under-electrified will impose significant new pressures on existing grid infrastructure. Nevertheless, decarbonisation via electrification also inevitably implies that the electricity generation is likewise decarbonised.

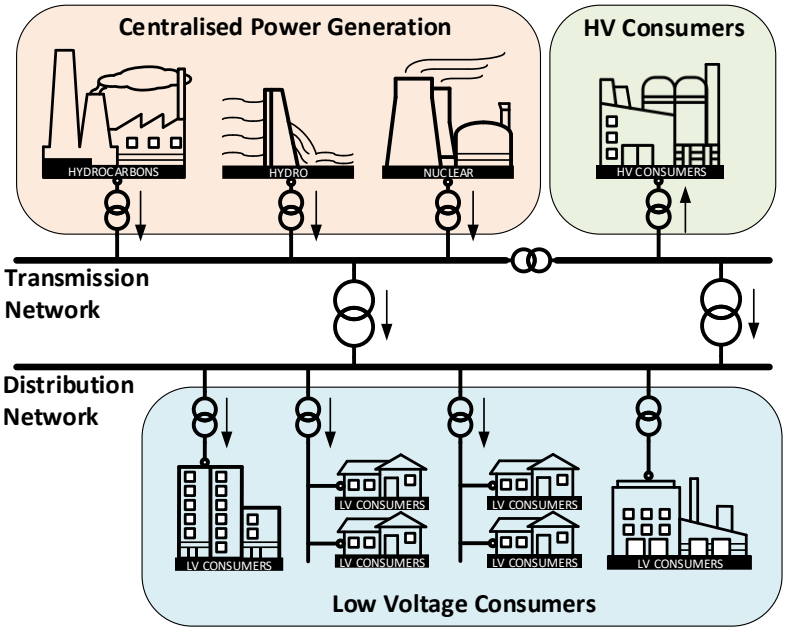

FIGURE 1.2 Overview of the structure of conventional large-scale centralised power system (CPS) with electrical grid based on interconnected transmission and distribution networks.

1.1.2 Distributed Power Systems (DPS): a paradigm shift towards decentralisation

Conventional AC power distribution, as represented in Figure 1.2, involves generating power in large capacity power plants. Long-distance power distribution via networks of power lines and substations until termination at individual consumers at a low voltage[1] level. This top-down structure is increasingly challenged by the emergence and proliferation of multiple localised power generators enabled by so called "distributed energy" technologies such as solar PV, wind turbines, energy storage devices, and various engines. These ultimately influence how modern electrical power systems are designed, operated, and maintained.

A promising type of DPS is called a *microgrid,* originally proposed in [9] as a building block for future decentralized power systems. The term microgrid has no

[1] Depending on context, the term low voltage (LV) can refer to different voltage levels. The IEC definition for LV and extra-LV is anything less than 1kV AC RMS or 1.5kV DC [123].

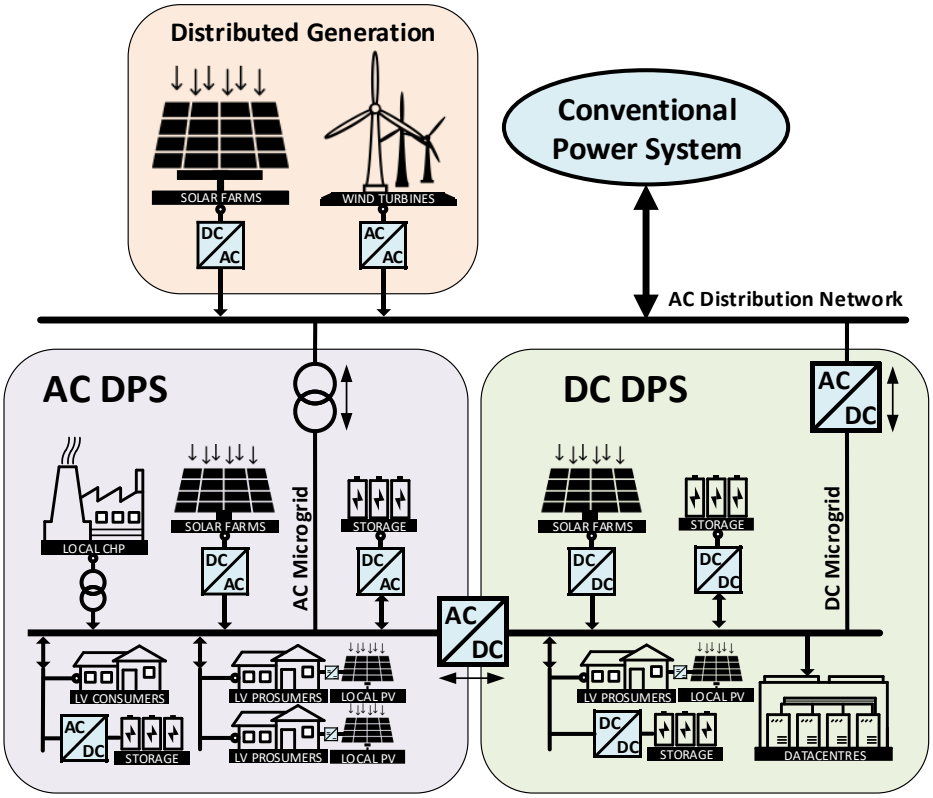

FIGURE 1.3 Example of AC and DC DPS architectures and microgrids.

standardised definition and can encompass many types of power systems with their design and implementation differing based on specific local requirements. Figure 1.3 represents possible microgrids or DPSs. In general, microgrids can be characterized by having many smaller local generation units and local loads (and increasingly energy storage) distributed throughout the system. These modular systems must be able to operate independently from a centralised grid, known as standalone or islanding mode, and manage energy flows intelligently. Examples include power generation/delivery in remote areas and transportation applications (e.g., aerospace and marine). Some microgrids, however, are designed to be interfaced to a central grid system as shown in Figure 1.3. The point of interconnection between the bulk grid and microgrid services the transition between islanding and grid-connected modes, providing the benefits of both a centralised and a distributed system [10], [11]. In this regard, future DPSs need not displace the status quo as they can exist concurrently with existing networks.

Microgrids can be perceived as an extension of the traditional low voltage distributed power systems seen in telecom, data centres, and transportation. With the integration

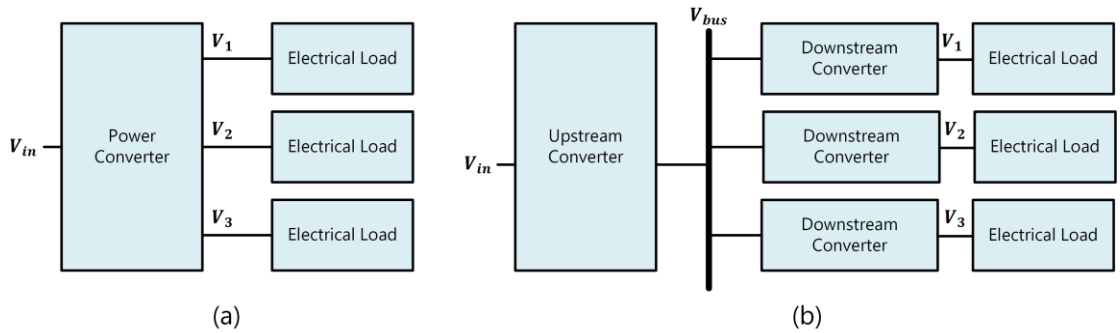

FIGURE 1.4 (a) Power supply topology as a CPS: single converter supplying multiple outputs to individual loads; **(b)** Power supply topology as a DPS: power distribution through an intermediate bus V_{bus} supplying multiple point-of-load converters.

of modern and newly economically feasible technologies resulting from advanced power electronics converters, increased renewable generation, decentralised energy storage, and improved control, the grid's structure does not need to follow past conventions. Consequently, great interest is shown from both the public and private sector in microgrids for new residential and industrial applications which account for the majority of electrical power consumption in the world. Major key drivers for their use are their advantage in efficiency, resiliency, and availability [1], [3], [4], [12]—ultimately addressing the issue of sustainability.

DPSs can also be viewed in the context of power supply designs used in electronic equipment and embedded applications. Figure 1.4 shows two possible configurations of a power supply based on a CPS and DPS architecture. The centralised power supply in Figure 1.4(a) contains multiple conversion stages within a single unit to provide the required power/voltage levels to individual loads; while Figure 1.4(b) shows a front-end supply regulating the voltage of an intermediate bus that feeds multiple point-of-load converters.

As is the case with microgrids, the DPS concept in power supplies offers numerous benefits compared to traditional CPSs. Individual power converters can be standardised to specific input/output voltages and power levels thereby reducing engineering effort. An intermediate bus enables the distribution of power to high current loads located near the point-of-load. This often simplifies the cable and PCB track requirements by minimising system I^2R losses, improving efficiency, as well as easing thermal management. It is possible to improve fault tolerance and reliability, for example in Figure 1.4(b)

multiple redundant upstream converters used in parallel to supply the same bus so that failure in one converter does not lead to failure of the complete power system.

The paradigm shift towards decentralisation through the use of DPSs is underway in grid infrastructure and many other sectors such as transportation. This introduces numerous new degrees of freedom into the design of modern power systems in terms of topologies and power distribution characteristics—for example, voltage levels and the choice between AC or DC power distribution.

1.1.3 The case for Low-Voltage Direct-Current (LVDC) DPS

The dominance of AC over DC in power distribution and transmission networks is largely due to historical factors of the early 20th century, with the contest often referred to as the "*battle of the currents"* [4]. DC-based power systems were constrained by the complexity of DC motors and the inability of DC-DC voltage conversion, whereas the development of asynchronous motors and the simplicity of transformers facilitated the spread of AC-based power systems. Nevertheless, DC continued and grew with the use of variable speed motor drives in rail and industrial applications.

While legacy effects favour AC and has been adequate for the needs of the 20th century, modern 21st century developments provide a plethora of increasingly compelling arguments for future (LV)DC DPSs [4], [5], [11], [13]:

- Local renewable energy generation is typically DC-based:
  - Photovoltaic (PV) cells generate DC output,
  - Wind turbines are variable speed generators that feed an intermediate DC-link within the power electronic interfaces,
  - Energy storage systems are commonly DC (e.g., batteries and fuel cells).
- Simplification in control due to lack of reactive and harmonic power flows, and no need for synchronisation efforts.
- Electrification enabled by power electronics—a trend towards greater use and quantity of DC loads (e.g., electronics, variable speed drives, and lighting systems).
- Already widely used in transportation (i.e., maritime, automotive, and aerospace).
- Elimination of inverters and rectifiers to reduce cost, and increase efficiencies by reducing AC-DC conversion losses.

Today, DC systems are dominant at the very-HV range (e.g., HVDC power transmission) and the extra-LV range (e.g., embedded applications). Recent years has seen a gradual convergence towards adoption of DC to applications between these two extremes—into the LV range—with the changing nature of electrical generation and ongoing electrification in end-use. LVDC can better meet energy system objectives by enabling modular and decentralized power architectures. As such, modern LVDC DPSs are becoming an increasingly important innovation towards sustainability.

To facilitate a widespread adoption of LVDC DPS, the design of these systems must ensure stable operation during disturbances over a wide range of operating conditions. This involves system modelling, stability analysis, and assessment of the impact of uncertainty—establishing the broader context for the thesis. The challenges associated with these issues are introduced in Section 1.2 with the research scope outlined in Section 1.3.

1.2 Challenges for LVDC Distributed Power Systems

In many applications, the adoption of LVDC DPS with the ever-increasing proliferation of power-electronic converters presents several challenges to both system design and operation. These power systems are subject to several conflicting objectives, including cost, performance, reliability, while their operation must contend with tighter margins, harsher environments, and function for longer. Nevertheless, LVDC DPS must still ensure the reliable delivery of electrical power with stable operation over a wide range of operating conditions and multiple uncertainties. The aim of this section is to establish the major themes and challenges to set the stage for the main research questions and thesis objectives (Section 1.3).

This section is structured as follows. Firstly, we provide an introductory overview on the topic of power system stability, comparing traditional AC DPS with DC DPS stability. LVDC DPSs are increasingly prone to small-signal oscillatory instability—where *small-signal stability* is concerned, the constant power load (CPL) behaviour of

power electronic interfaces and the declining damping of the resonant characteristics of distribution networks are proving critical.

Secondly, we introduce briefly the two distinct interaction mechanisms that may influence small-signal dynamics: *source-load interactions* and *modal interactions*. Both types of interactions occur as a result of the properties of linearised power systems and arise as a result of the interconnection of various power system components. Source-load interactions emerge from the feedback properties of cascaded power converters, whereas modal interactions are from the internal resonant properties of the network. While stability is studied under small-signal conditions, the impact of the two interaction phenomena on small-signal dynamics can be highly nonlinear over parameter variations and uncertain operating points in LVDC DPSs.

Thirdly, power systems need to be modelled appropriately to study the effect of interactions between subsystems and parameters in detail. Small-signal analysis requires linear approximations of nonlinear power systems at various steady-state operating conditions. Therefore, in order to properly account for uncertainty and changing operating points, nonlinear modelling suitable for symbolic linearisation is to be addressed. The two prevalent techniques for small-signal analysis are discussed: impedance-based frequency response analysis and state-space eigenvalue analysis.

Finally, often overlooked in literature are the inherent parametric uncertainties present in LVDC DPSs. Deterministic approaches to small-signal stability assessment are often no longer appropriate due to the profound impact uncertainty has the operating point and thus the small-signal dynamics. Introduced here are global sensitivity analysis techniques that are promising for assessing the impact of parameters over the full range of uncertainties.

1.2.1 Power system instability: a background

A reliable supply of electrical power to loads requires the stable and predictable operation of power systems. Modern DC systems face many of the same challenges as traditional AC systems. We first begin with a brief introduction to instability phenomena from the AC power system perspective. Increased susceptibility to stability problems in these systems can be attributed to changes to the structure of the network through the

proliferation of power electronic interfaces and distributed generation. Here, two factors are of interest—instability in grid frequency due to lower inertia, and rotor angle instability from poorly damped electromechanical oscillations. While the emphasis is not on AC systems, the instability phenomena observed in DC systems are conceptually analogous. With changing system characteristics caused by the transition towards LVDC DPSs dominated by power electronics, the network is becoming far more susceptible to voltage instability following small disturbances. Factors that impact this type of instability are primarily from the poor damping of the electrical networks and the *negative impedance* characteristics of the CPLs.

The following definition is used to describe power system stability [14]: *"Power system stability is the ability of an electric power system, for a given initial operating condition, to regain a state of operating equilibrium after being subjected to a physical disturbance, with most system variables bounded so that practically the entire system remains intact."*

Power system instabilities that can occur are then further classified into three categories [14]: the nature of instability indicated by the main system variable (e.g. voltage, frequency, rotor angle); the magnitude of disturbance (small-signal disturbances or large-signal disturbance); and the time frame required to observe instability (short-term or long-term).

Traditional large-scale AC power systems are reliant on the combined inertia of interconnected synchronous generators to maintain long-term frequency stability. Synchronous generators store kinetic energy within their rotating mass to deliver an inertial response when an imbalance occurs between mechanical and electromagnetic torque in the electrical grid, as represented by the well-known swing equation [15]. As generators are synchronously linked, any deviation in the synchronous speed of a single machine is opposed by the total combined inertia of the remaining generators. Sufficient power system inertia is required to maintain an active power balance with nominal grid frequency.

The power system inertia also supports synchronism of the rotor angle dynamics between multiple generators. Following grid disturbances, the significant inertia prevents large deviations in grid frequency which provides sufficient time for other control algorithms to respond in rebalancing rotor angle swings. While excitation systems with fast response provide synchronising torque to improve transient rotor angle stability, an

insufficient damping torque is known to cause small-signal electromechanical oscillations [16], [17]. The frequency and damping characteristics associated with these oscillations are described in terms of power system *modes* [18]. These *modes* arise from the complex interactions occurring between various components of the power system, including mechanical characteristics of the generators, electrical characteristics of the network, and controller dynamics of active devices [19]. Weak coupling between different synchronous generators from a change of network structure can cause the poor damping of certain modes and lead to unstable rotor oscillations. While a detailed investigation of small-signal rotor angle stability is outside of the scope of the present work, analysis techniques in literature are relevant here. In particular, those relating to modal interactions introduced later in Section 1.2.2.

With the transition to AC DPS, lower levels of overall power system inertia and damping are expected as large synchronous generators are displaced by non-synchronous generators. These smaller, power electronics-based generators do not inherently contribute rotational inertia or damping to the system—photovoltaics have no mechanical inertia, and variable speed wind turbines are decoupled from the grid through an intermediate DC-link. A weak grid, characterised by low inertia, increases the rate of change of frequency following a shift in generation-load balance. Therefore, systems with insufficient inertia may result in excessive frequency deviations after disturbances. Grid frequencies exceeding rated limits can lead to the poor performance of connected devices and may result in long-term frequency instability and failure.

Poor damping of oscillations in AC DPS results in small-signal instability through the loss of generator synchronicity with the network. While in conventional power systems low-frequency oscillations are typically the result of insufficient damping torque of electric machines, AC DPSs are dominated by power electronic converters where no physical rotor exists. Here, grid synchronism is performed through embedded control methods, commonly based on PLLs including VSGs-based converters and synchronverters [20]. Undamped oscillations due to poorly tuned control parameters becomes a new concern for system stability. PLLs modify the dynamics of power converters and may introduce a negative damping component thus destabilising the system. Unlike the low-frequency instability of conventional AC systems, higher frequency resonance

oscillations are known to occur from dynamic interactions between power filters, parasitic feeder capacitances, and controls systems [21]–[23], [23].

The principles of DC power systems are highly analogous to those based on AC. Instead of AC frequency as the main variable for (active) power balance, DC systems rely on regulating voltage to manage power variations. While instantaneous frequency response is provided by the stored kinetic energy in the inertia, DC grid voltage is supported by the stored electric potential energy in capacitance—both inertia and capacitance are used to prevent large changes in frequency and voltage following a disturbance, respectively. Disturbances that cause excessive voltage deviations in DC networks are known to be an issue for the operation of sensitive loads [24]. Such disturbances typically arise from discrete events including step changes in load demand or fault conditions. Weak DC network conditions—characterised by low capacitance—are especially susceptible. Source converters may have an insufficient transient response time to maintain a nominal voltage, and this sudden change may result in loss of output regulation in downstream converters. This transient behaviour is associated with large-signal instabilities.

Modern DC DPSs, much like AC DPS, are becoming increasingly vulnerable to instability due to undamped oscillations following small disturbances. Contributing to small-signal instability are the poor damping of resonant circuits in the distribution network (including power lines, and input and output filters of switching converters) and the introduction of CPL dynamics of tightly regulated point-of-load converters. A cascaded system is formed when an upstream feeder is interfaced to a downstream load by connecting their output and input terminals, respectively. This resembles a feedback connection between two subsystems where the combined closed-loop behaviour can be fully determined by their transfer characteristics as viewed from the interface terminals. Nonetheless, small-signal stability can be more easily tested by applying the classical single-loop Nyquist criterion where the open-loop transfer function[2] is the input/output impedance ratio between the subsystems. Below we provide a brief discussion on source-side and load-side characteristics responsible for the susceptibility of LVDC DPSs to small-

[2] The *open-loop transfer function* is often referred to as the *minor-loop gain* when discussing cascaded power systems, originating from the seminal works by Middlebrook et al. [36], [37].

signal instability, while the underlying mechanisms of interaction and stability analysis are introduced in more detail in Section 1.2.2.

Poor damping in LVDC DPS is an unwanted side-effect of ongoing trends affecting the electrical properties of these networks. In essence, a passive power distribution network can be described as an electrical circuit comprised of a combination of resistances, capacitances, and inductances. These elements form a series of resonant circuits that can approximate the network characteristics in terms of the damping coefficient and frequency of one or more modes. The damping coefficient governs whether oscillations occur following a disturbance. The most basic configuration of a damped circuit is the *RLC* filter. We can expect far less damping in future networks by considering the relative changes to R, L, and C as systems evolve.

Firstly, LVDC DPSs are increasingly characterised by their small system capacitances. Capacitors are an essential part in applications dominated by power electronics and are typically located at both the output and input terminals of converters. They serve two main functions: energy storage and filtering. Large capacitances (provided by what is often referred to as *bulk* or *reservoir* capacitors) provide stabilizing energy to prevent sudden deviation in voltage following transients and to filter low-frequency ripple. This smooths the voltage locally providing enough time for converter feedback loops to adequately regulate output. In contrast, filtering at higher frequency (using *decoupling* capacitors) is also required to prevent the harmonics generated by the switching converter from reaching power lines. Likewise, these high-frequency filters prevent any harmonics already present in power lines from affecting the power converter. These capacitors are typically paired with an inductor to form of a 2^{nd} order filter for greater attenuation of unwanted frequencies with minimal DC losses.

The design of power electronic converters in recent years has focused on reducing the size of passive components, including capacitors, to achieve higher power densities. A prime example of this is in transport applications due to limited onboard space and stringent payload requirements. Switching frequencies have steadily increased over the years thereby reducing the voltage ripple enabling a lower DC bulk capacitance and both input and output terminals. Additionally, harmonic filters may be designed with higher cut-off frequencies to minimize their footprint through smaller inductors and/or capacitors. While the capacitance may be optimised for density in individual power converters,

this comes at an expense to the damping characteristics of the modes of the wider power system network. Assuming all other parameters are held constant, this results in a shift towards a less stable operating region leading to larger voltage overshoots and potentially resonance.

Secondly, damping of oscillations is mainly governed by resistive circuits such as snubbers. However, resistive losses are undesirable and are typically minimised to maximise efficiency. This has led to a vast body of literature on the design and implementation of passive and active control methods to introduce damping by reshaping the impedances of power converters [25]–[29].

Lastly, in real-world LVDC DPSs, sources and loads are interconnected via inductive lines—a DC distribution bus that is entirely capacitive is unfeasible. Often LVDC networks are modular and power paths are through cables over a long distance. Together with reduced capacitive and resistive characteristics, inductive properties may begin to dominate. Due to the fact that both inductance and resistance scale linearly with cable length, it is possible for the power network to inherently have low damping.

Another factor is the introduction of CPLs. An increasingly prevalent class of electrical and electronic systems operate on either a fixed voltage or fixed current with power conversion achieved through tight regulation of switching power converters. To maintain conversion with high efficiency the voltage/current should vary inversely: for example, the converter draws less current as the source voltage increases and vice versa. Therefore, within the regulator bandwidth, these load converters appear to exhibit CPL behaviour with negative incremental resistance to the source-side network [29]–[31]. This effectively adds a negative damping characteristic to the system.

In literature, much of the early work in analysing the effect of tightly-controlled converters have used the ideal model of a CPL and its linearised equivalent [32], [33]. While this typically indicates the worst-case condition, the clear disadvantage of this approach is that this yields overly-conservative analysis and does not show the impact of controller interactions [19], [31], [34]. Detailed models are required to investigate the impact on system behaviour.

The proliferation of power electronic interfaces in LVDC power systems with stringent requirements for efficiency and power density is leading to less overall damping of power distribution networks. Likewise, point-of-load regulators appear as CPLs which

introduce negative damping. Together, these two factors increasingly challenge the stability of these networks. Of particular interest is the stability of LVDC DPS when subjected to continual small disturbances (such as random noise, parameter variations, ambient temperature, and minor load changes). Excessive oscillations are well known to trigger protection devices, damage components, result in overheating, and reduce system lifespan.

1.2.2 Interactions influencing small-signal stability

In the previous section, we introduced two critical ongoing developments in LVDC DPSs that will impact small-signal dynamics. First, the resonant properties of power networks often become poorly damped. Second, converters based on power electronics typically behave as CPLs, introducing negative damping. Together, these factors are well known to have a significant impact on the interactions between power system components that may lead to excessive oscillations and instability.

The focus of this thesis is on the small-disturbance stability of DC power systems. Here, instability is associated with a negative damping of modes such that the system variables associated with those modes (i.e., the voltages and currents) will begin to self-oscillate with exponential behaviour following small-signal perturbations. Chapter 2 introduces this phenomenon in more detail.

LVDC DPSs are composed of many interconnected subsystems. The dynamic response of the complete system is a function of the individual subsystems and the interactions that occur between subsystems. Here, we make a distinction between two types of interactions that may contribute to the combined dynamics: *source-load interactions* and *modal interactions*.

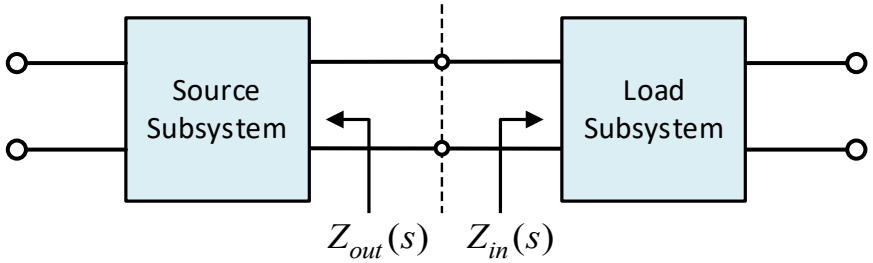

FIGURE 1.5 Circuit representation of a DC system with source and load subsystem.

1.2.2.1 Source-load interactions

Any DC power system, as shown in Figure 1.5, can be divided into a cascaded source and a load subsystem. Dynamics of this cascaded system is a function of the interaction between the source and load—through closed-loop feedback (see Section 2.3). Load-side dynamics can excite oscillatory modes in the source-side circuit. As such, we will refer to this phenomenon as *source-load interaction.*

The source-side subsystem in Figure 1.5 may have natural modes of oscillation from its inherent circuit characteristics. Considering a simple low-pass LC filter, the voltage and current will oscillate when inductive reactance ($\mathrm{X_L} = \omega L$) and capacitive reactance ($\mathrm{X_C} = 1/\omega C$) are of equal magnitude ($\mathrm{X_L} = \mathrm{X_C}$) at a resonant natural frequency (ω_n), with solution given in (1.1):

$$\omega_n = 1/\sqrt{LC} \tag{1.1}$$

In a practical filter, the presence of a resistive component in the circuit (e.g., inductor's parasitic DC resistance) results in harmonic oscillations decaying over time. In an RLC circuit, the resistance contributes to damping (ζ) and also reduces the peak resonant frequency the oscillation. In the underdamped case, the dynamics of the circuit represented by $x(t)$ will have solution of the form shown in (1.2):

$$x(t) = a_1 e^{\lambda_1 t} + a_2 e^{\lambda_2 t} \tag{1.2}$$

Where,

$$\lambda_{1,2} = \omega_n(-\zeta \pm j\sqrt{1-\zeta^2}) \tag{1.3}$$

The constants a_1 and a_2 are initial conditions, ζ is the damping ratio, and natural frequency is ω_n as before.

The addition of a load at the output of the source-side circuit forms a cascaded closed-loop system. Compared to an unterminated source, the closed-loop feedback with the load influences the characteristics of the oscillatory modes. It has been well demonstrated in literature that the addition of active loads, with fast controller dynamics, (i.e. CPLs) present as a negative input impedance at the output of poorly damped networks (i.e. filters) which can form a unstable cascaded system [33], [35]–[37]. This indicates that the critical mode's damping ratio has shifted—damping has become negative and thus the system is pushed into instability.

With source-load interaction, the combined system dynamics are changed with the damping and frequency of a single (local) mode. This is in contrast to modal interactions, which will be introduced next, where the dynamic properties of multiple modes are coupled together.

1.2.2.2 Modal interactions

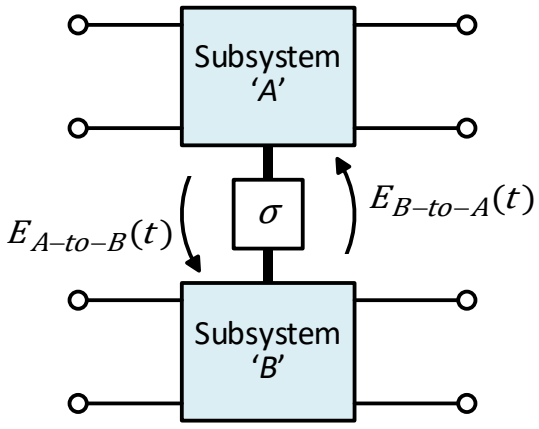

FIGURE 1.6 Circuit representation of a DC system with modal coupled subsystems. A coupling factor σ influences energy exchange between subsystem A and B.

Another type of interaction is referred to as *modal interaction,* in which two or more oscillatory modes become coupled thereby having mutually dependent properties. Frequency and damping characteristics are therefore no longer independent between the modes.

When multiple modes at similar frequencies exist in the system, they may interact with each other and exchange energy. This is represented by Figure 1.6. Subsystems

may be coupled through some parameter(s), or coupling factor σ, which can alter the damping properties, potentially establishing conditions for sustained oscillations. These modal interactions have been known cause unexpected small-signal characteristics in power systems over parameter variations [17], [38], [39], and potentially problematic to the reliable operation of future LVDC DPSs.

Modal interaction phenomena occur in multiple other engineering fields, including mechanics [40], electromagnetics [41], acoustics [42]. A vast body of literature suggests that modal interaction phenomena may have a significant impact on response dynamics and stability in sensitive systems [21], [23], [43]–[47]. Sometimes this phenomenon is referred to in literature as eigenvalue interaction, resonance interaction, mode coupling.

One of the well-known examples of modal coupling phenomenon in traditional power system is the condition of subsynchronous resonance. The mutual exchange of energy below the synchronous system frequency through coupling between turbine generators and natural modes of the grid has been observed to result in unstable oscillations [48]. These so called 'inter-area' modes pose risk if poorly damped [49], [50] and have received increased attention in the power systems community in the past decades.

Existing literature on LVDC DPSs has often been limited to investigating and mitigating instability due to only source-load interactions. Often network dynamics are neglected or lumped together by modifying impedance to reduce to a simplified model. This ignores the impact of changing the operating point on the rest of the system. In a realistic LVDC DPSs, there a very real possibility that coupling occurs between multiple modes, as indicated by [26], [51]. These interactions are typically encountered in power systems as resonances, with an exchange of energy between different subsystems where multiple natural frequencies coalesce.

Recent evidence suggests that the small-signal stability of LVDC DPSs can be significantly influenced by both *source-load interactions* and *modal interactions* [26], [51]. The impact and the relationship between these interactions on small-signal dynamics must therefore to be understood and quantified. A more detailed theoretical preliminary on modal interactions is given in Section 2.4.

1.2.3 System modelling and stability analysis techniques

Modern LVDC DPS architectures are characterized by the interconnection of multiple components across distribution lines, potentially including a wide array of different power electronic-based interfaces, generators, and loads. These devices have a fundamentally nonlinear behaviour. While all components may be designed to be individually stable, the interconnection between them forms a circuit with feedback. As a result, the combined system dynamics is determined by a nonlinear combination of the individual component dynamics and their interactions.

The study of LVDC DPS stability relies on a suitable representation of the real-world behaviour using mathematical modelling, such that system's dynamic phenomena under consideration is adequately captured. Small-signal analysis assesses power system's dynamic behaviour around a known equilibrium point following small perturbations. In practice, following a disturbance the system will either converge back to the previous (small-signal stable) equilibrium or diverge with increasing amplitude (small-signal unstable). Under these conditions, a linear approximation of the system is sufficient, and enables the use of a wide variety of mathematical methods developed for linear time invariant (LTI) systems, with some shown in Figure 1.7.

While system dynamics under small perturbations can be assessed using a linearised system model, the model itself varies nonlinearly with changes to the individual components, their parameters, and operating conditions. As a result of interactions, the dynamic characteristics of the aggregate system are a nonlinear combination of the individual components. Furthermore, modern switching converters have complex internal dynamics and fast controls that have been shown to interact and impact power network stability [19], [52], especially those DPSs consisting of multiple nodes and uncertainties [53], [54].

The dynamic behaviour under large disturbances is referred to as large-signal stability analysis. Stability can be assessed with a wide range of parameter variation and operating points [55]–[57]; however, this also includes stability after step changes such as start-up/shut down of loads and any faults conditions. While large-signal stability can be assessed, identification and quantification of interaction phenomena based on nonlinear models can be highly demanding in terms of modelling effort and computational cost

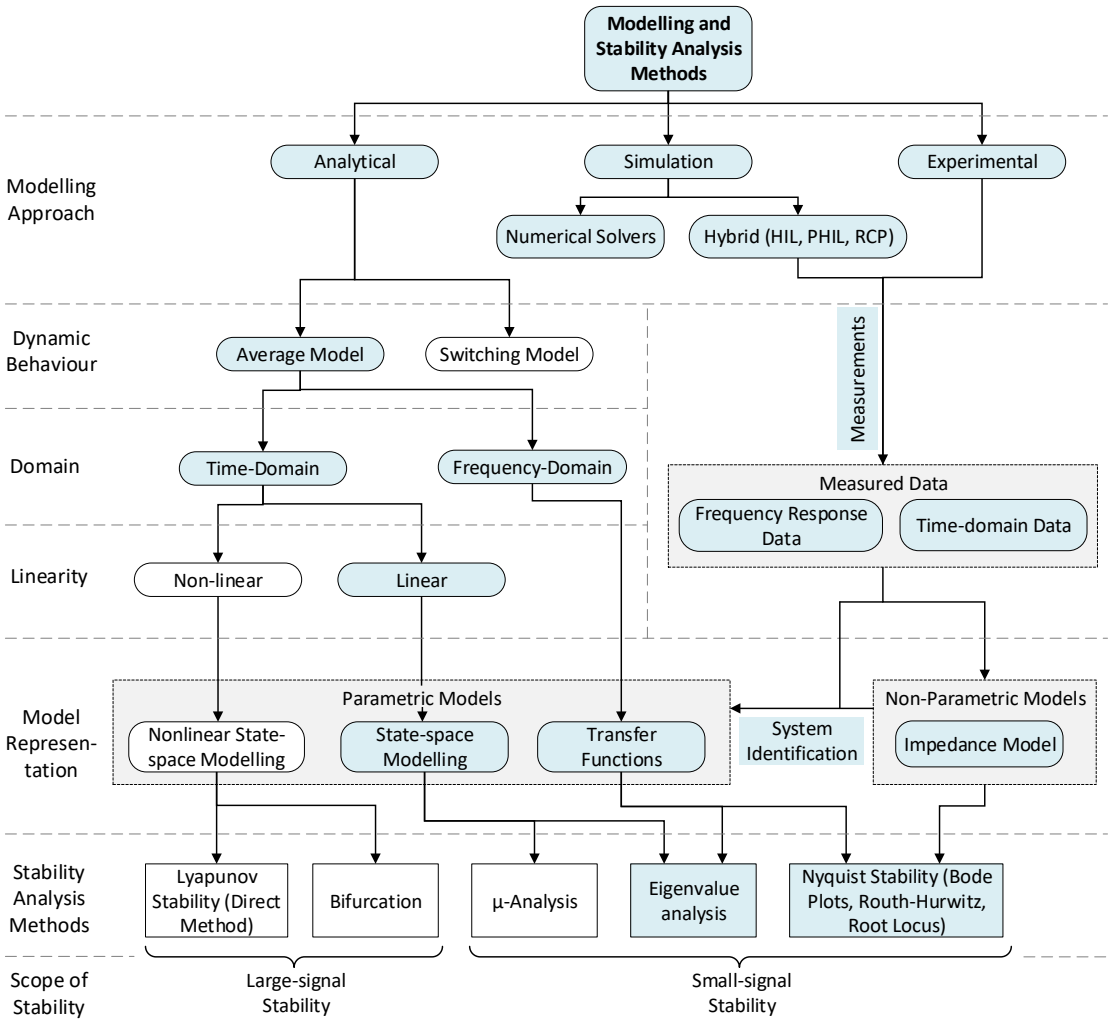

FIGURE 1.7 An overview of modelling and stability analysis methods used for power electronics-based LVDC DPSs. Those highlighted in blue are within the scope of this thesis.

[58]. Likewise, robust stability assessment based on a μ-analysis enables the inclusion of multiple uncertain parameters on system dynamic behaviour to determine robust stability margins [53], [54], [59]–[61]. These methods are based on computation of bounds on μ, and cannot be used to investigate interaction effects.

Understanding how interactions contribute to nonlinear behaviour becomes fundamental to avoiding unstable power system oscillations. Continual effort has been made for methods for stability and interaction analysis, and often these benefit from the development of nonlinear averaged models that a can used to derive the linear model at given operating parameters and inputs [62], [63].

As illustrated in Figure 1.7, linear stability analysis techniques for power systems fall into two broad categories: impedance-based frequency domain analysis and state-space eigenvalue analysis.

Impedance-based methods, based on the application of the Nyquist stability criterion, are commonly used in literature to assess the small-signal stability of LVDC DPSs and to formulate design criteria that guarantee stability. Originally introduced to study cascaded DC-to-DC converter systems by Middlebrook et al. [36], these considered source-load impedance interactions at an interface. Referring to source-load system in Figure 1.5, the Nyquist stability criterion can be applied to the open-loop transfer function, the ratio between the output and input impedances ($Z_{out}(s)/Z_{in}(s)$); further detail is given in Section 2.3. To guarantee that the open-loop transfer remains stable following connection Middlebrook et al. proposed the sufficient condition of $|Z_{in}(s)| \gg |Z_{out}(s)|$[37]; while many others developed less conservative design-oriented stability criteria [64]–[66]. Application of impedance-based analysis, however, is not prevalent for medium to large power systems.

Impedances of subsystems are often determined by practical measurement. Converters are considered as state-less, 'black-box', two-port networks [33]; without needing parametric modelling or detailed knowledge of internal structure of these circuits. These measured models can be easily combined to find stability margin or be used to define boundary conditions for any additional subsystem. However, parameter variations cause the small-signal dynamics to vary nonlinearly with operating point [20], typically requiring a parameterised time-domain nonlinear model to calculate the impedances over possible operating points [63]. Determining parameter influence on states and small-signal interaction phenomena via impedance-based methods becomes a challenge, providing limited insight in practical uncertain systems.

A state-space representation can be used to model large power systems, with the small-signal dynamics assessed via eigenvalue analysis. This method decomposes a combined linear system of differential equations, represented by equation (1.4), into a set of eigenvalues. Eigenvalues denote the oscillatory modes and are calculated by solving the characteristic equation in (1.5).

$$dx(t)/\mathrm{dt} = Ax(t) \tag{1.4}$$

$$(\lambda \mathrm{I} - \mathrm{A})\psi = 0 \tag{1.5}$$

Where A is the linearised system state matrix, x are the state variables, ψ is the right eigenvector. The damping ratios and frequencies of each of the eigenvalue modes are defined previously in (1.3).

The advantage of eigenvalue analysis is that calculations in in (1.5) are straightforward [67], provided the system has been appropriately linearised at a given operating point. Unlike impedance-based methods, which depends on analysis at a given interface, the eigenvalue-based approach finds the finds the frequency and damping factor (and therefore stability) of all modes in the entire system. This is particularly important for LVDC DPSs where critical destabilising modes are not known *a priori*. Furthermore, participation analysis may be used to identify of which states variables influence which modes, and vice versa.

The trajectory of eigenvalues movement under parameter variations may be studied, showing the changes to shape of modes [19], [68]. In power systems these parameter variations may represent load changes, component aging, environmental temperatures, and other uncertainties. If and when the locus of eigenvalues crosses into the positive right-half plane, then the power system is unstable under small-signal conditions.

The challenge in applying these techniques to LVDC DPSs is the effort and complexity of modelling. The full system model of a LVDC DPS is formed by the interconnection of many individually modelled lower-order subsystems. The subsystems, often power electronics based, have nonlinear dynamics over a wide range of operating points therefore requiring detailed (nonlinear) modelling. Conventional approaches typically linearise subsystem models prior to combining [19], [69]. However, linearisation requires knowing the precise operating point which can only be determined from the dynamics of the full, combined system. As such, stability and interaction analysis of a single linear model under nominal conditions becomes highly constrained when considering uncertainty.

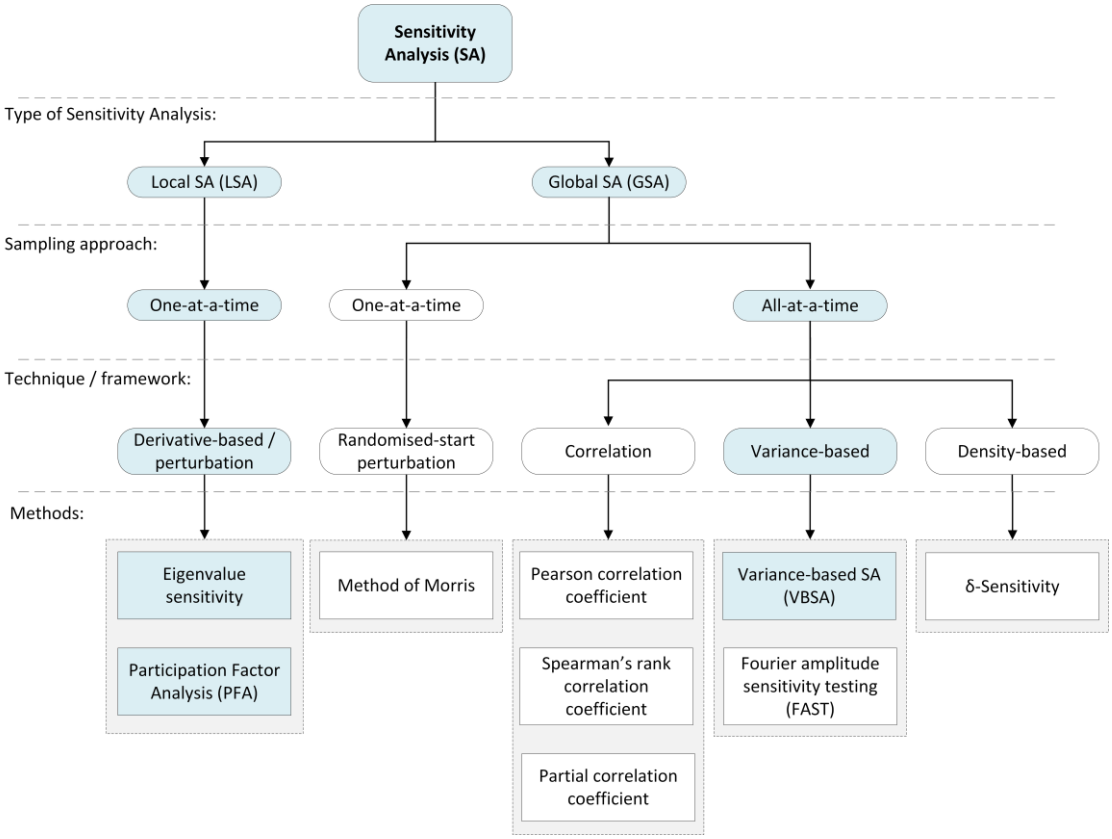

FIGURE 1.8 An overview of several methods used for sensitivity analysis. Methods that are highlighted in blue are within the scope of this thesis.

1.2.4 Identification of interactions in the presence of uncertainties

When analysing the stability and interaction dynamics of power systems, it is convenient to assume that models, regardless of their fidelity, are a precise representation of real behaviour. In reality, however, uncertainties are unavoidable. This is a particular problem for future LVDC DPSs, with highly variable system conditions, proliferation of intelligent power electronic converters, harsh environments, and often an evolving topology over time.

Today, engineers need new methods to examine a vast number of possible operating conditions to determine the likelihood of poorly damped or unstable modes due to increasing and complex interactions between subsystems.

There are two major concepts when dealing with uncertainty. The first is *uncertainty quantification* that aims to identify and characterise different forms of uncertainty in system models. These are comprised of aleatory (irreducible) uncertainties (e.g., random variation over time due to environment, component aging effects), and epistemic (reducible) uncertainty (e.g., due to model simplification, inaccurate parameter data) [70]. Aleatory uncertainty will always be present and should be explicitly modelled, most commonly using probability distributions [71] or bounds [60]. Epistemic uncertainty can be reduced with model refinement and measurements, however, in practice this proves burdensome and still must be modelled with probabilities based on experimental data (e.g., component value tolerances).

The second is concept is *sensitivity analysis* (SA). While precise quantification of uncertainty can be worthwhile, it is often unnecessary. Some system parameters might have little to no effect on the system's dynamics over their possible values. SA aims to determine of the influence of different parameter values on a phenomenon of interest (e.g., system outputs or metrics such damping factor). Identification of the most influential parameters allows for better management of risks to stability of future LVDC DPSs.

Figure 1.8 shows the key SA methods applied to power systems. Local SA methods are applied to a single (nominal) model and are based on calculating partial derivatives. Application of these methods to power systems are typically through participation factor analysis [19] and eigenvalue sensitivity analysis [72]. However, analyses of nominal models are not able to identify nonlinear effects and parameter interactions over a wide range of uncertainties. To overcome limitations of local SA, probabilistic global SA methods are proposed to evaluate the influence of parameters across their full (global) uncertain range [73].

The method of Morris extends partial derivative calculations by a *one-at-a-time* variation of inputs to sample the system at different operating points [73]. While able to establish nonlinearity and interaction effects, the Morris method cannot discriminate between the two. To identify parameter interactions, variation of inputs over possible operating points is required, known as *all-at-a-time* variation. Alternative methods for this approach can be categorised as correlation-based, variance-based, and density-based—as shown in Figure 1.8. A good candidate for application to LVDC DPSs is variance-based sensitivity analysis (VBSA) [73]–[75], introduced in detail in Chapter 2.

1.3 Research Aims and Objectives

The thesis focuses on the small-signal stability of power electronics dominated LVDC DPS and the analysis of interactions between system components. Compared to traditional power systems, DPSs are increasingly prone to small-signal instability risks with the introduction of fast control loop dynamics of power electronic interfaces interacting with poorly damped oscillatory modes of the distribution network. These systems are subject to many inherent uncertainties and a wide range of operating conditions. Interactions occurring between components may influence the small-signal stability in a nonlinear manner, therefore extrapolating behaviour based on nominal models in no longer sufficient for highly uncertain systems. Therefore, the impact of interactions on stability assessment under uncertainty poses a significant challenge for analysis of LVDC DPS model behaviour. Identifying, quantifying, and understanding the nature of these interactions is an important first step towards further design, analysis, and system integration.

A primary concern in the development of LVDC DPS is ensuring the stable steady-state operation under small-signal disturbances and shifts in operating point due to parametric uncertainties. This work proposes the application of variance-based global sensitivity analysis to identify the critical parameters influencing interactions between components over the full range of uncertainties. We aim to develop suitable modelling and analysis tools that enable probabilistic analysis while incorporating detailed subsystem models including controller dynamics. Additionally, we aim to validate modelling results through numerical simulation and laboratory experiments.

A case example where interaction phenomena critically impact stability is the modal coupling between parallel-connected input filters of CPLs fed by a common point through a non-ideal source. In this configuration, the precise nature of the effect of source-side characteristics on modal coupling has been so far unaddressed. A contention exists in the state-of-art as to the effect of resistive characteristics at the source on system small-signal stability—an apparent dichotomy exists, previously demonstrating that resistance can contribute to both an increase in stability margin [51] and a decrease in stability margin [26]. Following VBSA to find the critical factors affecting small-signal stability, we aim to address the modal coupling phenomena systematically through modal

analysis to finally resolve the contention. The developed tools and methodology are expected to find further application in the study of parameter uncertainties on interaction phenomena in LVDC DPSs.

The following research objectives have been established to address the knowledge gaps and above-mentioned aims:

1. To investigate the underlying mechanisms leading to small-signal instability in LVDC systems with high penetration of tightly-regulated power electronics interfaces under weak DC distribution grid conditions. In addition, to compare the dynamics of ideal CPLs to the input impedance characteristics of point-of-load converters with output regulation.
2. To establish a methodology for the analysis of parameter interactions and to develop a set of practical tools for fast and accurate probabilistic small-signal analysis of LVDC DPSs. This enables evaluation of the novel technique of VBSA to study the influence of parametric uncertainties on system dynamics.
    a. Development of a MATLAB toolbox to automate the generation of nonlinear symbolic system models based on the input-output interconnection of different components; to create a library of component models to accurately describe the dynamics of power electronics interfaces with detailed circuit representation and feedback controllers.
    b. Based on the generated system models, perform probabilistic small-signal stability analysis through linearisation and calculation of eigenvalues over multiple parameter uncertainties simultaneously.
    c. Identify the most influential parameters and their interactions through the computation of *variance-based sensitivity* indices.
3. To investigate the dichotomy in the effect of source-side resistance on small-signal stability due to modal coupling between parallel-connected input filters feeding CPLs.
    a. Apply linear modal coupling theory to investigate the causal relationship of source-side resistance characteristics on the sensitivity and location of eigenvalues related to the resonant modes of input filters.

1.4 Main Contributions and Outline of the Thesis

The dynamics and stability of future electrical networks is a major concern as they transition towards power electronics dominated DPS. The proliferation of renewable energy sources and electrification of end-uses has given rise to an increased interest in LVDC DPS. However, concerns exist over the stability in these systems as interactions between source and load subsystems which are known to occur. Power-electronic interfaced loads can introduce a destabilizing effect due to their negative impedance characteristics at the same time as the inherent damping of networks are weaker in DPS compared to traditional CPS.

This thesis focuses on the issue of modelling and small-signal stability analysis of LVDC power networks with the practical consideration of parametric uncertainty. Existing literature has often neglected the effects of multiple changing parameters on the occurrence and impact of subsystem interaction on stability and dynamic performance. Probabilistic small-signal studies with high-fidelity models require new computationally efficient tools to be developed. This enables the study of parameter interactions through the application of VBSA allowing identification and quantification of interactions between two or more factors. One such interaction phenomenon, understudied in the literature, is the modal coupling phenomena between parallel loads influenced by the characteristics of supply-side interfaces.

Chapter 2 begins with an overview of the distribution structures which provide the functions to create more complex LVDC DPSs—paralleling, cascading, stacking, source-splitting, and load-splitting. Using a basic model of two cascaded subsystems, the theoretical basis of the instability phenomenon in LVDC DPS is introduced. The feedback interaction between a downstream CPL and a poorly damped upstream circuit causing instability is analysed using impedance-based stability analysis. Also, the current state-of-the-art mitigation and control methods to address this problem are reviewed.

Chapter 2.6 presents a systematic modelling framework for the detailed dynamic modelling of LVDC DPS suitable for small-signal analysis. Individual sources and loads (including controller dynamics), as well as the power distribution network, are all modelled as individual subsystems. To account for parameter uncertainties, a wide range of

operating points, and nonlinear dynamics of various subsystems, the subsystems are represented by nonlinear ordinary differential equations in symbolic form. To construct the full nonlinear dynamic model of the system, each subsystem is combined based on input-output connections. In contrast to previous approaches in the literature, symbolic linearisation is performed with steady-state equilibrium values calculated based on the nonlinear model allowing an analytically tractable and computationally efficient model for small-signal analysis applicable for probabilistic studies (in Chapter 5). A new MATLAB toolbox, called *SymMIAL* (*Symbolic Model Interconnection and Linearisation*), was developed to automate the modelling procedure, linearisation, and small-signal stability assessment.

Modelling and small-signal stability analysis using eigenvalues are demonstrated on several examples small-scale LVDC DPS with results verified, through both time-domain simulation studies and laboratory experiments, validating the applicability of the specified procedure. Additionally, individual subsystem impedances are derived with this framework which is used for stability analysis through the Nyquist stability criterion. Further results show that tightly controlled load-side converters can have their dynamic modelling reduced to ideal CPLs depending on controller parameters (used in Chapter 6).

Chapter 4 describes the experimental system and simulations used to validate the applicability of the modelling procedure (Chapter 2.6) and to verify the analysis of modal coupling phenomenon investigated in Chapter 6. A single active load comprised of an input LC filter with a tightly-controlled synchronous buck converter feeding a resistive load is presented. The description of the hardware implementation, digital controller design, and experimental measurements are given, and comparisons between theoretical models and experimental data are shown to closely match. Additionally, the experimental setup with the parallel operation of two active loads (studied in Chapters 5 and 6) is presented.

Chapter 5 outlines the foundation for VBSA as a probabilistic framework for identifying and quantifying first-order and total-order effects of parameters, including parameter interactions, across all possible operating conditions. This work develops a novel procedure for applying VBSA to practical models of LVDC DPS to assist the

understanding of parameter effects on the small-signal stability. Advantages over conventional sensitivity analysis based on single nominal models is discussed.

VBSA is applied to a number of different LVDC DPS models to demonstrate its applicability. In cascaded systems with multiple loads, the influence of parameters differed substantially between scenarios. In the first case study, VBSA was used to identify and select the critical subsystems with load and controller bandwidth uncertainties in a network of *N*-parallel loads. In the second case study, VBSA was performed on two systems with identical structure but with different nominal values. Results indicated that the effectiveness of source-side resistive damping was reduced when resonant frequencies of load input filters are nominally matched. Interactions are present between parallel loads and source-side resistances, and these results are verified against conventional derivative-based sensitivity analysis and discussed. For the first time, the apparent dichotomy in the effect of source-side line resistance is revealed: line resistance can act as both a stabilizing and destabilizing element on the overall system depending on operating conditions.

Chapter 6 contains a detailed analysis of the effect of the resonant coupling phenomenon between parallel loads reported in the literature (Chapter 2). Subsequently, it was revealed that stability is influenced by the interaction of source-side resistance and active loads in Chapter 5. Linear modal coupling theory is extended to analyse this phenomenon. Divergence of eigenvalue loci between the coupled-system model and the equivalent decoupled-system model is used to quantify the effect of the coupling phenomenon, as well as predict the best and worst-case system damping. Through analysis of the coupled/decoupled-system models, the dichotomy presented in Chapter 5 is resolved: line resistance can be apportioned to both subsystem damping and contribute to the coupling between subsystems. Line resistance is destabilizing when the contribution of coupling exceeds that of the damping contribution and vice-versa.

The trajectory of eigenvalues under parametric perturbations is also shown to exhibit a mode swapping behaviour, where continuous eigenvalues exchange modal properties instead of diverging. To address this phenomenon, an algorithm based on participation factor analysis has been developed to ensure the conformity of eigenvalues to given subsystems.

Small-signal stability and sensitivity analysis of the system models are validated through experimental results, and several scenarios are presented showing the impact of the modal coupling phenomenon on stability.

This chapter also demonstrates that a resistive-based active damping controller implemented alongside source-side voltage regulators can produce a destabilizing effect on parallel-connected active loads. This further confirms that controller dynamics can interact with the overall system dynamics to impact overall system stability and must be modelled in detail. Simulation studies confirm behaviour.

Chapter 7 summarises the major research outcomes of this thesis and provides recommendations for future work.

As part of this thesis the following journal paper was published, *'Influence of parametric uncertainties and their interactions on short-signal stability: A case example of parallel-connected active loads in a DC microgrid*' [76] relating to the research further expanded upon in Chapter 5. This work was also presented at the 9th IET International Conference on Power Electronics, Machines and Drives (PEMD 2018).

Chapter 2

Preliminaries on Interaction Phenomena in LVDC Distributed Power Systems

ABSTRACT This chapter provides a background to the phenomena of dynamic interactions in LVDC Distributed Power Systems (DPSs). In cascaded systems, the negative input impedance characteristics of a constant power loads is shown to interact with the output impedance of poorly damped source-side networks. With linear feedback analysis in the frequency-domain, it can be shown that the ratio between input and output impedance must satisfy the Nyquist criterion (or a derived design-oriented impedance-based criteria) in order to guarantee stability.

This thesis uses the linear state-space modelling approach and its subsequent modal decomposition to investigate small-signal stability. The advantages of state-space are made clear in relation to the study of modal interactions—introduced within—and the need for a generalised modular modelling framework to develop large system models (addressed in Chapter 2.6). This chapter discusses the state-of-art and contains the theoretical preliminaries for the remainder of the thesis.

2.2 Introduction

The growing importance of LVDC power networks to future decentralized low-carbon infrastructure is being enabled by power electronic converters, as previously discussed in Chapter 1. As such, the structure of these power networks is transitioning from one based on a single CPS to many DPSs. With this change, new challenges are emerging to the stability of DPSs and therefore is a prime concern to their implementation and adoption.

The rest of the chapter is structured as follows. Section 2.3 establishes the background to the fundamental problem of source-load interactions on small-signal (in)stability in cascaded power systems using the well-established frequency domain approach. The dynamic characteristics and impact of both CPLs and poorly damped source-side filters are shown using impedance-based stability criteria. As an alternative to the frequency domain, Section 2.4 sets out the theory for time-domain state-space system modelling for modal decomposition and eigenvalue analysis. Using the state-space representation, Section 2.5 introduces the phenomenon of modal interactions (also referred to a modal coupling or resonant interactions) and their impact on small-signal stability; demonstrated by tracing the behaviour of system eigenvalues under parametric variation. Finally, Section 2.6 summarises the chapter.

2.3 Source-load Interactions

The early 1970's saw dramatic developments of power electronic switch-mode converters with the introduction of commercially available power MOSFETs. Due to their switching nature, unwanted signals are generated and the input and output terminals of these power regulator that cause electromagnetic interference (EMI) [33]. Low-pass differential-mode power line filters and common-mode chokes have been a typical measure ever since for limiting conducted EMI from converter inputs impacting the power quality of upstream distribution [77].

However, the addition of input filters to regulated converters was observed to cause unstable voltage oscillations in the filters. With the advent of fundamental research on the modelling and analysis of power electronic converters, such as state-space averaging techniques pioneered by Middlebrook and Ćuk [32], [78], it was determined that the feedback interaction mechanism from the cascade-connection of individually stable subsystems could result in a violation of the Nyquist stability criterion. Herein the phenomenon shall be referred to as source-load interactions. Middlebrook proposed a simplified criterion on the input and output impedances to ensure sufficient system stability by analysing the dynamic interaction via the open-loop transfer function, often referred to as the minor-loop gain. A plethora of less restrictive stability criteria have also been developed in the following years [64]. Ensuring stability is typically addressed by damping the resonant peaks of source's output impedances.

Today, the transition to DPS is marked by the need for greater renewable penetration and electrification of loads. Large systems of many interconnected power electronic converters and distribution lines are increasingly more common which ultimately results in many new interface points where source-load interactions may result in instability.

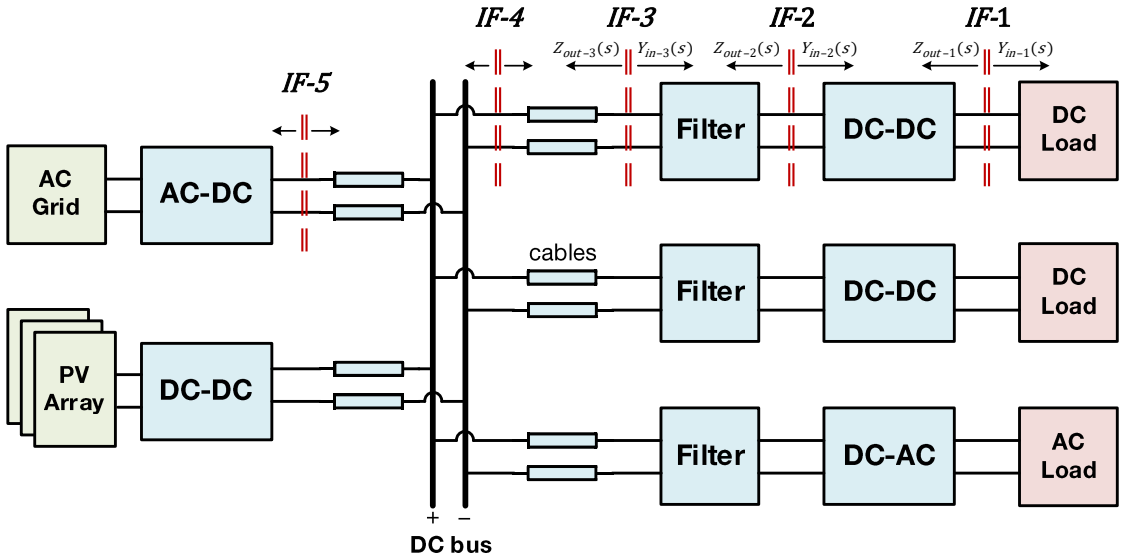

FIGURE 2.1 An example LVDC distributed power system. The source-load interfaces (*IF-1* to *IF-5*) are subject to impedance interactions.

Figure 2.1 shows an example of a LVDC DPS. Multiple DC-to-DC or AC-to-DC converters supply energy and regulate the voltage of the primary distribution bus. Shown explicitly are the cables between the different subsystems that are an important contributor to the network characteristics [13], [72]. Many independent filter-converters feed AC and/or DC loads. It is important to emphasise that these loads may also represent its own power network, such as those seen in intermediate bus architectures [79]. In this diagram it is crucial to understand that all interfaces, such as those denoted as $IF-1$ to $IF-5$, have the potential for source-load interaction as seen from the interface. More broadly, any arbitrary interface between different cascaded subsystems may result instability. Dynamics of lines due to cable characteristics can also be viewed unique subsystem with their own input/output interfaces.

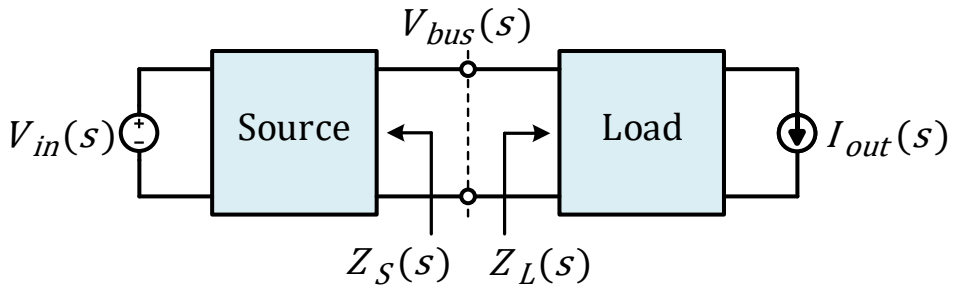

FIGURE 2.2 Cascaded two-stage power system with source-load interaction due to source-side output impedance $Z_S(s)$ and load-side input impedance $Z_L(s)$.

A most basic example, as it relates to destabilisation, is when the source subsystem is a low-pass power line filter and the load subsystem is a regulated DC-to-DC converter. Referring to Figure 2.2, the combined behaviour of cascaded system can be expressed as the voltage-gain transfer function, ratio of $V_{bus}(s)$ to $V_{in}(s)$, in (2.1):

$$\frac{V_{bus}(s)}{V_{in}(s)} = \frac{Z_L(s)}{Z_S(s) + Z_L(s)} = \frac{1}{1 + T_{OL}(s)} \tag{2.1}$$

Where $T_{OL}(s)$ is defined as the open-loop (OL) transfer function and often referred to as the minor loop gain [33], [37], given in (2.2):

$$T_{OL}(s) = Z_S(s)/Z_L(s) \tag{2.2}$$

The function $1/(1 + T_{OL}(s))$ can be viewed as the source-load interaction between $Z_S(s)$ and $Z_L(s)$. If $T_{OL}(s)$ is zero for all values of $s = j\omega$, then the source and load can be considered fully decoupled and no interaction will occur. Establishing stability can be achieved by analysing just $T_{OL}(s)$ by its encirclements of $(-1,0)$ in the clockwise direction on a Nyquist plot [80]. Each encirclement signifies that an unstable pole exists in the closed-loop characteristic equation.

The next subsection 2.3.1 shows that the input impedance of an ideal CPL (as the downstream converter, $Z_L(s)$), has a negative resistance characteristic.

2.3.1 Negative input impedance characteristic of downstream constant power loads (CPLs)

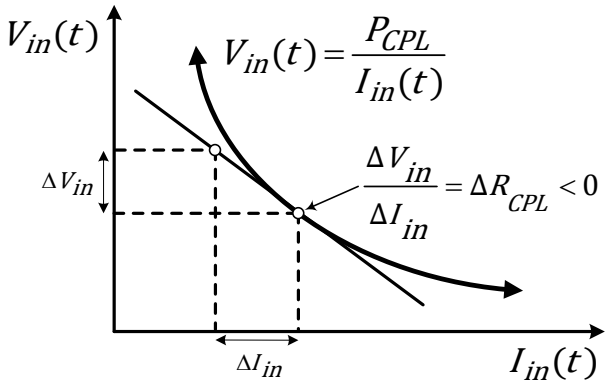

FIGURE 2.3 The negative incremental impedance characteristic ($\Delta R_{CPL}<0$) of an ideal CPL.

An increasingly prevalent class of electrical and electronic systems operate on either a fixed voltage or fixed current with power conversion achieved through tightly regulated switching power converters as an interface. To maintain this regulation with high efficiency, as the source voltage increases the interfacing converter draws less current and similarly as the source voltage decreases the converter draws more current. As a result, within the regulator's bandwidth, these systems, also known as point-of-load converters, appear as CPLs to the source [29], [81], with equation in (2.3).

$$V_{in}(t) = \frac{P_{CPL}}{I_{in}(t)} \tag{2.3}$$

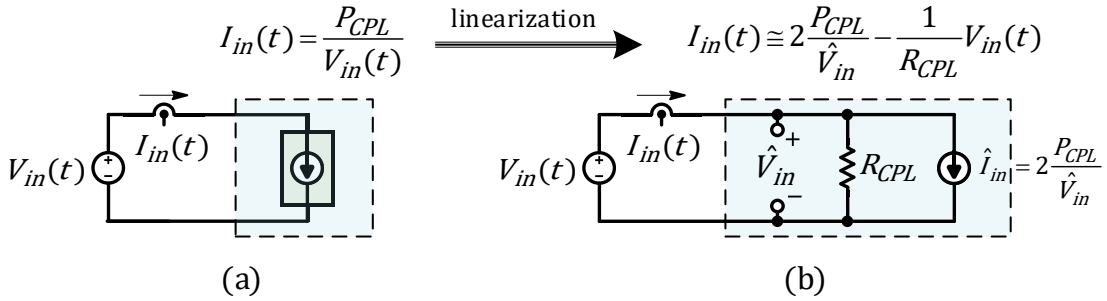

FIGURE 2.4 Circuit diagrams of an **(a)** ideal CPL; and its **(b)** linearised equivalent.

Mathematically, the negative impedance characteristic of converters can be shown by considering the incremental resistance of an ideal CPL. Referring to Figure 2.3, the ideal CPL shows a nonlinear voltage-current relation so that at any operating point the linearised incremental impedance always negative.

The incremental impedance of a CPL can be derived through linearisation at an operating point ($\hat{I}_{in}$) of the ideal CPL equation, $V_{in}(t) = f_{CPL}\big(I_{in}(t)\big) = P_{CPL}I_{in}(t)$, by first-order Taylor linearisation in (2.4).

$$f_{CPL}(I_{in}) \cong f_{CPL}\big(\hat{I}_{in}\big) + \left.\frac{\partial f(I_{in})}{\partial I_{in}}\right|_{I_{in}=\hat{I}_{in}} \big(I_{in} - \hat{I}_{in}\big) \tag{2.4}$$

$$\begin{aligned} f_{CPL}(I_{in}) &= \frac{P_{CPL}}{\hat{I}_{in}} - \frac{P_{CPL}}{\hat{I}_{in}^2}\big(I_{in} - \hat{I}_{in}\big) \\ &= 2\frac{P_{CPL}}{\hat{I}_{in}} - \frac{P_{CPL}}{\hat{I}_{in}^2} I_{in} \end{aligned} \tag{2.5}$$

Substituting equations $P_{CPL} = \hat{I}_{in}^2 R_{CPL}$ and $R_{CPL} = \hat{V}_{in}/\hat{I}_{in}$ into (2.5) yields the following equations that show the instantaneous linear relation between voltage and current of an ideal CPL at operating point ($\hat{V}_{in}, \hat{I}_{in}$) (2.6)-(2.7).

$$V_{in}(t) = 2\frac{P_{CPL}}{\hat{I}_{in}} - R_{CPL}I_{in}(t) \tag{2.6}$$

$$I_{in}(t) = 2\frac{P_{CPL}}{\hat{V}_{in}} - \frac{1}{R_{CPL}}V_{in}(t) \tag{2.7}$$

With equation (2.7), the linearised CPL model can therefore be represented by the circuit featuring a resistor and current source in parallel, in Figure 2.4(b).

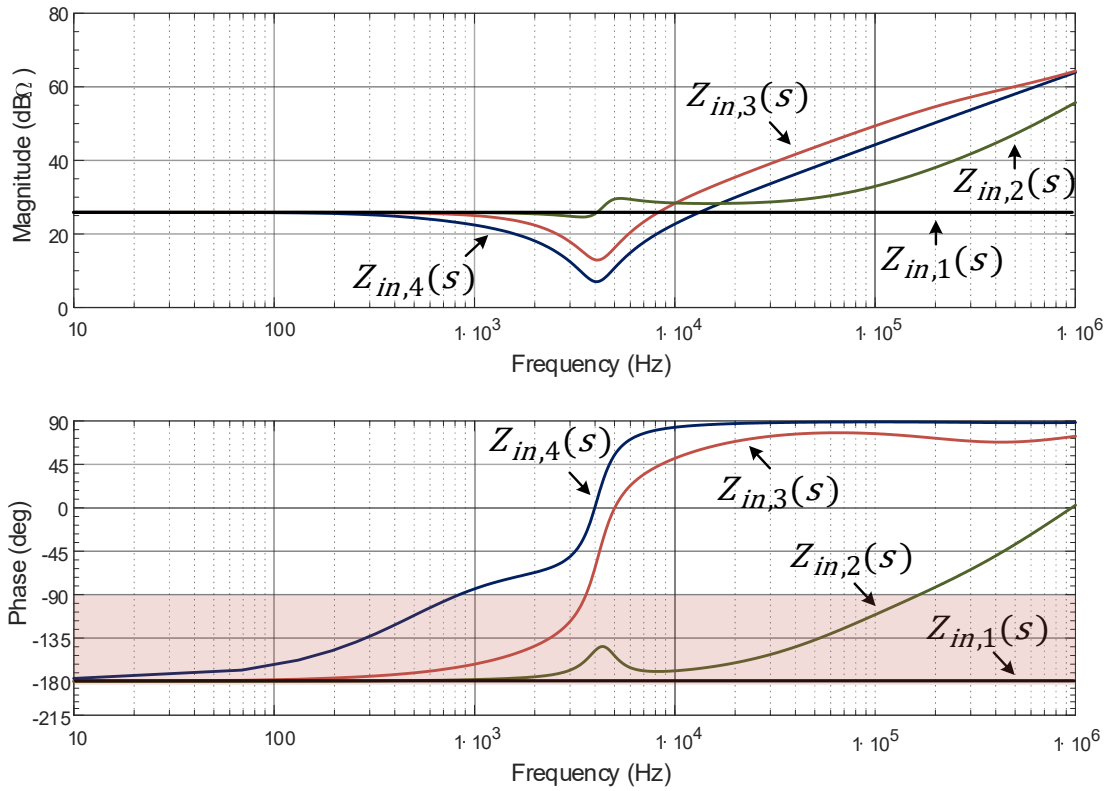

FIGURE 2.5 Input impedance of different output regulated converters, $Z_{in,2}(s)$, $Z_{in,3}(s)$, $Z_{in,4}(s)$, and that of an ideal CPL, $Z_{in,1}(s)$. The region in red indicates the frequencies at which input has a negative incremental resistance.

Ideal CPLs do not exist in practice. CPL behaviour is only exhibited within a limited closed-loop control bandwidth of a practical converter. The negative resistance behaviour of the frequency response is only when the phase is between −90-degree and −180-degree ($\cos(\theta) < 0$ for $-\pi < \theta < -2\pi$). This is highlighted by the red region in the phase plot of the Bode diagram in Figure 2.5. The input impedance curves $Z_{in,2}$, $Z_{in,3}$, $Z_{in,4}$ are examples showing the frequency responses of practical converters with a finite control bandwidth. At higher frequencies, practical converters have a positive impedance characteristic.

2.3.2 Output impedance characteristics of poorly damped resonant upstream networks

Low damping of source-side networks mathematically corresponds to a high gain at the resonant frequency. To demonstrate, this section shows the frequency response characteristics of the output impedance $Z_{out}(s)$ of a simple low-pass filter model which can be viewed as a second-order (damped) harmonic oscillator.

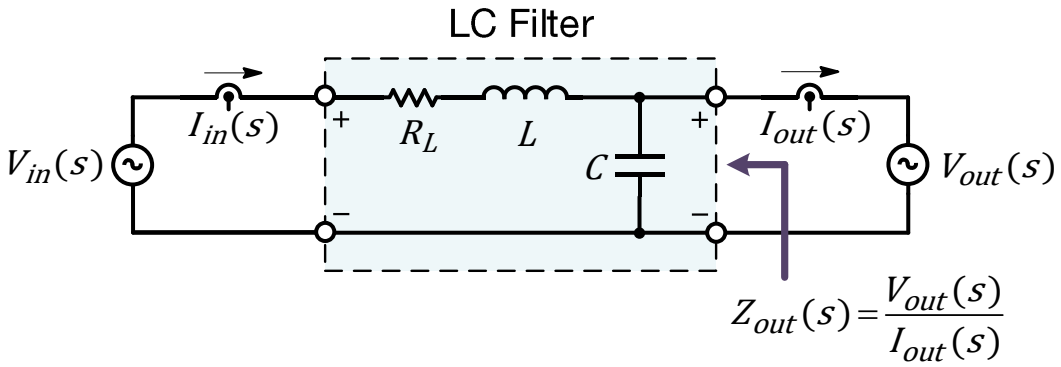

FIGURE 2.6 Circuit diagram of an 2nd-order LC filter with DCR (R_L).

Figure 2.6 shows the circuit diagram of a typical LC filter with output impedance when V_{in} is shorted given by transfer function in (2.8).

$$Z_{out}(s) = \frac{sL + R_L}{s^2LC + sR_LC + 1} \tag{2.8}$$

For simplicity, we can rewrite the output impedance of filter dynamics as a harmonic oscillator with damping. The transfer function for the harmonic oscillator model equivalent to the $Z_{out}(s)$ of Figure 2.6 takes form (2.9):

$$Z_{out}(s) = \frac{V_{out}(s)}{I_{out}(s)} = \frac{\kappa(s\frac{\omega_0}{2\zeta} + \omega_0^2)}{s^2 + s(2\zeta\omega_0) + \omega_0^2} \tag{2.9}$$

Where, ζ is the damping ratio, ω_0 is the natural frequency, and κ represents the DC gain (as this can be viewed as a function of R_L, $\kappa < 1$ indicating a loss factor).

And, in terms of the circuit elements, we can use the following substitutions (2.10):

$$\omega_0 = \frac{1}{\sqrt{LC}}, \quad \zeta = \frac{R_L C \omega_0}{2} \tag{2.10}$$

As previously discussed in Section 1.2.1, it is clear that increasing capacitance and resistance will improve the damping ratio by examining relation in (2.10). The resonant frequency ω_r at which maximum gain $|Z_{out}(s)|$ occurs can be calculated by the approximate relation in (2.11):

$$\begin{aligned} \omega_r &= \omega_0\sqrt{1-2\zeta^2} \\ |Z_{out}(j\omega_r)| &= 1/(2\zeta) \end{aligned} \tag{2.11}$$

Figure 2.7, below, shows the Bode plot of the output impedance of second-order filters with differing damping ratios but identical crossover frequency. The critically damped $Z_{out,3}$ shows no peaking and therefore will not oscillate at the resonant frequency.

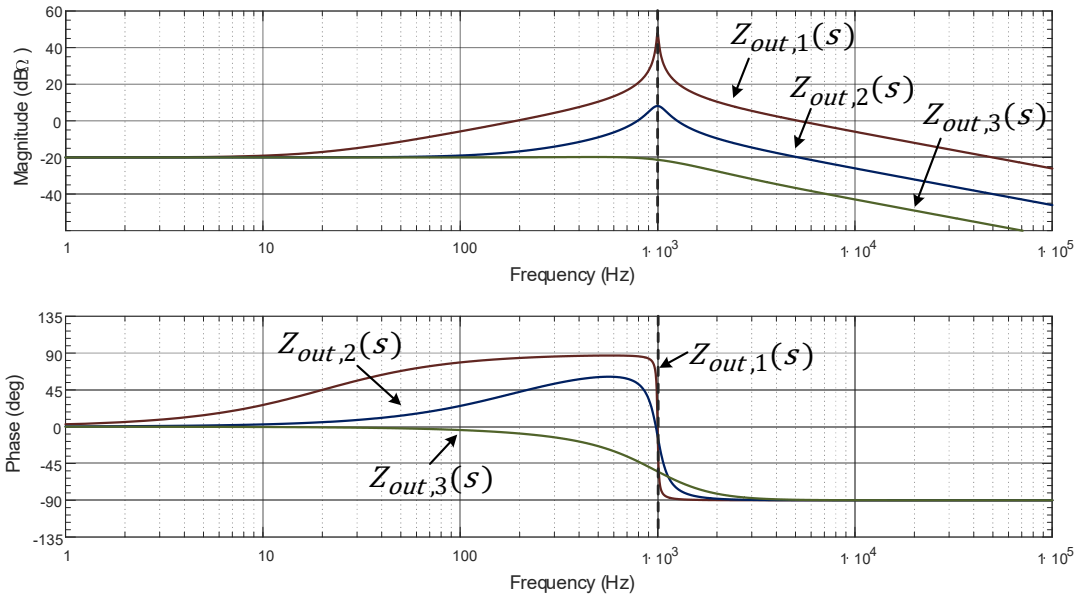

FIGURE 2.7 Output impedance of low-pass LC input filters, $Z_{out,1}(s)$, $Z_{out,2}(s)$, $Z_{out,3}(s)$, at different damping ratios, $\zeta = \{0.01, 0.1, 0.707\}$ at $f_0 = 1\text{kHz}$.

It will be shown in the following section that $Z_{out}(s)$ may cause positive feedback in the open-loop transfer function depending if $|T_{OL}(s)| > 1$ when $\angle T_{OL}(s) = -90°$.

2.3.3 Instability caused by interaction between a poorly damped source-side filter and a CPL

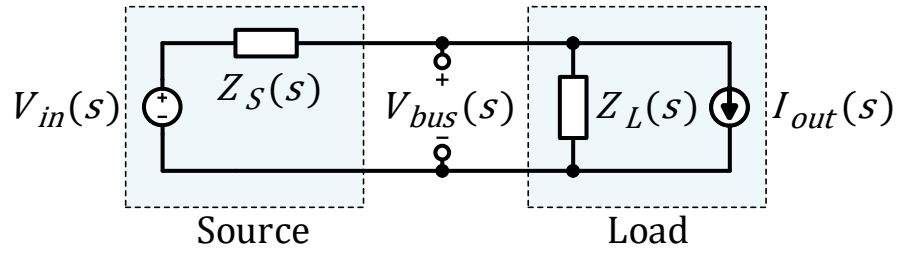

FIGURE 2.8 Simplified circuit diagram of a cascaded system with source-side output impedance $Z_S(s)$ and load-side input impedance $Z_L(s)$.

The stability of a cascaded source-load system can be analysed by the circuit shown in Figure 2.8. Let us consider a source-side input filter feeding an ideal CPL. Deriving the response of the variables at the intermediate interface subject to small perturbations at the inputs is used to find the small-signal stability. Here, effect of perturbation of load current $I_{out}(s)$ on the response of the load's input voltage $V_{bus}(s)$ is given by (2.12):

$$\frac{V_{bus}(s)}{I_{out}(s)} = -\big(Z_S(s) \parallel Z_L(s)\big) = -\frac{Z_L(s)}{1 + Z_S(s)/Z_L(s)} \tag{2.12}$$

As discussed previously, this is a typical feedback loop and can be analysed by applying the Nyquist criterion to *OL* transfer function $T_{OL}(s) = Z_S(s)/Z_L(s)$.

For this example, the analytical expressions for input and output impedances are taken from Section 2.3.1 and Section 2.3.2, and is given below in (2.13):

$$Z_S(s) = \frac{sL + R_L}{s^2LC + sR_LC + 1}, \qquad Z_L(s) = -R_{CPL} \tag{2.13}$$

Substituting (2.13) into (2.12) results in:

$$\frac{V_L(s)}{I_{out}(s)} = -\frac{Ls + R_L}{LCs^2 + \left(R_LC - \frac{L}{R_{CPL}}\right)s + 1 - R_L/R_{CPL}} \tag{2.14}$$

The denominator of the transfer function in (2.14) is the characteristic equation and is used to establish stability. In this analytical form, the Routh-Hurwitz criterion[1] can be readily applied. Assuming that $(1 - R_L/R_{CPL} > 0)$, the stability condition is given by the following equation in (2.15):

$$R_L C - \frac{L}{R_{CPL}} > 0 \tag{2.15}$$

Rearranging (2.15), with following substitutions for the inductor Q-factor ($Q_L = \omega_0 L/R_L$) at the resonant frequency ω_0 and reactance of the capacitor ($X_C = 1/\omega_0 C$) to yield the inequality:

$$R_{CPL} > \frac{L}{R_L C} \cong \frac{Q_L}{\omega_0 C} = Q_L X_C \tag{2.16}$$

By taking only the magnitude of the left and right-hand terms of (2.16), it can be reasoned that the peak of the source-side output impedance (occurring at ω_0) must be less than the peak of load-side input impedance, as given in (2.17).

$$|R_{CPL}| > |Q_L X_C| \cong \frac{1}{2\zeta} \tag{2.17}$$

Where the relationship between the magnitude of Q_L and damping factor is $Q = 1/2\zeta$.

More generally, and over all frequencies, the condition for stability can be expressed in terms of impedance $Z_S(s)$ and $Z_L(s)$, as was originally proposed by Middlebrook [36]:

$$|Z_L(s)| > |Z_S(s)| \tag{2.18}$$

[1] While the Routh-Hurwitz criterion is used here, the Nyquist stability criterion is viewed as a more general (numerical) approach that permits stability analysis of *experimentally* measured transfer functions that the former criterion does not.

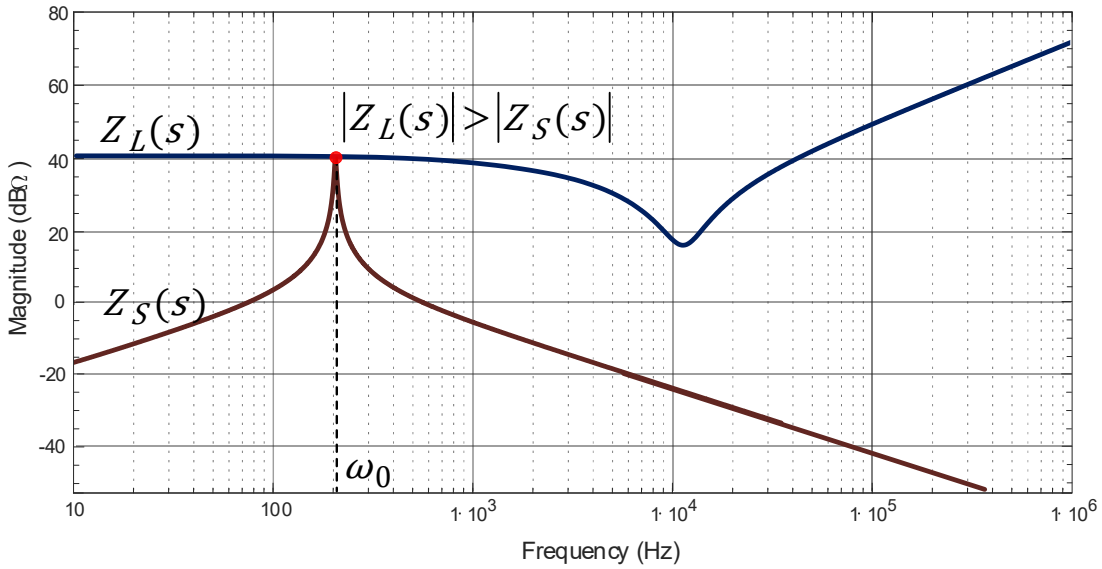

FIGURE 2.9 Bode plot representation of the Middlebrook stability criterion showing conditions for source-side output impedance $Z_S(s)$ (input filter) and load-side input impedance $Z_L(s)$ (CPL).

In Figure 2.9, the magnitude of the filter's output impedance becomes greater than the input impedance of the CPL near ω_0 (i.e., if $|Z_s(j\omega_0)| > |Z_L(j\omega_0)|$) under two possible conditions. Firstly, if the damping of the filter decreases. Secondly, an increase in load demand of the CPL. Both changes would violate Middlebrook stability criterion, and could potentially destabilise the cascaded system.

2.4 Small-signal Modelling and Stability Analysis of LVDC DPSs

As set out in Section 2.3, the phenomenon of source-load interaction has been identified as a major factor contributing to instability in cascaded power system components. Demonstrated in the frequency domain, the dynamics of a cascaded system is modified by the open-loop transfer function, the ratio between input and output impedances at the interface of two interacting components. While the individual components are stable, the interconnected system may not be if the closed-loop system violates Nyquist stability criterion. The interaction formalism using the more straightforward Middlebrook stability criterion guarantees adherence to the more general Nyquist criterion. Any large system may be split into two cascaded subsystems to which frequency domain analysis can be applied. However, oscillations can occur not only due to the interactions between an input filter and a converter but also due to the possible interactions between several stages in cascade [82], [83]. It is therefore not possible to identify *a priori* at which interface the destabilising interaction will occur. Therefore, a more complete system-level or global method for assessing small-signal stability becomes paramount.

So far, the modelling has used the assumption of ideal model dynamics, in particular related to load-side power electronic converters. Much of the early research has analysed source-load interaction using an ideal model of a CPL (or its linearised equivalent) [81], [84]. However, this is only a simplified model of a practical tightly regulated closed-loop converter which inherently feature more complex internal dynamics. Effect of controller parameters are neglected, therefore investigation into how controller variations influence system interactions are not possible. In particular, several methods have been proposed to modify controller dynamics to include active stabilisation (e.g. [51]). While the ideal CPL model is the worst-case from a small-signal perspective [85], unless the system has unique conditions (e.g. [34]), it is important to model the converter dynamics with high-fidelity including parasitic elements and control parameters.

With these objectives in mind, a *complete* mathematical description of system dynamics is warranted. The sections below introduce state-space modelling technique and how this may be used to study small-signal dynamics. Specific model descriptions of the components present in typical LVDC DPSs are covered in the next chapter, Section 3.3.

2.4.1 Frequency domain techniques and impedance-based stability criteria

This section introduces the frequency domain two-port structure that can be used to model sources and loads in cascade. Tightly regulated converters can be represented by four terminals, irrespective of converter topology or internal control structure, as long as the port conditions are satisfied—that current entering a port is the same as the current leaving that same port. Conventional impedance-based stability analysis for source-load interactions can be elaborated from cascaded two-port models, and is also used to highlight the limitations of this approach for stability and interaction analysis for larger DPSs.

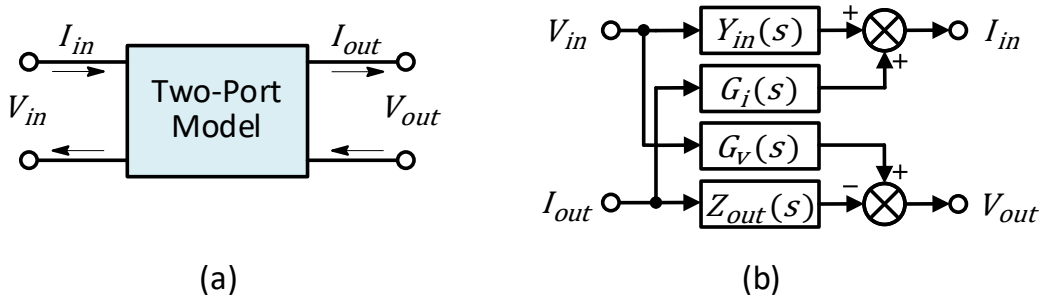

FIGURE 2.10 A two-port network model: (a) circuit level representation, (b) frequency domain block diagram.

The two-port network model in Figure 2.10 is made up of four transfer functions known as the inverse hybrid (g-)parameters. This representation is used for circuits that are commonly viewed as voltage input/output such as DC-DC converters and line filters. Frequency domain equations of the two-port network model are given in (2.19):

$$\begin{aligned} \mathrm{I}_{in}(s) &= Y_{in}(s)V_{in}(s) + G_i(s)I_{out}(s) \\ V_{out}(s) &= G_v(s)V_{in}(s) - Z_{out}(s)I_{out}(s) \end{aligned} \tag{2.19}$$

Where the internal transfer functions are defined as the following,

Input admittance, $Y_{in}(s) = \left.\frac{\bar{\mathrm{I}}_{in}}{\bar{V}_{in}}\right|_{\bar{I}_{out}=0}$

Reverse transfer function, $G_i(s) = \left.\frac{\bar{\mathrm{I}}_{in}}{\bar{I}_{out}}\right|_{\bar{V}_{out}=0}$

Audio susceptibility, $G_v(s) = \left.\frac{\bar{\mathrm{V}}_{out}}{\bar{V}_{in}}\right|_{\bar{I}_{out}=0}$

Output impedance, $Z_{out}(s) = \left.\frac{\bar{\mathrm{V}}_{out}}{\bar{I}_{out}}\right|_{\bar{V}_{out}=0}$

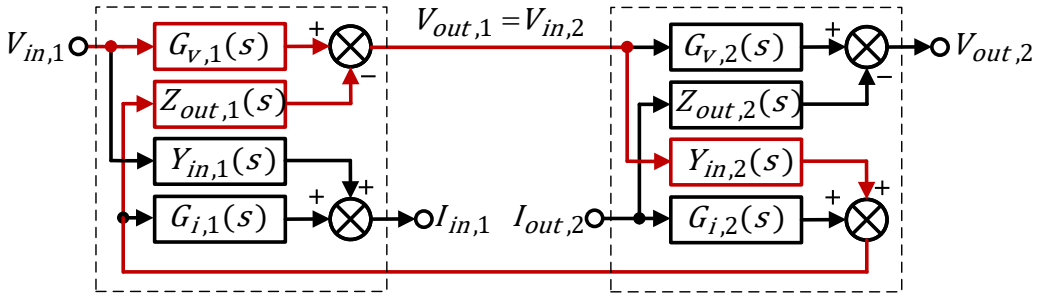

FIGURE 2.11 Frequency domain block diagram of cascaded two-port models.

Figure 2.11 shows the block diagram of cascaded two-port models of the form Figure 2.10(b)—a source (denoted by subscript 1) and a load (denoted by subscript 2). Assuming steady-state conditions on all input variables other than $V_{in,1}$, the voltage transfer function $V_{out,1}/V_{in,1}$ (red highlighted feedback path in Figure 2.11) is given as (2.20):

$$\frac{V_{out,1}(s)}{V_{in,1}(s)} = G_{v,1}(s)\left(\frac{1}{1 + Y_{in,2}(s)Z_{out,1}(s)}\right) \tag{2.20}$$

Using the notation of source and load used in Section 2.2 previously, $Z_S(s) = 1/Y_{in,2}(s)$ and $Z_L(s) = Z_{out,1}(s)$, the feedback has the open-loop transfer function given in (2.21) below.

The condition set out in (2.18) is referred to as the Middlebrook stability criterion and is represented in Figure 2.12. This satisfies the more general Nyquist criterion as the open-loop transfer function $T_{OL}(s)$ has a magnitude less that unity in (2.21) below. This ensures that the Nyquist contour has no encirclements of the (-1,0) point.

$$|T_{OL}(s)| = \frac{|Z_S(s)|}{|Z_L(s)|} < 1 \tag{2.21}$$

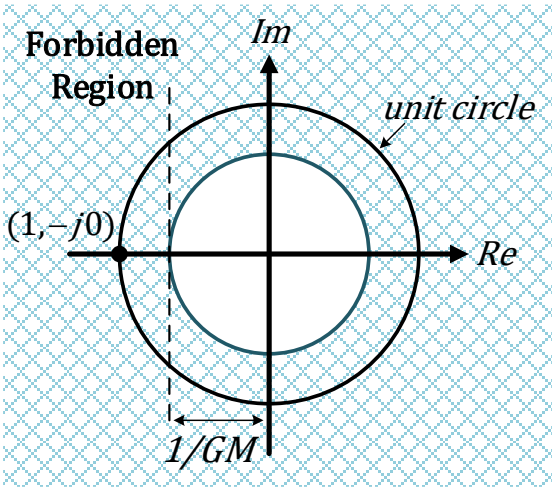

FIGURE 2.12 The Middlebrook Stability Criterion [36] represented on the complex plane. Valid stability region lies within the unit circle offset by a suitable gain margin (GM), $|T_{OL}(s) \leq 1/GM|$.

Many alternative stability criteria have been developed in the literature based on frequency-domain analysis of the minor-loop gain where forbidden regions are defined to satisfy Nyquist. The Middlebrook criterion is based solely on the magnitudes of the impedances of sources and loads, and it is often modified to ensure a specific gain margin to avoid operation near (-1,0) thereby making it more conservative. Noting that Middlebrook imposes an infinite phase margin, whereas other less conservative stability criteria take into consideration the phase margin. Comparative studies between different stability criteria for source-load interactions can be found in [27], [31], [64], [66], [86], [87].

LVDC DPSs are comprised of multiple subsystems interconnected. The application of any of these stability criteria only considers a single interface where the open-loop transfer function is linearised at a given operating point. Referring to the cascaded system in Figure 2.11, the impact of additional subsystems (e.g., another system in cascaded or parallel) on the linear transfer functions, $Z_L(s)$ and $Z_S(s)$, is not considered. As parameters of the system vary, the open-loop transfer function may vary with $Z_L(s)$ and $Z_S(s)$ at an interface. The influence of these parameters must therefore be investigated, where a state-space representation becomes a more practical approach—discussed in the next section.

2.4.2 State-space techniques and modal decomposition

Interconnection of the various components that make up the complete DC power system—generators, power electronic-based loads, distribution lines, controllers—forms a complete power system which in the most broad sense can be characterized as nonlinear and time-variant [33]. To study the system behaviour when subject to small disturbances it is often appropriate to simplify the system to that of its low-frequency steady-state dynamics through the process of linearisation [33]. However, finding the precise steady-state equilibrium point still requires an accurate, typically nonlinear, power system model.

Power systems are modelled to study their dynamic behaviours and as such are described by a system of differential equations, if the form of a vector of continuous-time nonlinear space-space equations in (2.22) and (2.23).

$$\frac{dX(t)}{dt} = F\big(X(t), U(t)\big) \tag{2.22}$$

$$Y(t) = G\big(X(t), U(t)\big) \tag{2.23}$$

Where,

$X(t) = [x_1(t), \quad \dots \quad x_n(t)]^T$ is a vector of n dynamic state variables,

$Y(t) = [y_1(t), \quad \dots \quad y_m(t)]^T$ is a vector of m system outputs,

$U(t) = [u_1(t), \quad \dots \quad u_q(t)]^T$ is vector of q system input variables,

$F(\dots) = [f_1(\dots), \quad \dots \quad f_n(\dots)]^T$ is a vector of n 1st-order state equations,

$G(\dots) = [g_1(\dots), \quad \dots \quad g_m(\dots)]^T$ is a vector of m output (observation) equations.

If the initial states are known $X(t = 0)$ together with set inputs $U(t)$, then the non-linear state-space equations in (2.22)-(2.23) uniquely define the system's state and output response over time ($X(t \to \infty)$, $Y(t \to \infty)$).

When the differential state equations in (2.22) reach an equilibrium steady-state point ($X = X_0$ and $U = U_0$), then the state dynamics no longer vary with time (2.24):

$$F(X_0, U_0) = 0 \tag{2.24}$$

Under this steady-state condition, denoted as (X_0, U_0), we can define a set of deviation variables measuring the difference (2.25):

$$\begin{aligned} \delta_x(t) &:= X(t) - \mathrm{X}_0 \\ \delta_u(t) &:= U(t) - U_0 \end{aligned} \tag{2.25}$$

In effect, this redefines the zero point of the function to (X_0, U_0). Substituting (2.25) into (2.22) gives the following exact equation (2.26):

$$\frac{d\delta_x(t)}{dt} = F\big(\mathrm{X}_0 + \delta_X(t), U_0 + \delta_U(t)\big) \tag{2.26}$$

Noting that derivative $F(X_0, U_0) = 0$ at steady-state, using a first-order Taylor expansion (ignoring higher-order terms) of (2.26) yields (2.27):

$$\frac{d\delta_X(t)}{dt} \approx \left.\frac{\partial F}{\partial X}\right|_{(X_0,U_0)} \delta_X(t) + \left.\frac{\partial F}{\partial U}\right|_{(X_0,U_0)} \delta_U(t) \tag{2.27}$$

The above is valid for small-signal conditions, i.e., the deviation variables δ_X and δ_U are small.

Likewise, the same linearisation procedure around point (X_0, U_0) can be applied onto the output equations (2.23). Taken together, this procedure yields the LTI state-space representation (2.28) and (2.29):

$$\frac{d\delta_X(t)}{dt} = A\delta_X(t) + B\delta_U(t) \tag{2.28}$$

$$\delta_Y(t) = C\delta_X(t) + D\delta_U(t) \tag{2.29}$$

Where A, B, C, and D in (2.28)-(2.29) are the Jacobian matrices of the system, evaluated at the operating point, defined in (2.30):

$$A = \left.\frac{\partial F(X,U)}{\partial X}\right|_{(X_0,U_0)} = \begin{bmatrix} \dfrac{\partial f_1(X,U)}{\partial x_1} & \cdots & \dfrac{\partial f_1(X,U)}{\partial x_n} \\ \vdots & \ddots & \vdots \\ \dfrac{\partial f_n(X,U)}{\partial x_1} & \cdots & \dfrac{\partial f_n(X,U)}{\partial x_n} \end{bmatrix} \tag{2.30}$$

$$B = \left.\frac{\partial F(X,U)}{\partial U}\right|_{(X_0,U_0)} = \begin{bmatrix} \frac{\partial f_1(X,U)}{\partial u_1} & \cdots & \frac{\partial f_1(X,U)}{\partial u_q} \\ \vdots & \ddots & \vdots \\ \frac{\partial f_n(X,U)}{\partial u_1} & \cdots & \frac{\partial f_n(X,U)}{\partial u_q} \end{bmatrix}$$

$$C = \left.\frac{\partial G(X,U)}{\partial X}\right|_{(X_0,U_0)} = \begin{bmatrix} \frac{\partial g_1(X,U)}{\partial x_1} & \cdots & \frac{\partial g_1(X,U)}{\partial x_n} \\ \vdots & \ddots & \vdots \\ \frac{\partial g_n(X,U)}{\partial x_1} & \cdots & \frac{\partial g_n(X,U)}{\partial x_n} \end{bmatrix}$$

$$D = \left.\frac{\partial G(X,U)}{\partial U}\right|_{(X_0,U_0)} = \begin{bmatrix} \frac{\partial g_1(X,U)}{\partial u_1} & \cdots & \frac{\partial g_1(X,U)}{\partial u_q} \\ \vdots & \ddots & \vdots \\ \frac{\partial g_n(X,U)}{\partial u_1} & \cdots & \frac{\partial g_n(X,U)}{\partial u_q} \end{bmatrix}$$

Modal decomposition is a linear transformation of a LTI state-space model into a new coordinate system which satisfies the superposition principle in system responses. The total system response becomes the sum of individual modal responses. This new coordinate system is referred to as the modal coordinates.

The modal decomposition (and subsequent small-signal stability analysis) of a linear system can be expressed through the scalar eigenvalues, λ. These eigenvalues are determined by calculating all of the roots of $\det(\lambda I - A)$, such that (2.31) and (2.32) are satisfied:

$$A\psi_i = \lambda_i \psi_i \tag{2.31}$$

$$A\phi_j = \phi_j \lambda_i \tag{2.32}$$

Where,

ϕ_j is the left eigenvector corresponding to λ_i,

ψ_i is the right eigenvector corresponding to λ_i.

For convenience, the orthogonality of the eigenvectors are normalised to unity, therefore satisfy following relation in (2.33):

$$\psi_j \phi_i = \begin{cases} 1, & \text{if } i = j \\ 0, & \text{if } i \neq j \end{cases} \tag{2.33}$$

In addition, the matrix Λ is defined with all eigenvalues of A as diagonal elements (2.34):

$$\Lambda = \psi A \phi = \begin{bmatrix} \lambda_1 & & 0 \\ & \ddots & \\ 0 & & \lambda_n \end{bmatrix} \tag{2.34}$$

Where,

ψ is a matrix formed by the columns of the right eigenvectors,

ϕ is a matrix formed by the rows of the left eigenvectors.

Eigenvalues may be rewritten with rectangular coordinates, α and β, or in polar terms of damping ratio ζ and natural frequency ω_n, given in (2.35):

$$\lambda = \alpha \pm j\beta = -\zeta\omega_n \pm j\omega_n\sqrt{1-\zeta^2} \tag{2.35}$$

To convert between the coordinates, the following relations are given (2.36):

$$\begin{aligned} \zeta &= -\frac{\alpha}{\sqrt{\alpha^2+\beta^2}} \\ \omega_n &= \sqrt{\alpha^2+\beta^2} = \alpha/\zeta \end{aligned} \tag{2.36}$$

In this thesis, the numerical modal decomposition of the system state-space matrix A is performed with MATLAB function *eig()*.

Assume that the matrix A has n unique eigenvalues, $\lambda_1, \ldots, \lambda_n$. The response of the initial condition can be written as a linear combination of the eigenvalue modes. To demonstrate, let the decomposition have all real eigenvalues with their associated right eigenvectors, $\psi_1, \ldots, \psi_n$. These eigenvectors are linearly independent such that the initial condition $x(0)$ can be written as (2.37):

$$x(0) = a_1\psi_1 + a_2\psi_2 + \cdots + a_n\psi_n \tag{2.37}$$

Where the constants $a_1 \ldots a_n$ are initial condition constants.

With the linearity property, the initial condition response can be given as (2.38):

$$x(t) = a_1 e^{\lambda_1 t}\psi_1 + a_2 e^{\lambda_2 t}\psi_2 + \cdots + a_n e^{\lambda_n t}\psi_n \tag{2.38}$$

Qualitatively, the behaviour and stability of the system is evident by the value of the eigenvalues λ in (2.38). The different modes grow or decay as a function of $e^{\lambda_i t}$. If the real part of an eigenvalue is positive, then the dynamic response of the associated state variables grows exponentially and is therefore unstable. Real eigenvalues with no complex component results in non-oscillatory behaviour. Negative real values indicate a decaying function. Complex-valued eigenvalue occur as conjugate pairs and will result in oscillatory behaviour.

2.5 Modal (Resonance) Interactions

2.5.1 Nonlinear behaviour of eigenvalues

The concept of modal interaction between subsystems was introduced in *Chapter 1* and represented by Figure 1.6. In the previous section we described how a linear system model may be transformed into a linear combination of eigenvalue modes (or simply referred to as *modes)*. The concept of modal interaction exists when energy is exchanged between different modes. In essence, two or more modes are mutually excited and share dynamic behaviours, and must be treated as coupled modes. To ease discussion, a coupling parameter σ was introduced to signify that coupling between modes arise as a function of some system parameter(s). Here, σ is not used in any mathematical sense for analysis but only as means by which to discuss the phenomena of modal interactions.

Modal interactions are known to occur near resonance when one oscillatory mode coincides with another in terms of frequency and damping. As coupling occurs, eigenvalues appear to diverge on the complex eigenspace, therefore small-signal dynamics. Issues surrounding this phenomenon are studied extensively in several applications (e.g. power systems [18], [46], [48], [50], [88], antennas [41], mechanics [89]) and are sometimes referred to as *curve veering* or *eigenvalue avoidance*.

While the scope of this thesis is LVDC DPSs, the majority of literature investigating modal interaction phenomena is within the traditional AC systems domain. Due to the high degree of analogy between AC and DC systems, modelling principles and analysis techniques are equivalent. For example, power systems with series-compensated transmission lines are prone to small-signal stability. Subsynchronous resonance arises from the interaction between the mechanical (torsional dynamic) mode and electrical damping mode and can lead to instability with sustained oscillations [16]–[18], [90], [91]. Similarly, mode coupling can degrade stability margins in DPSs due to the resonance interaction between parallel LCL filters [21]–[23], [43], [44], [92] and demonstrated in [21] to be the result of coupling via circulating currents between filters.

In DC power systems, the existence of modal interaction phenomenon is often exhibited but understudied. The work in [51] implemented a source-side virtual resistance-based compensator capable of stabilising multiple parallel filter and CPLs in cascade,

however it observed that the effectiveness is reduced when input filter resonant frequencies were coincident. Similarly, [26] identifies similar interaction effects between parallel filters, but demonstrate that source impedances is the cause for coupling between modes. This inconsistency between [51] and [26] appears to be the reuslt of interactions that are strongly dependent on parameter values and operating point.

2.5.2 Modelling of coupled subsystems

A nonlinear power system model changes its linear approximation over a variation in parameters of the model. Therefore, the impact of parameter changes on modal interactions must therefore be assessed and becomes a critical point of research in highly uncertain LVDC DPSs.

Section 2.5.2.1 presents a simplified example of modal interaction of a theoretical 2×2 linear system model showing the possible behaviours of eigenvalues over parameter changes, with a numerical example given in Section 2.5.2.2.

2.5.2.1 Modal decomposition of a simple 2 × 2 system

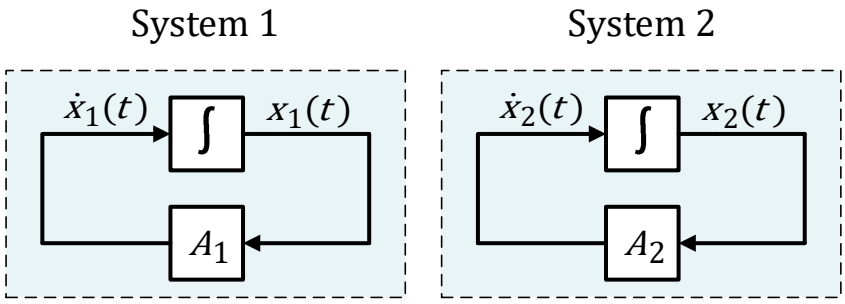

FIGURE 2.13 System of two uncoupled subsystems described dynamics of two independent states, $dx_1/dt=A_1x_1$ and $dx_2/dt=A_2x_2$.

Two uncoupled systems in given by block diagram in Figure 2.13. These are modelled by differential equations (2.39) and (2.40), below:

$$\frac{dx_1(t)}{dt} = (\alpha_1 \pm j\beta_1)x_1(t) \tag{2.39}$$

$$\frac{dx_2(t)}{dt} = (\alpha_2 \pm j\beta_2)x_2(t) \tag{2.40}$$

Complex valued state dynamics have been used to simplify the modal decomposition, so that equations (2.39) and (2.40) can be rewritten directly in terms of eigenvalues λ in (2.41) and (2.42):

$$\frac{dx_1(t)}{dt} = \lambda_1' x_1(t) \tag{2.41}$$

$$\frac{dx_2(t)}{dt} = \lambda_2' x_2(t) \tag{2.42}$$

Where the apostrophe indicates the eigenvalue of the *uncoupled* system,

$$\begin{aligned} \lambda_1' &= \alpha_1 \pm j\beta_1 \\ \lambda_2' &= \alpha_2 \pm j\beta_2 \end{aligned} \tag{2.43}$$

Representing the two uncoupled systems together as one aggregate system mode, such that $X(t) = [x_1(t), x_2(t)]^T$, to result in the state-space representation in (2.44):

$$\frac{dX(t)}{dt} = AX(t) \tag{2.44}$$

Where the state matrix A is given as (2.45):

$$A = \begin{bmatrix} \lambda_1' & 0 \\ 0 & \lambda_2' \end{bmatrix} \tag{2.45}$$

The initial state response of $x_1(t)$, $x_2(t)$ in (2.44) can be given as (2.46), (2.47):

$$x_1(t) = x_1(0)e^{\lambda_1' t} + x_1(0)e^{\overline{\lambda_1'} t} \tag{2.46}$$

$$x_2(t) = x_2(0)e^{\lambda_2' t} + x_2(0)e^{\overline{\lambda_2'} t} \tag{2.47}$$

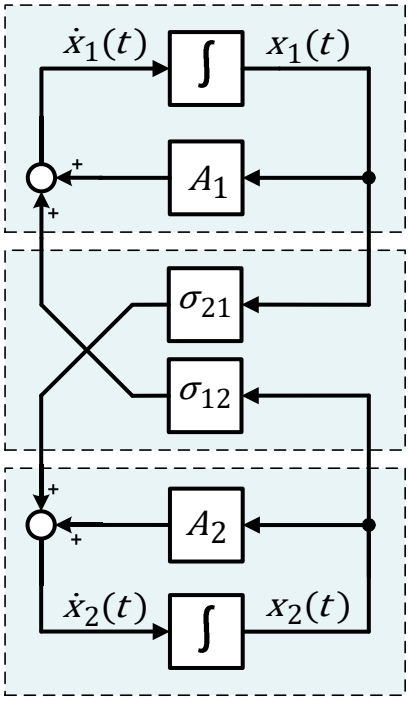

FIGURE 2.14 System as two coupled subsystems showing state variable dependence on coupling factors (σ), dx/dt=Ax+σx.

Now let us assume that the previous uncoupled systems in Figure 2.13 have become linked through coupling factors σ_{12} and σ_{21}, shown by Figure 2.14, thereby forming a coupled system. This coupled system has the dynamic equations (2.48):

$$\begin{aligned} \frac{dx_1(t)}{dt} &= \lambda_1' x_1(t) + \sigma_{12} x_2(t) \\ \frac{dx_2(t)}{dt} &= \lambda_2' x_2(t) + \sigma_{21} x_1(t) \end{aligned} \tag{2.48}$$

For simplicity, assume that the coupling parameters are equal, $\sigma_{12} = \sigma_{21} = \sigma$. The state-space system matrix A is given in (2.49):

$$A = \begin{bmatrix} \lambda_1' & \sigma_{12} \\ \sigma_{21} & \lambda_2' \end{bmatrix} \tag{2.49}$$

By performing modal decomposition, $AX = \Lambda X$, the aim is to find the eigenvalues of the coupled system denoted by λ_1 and λ_2 in (2.50):

$$\Lambda = \begin{bmatrix} \lambda_1 & 0 \\ 0 & \lambda_2 \end{bmatrix} \tag{2.50}$$

It is evident that due to the coupling, the eigenvalues of the coupled system is a function of the eigenvalues of the uncoupled system (denoted by apostrophes as before) and the coupling factors, represented in (2.51):

$$\lambda_1, \lambda_2 = f(\lambda_1', \lambda_2', \sigma_{12}, \sigma_{21}) \tag{2.51}$$

As this problem has been formulated as a simple 2×2 form, we can express the eigenvalues explicitly by analytically solving using the characteristic polynomial of a 2×2 matrix to get the coupled system eigenvalues. This is given in (2.52):

$$\lambda_{1,2} = \frac{\lambda_1' + \lambda_2'}{2} \pm \frac{\sqrt{(\lambda_1' - \lambda_2')^2 + 4\sigma_{12}\sigma_{21}}}{2} \tag{2.52}$$

The initial state response dynamics of $x_1(t)$ and $x_2(t)$ are now coupled depending on the values of the coupling factors. Noting that if $\sigma_{12} = 0$ or $\sigma_{21} = 0$ then the system is reverted back to two separate uncoupled systems.

By studying the coupled system eigenvalues in (2.52) as a function of the uncoupled eigenvalues, we can draw conclusions about the impact of coupling on their location.

Consider Case 1 when the eigenvalues of the uncoupled system are coincident or approach each other (i.e., $\lambda_1' \to \lambda_2'$). Here, the coupling terms begin to dominate (2.53):

$$4\sigma_{12}\sigma_{21} \gg (\lambda_1' - \lambda_2')^2 \tag{2.53}$$

So that the coupled eigenvalues are averaged and offset by a function of coupling parameters in (2.54):

$$\lambda_{1,2} = \frac{\lambda_1' + \lambda_2'}{2} \pm \sqrt{\sigma_{12}\sigma_{21}} \tag{2.54}$$

It can be said these eigenvalues are modally interacting depending on coupling factors.

Consider Case 2 when the eigenvalues of the uncoupled system are very well separated (i.e. $\lambda_1' \neq \lambda_2'$) so that the coupling terms can be neglected, as given in (2.55):

$$\begin{aligned} &4\sigma_{12}\sigma_{21} \ll (\lambda_1' - \lambda_2')^2 \\ &4\sigma_{12}\sigma_{21} \to 0 \\ &\lambda_{1,2} = \frac{\lambda_1' + \lambda_2'}{2} \pm \frac{\sqrt{(\lambda_1' - \lambda_2')^2}}{2} \\ &\begin{cases} \lambda_1 = \lambda_1' \\ \lambda_2 = \lambda_2' \end{cases} \end{aligned} \tag{2.55}$$

When the uncoupled system eigenvalues are located far away, coupling does not influence the location of the coupled system eigenvalues.

It is important to note here that λ_1 of the combined system is defined as being related to λ_1'. This need not be the case as the ordering of $\lambda_{1,2}$ is arbitrary and can be swapped. Here, it is assumed that the states participating in λ_1 are the same as λ_1'. This problem of definition between state and eigenvalues are discussed further in Chapter 6.

2.5.2.2 Numerical example

In this example, numerical values are assigned to the coupled system equations in (2.48) to illustrate the phenomena of modal coupling. Let the system shown in Figure 2.14 be defined with equations (2.56):

$$\begin{aligned} \frac{dx_1(t)}{dt} &= A_1'(p_1)x_1(t) + \sigma_{12}x_2(t) \\ \frac{dx_2(t)}{dt} &= A_2'(p_2)x_2(t) + \sigma_{21}x_1(t) \end{aligned} \tag{2.56}$$

Where variables A_1', A_2', σ_{12}, σ_{21} are specified by:

$$\begin{aligned} A_1'(p_1) &= -1 \pm j\rho_1 \\ A_2'(p_2) &= -1 \pm j\rho_2 \\ \sigma_{12} &= \sigma_{21} = \sigma \end{aligned} \tag{2.57}$$

The state matrix in (2.58), below, is therefore a function of parameters p_1, p_2, σ:

$$A(p_1, p_2, \sigma) = \begin{bmatrix} -1 \pm j\rho_1 & \sigma \\ \sigma & -1 \pm j\rho_2 \end{bmatrix} \tag{2.58}$$

With (2.58), and assigning numeric values to parameters, the trajectories of eigenvalues can be plotted. Fixing $\rho_2 = 1$ and $\sigma = 1$, while varying parameter $\rho_1 = [-5, 5]$.

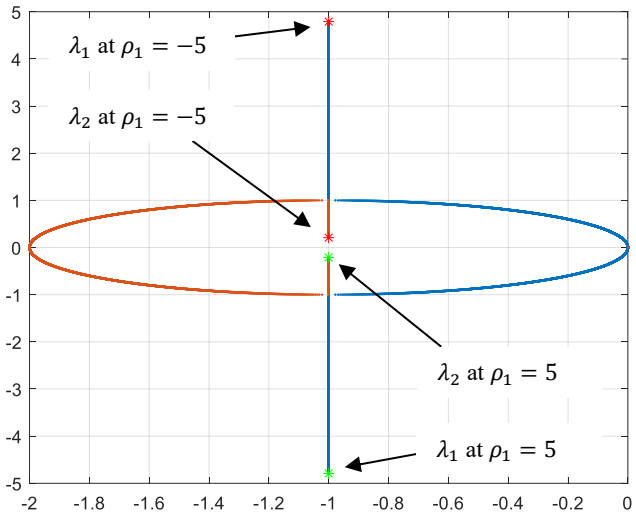

FIGURE 2.15 Trajectory of the eigenvalues of the coupled system, as a parameter ρ_1 is varied from -5 to 5 in steps of +0.0005.

Figure 2.15 illustrates the behaviour of eigenvalues of the coupled system as a single parameter is varied. Values were selected so that the eigenvalues of (the independent terms) A_1' and A_2' cross each other at the point (-1,0). Due to the off-diagonal coupling term σ, the eigenvalues of the combined system A can be seen to diverge away from each other. Based on the solutions to the characteristic equation in (2.52), at $\rho_1 = 0$, when matched, the eigenvalues are demonstrated to be $\lambda_{1,2} = \frac{\lambda_1' + \lambda_2'}{2} \pm \sigma^2 = -1 \pm 1$. Similarly, at points well-away from $\rho_1 = 0$, $\lambda_1 \cong \lambda_1'$ and $\lambda_2 \cong \lambda_2'$ indicating that the system can be approximated as two decoupled systems. However, during the transition between being fully-decoupled and being fully matched, the eigenvalue behaviour is not so straightforward—sensitivity of eigenvalues to parameter changes are drastically different as the systems become coupled (observing the change in behaviour at points (-1,1) and (-1,-1) in Figure 2.15).

From this simplified example, the aim is for the reader to gain an appreciation to the complex dynamic behaviour of the eigenvalues as parameters vary. At present, the

phenomena of mode coupling on small-signal stability is under-studied in the literature for LVDC DPSs. In particular due to the high levels of uncertainty in modern LVDC DPSs, the possibility of mode coupling should firstly be identified, and secondly, effects of mode coupling should be quantified.

2.6 Summary

This chapter has established the theoretical background to the problem of small-signal instability in DC power systems with parameter uncertainties. A summary of the basic problem of source-load interaction instability was presented.

The key modelling and analysis techniques are contained in this chapter which are used throughout in this thesis. In contrast to frequency domain techniques, we opt for a time domain representation via state-space modelling. The theoretical preliminaries of linearisation, modal decomposition and small-signal stability (eigenvalue) analysis have been covered.

Procedures for building a full system model are addressed in the next chapter. To emphasise here however, due to the many parameter uncertainties, the system model should be able to represent small-signal dynamics over all possible operating conditions. This is particularly important in systems that exhibit modal interactions and well as source-load interactions.

The following chapters will use the basics established here to perform a thorough investigation into the effects of parameter uncertainties on small-signal dynamics of LVDC power systems.

Chapter 3

Modelling Framework for Small-Signal Stability Analysis of LVDC Distributed Power Systems

ABSTRACT This chapter outlines a systematic approach to the development of system models of LVDC DPSs for subsequent small-signal analysis. In many real-world applications, these systems often undergo changes through the addition and removal of different components. Constructing a new system model each time can prove to be both laborious and error-prone. A modular modelling approach is presented whereby the full system can be developed in a piecewise fashion. To account for dynamics over parameter uncertainties and a wide range of operating points, subsystems are modelled individually using symbolic nonlinear time-invariant state-space equations. These include high-fidelity models of switching converters (using state-space averaging), feedback controllers, and passive networks. A new MATLAB toolbox, *SymMIAL,* has been developed here to automate the process for combining models to reduce formulation time. In contrast to earlier methods, model nonlinearity is retained to allow accurate calculation of steady-state equilibrium values prior to small signal analysis. This is particularly important for the probabilistic studies in Chapter 5.

The modelling procedure is validated on a filter-converter system using time-domain simulations and laboratory experiments. Further results here show that tightly controlled load-side converters can be simplified to ideal CPLs depending on controller parameters.

3.1 Introduction

A complete dynamic state-space model linearised at the steady-state operating point is often used to investigate the small-signal behaviour of LVDC distributed power systems. Whether operating as an autonomous network or in conjunction with a larger grid, these systems consist of multiple interconnected components such as distribution lines, filters, controllers, and switch-mode converters. Changes to the structure of a DPS by adding or removing components requires an updated small-signal system model—wherein deriving a new model can often be laborious and open to error. Moreover, the presence of parameter uncertainty is known to significantly influence the steady-state operating conditions and the small-signal characteristics (covered more comprehensively in Chapters 5 and 6). Therefore, any conclusions based on analysis of a single linear model under nominal conditions may be severely limited or invalid over the full range of uncertainty.

This chapter presents a modular modelling framework in which a large complex power system model is developed by combining multiple lower-order subsystems. Subsystems are modelled using nonlinear state-space representation in symbolic form to represent the dynamics over all the possible operating conditions. The well-known state-space averaging (SSA) technique, introduced in [78], is used to derive switch-mode converter models valid under CCM operation. In contrast to the conventional two-port converter representation [33] where closed-loop control feedback dynamics are already embedded in the model, a more general multi-port representation is considered.

The use of nonlinear averaged models of the converters with an open-loop structure, having control variables as inputs to the subsystem, enables a more modular approach to system model development. Controllers and power stage subsystems may be modelled separately prior to feedback for closed-loop regulation. The model structure is therefore flexible and can be extended with ease. Connections between individual subsystems are specified by algebraic equations linking the model inputs and outputs.

A toolbox for MATLAB, called *SymMIAL (Symbolic Model Interconnection and Linearisation),* was developed to automate the procedure for combining subsystems. Symbolic manipulation based on MATLAB's *Symbolic Math Toolbox* is used to rearrange and solve model equations to generate a full system model with a nonlinear state-

space representation. In contrast to previous modelling approaches, for example in [69], [93]–[95], nonlinear expressions are preserved wherever possible. By keeping the Jacobian matrices in symbolic form, the linear state-space model representing all possible operating points is derived *only once*. Likewise, realizing loop transfer functions between any subsystem input to subsystem output becomes automatic.

The rest of this chapter is structured as follows. Section 3.2 details the modular modelling approach for a large-scale DC power system by combining smaller independently modelled subsystem components. Section 3.3 describes the individual subsystem dynamic models of the common elements or "*building-blocks"* of a larger system – passive networks, active power components, feedback controllers. Section 3.4 introduces the *SymMIAL* toolbox that has been developed to provide an easy to use, flexible and efficient tool for constructing and combining symbolic models for later use in small-signal analysis. To demonstrate the use of the tool for modelling and analysis, Section 3.5 validates the modelling using detailed model simulations and experiments for two example test cases. Section 3.6 summarises this chapter and contributions.

3.2 Modular Modelling of DC Power Systems

This section details the basic mathematical structure of the power system as the interconnection of many different nonlinear state-space models. The primary objective of this modular modelling approach is to develop a database of individual subsystem models which can then be combined based on connection rules to generate a complete high-fidelity system model suitable for small-signal analysis. The synthesis of complete system model of typical DPSs, however, may prove to be a time consuming and error-prone process if done by hand. Several authors have proposed similar techniques to alleviate this burden, for example [69], [94], [96].

3.2.1 Nonlinear state-space system model

The canonical form of a nonlinear, time-invariant, state-space system model is given in (3.1) and represented by as a MIMO block diagram in Figure 3.1. In this form, the system model can be used accurately represent the dynamics, from input in $U(t)$ to

outputs in $Y(t)$, over some parameter space, P. Here we make the following assumption that functions F and G, below, are strictly continuous models.

$$\frac{dX(t)}{dt} = F(X(t), U(t), P)$$
$$Y(t) = G(X(t), U(t), P) \tag{3.1}$$

Where,

$\mathrm{X(t)} = [\mathrm{x_1(t)}, \quad \ldots \quad x_n(t)]^T$ is a vector of n dynamic state variables,

$\mathrm{Y(t)} = [\mathrm{y_1(t)}, \quad \ldots \quad y_m(t)]^T$ is a vector of m system outputs,

$\mathrm{U(t)} = [\mathrm{u_1(t)}, \quad \ldots \quad u_q(t)]^T$ is vector of q system input variables,

$P = [p_1, \quad \ldots \quad p_r]$ is vector of r parameters,

$F(\ldots) = [f_1(\ldots), \quad \ldots \quad f_n(\ldots)]^T$ is a vector of n 1st-order differential state equations,

$G(\ldots) = [g_1(\ldots), \quad \ldots \quad g_m(\ldots)]^T$ is a vector of m output equations.

If initial states $X(t = 0)$ are known, and inputs $U(t)$ defined, the nonlinear state-space equations in (3.1) have a unique trajectory of the outputs $Y(t = 0 \rightarrow \infty)$ under normal/mild conditions.

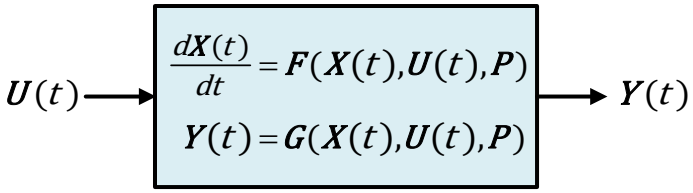

FIGURE 3.1 Block diagram representation of a time-invariant, MIMO nonlinear state-space model.

3.2.2 System as a network of subsystems

To simplify the modelling effort, we can decompose the system on separate subsystems. A single arbitrary subsystem is denoted by S_a where a is an index. Each subsystem is symbolically represented and modelled by their governing state and output equations, where state and output equations can be aggregated into two separate vector functions, F and G. Some subsystems are linear and thus equate to a linear state-space model. The interfaces between subsystems, showing connection between inputs and

outputs, is defined solely by algebraic equations. The aim is to combine and transform individual subsystem models with connection rules to derive a full system model, described as a nonlinear state-space model.

A complete system can be formed by the interconnection of multiple subsystems specified by a netlist which describes how inputs and outputs of subsystems are connected together. The technique to combine separate subsystems is based on aggregating all subsystems, substituting for individual subsystem input variables based on the connections, and the algebraic elimination of variables that are deemed intermediates (i.e. those variables that are not parameters, inputs or outputs of the full system). Through this partitioning, it becomes natural to represent the system diagrammatically as shown in Figure 3.2.

3.2.3 Linearising and extracting transfer functions

Small-signal analysis can be done be linearising the above and using the nonlinear equation to find X_0. All posible transfer functions can be derived. The representation of the combined system model has a form similar to that of the individual subsystems.

$$H(s) = \frac{Y(s)}{U(s)} = C(sI - A)^{-1}B + D \tag{3.2}$$

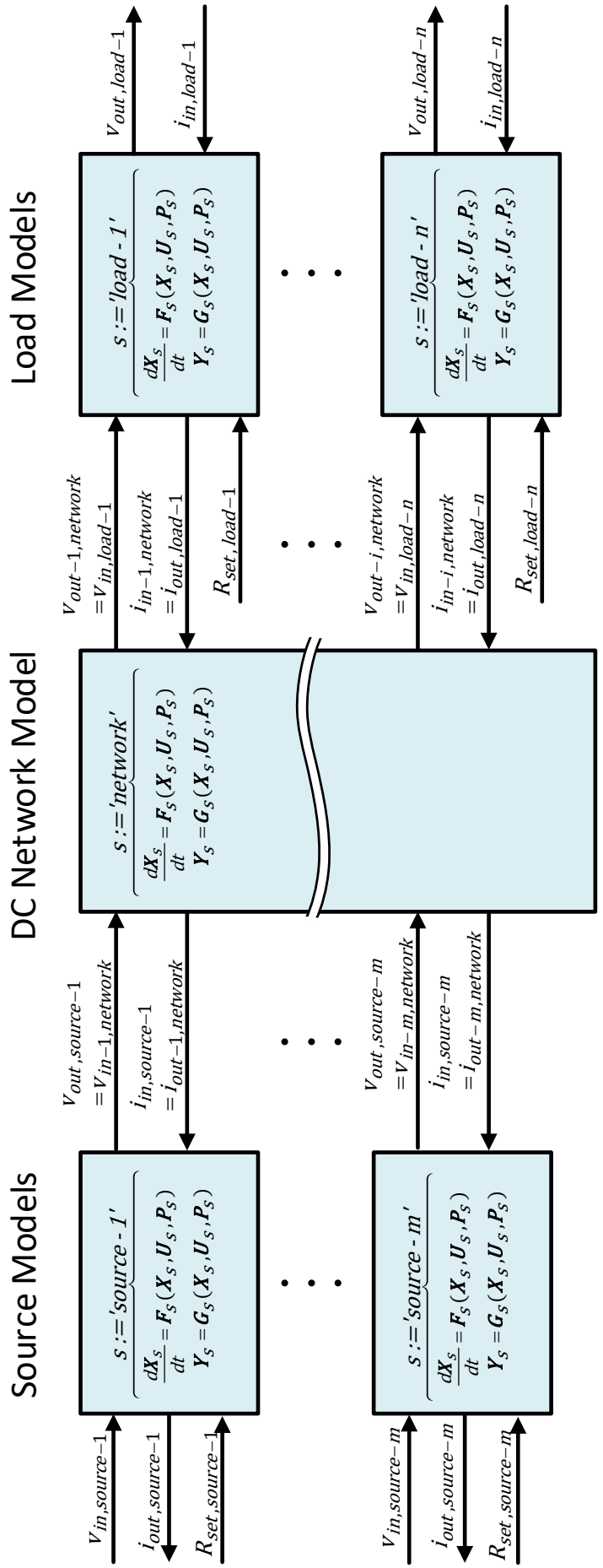

FIGURE 3.2 Block diagram representation of a full-order DC power system, made up of an interconnection of many smaller subsystems.

3.3 Subsystem Component Models

This section describes the models of individual subsystem components used in DC power systems, which include the passive networks, filters, PWM DC-to-DC converters, and feedback controllers. To keep generality of the building blocks, parasitic elements and controller dynamics are included for accurate symbolic modelling over the full range of operating conditions and are necessary in the analysis of parameter interactions between individual components.

As previously discussed in Sections 2.3-2.5, the timescales relevant for small-signal instability in LVDC DPSs occur well below the switching periods of the PWM converters. As such, the complex time-varying switch dynamics are appropriately omitted through averaging techniques. Even though subsequent analysis is based on small-signal assumptions, converter subsystem models are kept with their averaged dynamics using a nonlinear state-space representation. In contrast to conventional approaches, where models are merged using their linearised form [19], [94], our aim is to maintain model nonlinearity throughout the merging process wherever possible. Precise steady-state operating points can then be determined based on the complete nonlinear power system model.

3.3.1 Passive network components

Figure 3.4 shows the two-port schematic representation of a DC network used to describe passive circuits such as power line filters and distribution cables. Both input and output ports are indicated by a pair of terminals as the connection interface to upstream and downstream circuits. As with any two-port mathematical representation (e.g. z-parameters), the dynamic relationship between the four external variables – terminal voltages and currents – can be fully specified as a 2×2 MIMO system [33]. Assuming a known model of a linear electrical network, if any two of these variables are independently driven by an external source, the remaining (dependent) variables can be determined.

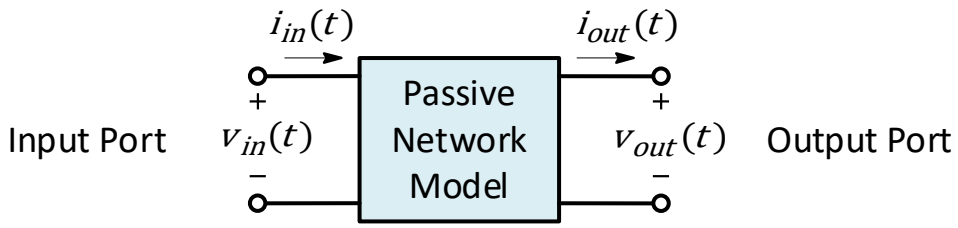

FIGURE 3.3 Two-port representation of a passive distribution network.

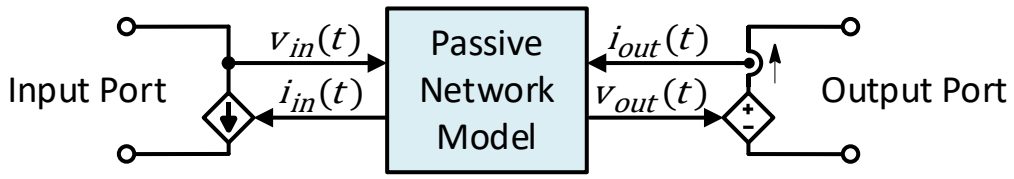

FIGURE 3.4 Circuit representation of a passive distribution network, $v_{in}(t)$ and $i_{out}(t)$ selected as independent model input variables.

The linear state-space representation in (3.2) is used to model passive network given in Figure 3.4. T*he* input port voltage $v_{in}(t)$ and output current $i_{out}(t)$ are selected as the state-space model input variables. The output voltage $v_{out}(t)$ and input current $i_{in}(t)$ are therefore treated as the mode output variables. In this form, the cascade connection of multiple state-space models becomes straightforward. The output voltage of an upstream subsystem directly corresponds to the input voltage of the downstream subsystem. Likewise, output (load) current on the upstream subsystem equals the input current sourced by the downstream subsystem.

$$\begin{aligned} \frac{dX(t)}{dt} &= A(P)X(t) + B(P)\begin{bmatrix} v_{in}(t) \\ i_{out}(t) \end{bmatrix} \\ \begin{bmatrix} v_{out}(t) \\ i_{in}(t) \end{bmatrix} &= C(P)X(t) + D(P)\begin{bmatrix} v_{in}(t) \\ i_{out}(t) \end{bmatrix} \end{aligned} \tag{3.2}$$

where vector *P* contains all parameters of fixed value, input $u(t) = [v_{in}(t), i_{out}(t)]^T$, output $y(t) = [v_{out}(t), i_{in}(t)]^T$, and A, B, C, D are the state-space Jacobian matrices.

Network subsystem blocks are assumed to be purely passive with no internal independent sources and can be modelled using lumped-elements. The number of states is

therefore determined by the number of reactive components in the model, where state variables are defined as only inductor currents and capacitor voltages. The number of elements used to model the dynamics of a real network ultimately depends on the required accuracy to measured data.

The examples below illustrate the development of a typical network model used as building-block in larger DC systems. A library of such components is provided with the SymMIAL toolbox (Section 3.4)

Example 3.1: Modular model of an LC filter with parasitics

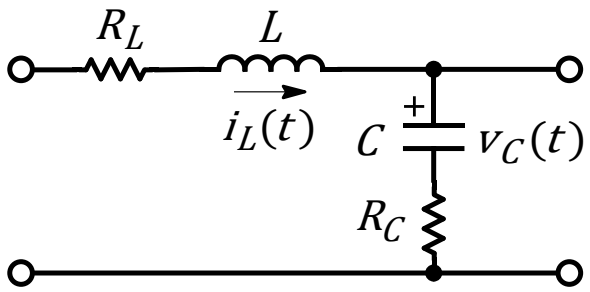

FIGURE 3.5 Circuit diagram of an LC filter with parasitic resistances.

The equivalent circuit of a passive low-pass power filter is shown in Figure 3.5. Parasitic circuit resistances for the reactive components are included. Both the DCR and ESR values are provided in datasheets, often with a wide tolerance, and subject to significant aging effects. In particular, the DCR of the inductor provides a series damping effect on the resonant peak of the filter, and provide a voltage drop for capacitor steady-state operating voltage. These parasitics therefore have a fundamental effect on the small-signal behaviour in source-load systems and their relative contribution to interactions must be assessed.

The linear model of the above LC filter yields the following circuit equations in (3.3).

$$\begin{aligned} C\frac{dv_c(t)}{dt} &= i_L(t) - i_{out}(t) \\ L\frac{di_L(t)}{dt} &= v_{in}(t) - v_C(t) - (\mathrm{R_C} + \mathrm{R_L})i_L(t) + \mathrm{R_C}i_{out}(t) \end{aligned} \tag{3.3}$$

$$i_{in}(t) = i_L(t)$$

$$v_{out}(t) = v_C(t) - R_C i_{out}(t) + R_C i_L(t)$$

And then rearranged into the linear state-space form of below in (3.4).

$$\frac{dX(t)}{dt} = \begin{bmatrix} 0 & \frac{1}{C} \\ -\frac{1}{L} & -\frac{(\mathrm{R_C} + \mathrm{R_L})}{L} \end{bmatrix} X(t) + \begin{bmatrix} 0 & -\frac{1}{C} \\ \frac{1}{L} & \frac{R_C}{L} \end{bmatrix} U(t)$$
$$Y(t) = \begin{bmatrix} 1 & R_C \\ 0 & 1 \end{bmatrix} X(t) + \begin{bmatrix} 0 & -R_C \\ 0 & 0 \end{bmatrix} U(t) \tag{3.4}$$

Where,

$X(t) = [v_C(t), i_L(t)]^T$,

$Y(t) = [v_{out}(t), i_{in}(t)]^T$,

$U(t) = [v_{in}(t), i_{out}(t)]^T$.

Example 3.2: One-port networks (e.g., resistive load)

Subsystems that do not feature an output port can be simplified to a one-port network. These components can be expressly modelled as an input impedance (or admittance), keeping the existing convention of voltage-as-input variable:

$$i_{in}(s) = (1/Z_{in}(s))v_{in}(s) \tag{3.5}$$

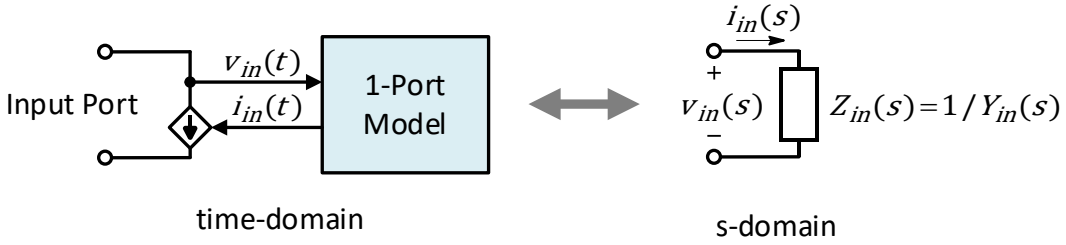

FIGURE 3.6 Circuit diagram of a one-port subsystem in time domain and s-domain.

Noting that we have expressed equation (3.5) is the *s*-domain, which must be converted to a valid state-space representation. Assuming the analytic transfer function expression is known for $Z_{in}(s)$, a time-domain state-space model can therefore be

realised using one of the so-called *canonical* forms [97] . With this, the number of poles corresponds to the number of states.

In the case of a constant input impedance over all frequencies, i.e., no reactive elements with a fixed resistance, $Z_{in}(s) = R$, this trivial example becomes Ohm's law in (3.6):

$$i_{in}(t) = (1/R)v_{in}(t) \tag{3.6}$$

After successive power conversion stages, the end-loads in DC power distribution systems typically have a dominant resistive characteristic (e.g., heating elements, digital electronics), and can be modelled as such.

3.3.2 Active components: PWM DC-to-DC power converters

Referring back to previous discussions in Section 2.3, the complex dynamic behaviour of active loads has been understood to be as important factor in the small-signal stability of DC DPSs. While ideal CPL dynamics are often used to model active loads for source-load instability, in recent years it has been established a need for more detailed mathematical models of practical converters. Inclusion of controller dynamics and circuit parameters provides more insightful analysis on the impact of critical parameters influencing system stability that CPLs neglect [19], [98].

Unlike conventional approaches, where converters are modelled and combined using their linearised form [94], the modelling aim is to preserve nonlinearity ensuring validity for all operating points. The precise steady-state operating point of inherently nonlinear subsystems is dependent on other interconnected components. Therefore, steady-state operating points must be evaluated with respect to the complete power system model.

Figure 3.7 shows the two-port schematic representation of an averaged time-domain power stage. The DC-to-DC converter circuit is comprised of switching semiconductor elements (e.g., MOSFETs, IGBTs, diodes) and passive elements. The switches are assumed to have two states, *on* and *off*, and are controlled by periodic pulse waveforms $q(t)$ from a PWM modulator. In turn, the PWM modulator is driven by a continuous-time input signal referred to as the duty cycle $d(t)$. For simplicity we have

only shown a single control input variable, however this modelling may be extended to multiple control inputs.

To derive the dynamic equations for a converter, the method of state-space averaging (SSA) is applied to the discrete time-varying switching dynamics. This method firstly splits the power stage into the equivalent (sub)circuits under each switch state. Effectively replacing the switches with an open or a short, each subcircuit becomes a time invariant linear system. Therefore, linear state-space model can be found for each subcircuit. These dynamic models are then averaged over the duty cycle yielding the average power stage model. As a result, a nonlinear relationship between circuit variables and control inputs arises in the average model. A more comprehensive treatment of the SSA method may found in [32], [33], [78], [99].

The general nonlinear state-space representation in (3.1) is used to represent the averaged converter model in Figure 3.7.

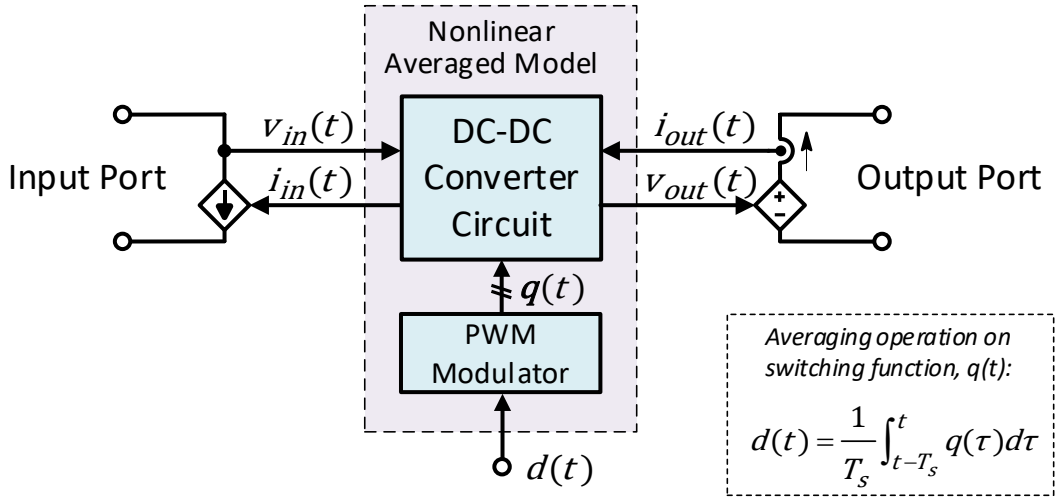

FIGURE 3.7 Circuit representation of a switch-mode DC-to-DC converter with averaged power stage dynamics.

The following example demonstrates the derivation of the nonlinear average model of synchronous buck converter using the SSA technique. This approach is used to derive symbolic models for the remaining primitive DC-to-DC topologies (i.e., boost, and buck-boost), with assumption of instantaneous synchronous switches and CCM operation, as part of *SymMIAL* toolbox component libraries.

In practice, however, it is important to acknowledge that the internal dynamics are far more complex than the above continuous-time-invariant assumptions. Power

semiconductor switches and modulators introduce discrete behaviours with delay effects. For the purposes of small-signal stability analysis, where important interaction phenomena occur at low frequencies, we may neglect high-frequency converter dynamics and time delays of modulators.

Example 3.3: Synchronous buck converter power stage under CCM

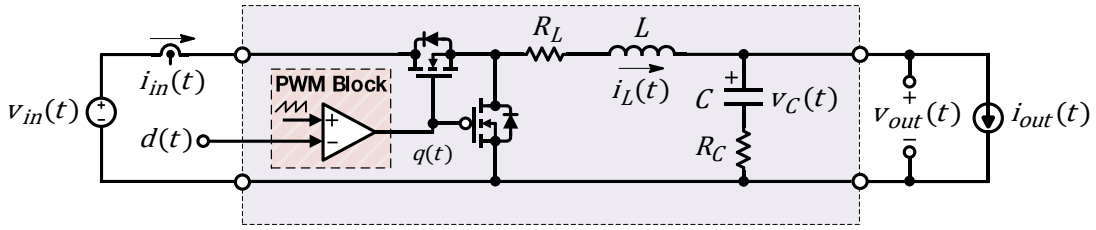

FIGURE 3.8 Circuit diagram of a synchronous buck converter.

Figure 3.8 shows the circuit diagram of a step-down synchronous buck converter. The states variables are the capacitor voltage and inductor current.

$$x(t) = [v_C(t) \quad i_L(t)]^T \tag{3.7}$$

The input variables include the source voltage, load current and duty cycle.

$$\mathrm{u(t)} = [v_{in}(t) \quad i_{out}(t) \quad d(t)]^{\mathrm{T}} \tag{3.8}$$

The output voltage and the input current from the source are the output variables:

$$\mathrm{y(t)} = [\mathrm{v_{out}(t)} \quad \mathrm{i_{in}(t)}]^{\mathrm{T}} \tag{3.9}$$

The MOSFETs Q1 and Q2 are complementary and assumed to have instantaneous switching behaviour with no deadtime. With this, Q1 and Q2 together can be considered as an ideal single-pole double-throw switch controlled by a Boolean switching function $q(t) = \{0,1\}$. The converter may therefore be split into two modes of operation, with different subcircuit model, over a switching period:

1) Source-connected; inductor charging; $q = 0$

2) Source-disconnect; inductor discharging; $q = 1$

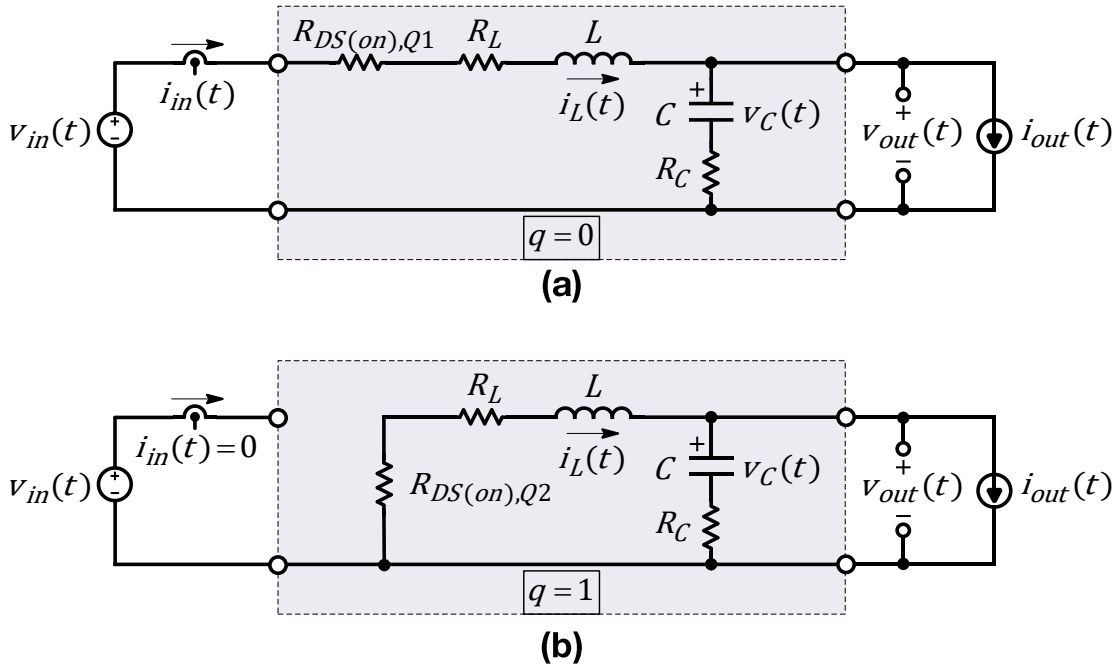

FIGURE 3.9 The two subcircuits of the synchronous buck converter at different switching state: **(a)** $q(t) = 0$, **(b)** $q(t) = 1$.

In the above subcircuits, Q1 and Q2 MOSFETs have been replaced by their drain-to-source channel on-state resistance $R_{DS(on)}$.

On State:

Subcircuit in Figure 3.9(a) can be used to derive the linear equations for the *on* state, shown below:

$$\left.\frac{di_L(t)}{dt}\right|_{q(t)=0} = -\frac{v_c(t)}{L} + \frac{v_{in}(t)}{L}$$
$$\left.\frac{dv_c(t)}{dt}\right|_{q(t)=0} = \frac{i_L(t)}{C} - \frac{i_{out}(t)}{C} \qquad (3.10)$$
$$v_{out}(t)|_{q(t)=0} = v_c(t)$$
$$i_{in}(t)|_{q(t)=0} = i_L(t)$$

Off State:

Subcircuit in Figure 3.9(b) can be used to derive the linear equations for the *off* state, shown below in:

$$\left.\frac{di_L(t)}{dt}\right|_{q(t)=1} = -\frac{v_c(t)}{L}$$

$$\left.\frac{dv_c(t)}{dt}\right|_{q(t)=1} = \frac{i_L(t)}{C} - \frac{i_{out}(t)}{C} \tag{3.11}$$

$$v_{out}(t)|_{q(t)=1} = v_c(t)$$

$$i_{in}(t)|_{q(t)=1} = 0$$

Averaging:

The buck converter exists in the $q(t) = 1$ state for an average period of:

$$\frac{t_{on}}{t_{on} + t_{off}} = d(t) \tag{3.12}$$

Likewise, in the system exists in the $q(t) = 0$ state for an average period of:

$$\frac{t_{off}}{t_{on} + t_{off}} = 1 - d(t) \tag{3.1}$$

Averaging both subcircuit models over the full switching period yields (3.13):

$$\begin{aligned}\frac{dv_c(t)}{dt} &= d(t)\left.\frac{dv_c(t)}{dt}\right|_{q(t)=1} + \big(1 - d(t)\big)\left.\frac{dv_c(t)}{dt}\right|_{q(t)=0} \\ \frac{di_L(t)}{dt} &= d(t)\left.\frac{di_L(t)}{dt}\right|_{q(t)=1} + \big(1 - d(t)\big)\left.\frac{di_L(t)}{dt}\right|_{q(t)=0}\end{aligned} \tag{3.13}$$

Substituting and simplifying, the averaged (nonlinear) synchronous buck converter model can therefore be described by the following equations in (3.14):

$$\frac{dv_c(t)}{dt} = \frac{i_L(t)}{C} - \frac{i_2(t)}{C}$$

$$\frac{di_L(t)}{dt} = -\frac{v_c(t)}{L} + \frac{v_1(t)d(t)}{L} \tag{3.14}$$

$$v_2(t) = v_c(t)$$

$$i_1(t) = i_L(t)d(t)$$

3.3.3 Feedback controllers

Linear feedback control is assumed and represented in the classic state-space form, below. In DPSs, primary control refers to regulation of current or voltage as well as power sharing in the case of parallel sources.

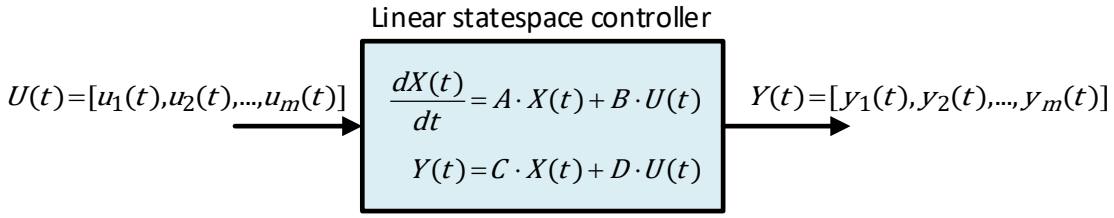

FIGURE 3.10 General block representation of a linear controller in state-space form.

$$\frac{dX_C(t)}{dt} = \mathrm{A_C}X_C(t) + B_C U_C(t)$$
$$U(t) = C_C X_C(t) + D_C U_C(t) \tag{3.15}$$

Example 3.4: Type-III Analogue Compensator

For buck converter control, a type-III compensator is often used to shape the closed-loop dynamics to a desired specification.

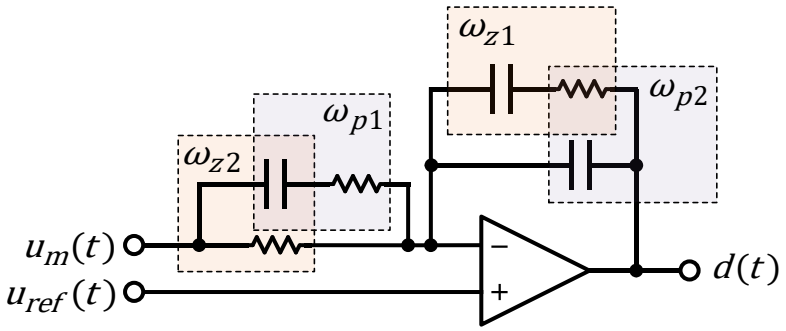

FIGURE 3.11 Circuit diagram of a *type-III* analogue compensator.

The type-III analogue compensator shown in Figure 3.11 is characterised by three poles (with one pole at the origin) and two zeroes. Controller designs of this form are

almost always exclusively done in the frequency domain, with the open-loop power stage dynamics determining suitable poles and zeros locations. After, the required resistor and capacitor values in the compensator can be calculated directly using the procedures outlined in [100]. The zeros are included to damp the double pole resonance of the output filter. The overall transfer function of the compensator $H(s)$ can be given by equation:

$$H(s) = \frac{d(s)}{u_{err}(s)} = K_{DC}\frac{\left(1+\frac{s}{\omega_{z1}}\right)\left(1+\frac{s}{\omega_{z2}}\right)}{s\left(1+\frac{s}{\omega_{p1}}\right)\left(1+\frac{s}{\omega_{p2}}\right)} \tag{3.16}$$

Where the error signal is $u_{err}(s) = u_{ref}(s) - u_m(s)$.

K_{DC} determines the gain at DC and consequently the open-loop phase crossover frequency (which is close the closed-loop -3dB bandwidth)

Conversion of the transfer function (3.17) to an equivalent state-space representation can be done by finding a set of state-space matrices such that $H(s) = C(sI - A)^{-1}B + D$.

A possible time domain realisation of the type III compensator is equivalent to the three-state system below in (3.17):

$$\frac{dX}{dt} = \begin{bmatrix} -(\omega_{p1}+\omega_{p2}) & 1 & 0 \\ -\omega_{p1}\omega_{p2} & 0 & 1 \\ 0 & 0 & 0 \end{bmatrix} X + \begin{bmatrix} \omega_{p1}\omega_{p2}/(\omega_{z1}\omega_{z2}) \\ \omega_{p1}\omega_{p2}(1/\omega_{z1}+1/\omega_{z2}) \\ \omega_{p1}\omega_{p2} \end{bmatrix} U_{err} \tag{3.17}$$

$$d(t) = [K_{DC} \quad 0 \quad 0]X$$

Where, $U_{err} = \left(u_{ref} - u_m\right)$ and $X = [x_1, x_2, x_3]^T$ are the state variables corresponding to stored voltage in the capacitors.

A good approximation for a controller with a type III realisation can be expressed in terms of the buck converter power stage parameters, below in the s-domain:

$$H(s) = \omega_{-3dB} \cdot \frac{\omega_{sw}\left(s\sqrt{LC}+1\right)^2}{sVin.(s.2+\omega_{sw}).(sC.ESR+1)} \tag{3.18}$$

3.4 SymMIAL: A MATLAB Toolbox for Symbolic Model Interconnection and Linearisation

3.4.1 Purpose and overview

The purpose of the newly developed toolbox, *SymMIAL,* is to provide users with a convenient and efficient way to modelling large power systems within a nonlinear state-space framework. Specifically, the easy construction and combination of arbitrary models defined in a library of common parts.

SymMIAL toolbox source code is available along with documentation and numerous examples files based on the studied systems contained within this thesis. See Appendix A for further implementation details. The toolbox was developed initially under *MATLAB 9.2 R2017a* with revisions made up to version *MATLAB 9.7 R2019b*.

3.4.2 Program implementation

This section describes the step-by-step the process of combining separate (symbolic) subsystems to simplify the modelling process while preserving system model nonlinearities. Parameter vector P are omitted in the equations for brevity. Subscript notation ($sub\text{-}i$) herein is used to indicate the i-th subsystem. Figure 3.12 shows the flow diagram of the developed procedures, discussed herein:

1. Concatenate all subsystems

Vectors:

$$\frac{dX_{concat}}{dt} = \left[\frac{dX_{sub\text{-}1}}{dt}, \frac{dX_{sub-2}}{dt}, \dots, \frac{dX_{sub-n}}{dt}\right]^T \tag{3.19}$$

$\mathrm{X}_{concat} = [X_{sub\text{-}1}, X_{sub-2}, \dots, X_{sub-n}]^T$

$\mathrm{Y}_{concat} = [Y_{sub\text{-}1}, Y_{sub-2}, \dots, Y_{sub-m}]^T$

$U_{concat} = [U_{sub\text{-}1}, U_{sub\text{-}2}, \dots, U_{sub-m}]^T$

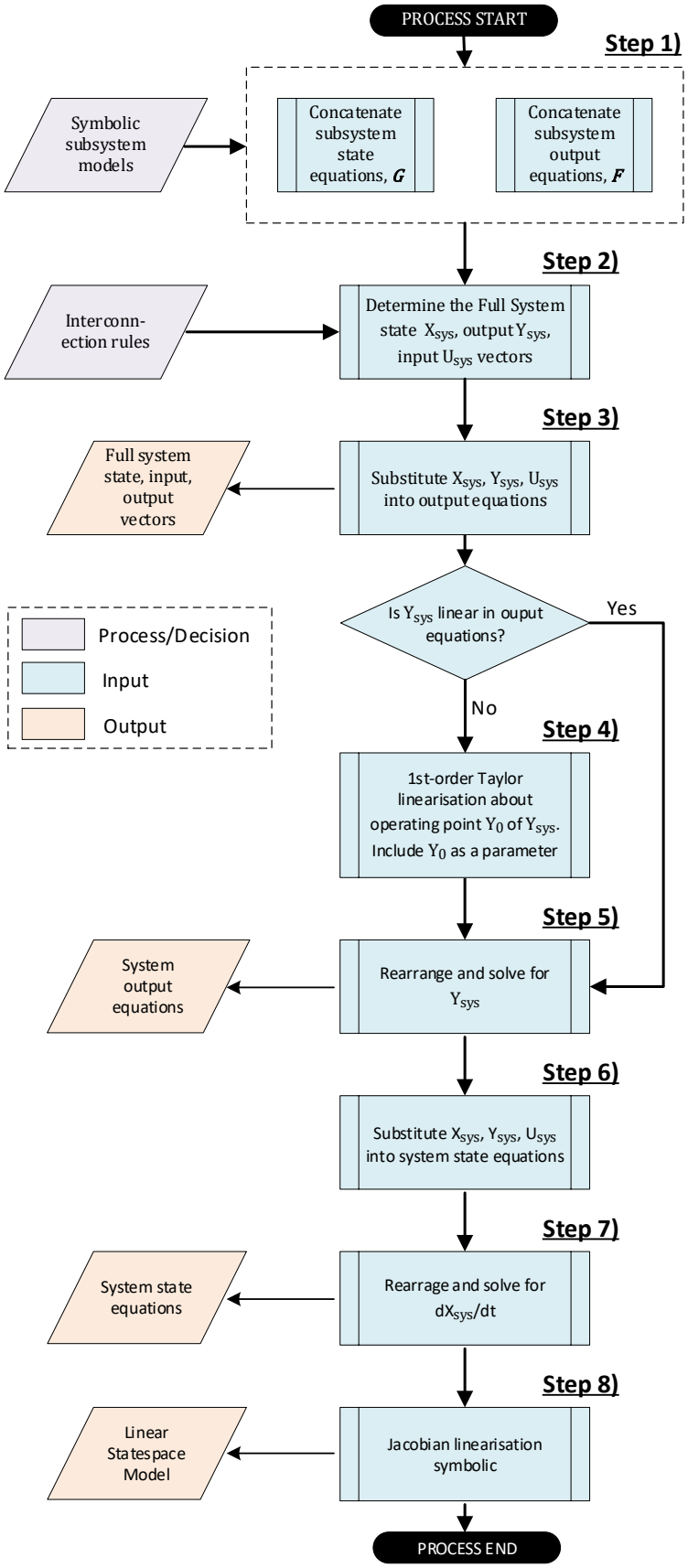

FIGURE 3.12 Program flow showing steps for generating a full system model from subsystems.

Equations: Group all state and output equations together.

$$\mathrm{F}_{\mathrm{concat}} = \begin{bmatrix} \mathrm{F}_{\mathrm{sub-1}}(X_{\mathrm{sub-1}}, U_{\mathrm{sub-1}}) \\ \mathrm{F}_{\mathrm{sub-2}}(X_{\mathrm{sub-2}}, U_{\mathrm{sub-2}}) \\ \vdots \\ \mathrm{F}_{\mathrm{sub-n}}(X_{\mathrm{sub-n}}, U_{\mathrm{sub-n}}) \end{bmatrix} \tag{3.20}$$

$$\mathrm{G}_{\mathrm{concat}} = \begin{bmatrix} \mathrm{G}_{\mathrm{sub-1}}(X_{\mathrm{sub-1}}, U_{\mathrm{sub-1}}) \\ \mathrm{G}_{\mathrm{sub-2}}(X_{\mathrm{sub-2}}, U_{\mathrm{sub-2}}) \\ \vdots \\ \mathrm{G}_{\mathrm{sub-n}}(X_{\mathrm{sub-n}}, U_{\mathrm{sub-n}}) \end{bmatrix} \tag{3.21}$$

2. Finding X_{sys}, Y_{sys}

$$\begin{aligned} X_{sys} &= \mathrm{X}_{concat} \\ Y_{sys} &= \mathrm{Y}_{concat} \end{aligned} \tag{3.22}$$

3.a. Finding U_{sys}

The connectivity netlist is a set of algebraic equations relating subsystem output connections to subsystem inputs, and is represented by matrix L in the following equation (3.23):

$$U_{net} = L.Y_{sys} \tag{3.23}$$

Y_{sys} represents all outputs of system. Noting that not all outputs are necessary fed back to inputs.

U_{net} is a vector of all input variables of different subsystems that are connected to outputs, thereby forming a closed-loop feedback system.

The set difference of U_{concat} and U_{net} is the set of elements in U_{concat} but not in U_{net} (3.24):

$$\mathrm{U}_{\mathrm{sys}} = \mathrm{U}_{\mathrm{concat}} \backslash \mathrm{U}_{\mathrm{net}} = \{x \in U_{concat} \mid x \notin U_{net}\} \tag{3.24}$$

Where U_{sys} are all the inputs that are left unconnected to any outputs, i.e., left as open-loop input, and are therefore defined as the system inputs

3.b. Establish required system representation / form

The required form of the combined system is given below in (3.25):

$$\frac{dX_{sys}}{dt} = F_{sys}(X_{sys}, U_{sys})$$
$$\mathrm{Y_{sys}} = G_{sys}(X_{sys}, U_{sys}) \tag{3.25}$$

Where X_{sys}, U_{sys} and Y_{sys} have been previously specified in Step 1-2.

The aim is to find the equations F_{sys} and G_{sys}.

3.c. Finding G_{sys}

The superscript * denotes a modification to the original function:

subsitute for system state:

$$Y_{sub-i} = \mathrm{G}^{*}_{sub-i}(X_{sys}, U_{\mathrm{sub-i}}) \tag{3.26}$$

subsitute for system output:

$$Y_{sub-i} = \mathrm{G}^{*}_{sub-i}(X_{sys}, U_{\mathrm{sys}}, Y_{sys}) \tag{3.27}$$

We have replaced $U_{\mathrm{sub-i}}$ with U_{sys} and Y_{sys}. Noting that if G_{sub-i} contains no system inputs, i.e. all subsystem inputs have been connected by other subsysytem outputs, then G_{sub-i} becomes (3.28):

$$Y_{sub-i} = \mathrm{G}^{*}_{sub-i}(X_{sys}, Y_{sys}) \tag{3.28}$$

In other words, the relation between a subsystem ouput Y_{sub-i} is dependent only on the state variables and the outputs of other subsystems.

Replacing this to create:

$$\mathrm{Y_{sys}} = \mathrm{G}^{*}_{concat}(X_{sys}, U_{\mathrm{sys}}, Y_{sys}) \tag{3.29}$$

4.a. If Y_{sys} linear

If G_{concat} can be written in linear w.r.t. X, U, and Y, i.e.

$$\mathrm{Y_{sys}} = CX_{sys} + \mathrm{D}U_{\mathrm{sys}} + EY_{sys} \tag{3.30}$$

For some matrices $C\ D\ E$, (3.30) can be rearraged into the following form:

$$\begin{aligned} \mathrm{Y_{sys}} &= CX_{sys}(I-E)^{-1} + \mathrm{D}U_{\mathrm{sys}}(I-E)^{-1} \\ &= G^*(X_{sys}, U_{\mathrm{sys}}) \end{aligned} \tag{3.31}$$

This shows that Y_{sys} can be rearraged and uniquely solved as a function of X_{sys} and U_{sys}

4.b. If Y_{sys} nonlinear

However, problems arise if function G^* in (3.29) is nonlinear on the term Y_{sys}, meaning it cannot be linearly transformed into the form (3.31).

To address this, we can linearise this nonlinear G^* in (3.29) w.r.t variables Y_{sys} to approximate the solutions to the system of equations around some point $Y_{sys,0}$.

Applying first-order Taylor linearisation about $Y_{sys,0}$ to (3.29), we get the following expression (3.32) (while also omitting subscript sys for simplicity):

$$\mathrm{Y} = G(X, U, Y_0) + \nabla G(X, U, Y_0) \cdot (Y - Y_0) \tag{3.32}$$

Rearranging and solving for Y in (3.32) yeilds the following (3.33):

$$\mathrm{Y} = (G(X, U, Y_0) - \nabla G(X, U, Y_0)Y_0)\big(I - \nabla G(X, U, Y_0)\big)^{-1} \tag{3.33}$$

As Y_0 is a constant, it can be treated as part of the parameters of function G. Noting that the right hand side of equation (3.33) is now a function of variables X and U only, and (3.33) can be written as simply (3.34):

$$\mathrm{Y_{sys}} = G_{sys}(X_{sys}, U_{\mathrm{sys}}) \tag{3.34}$$

This thereby effecivly represents all of the output equations in the valid form expected by the nonlinear state-space equation in (3.25).

Later on we will discuss the problem of finding a suitable value Y_0 required for linearisation. For now, we treat Y_0 as an addition to the system parameters and is an a-priori known.

5. Finding F_{sys}

Similar to replace subsystem inputs with system outputs based on connections to get:

$$\frac{dX_{sys}}{dt} = F^*_{concat}\left(X_{sys}, U_{sys}, Y_{sys}\right) \tag{3.35}$$

As Y_{sys} is known, subsitituting (3.34) into above (3.35):

$$\frac{dX_{sys}}{dt} = F^*_{concat}\left(X_{sys}, U_{sys}, G_{sys}(X_{sys}, U_{\text{sys}})\right) \tag{3.36}$$

F^*_{concat} is now a function of only X_{sys} and U_{sys}, which (3.36) can be rearranged and simplifed to (3.37):

$$\frac{dX_{sys}}{dt} = F_{sys}\left(X_{sys}, U_{sys}\right) \tag{3.37}$$

Both F_{sys} and G_{sys} are now in the valid nonlinear state-space form (3.25).

6. Finding linear model

6a. symbolic linear state-space model

The nonlinear system equations F and G in (3.34) and (3.37) can be linearised about an arbitrary equilibrium (X_0 and U_0). Evaluated at this point, the corresponding linear state-space model can be represented by equations (3.38), where A, B, C, and D are constant Jacobian matrices.

$$\begin{aligned} \frac{dX}{dt} &= AX + BU \\ Y &= CX + DU \end{aligned} \tag{3.38}$$

Where,

$$A(X_0,U_0)=\frac{\partial F(X,U)}{\partial X}\Big|_{\substack{X=X_0\\U=U_0}}=\begin{bmatrix}\frac{\partial f_1(X,U)}{\partial x_1} & \cdots & \frac{\partial f_1(X,U)}{\partial x_n}\\ \vdots & \ddots & \vdots\\ \frac{\partial f_n(X,U)}{\partial x_1} & \cdots & \frac{\partial f_n(X,U)}{\partial x_n}\end{bmatrix}$$

$$B(X_0,U_0)=\frac{\partial \mathrm{F(X,U)}}{\partial \mathrm{U}}\Big|_{\substack{X=X_0\\U=U_0}}=\begin{bmatrix}\frac{\partial \mathrm{f_1}(X,U)}{\partial \mathrm{u_1}} & \cdots & \frac{\partial \mathrm{f_1}(X,U)}{\partial \mathrm{u_n}}\\ \vdots & \ddots & \vdots\\ \frac{\partial \mathrm{f_n}(X,U)}{\partial \mathrm{u_1}} & \cdots & \frac{\partial \mathrm{f_n}(X,U)}{\partial \mathrm{u_n}}\end{bmatrix}$$

$$C(X_0,U_0)=\frac{\partial \mathrm{G(X,U)}}{\partial \mathrm{X}}\Big|_{\substack{X=X_0\\U=U_0}}=\begin{bmatrix}\frac{\partial \mathrm{g_1}(X,U)}{\partial \mathrm{x_1}} & \cdots & \frac{\partial \mathrm{g_1}(X,U)}{\partial \mathrm{x_n}}\\ \vdots & \ddots & \vdots\\ \frac{\partial \mathrm{g_n}(X,U)}{\partial \mathrm{x_1}} & \cdots & \frac{\partial \mathrm{g_n}(X,U)}{\partial \mathrm{x_n}}\end{bmatrix}$$

$$D(X_0,U_0)=\frac{\partial \mathrm{G(X,U)}}{\partial \mathrm{U}}\Big|_{\substack{X=X_0\\U=U_0}}=\begin{bmatrix}\frac{\partial \mathrm{g_1}(X,U)}{\partial \mathrm{u_1}} & \cdots & \frac{\partial \mathrm{g_1}(X,U)}{\partial \mathrm{u_n}}\\ \vdots & \ddots & \vdots\\ \frac{\partial \mathrm{g_n}(X,U)}{\partial \mathrm{u_1}} & \cdots & \frac{\partial \mathrm{g_n}(X,U)}{\partial \mathrm{u_n}}\end{bmatrix}$$

Above, the subscript index ($X = X_0,\ U = U_0$) indicates the steady-state equilibrium as constant input. To satisfy this condition, this point is defined by the property (3.39):

$$\frac{dX_{sys}}{dt}=0 \tag{3.39}$$

The trajectories of the states $X(t)$, after small perturbations of the steady-state equilibrium, can be determined by the analysing the state equation in (3.38). The eigen-values of matrix A can be used to assess whether the system diverge or converge to the equilibrium point, indicating an unstable and stable systems, respectively.

Iterative methods are used to solve the nonlinear system of equations in (3.39) when all parameters and inputs are defined. The Newton-Raphson method is suitable for finding the equilibrium points as is commonly used in conventional load-flow problems [67].

In general, nonlinear systems may have multiple equilibrium points that can satisfy the steady-state condition (3.39). As is the case with power systems, typically, only one such point is feasible due to practical constraints in voltages and currents. To address

this, an estimation of the steady-state is firstly done by a detailed simulation under nominal conditions. This is used as the initial guess in Newton–Raphson iteration of the power equations. It was shown that even though steady state values change under varying parameters and inputs, this initial guess was suitable for convergence to the *correct* solution.

3.5 Example: Application to a Single Active Load System

An example of model development procedure using *SymMIAL* is demonstrated here on a single active load system in Figure 3.13. The equivalent control block diagram showing inputs, outputs and connections is given in Figure 3.13.

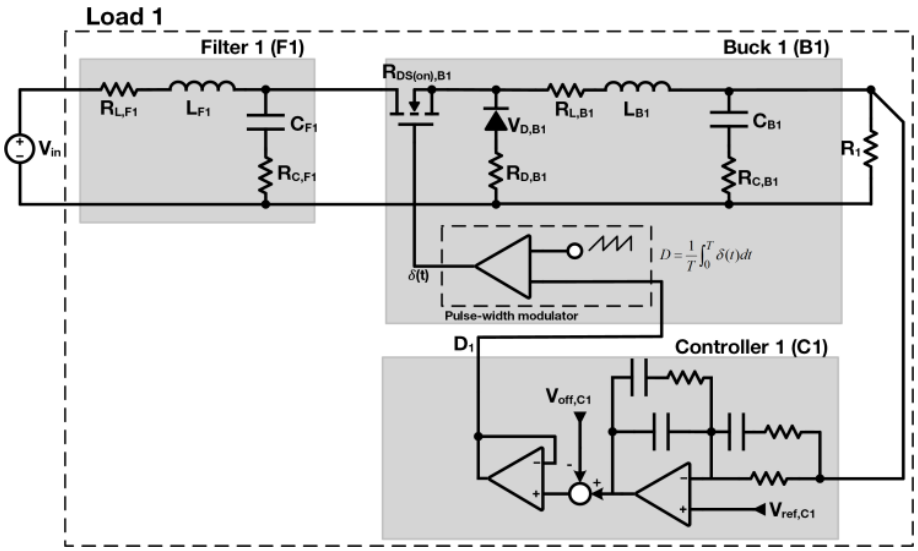

FIGURE 3.13 Circuit model of a single load based on a tightly regulated buck converter with an input filter and type-III compensator.

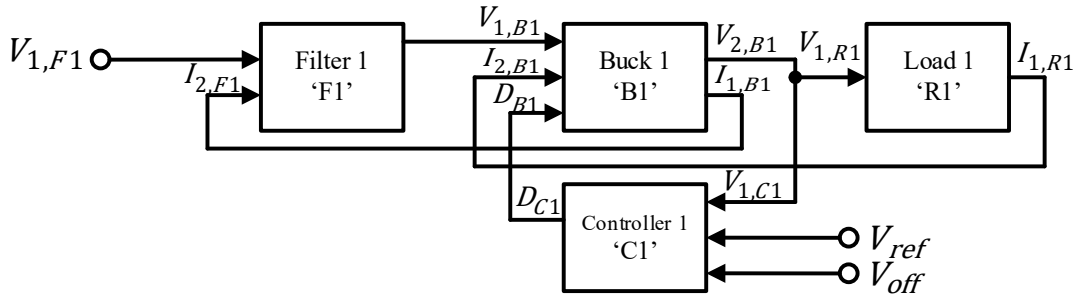

FIGURE 3.14 Block diagram representation of the single load system in Figure 3.13.

Each subsystem block is defined using the equations presented below:

Source Model
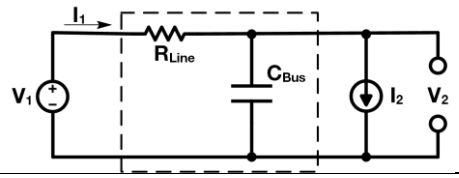
$X = [v_C]$ $U = [V_1 \quad I_2]^T$ $Y = [V_2 \quad I_1]^T$ $\dot{X} = F(X,U) = (V_1 - v_C)/(RC) - I_2/C$ $Y = G(X,U) = \begin{bmatrix} v_C \\ (V_1 - v_C)/R \end{bmatrix}$

LC Filter Model
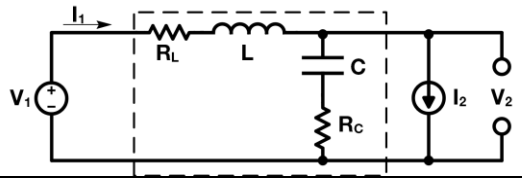
$X = [v_C \quad i_L]^T$ $U = [V_1 \quad I_2]^T$ $Y = [V_2 \quad I_1]^T$ $\dot{X} = F(X,U) = \begin{bmatrix} (i_L - I_2)/C \\ (V_1 - v_C - i_L(R_C + R_L) + I_2 R_C)/L \end{bmatrix}$ $Y = G(X,U) = \begin{bmatrix} v_C - I_2 R_C + i_L R_C \\ i_L \end{bmatrix}$

Buck Converter (Averaged Model)
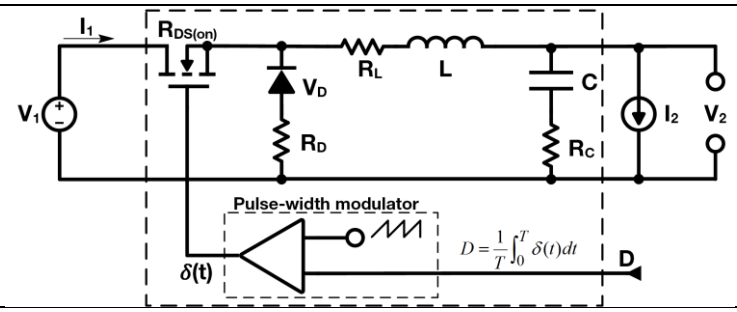
$X = [v_C \quad i_L]^T$ $U = [V_1 \quad I_2 \quad D]^T$ $Y = [V_2 \quad I_1]^T$ $\dot{X} = F(X,U)$ $= \begin{bmatrix} (i_L - I_2)/C \\ -(v_C + V_{\mathrm{D}} - \mathrm{D}(V_1 - V_{\mathrm{D}}) - I_2 R_C + i_L(R_C + R_L + R_D) + \mathrm{D}i_L(R_{DS(on)} - R_D))/\mathrm{L} \end{bmatrix}$ $Y = G(X,U) = \begin{bmatrix} v_C - I_2 R_C + i_L R_C \\ Di_L \end{bmatrix}$

Type III Compensator
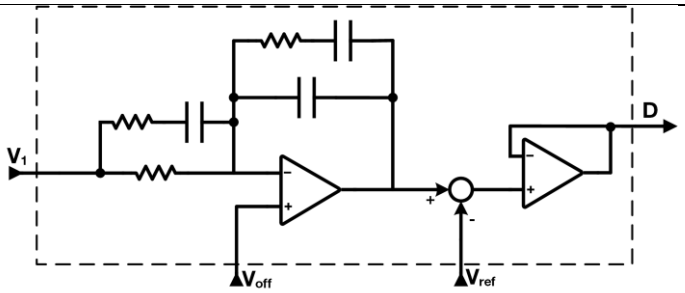
$X = [x_1 \quad x_2 \quad x_3]^T$ $U = [V_1 \quad V_{\mathrm{ref}} \quad V_{\mathrm{off}}]^T$ $Y = D$ $\dot{X} = F(X,U) = \begin{bmatrix} x_2 - x_1(\omega_{p2} + \omega_{p3}) - f_m k(V_{off} - V_{ref}) \\ x_3 - x_1\omega_{p2}\omega_{p3} - f_m k(\omega_{z1} + \omega_{z2})(V_{off} - V_{ref}) \\ -f_m k\omega_{z1}\omega_{z2}(V_{off} - V_{ref}) \end{bmatrix}$ $Y = G(X,U) = x_1 - V_{off} f_m - V_{ref} f_m$

The merging procedure begins with the interconnection rules, shown by the connections between subsystems:

Interconnection rules (Netlist)
$V_{1,B} = V_{2,F}$ $I_{2,F} = I_{1,B}$ $V_{1,C} = V_{2,B}$ $D_B = D_C$ $V_{1,R1} = V_{2,B}$ $I_{2,B} = I_{1,R1}$

After the substitution of interconnection rules algebraic equations into both the system and output equations:

System equations:

$$\dot{V}_{C,F} = -(I_{1,B} - I_{L,F})/C_F$$

$$\dot{I}_{C,F} = (V_{1,F} - V_{C,F} - I_{L,F}(R_{C,F} + R_{L,F}) + I_{1,B}R_{C,F})/L_F$$

$$\dot{V}_{B,F} = -(I_{1,R} - I_{L,B})/C_B$$

$$\dot{I}_{C,B} = -(V_{C,B} + V_{d,B} - D_C V_{2,F} - D_C V_{d,B} - I_{1,R1}R_{C,B} + I_{L,B}R_{C,B} + I_{L,B}R_{L,B} + I_{L,B}\,R_{d(on),B} + D_C I_{L,B}R_{DS(on),B} - D_C I_{L,B}R_{d(on),B})/L_B$$

$$\dot{X}_{1,C} = X_{2,C} - X_{1,C}(w_{p2,C} + w_{p3,C} - f_{m,C}k_C(V_{2,B} - V_{ref,C})$$

$$\dot{X}_{2,C} = X_{3,C} - X_{1,C}w_{p2,C}w_{p3,C} - f_{m,C}k_C(w_{z1,C} + w_{z2,C})(V_{2,B} - V_{ref,C})$$

$$\dot{X}_{3,C} = -f_{m,C}k_C w_{z1,C}w_{z2,C}(V_{2,B} - V_{ref,C})$$

Output equations:

$$V_{2,F} = V_{C,F} - I_{1,B}R_{C,F} + I_{L,F}R_{C,F}$$

$$I_{1,F} = I_{L,F}$$

$$V_{2,B} = V_{C,B} - I_{1,R}R_{C,B} + I_{L,B}R_{C,B}$$

$$I_{1,B} = D_C I_{L,B}$$

$$D_C = X_{1,C} - V_{off,C}f_{m,C} - V_{ref,C}f_{m,C}$$

$$I_{1,R} = V_{2,B}/R_1$$

Linearly rearrange output equations so that inputs are strictly on the left-hand side, and then factor the coefficients of the input Y to create a matrix of coefficients K, i.e., $KY = L$.

$$\overbrace{\begin{bmatrix} 1 & 0 & 0 & R_{C,F} & 0 & 0 \\ 0 & 1 & 0 & 0 & 0 & 0 \\ 0 & 0 & 1 & 0 & 0 & R_{C,B} \\ 0 & 0 & 0 & 1 & -I_{L,B} & 0 \\ 0 & 0 & 0 & 0 & 1 & 0 \\ 0 & 0 & -1/R_1 & 0 & 0 & 1 \end{bmatrix}}^{K} \overbrace{\begin{bmatrix} V_{2,F} \\ I_{1,F} \\ V_{2,B} \\ I_{1,B} \\ D_C \\ I_{1,R} \end{bmatrix}}^{Y} = \overbrace{\begin{bmatrix} V_{C,F} + I_{L,F}R_{C,F} \\ I_{L,F} \\ V_{C,B} + I_{L,B}R_{C,B} \\ 0 \\ X_{1,C} - V_{off,C}f_{m,C} - V_{ref,C}f_{m,C} \\ 0 \end{bmatrix}}^{L} \quad (3.40)$$

Performing Gauss-Jordan elimination on [K,L] using MATLAB's symbolic toolbox, *rref([K,L]),* we obtain,

$$\begin{bmatrix} V_{2,F} \\ I_{1,F} \\ V_{2,B} \\ I_{1,B} \\ D_C \\ I_{1,R} \end{bmatrix} = \begin{bmatrix} \left(V_{C,F} + I_{L,F}R_{C,F} - I_{L,B}R_{C,F}X_{1,C} + I_{L,B}R_{C,F}\,V_{off,C}f_{m,C} + I_{L,B}R_{C,F}V_{ref,C}f_{m,C}\right) \\ I_{L,F} \\ (R_1V_{C,B} + I_{L,B}R_{C,B}R_1)/(R_{C,B} + R_1) \\ -I_{L,B}(V_{off,C}f_{m,C} - X_{1,C} + V_{ref,C}f_{m,C}) \\ X_{1,C} - V_{off,C}f_{m,C} - V_{ref,C}f_{m,C} \\ (V_{C,B} + I_{L,B}R_{C,B})/(R_{C,B} + R_1) \end{bmatrix} \tag{3.41}$$

The above matrix equation is in the state-space form. Every output equation is now a function of only state and input variables.

3.6 Summary

A systematic modelling framework for the detailed dynamic modelling of LVDC DPS suitable for small-signal analysis based on a modular approach has been presented in this chapter. A MATLAB toolbox, *SymMIAL,* was developed to automate the modelling procedure, linearisation, and small-signal stability assessment.

In the next chapter, we will present the design and development experimental hardware of a cascaded power systems featuring poorly damped input filters and voltage-regulated buck converters with digital controls.

Chapter 4

Design and Verification of Power System Models: Experimental Hardware and Simulation

ABSTRACT This chapter describes the design and implementation of the experimental systems used throughout this thesis. A single active load comprising of an input LC filter cascaded with a tightly-regulated synchronous buck converter feeding a resistive load is described in detail. The synchronous buck converter operates with voltage-mode control implemented on an external microcontroller unit. This hardware is used to validate system modelling of Chapter 3 and later extended with the parallel operation of two active loads for Chapter 5 and Chapter 6. Comparisons between the theoretical models and experimental data are shown to closely match.

4.1 Introduction

The previous chapter established the theoretical modelling approach for small-signal stability analysis of LVDC DPSs. These models must be sufficiently accurate in predicting the dynamics of interest (e.g., point of instability) of the *real* system. This chapter focuses on verifying models through an agreement between the model outputs and the data collected from experimental test benches. Along with model verification, models are refined through the use of experimental data when specific model parameters cannot be determined beforehand to an acceptable accuracy. Presented in this chapter are the two LVDC DPS hardware test benches and test procedures used for experimental verification in the latter chapters (Chapter 5 and 6).

The test-bench developed is an experimental hardware prototype of an active load consisting of a cascaded system of an input filter and an output-voltage-regulated synchronous buck-converter feeding a resistive load. A digital controller is used for voltage regulation and is implemented on a TMS320F28379D microcontroller. This system is used to investigate the source-load interactions. A second active load, nominally identical to the first, is constructed for the study of modal coupling under parallel operation, for use in Chapter 6.

4.2 Input Filter Instability with an Active Load based on Synchronous Buck Converter under Voltage-mode Control

In this section, we present the design of the cascaded system depicted in Figure 4.1 based on a tightly-regulated synchronous buck converter with resistive load—referred to as an active load—which is fed by a poorly damped input filter. We describe the practical hardware implemented for the synchronous buck converter and the design and realisation of the digital voltage-mode controller suitable for tuning closed-loop bandwidth. Model refinement is achieved through parameter measurement and estimation based on experimental waveforms.

Experiments carried out show a good match between analytical predictions and observed behaviour. In Section 4.2.4, a study on the impact of the digital controller

parameters on CPL dynamics of the active load is presented. Finally, source-load interaction induced instability is experimentally demonstrated when the active load is fed by a poorly damped differential-mode LC input filter.

In Chapter 6, the phenomenon of modal coupling is investigated which relies on very accurate system parameter values to accurately predict dynamic behaviours. When modal coupling occurs, the system becomes very highly sensitive to certain parameter variation. Therefore, precise parameter values in analytical models become paramount when predicting real-world experimental behaviour.

4.2.1 System overview

The block diagram in Figure 4.1 provides an overview of the LVDC power system used for the experimental test bench. The rig consists of three parts: the laboratory programmable DC power supply, LC input filter, and the active load. The active load is comprised of a step-down buck converter with fixed load and an external microcontroller used to regulate the output voltage.

The rig was constructed in the Electrical Machines and Drives (EMD) Group at the University of Sheffield with test and measurement facilities of the Control and Power Systems (CAPS) Research Group. Images of the major components of experimental rig are shown in Figure 4.2. The following sections detail the implementation of the hardware prototype and test procedures.

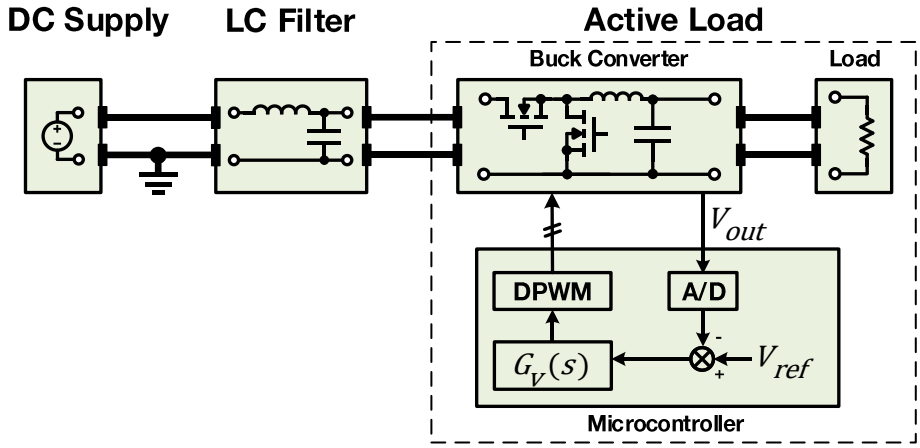

FIGURE 4.1 Block diagram of the experimental cascaded LVDC power system.

4.2.2 Description and design of experimental hardware

Figure 4.1 and Figure 4.2 show the system block diagram and experimental rig, respectively, for the cascaded LVDC power system based on a single active load. The active load is realised using a synchronous buck converter with a tightly regulated output and an input LC filter. Under nominal operating conditions, each buck converter designed to step-down a 48V DC input to 24V DC nominal output for a 10Ω load resistor (60W rated). Voltage mode control is achieved using a 3-pole 3-zero (3P3Z) compensator implemented digitally on a TMS320F28379D microcontroller with a controller bandwidth designed to be approximately 5kHz. The switching frequency of the PWM is set to a fixed 100kHz.

The variable voltage laboratory power supply is an Aim-TTi CPX400DP. Measurements are made using a Tektronix DPO2014B (100MHz) oscilloscope; TCP0030A current probes; and TPP0200 passive probes.

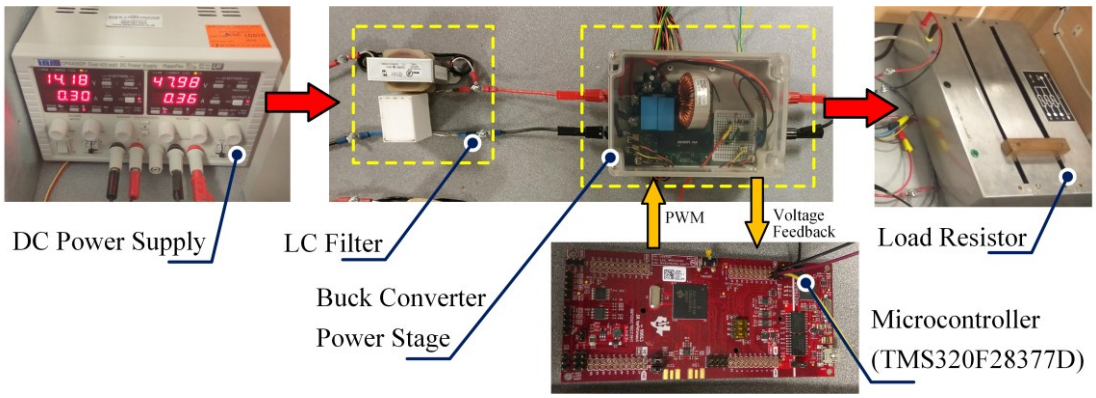

FIGURE 4.2 Test-bench of the experimental cascaded power system.

4.2.2.1 Input filter

Filters are typically required with SMPS to ensure that EMI standards or system requirements are met [77]. By their switching nature, power electronics converters generate interference through conducted emissions at both the input (line-side) and output (load-side) terminals. For example, in a typical buck-type converter, the DC input current is discontinuous over every switching cycle. This current induces a voltage ripple across

the input capacitor which can be a significant noise source that can interfere with the operation of devices connected at the same line—the source converter(s) or adjacent converter(s). Input filters must therefore be carefully designed for the given application to limit this conducted emission and comply with relevant standards.

The fundamental frequency of the conducted noise is at the switching frequency of the SMPS. While higher-order harmonics will appear, the EMI at the fundamental typically requires attenuation with additional input filtering to meet requirements. The LC filter in Figure 4.6 is a single stage differential-mode filter with attenuation slope of -40 dB/decade (i.e., one inductor and one capacitor). While the low component count often makes this filter cost effective, the gradual roll-off can yield a very low filter cut-off frequency to meet the required attenuation. As a result, the EMI input filter cut-off frequency is most commonly well below both the control-loop bandwidth defined as the voltage-loop crossover frequency of the converter, given in Figure 4.4.

For the experimental work, the low-pass input filter for converters is selected to have a -3dB cut-off frequency of approximately 850Hz based on availability of off-the-shelf inductors and capacitors. This corresponds to an 83.96dB filter attenuation at the fundamental 100kHz switching frequency. For the propose of investigations on input filter instability, the Q-factor is deliberately very high (i.e., very poorly damped) than is typical for any practical application.

The LC filter lumped parameter model used for analysis is shown as a subsystem in Figure 4.6. Table 4.1 provides component parameter values, with measurement procedures used for extracting precise values given in Appendix B. The filter inductor selected is a 1,000μH Hammond 157D 10A rated, 38mΩ, open-bracket DC filter choke. The filter capacitor is a 40μF KEMET C4AQLBW5400A3FK film capacitor with an additional 10μF TDK B32794D2106K film capacitor in parallel located at the input terminals of the buck converter.

4.2.2.2 Step-down buck converter power stage

This section discusses the hardware setup and model description of the synchronous buck converter feeding a resistor. Regulation is performed using a digital 3-pole-3-zero (3P3Z) compensator for voltage-mode control described in the next Section 4.2.2.3. Together, the buck converter, controller, and resistive load form a single active load.

A TDHBG2500P100 half-bridge evaluation board from Transphorm is configured as a synchronous buck converter power stage. The board is used as a building-block; Figure 4.3 giving the overview of the major components and the inputs and outputs.

Silicon Labs Si8230BB gate driver ICs are used to drive TPH3212PS 650V GaN MOSFETs. Deadtime is set to 120ns by external resistors to prevent shoot-through currents during synchronous switching of the high-side and low-side devices. The MOSFETS are in a TO220 package with 72mΩ drain-to-source on resistance $R_{DS(on)}$. It is important to note that modelling does not consider MOSFET transient dynamics during switching therefore switching losses are omitted in the analysis.

The buck converter output LC filter is comprised of a 460µH inductor with 25mΩ DCR based on a custom wound toroid with MPP core from Mag Inc C055439A2. The capacitance is from a parallel combination of a single 10µF TDK B32794D2106K film capacitor and two generic electrolytic capacitors to total approximately 110µF.

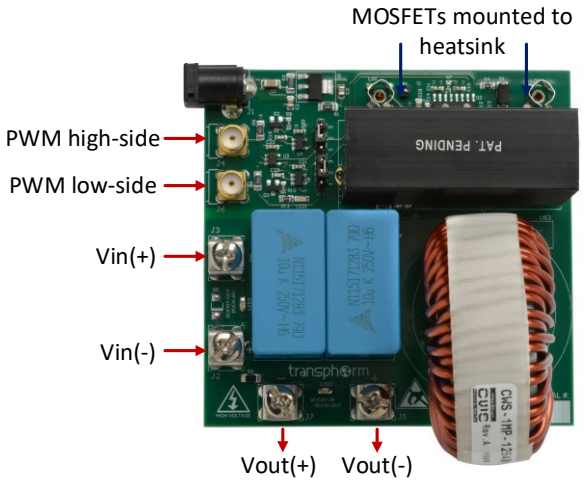

FIGURE 4.3 Synchronous buck converter power stage used for active loads.

The state-space model of this step-down buck converter was previously introduced in Chapter 3, Section 3.3.2. Assuming a fixed resistive load, the model can be simplified into having two-inputs, duty cycle $D(s)$ and input voltage $V_{in}(s)$, and two-outputs, output voltage $V_{out}(s)$ and input current $I_{in}(s)$. The control-to-output transfer function, the duty cycle-to-output voltage $G_{vd}(s)$, is used to design the compensation network for closed-loop control in the next section. Component parameters of the buck converter are measured offline using an LCR meter and values substituted into the lumped parameter model to obtain the transfer function. Figure 4.4 shows the control-to-output discrete-

time transfer function with sample time of 100kHz to match the switching frequency. Online frequency response characterisation using a vector network analyser to validate the model was not possible in this study, but is recommended for further validation.

4.2.2.3 Voltage feedback compensation

Shaping the closed-loop dynamics of the buck converter described above is achieved through a 3P3Z compensator which is the digital (discrete) implementation of a type-III compensator, previously introduced in Section 3.3.3. The plant model, control-to-output transfer function, is shown in Figure 4.4 and is generated using parameters from Table 4.1. The target specification for the designed compensator is to have a stable loop-transfer function with a >30-degree phase margin at approximately 5kHz. To reduce the frequency at which negative input impedance is exhibited by the active load, a 1kHz and 100Hz controller is also designed.

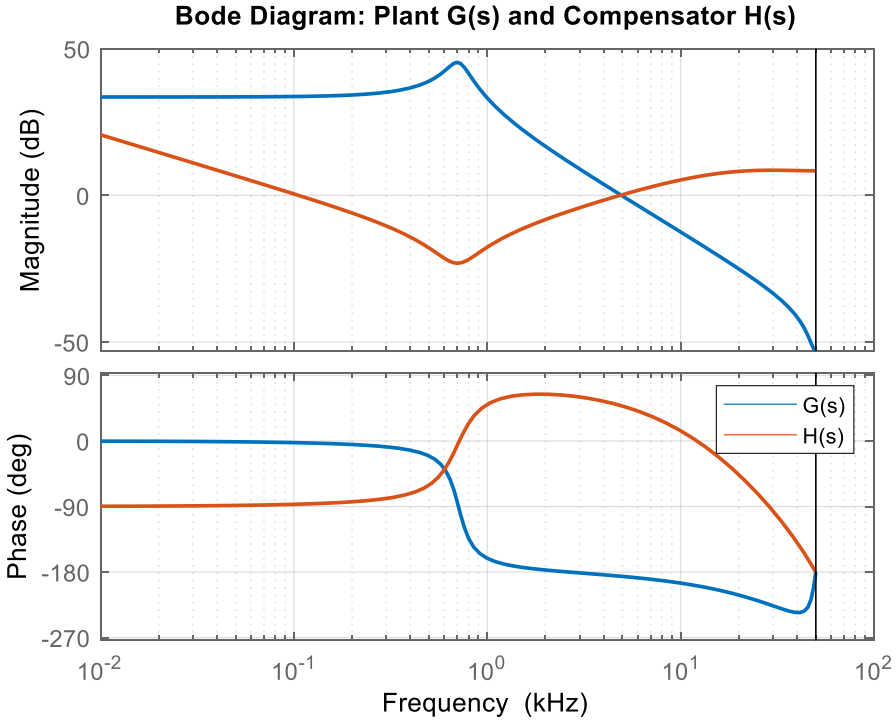

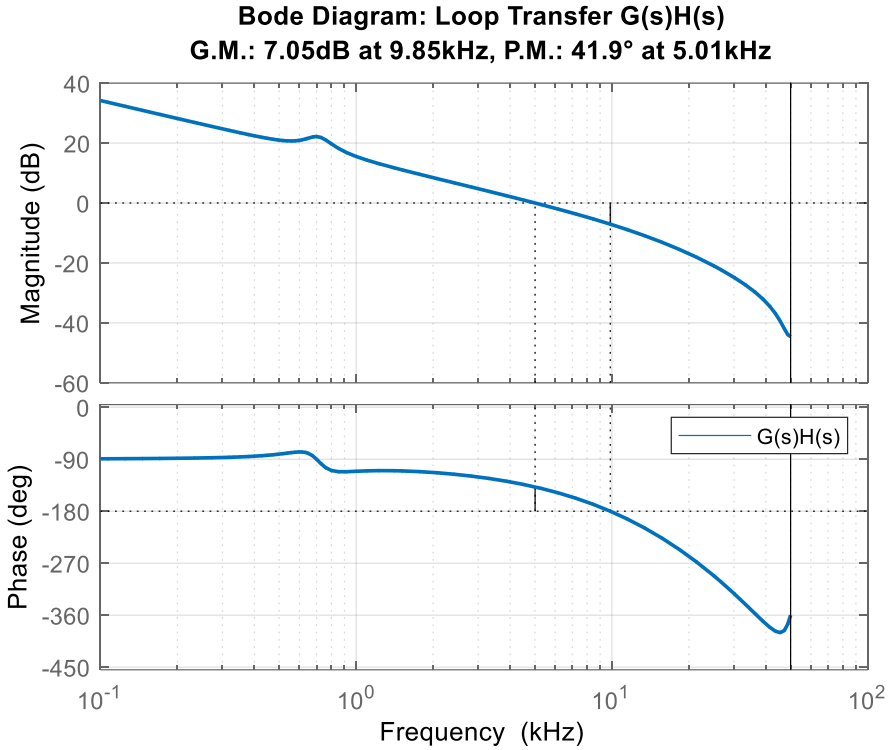

FIGURE 4.4 Bode plots of buck converter plant model (duty cycle-to-output voltage), 5kHz compensator, and open-loop transfer function showing gain and phase margins.

Referring to Figure 4.6, the feedback path contains a resistor divider to scale the output voltage to a range suitable to be sampled by the ADC. This sampled signal is then compared with a reference voltage that is user programmable. The difference between the output voltage and reference voltage (scaled and sampled) is the error voltage used for the feedback compensator and then the pulse-width modulator.

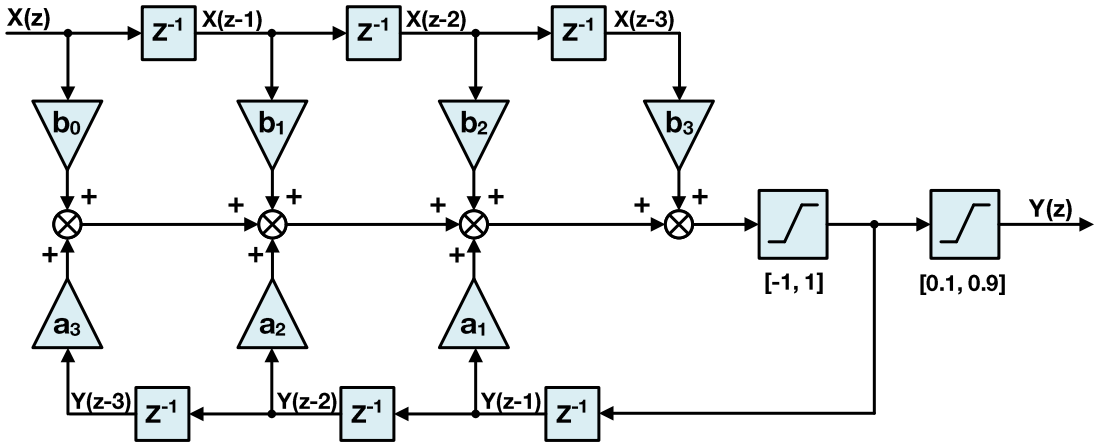

FIGURE 4.5 3P3Z control implementation as a 3rd-order digital IIR filter with Direct Form Type-I realization

The z-domain transfer function for the 3P3Z control law is given below in (4.1):

$$G_V(z) = \frac{D(z)}{V_{err}(z)} = \frac{b_{z3}z^{-3} + b_{z2}z^{-2} + b_{z1}z^{-1} + b_{z0}}{1 - a_{z3}z^{-3} - a_{z2}z^{-2} - a_{z1}z^{-1}} \tag{4.1}$$

Figure 4.5 shows the 3P3Z controller implemented in MATLAB Simulink used for code generation. The block implements a third order control law using an IIR filter structure with programmable output saturation. This type of controller requires three delay lines: one for input data and one for output data, each consisting of three elements.

The recursive nature of the IIR filter make it prone to overflows. To prevent this, the implementation has a negative lower bound saturation to allows for a negative state history in the feedback to prevent oscillations as a result of overflow. The final saturation block limits the output duty cycle to 10% to 90%.

To ensure that overruns do not occur due to limited performance of the floating-point unit of the microcontroller, the Q18-format fixed point data type was used for variables.

4.2.3 Experimental setup and test regime

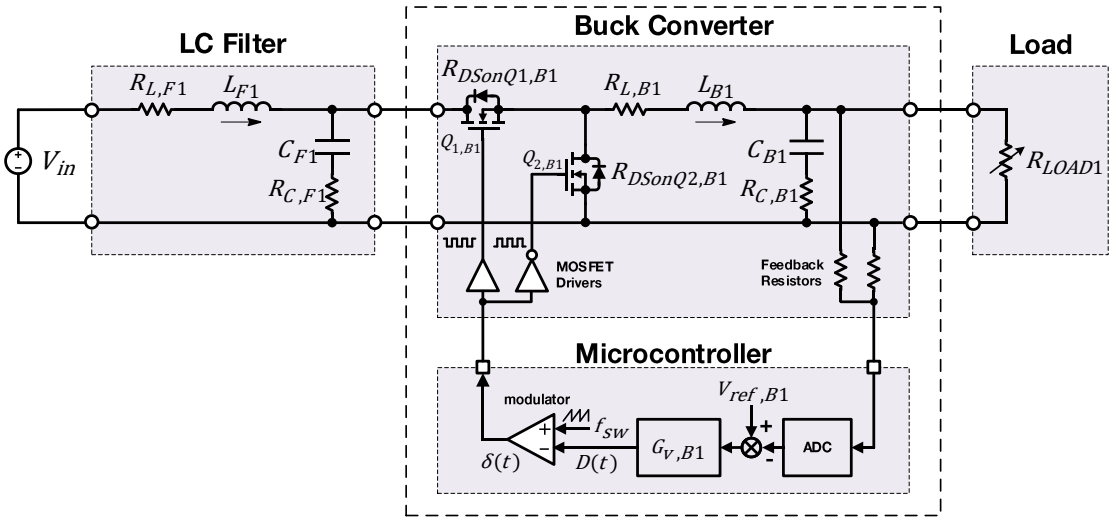

FIGURE 4.6 Circuit diagram of the experimental LVDC power system featuring an input LC filter and voltage-mode controlled buck converter.

The small-signal dynamics are studied similarly to that in Section 3.5. Figure 4.6 shows the schematic of the experimental system, and Table 4.1 provides the parameters of the experimental system: both nominal values and precise measured values (see Appendix B for details on component parameters measurement and refinement). The experiment is further supported with simulations using MATLAB/Simulink. Ideally, the experimental and simulations results should agree and validate theoretical predictions of dynamic behaviours (i.e., the point at which onset of instability occurs).

The active load acts as a CPL to induce instability in the input filter. Instability is evident by the sustained limit cycle oscillations in the filter's capacitor voltage and inductor current. The active load's input power is controlled by regulating the output voltage to the load resistor $P = V^2/R$. The selective low damping of the input filter enables instability to be observed at very low power levels. This ensures that experiments can be repeated without hardware failure or overstress requiring component replacement.

TABLE 4.1 Parameters of the experimental system.

Parameter	Symbol	Unit	Value		
			Nominal	Measured	Simulation
Input voltage	V_{in}	V	48	48.0	48
Reference voltage	V_{ref}	V	24	-	24
Filter inductance	L_{F1}	µH	1000	879.5	900
Filter capacitance	C_{F1}	µF	50	49.7	50
Filter DCR of L_{F1}	$R_{L,F1}$	mΩ	38	656.8	500
Filter ESR of C_{F1}	$R_{C,F1}$	mΩ	3.6	106.0	100
Buck inductance	L_{B1}	µH	460	456.1	460
Buck capacitance	C_{B1}	µF	110	121.1	110
Buck DCR of L_{F1}	$R_{L,B1}$	mΩ	25	330.0	25
Buck ESR of C_{F1}	$R_{C,B1}$	mΩ	4.2	120.5	4.2
Q1 Drain-source on resistance	$R_{DSonQ1,B1}$	mΩ	72	85	100
Q2 Drain-source on resistance	$R_{DSonQ1,B1}$	mΩ	72	85	100
Load resistance	R_{LOAD1}	Ω	10	10.0	10

The experimental system's controller parameters for the 3P3Z control law (see (4.1)), are given in Table 4.2:

TABLE 4.2 Values of the 3P3Z controller variables at different bandwidths.

Parameter	Controller bandwidth (f_{sw} = 100kHz)		
	100-Hz	1-kHz	5-kHz
b_{z0}	0	0	0
b_{z1}	0.0395	0.3499	2.022
b_{z2}	-0.07814	- 0.6922	-4
b_{z3}	0.03872	0.343	1.982
a_{z1}	1.476	1.476	1.476
a_{z2}	-0.5266	-0.5266	-0.5266
a_{z3}	0.05021	0.05021	0.05021

Small-signal stability analysis is performed using the continuous time domain state-space models. While the compensator is designed in the discrete domain, we approximate its implementation in the continuous domain by using the Tustin (bilinear) approximation. Equations (4.2) and (4.3) give the continuous time domain form as a transfer function and state-space, respectively, for use in small-signal predictions.

$$G_V(s) = \frac{D(s)}{V_{err}(s)} = \frac{b_{s3}s^3 + b_{s2}s^2 + b_{s1}s + b_{s0}}{a_{s3}s^3 + a_{s2}s^2 + a_{s1}s} \tag{4.2}$$

$$\begin{aligned} \frac{dX(t)}{dt} &= A_C X(t) + B_C V_{err}(t) \\ D(t) &= C_C X(t) + D_C V_{err}(t) \end{aligned} \tag{4.3}$$

TABLE 4.3 Controller parameters in continuous-time domain form used for small-signal stability analysis.

	Controller bandwidth (continuous-time model approximation)		
Parameter	100-Hz	1-kHz	5-kHz
b_{s3}	-0.05121	-0.4536	-2.621
b_{s2}	1.014e04	8.982e04	5.19e05
b_{s1}	1.945e07	1.723e08	9.953e08
b_{s0}	1.989e11	1.762e12	1.018e13
a_{s3}	1	1	1
a_{s2}	2.489e05	2.489e05	2.489e05
a_{s1}	1.503e10	1.503e10	1.503e10
A_C	$\begin{bmatrix} 0 & 1 & 0 \\ 0 & -1.03e5 & -2.59e6 \\ 0 & 0 & -1.46e5 \end{bmatrix}$	$\begin{bmatrix} 0 & 1 & 0 \\ 0 & -1.03e5 & -2.59e6 \\ 0 & 0 & -1.46e5 \end{bmatrix}$	$\begin{bmatrix} 0 & 1 & 0 \\ 0 & -1.03e5 & -2.59e6 \\ 0 & 0 & -1.46e5 \end{bmatrix}$
B_C	$[0 \quad 1102 \quad 147]^T$	$[0 \quad 2203 \quad 293.9]^T$	$[0 \quad 8813 \quad 1176]^T$
C_C	$[-902.7 \quad 4.706 \quad 120.4]$	$[-3998 \quad 20.85 \quad 533.4]$	$[-5775 \quad 30.11 \quad 770.5]$
D_C	$[-0.05121]$	$[-0.4536]$	$[-2.621]$

The bode plot in Figure 4.7 shows the input impedance $Z_{in}(s)$ of the active load model based on the experimental closed-loop converter with a 5kHz control-loop bandwidth.

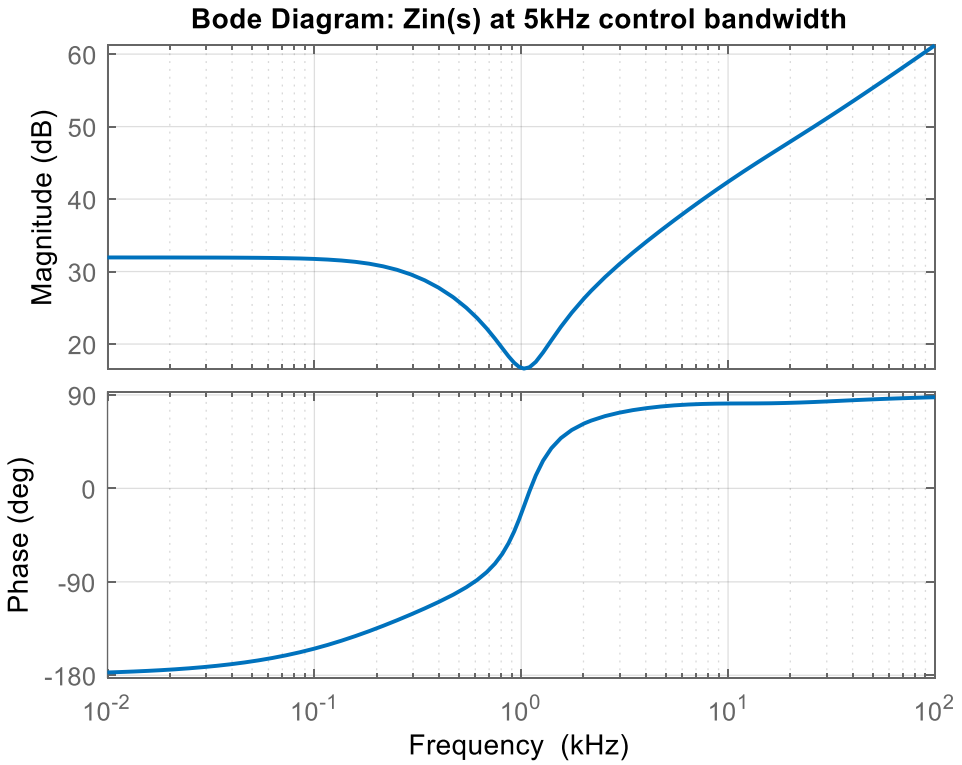

FIGURE 4.7 Input impedance $Z_{in}(s)$ of the model of the experimental closed-loop converter with 5kHz control loop bandwidth.

The experimental investigation on small-signal stability is carried by first putting the system into nominal steady-state operation. The input voltage is fixed and output voltage is regulated to the nominal reference value (24V). To push the system towards instability, a series of 1V step changes to the voltage command is done via the communication between the PC and microcontroller.

4.2.4 Stability analysis and experimental results

In this section, the experimental results from the experimental test rig are compared with stability analysis using the small-signal dynamic model. This is required to validate the modelling methodology from the previous chapter, which is then extended in the following chapters.

Three distinct small-signal models of system in Figure 4.6 are generated using parameters from Table 4.1 and from the three different controllers in Table 4.2 (differing bandwidths of 5KHz, 1KHz, and 100Hz). Using the small-signal model, eigenvalues are calculated for the case when the load demand varies by controlling the output voltage reference (V_{ref}) in the controllers. V_{ref} is varied from 24V to 33V in 1V steps (corresponding to 57.6W to 72.6W power demand).

Figure 4.8 shows the locus of the critical (right-most) eigenvalue under varying power of the system with 5kHz controller. Using the analytical model, the practical system is predicted to become unstable at $V_{ref} = 29V$. The Bode plot in Figure 4.15 uses the analytical model to generate load $Z_{in}(s)$ and filter $Z_{out}(s)$ at $V_{ref} = 28V$ to show that the Middlebrook stability criterion ($|Z_{in}(s)| > |Z_{out}(s)|$) is satisfied, thus stability should be guaranteed.

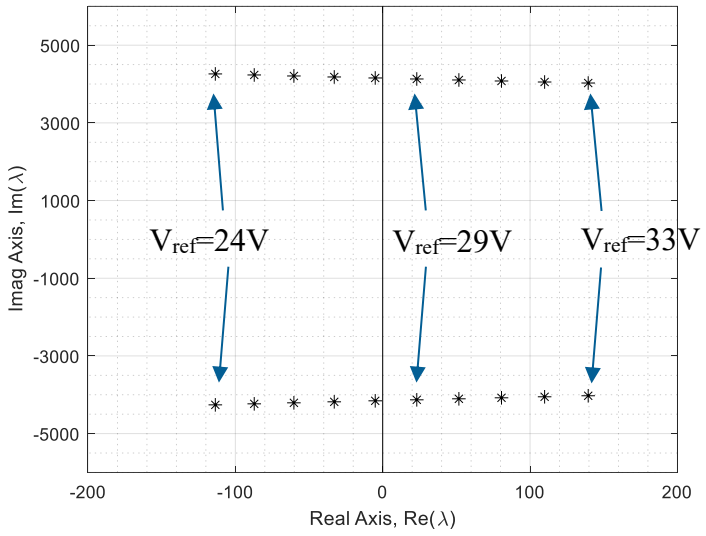

FIGURE 4.8 The critical eigenvalue plot from the system model with 5kHz bandwidth, stepwise variation of V_{ref} from 24V to 33V in 1V increments.

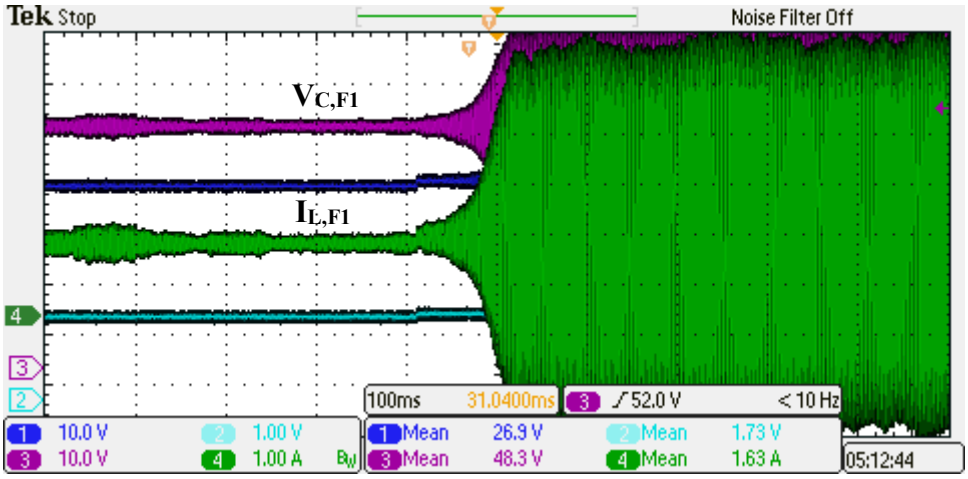

FIGURE 4.9 Measured waveforms from experimental system with a 5kHz bandwidth showing an onset of instability following a small step change in V_{ref}.

A similar procedure was used to experimentally determine point of instability of the experimental system. Stepwise changes to the load demand through the V_{ref} are performed while measuring the input filter's voltage and current as well as the output voltage. Figure 4.9 shows the experimental system waveforms under a 5kHz bandwidth.

In Figure 4.9, voltage and current oscillations begin to occur in the input filters at $V_{ref} = 27V$, indicating an unstable operation. The peak-to-peak voltage and currents do not grow unbounded (which is the case with the small-signal dynamic model) and are limited due to the practical nature of the system. Measured oscillations correspond closely to the filter resonant frequency, shown in Figure 4.14.

From Figure 4.8 and Figure 4.9, it can be seen that a reasonable agreement between the analytical model prediction and the experimental results is achieved. However, a source of concern is the lower measured instability V_{ref} point, corresponds to a smaller system stability margin, of the practical system compared to the theoretical model. The error corresponds to a less than 0.5W power difference between the results, and is likely attributable to imprecise parameter measurements and noise in the filter current and voltage (shown at $t = 0$ in Figure 4.9).

The same experiment is performed for the systems with the 1kHz and 100Hz bandwidth. Analytical and practical measurement results are shown in Figure 4.10 and Figure

4.11 for the 1kHz controller, respectively. Likewise, Figure 4.12 and Figure 4.13 are for the 100Hz system.

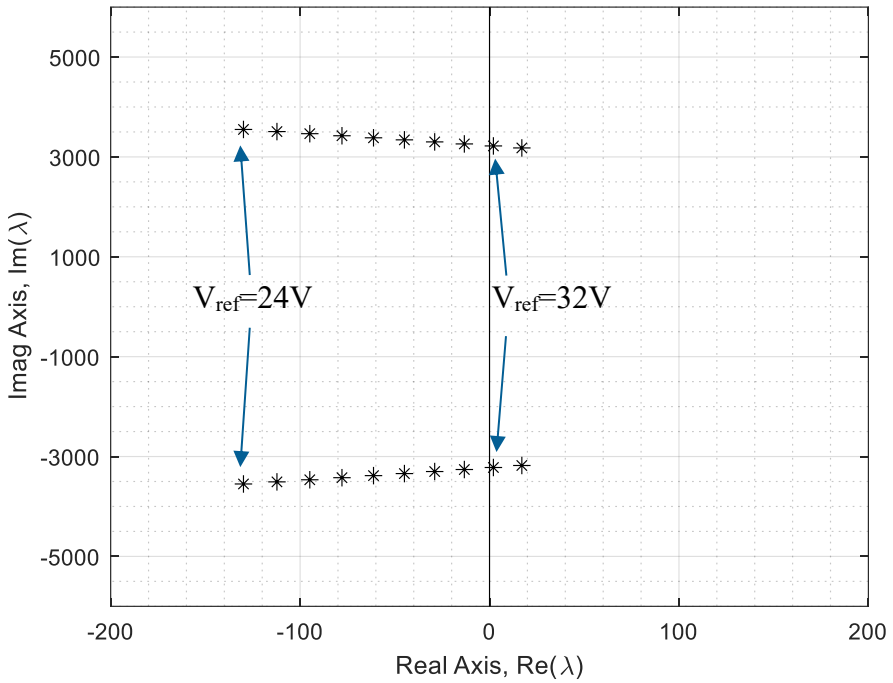

FIGURE 4.10 The critical eigenvalue plot from the system model with 1kHz bandwidth, stepwise variation of V_{ref} from 24V to 33V in 1V increments.

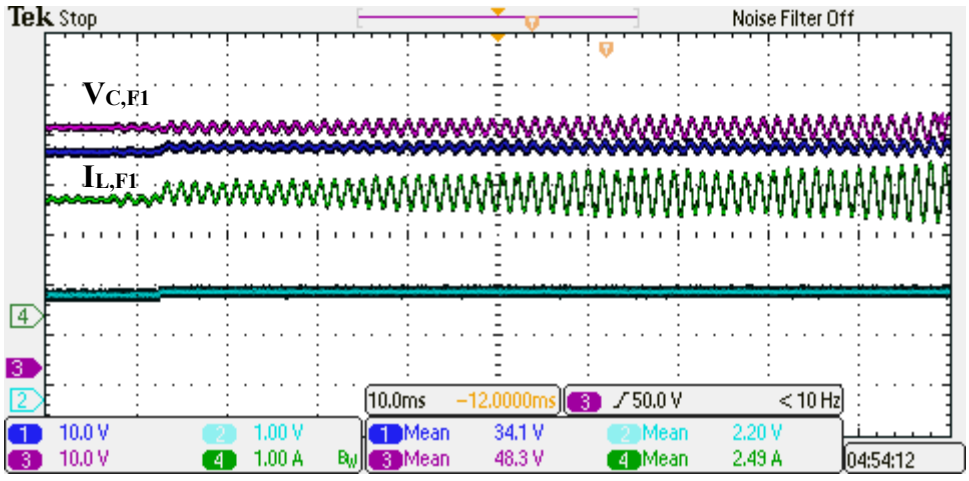

FIGURE 4.11 Measured waveforms from experimental system with a 1KHz bandwidth showing an onset of instability following a small step change in V_{ref}.

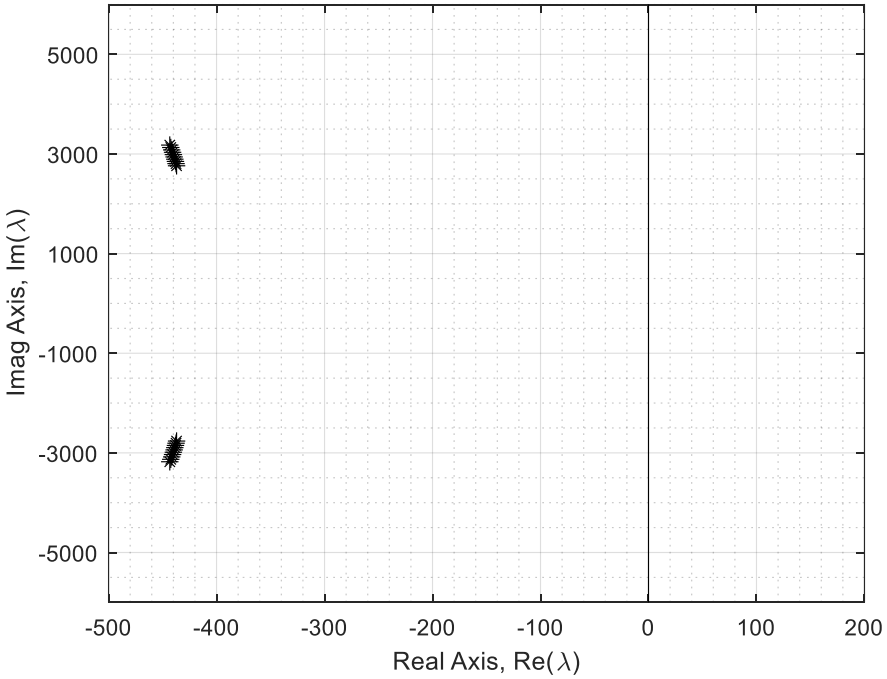

FIGURE 4.12 The critical eigenvalue plot from the system model with 100Hz bandwidth, stepwise variation of V_{ref} from 24V to 33V in 1V increments.

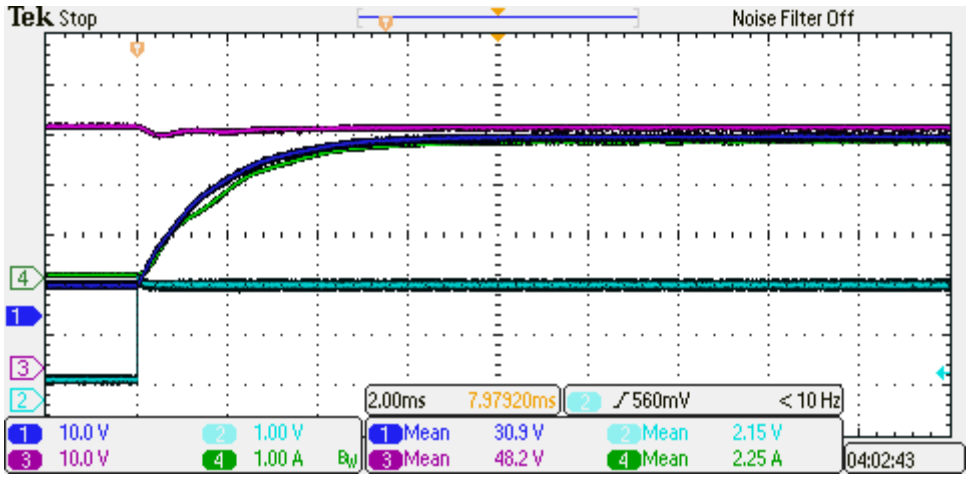

FIGURE 4.13 Measured waveforms of experimental system with a 100Hz bandwidth showing no overshoot following a large step change in V_{ref} (0 to 31V).

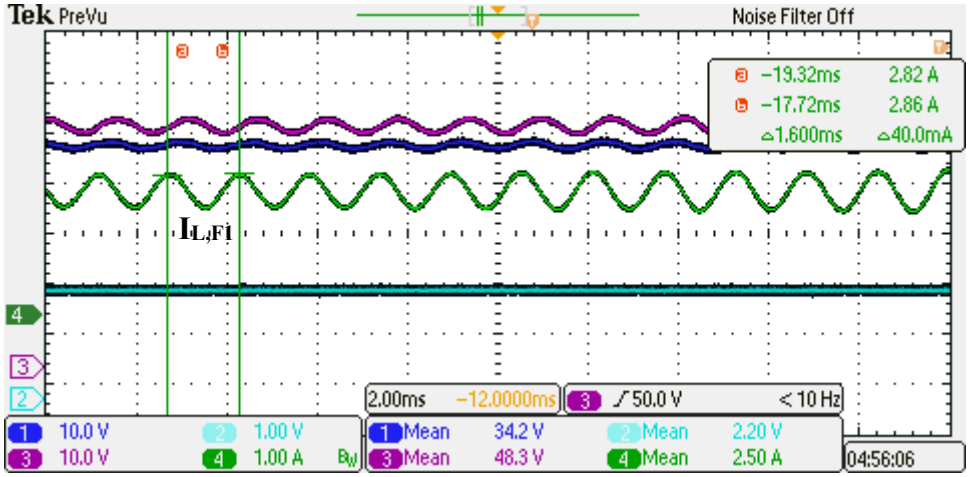

FIGURE 4.14 Experimental waveforms of the input filter voltage and current, showing an oscillation period of 1.56ms (641Hz).

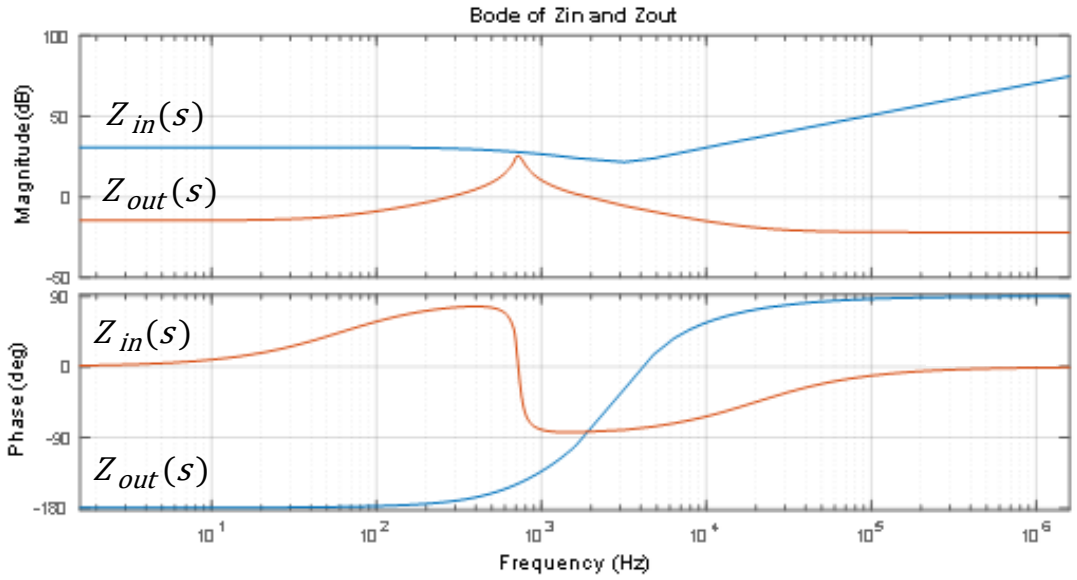

FIGURE 4.15 Bode plot of the input and output impedances of the experimental system under nominal operating conditions showing near instability

4.3 Summary

In this chapter, a detailed description of the hardware setup and experimental procedures are presented. Results from the developed test systems with practical CPLs—the hardware prototype—validate the analytical modelling of power systems for use in small-signal stability and sensitivity analysis. These are subsequently used to support the theoretical results in the remaining chapters.

The test-bench uses a hardware prototype of a switching POL regulator consisting of an output voltage-controlled synchronous buck converter feeding a resistive load. A digital 3P3Z compensator was implemented on a TMS320C28x series microcontroller. The POL regulator was demonstrated to exhibit CPL dynamics within its control loop bandwidth defined as frequencies below that of the open-loop crossover frequency (approximately). Frequency response measurements of passive components and experimental data was used to refine the model parameters. Results and waveforms meet design specifications and shown to match closely with the analytical models developed in Chapter 3.

Source-load interaction is experimentally shown to induce instability of cascaded power system following the addition of an input LC filter to the POL regulator. Practical results validate the developed power system models based on the approach in Chapter 3 to accurately describe system dynamics and predict the point-of-instability. Furthermore, reducing the detailed load models to ideal CPL characteristics is shown to be sufficiently accurate for small-signal studies as long as the source-side resonant characterises are well below the load's closed loop bandwidth.

This experimental system is extended later in Chapter 6. to include a second filter-converter system operating in parallel to investigate resonant modal coupling phenomena.

Chapter 5

Influence of Parameter Uncertainties and their Interactions on Small-Signal Dynamics based on VBSA

ABSTRACT Classical stability analysis techniques based on nominal models do not consider uncertainties in system parameters which may drastically alter the small-signal dynamics of practical LVDC DPSs. In this chapter, the method of variance-based sensitivity analysis (VBSA) is proposed to identify the most influential parameters and their interactions impacting small-signal stability. Based in the probabilistic framework, the procedures for applying VBSA to detailed power system models are outlined. VBSA is applied to an example system with two parallel filter-converters fed by a resistive line. Results indicate that the effectiveness of source-side damping of filter modes is reduced when filters become coupled. This is further investigated with derivative-based sensitivity analysis to reveal that the source-side resistance can contribute to the positive damping or negative damping of filter modes, depending on exact operating conditions. These behaviours are verified using time-domain simulations and measurements from the experimental system presented in Chapter 4.

This chapter is an extension of the publication, '*Influence of Parametric Uncertainties and their Interactions on Small-Signal Stability: a case example of parallel-connected active responsibilities in a DC Microgrid*' [21].

5.1 Introduction

Classical stability analysis techniques based on nominal models do not consider the uncertainty of system parameters and their interactions. These interactions are known to drastically change the dynamics of practical highly-coupled LVDC DPSs. In contrast to classical methods, a probabilistic approach on the other hand considers all uncertainties via multiple simulation to predict the true system behaviour more accurately over system inputs, parameters, and operating points.

In this chapter, we propose a novel application of VBSA to LVDC DPS models to investigate the influence of uncertain parameters and their interactions on small-signal stability. A VBSA methodology is implemented—in combination with the symbolic modelling of Chapter 3—enabling a computationally efficient and practical approach to address a number of unknowns regarding model behaviour over uncertainty: mapping and ranking parameters on the considered system phenomena (eigenvalues) along with identifying any higher-order interactions effects between parameters. Verification of identified modal interaction phenomena in an example LVDC DPS is performed using Simulink models and experimental system introduced in Chapter 4. Advantages over conventional sensitivity analysis based on single nominal models is made clear.

This chapter is structured as follows: Section 5.2 introduces the theoretical basis of VBSA as a probabilistic framework for identifying and quantifying first-order and total-order effects of parameters, including parameter interactions, over all possible operating conditions. Section 5.3 develops a novel procedure for applying VBSA to practical models of LVDC DPSs to assist the understanding of parameter effects and their interactions on the small-signal stability. Section 5.4 presents a case study that investigates a LVDC DPSs with parallel-connected input filters feeding CPLs with uncertain distribution lines. Contrastive VBSA results indicated that the effectiveness of source-side resistive damping was reduced when resonant frequencies of load input filters are nominally matched. Interactions are present between parallel loads and source-side resistances, and these results are verified against conventional derivative-based sensitivity analysis. For the first time, the apparent dichotomy in the effect of source-side line resistance is revealed: line resistance can act as both a stabilizing and destabilizing element depending on operating conditions. Finally, Section 5.5 summarises this chapter and main contributions.

5.1.1 Background

In small-signal modelling of conventional electrical power systems, network dynamics are generally neglected since their time constants are much smaller than those of synchronous generators and their control loops. Here, the effects of individual loads are insignificant (due to their small capacity) and thus loads can be aggregated and collectively modelled; whereas in DPSs the individual loads play a critical role in system stability and have to be included in stability analysis [19], [94].

Classical techniques to identify dynamic interactions through the use of participation factors in power system [19], [94] are based on analysis of nominal models. The work reported in [19] provides important insights into the complexity of coupling phenomena between the sources, the loads and the network. While these techniques are prevailing, they are insufficient for describing how the interactions change under possible variations of parameters. For example, the recent work [26] identifies a coupled resonance phenomenon between multiple parallel load-side filters in a simple DC system with CPLs. The observed filter coupling effects depend strongly on parameter values. This observation highlights the necessity of modelling system uncertainties, such as the uncertainties in the length of lines between different nodes in practical systems. Similarly, [51] identifies mutual coupling phenomena between multiple parallel load-side filters that must be considered at the design stage of the proposed stabilizing controller. And paper [45] illustrates reduction in stability margins due to coupling effects from between transmission line impedances and the source and multiple loads, including impedance in-between loads in an AC system. Recent publication [60] quantifies effects of multiple simultaneous parametric uncertainties on the stability of a power electronics system by applying the structured singular value -based stability analysis method.

To identify and analyse dynamic interaction phenomena, [18], [19], [68], [101] propose tracing eigenvalues over parametric changes to observe movement of oscillatory modes. This work shows that modal resonance effects in power systems, such as subsynchronous resonance, can be caused by interaction between two distinct modes, i.e., between torsional modes and sub electrical modes, and can be viewed as precursor to system instability. For problems with numerous multiple uncertainties, exhaustive testing of all possible combinations quickly becomes computationally infeasible. As a result,

there is increasing interest in applying global sensitivity analysis (SA) techniques which aim to quantify the behaviour of an output over the entire range of uncertainties. Probabilistic methods can be used to examine the scenarios from the whole range and are easily implemented using Monte Carlo (MC) techniques. Global SA techniques are reviewed in [102] and some considered for importance ranking of uncertain parameters in power networks in [70]. Of interest are those that can help identify different interactions between system parameters, such as VBSA [73]–[75].

Equations (5.1)-(5.3) are used to represent the difference between the techniques of local SA and global SA. Representation of a nominal model evaluation at point *i*:

$$X^i \xrightarrow{Y=f(X)} Y^i \tag{5.1}$$

Representation of local sensitivity analysis at point *i*

$$\begin{bmatrix} X^i + \Delta X_1 \\ X^i + \Delta X_2 \\ \vdots \\ X^i + \Delta X_n \end{bmatrix} \xrightarrow{Y=f(X)} Y^i + \begin{bmatrix} \Delta Y^i/\Delta \mathrm{X}_1 \\ \Delta Y^i/\Delta \mathrm{X}_2 \\ \vdots \\ \Delta Y^i/\Delta \mathrm{X}_\mathrm{n} \end{bmatrix} \Delta X \tag{5.2}$$

Representation of global sensitivity analysis overs points *i,j,…M :*

$$\{X^i, X^j, \dots, X^M\} \xrightarrow{Y=f(X)} \{Y^i, Y^j, \dots, Y^M\} \xrightarrow{ANOVA} \begin{pmatrix} sens[Y|{X_1}^{i,j,\dots M}] \\ sens[Y|{X_2}^{i,j,\dots M}] \\ \vdots \\ sens[Y|{X_n}^{i,j,\dots M}] \end{pmatrix} \tag{5.3}$$

Each parameter X is changed several times in (5.3) and the output is recorded, and the same is done for X_2, X_3 and so on. From the recorded input-output data, an *analysis of variance* (*ANOVA*) is performed to determine the influence of each parameter on the output over the complete space. The next section introduces VBSA that uses *ANOVA* to quantify the nonlinear (higher-order) interactions between each of the uncertain parameters.

5.2 Variance-based Sensitivity Analysis (VBSA)

This section firstly describes the theoretical approach to VBSA based on the decomposition of an arbitrary multivariate function (such as dynamic models of power systems) into an equivalent strictly additive model of lower-order functions. This decomposition is then used as a basis for defining a set of sensitivity indices using *ANOVA* to quantify the effect input variations to model output(s). Two sensitivity indices, the *first-order effects* and *total-order effects*, can be estimated using Monte Carlo integration over model outputs evaluated over randomly-sampled inputs [73]. Any interaction effects between variables can be accounted for by the difference between the total and first-order effects; in contrast to a perfunctory one-at-a-time sensitivity analysis neglects these interactions.

The next section (5.3) will detail how VBSA can be applied to LVDC DPSs for the purposes of small-signal sensitivity analysis with multiple system uncertainties.

5.2.1 Analysis of Variance

VBSA, also known as Sobol's method (based on the work in [103]), is a probabilistic technique used to quantify the effect of varying input variables on the output variance of a function in terms of its main (first-order) effects and higher order effects over all possible scenarios. This allows for the relative ranking of the parameters over the whole uncertainty space, as well as providing a quantitative indication on which parameters have a nonlinear relationship to the output through their parameter interactions. Probabilistic sampling of the whole input space together with Monte-Carlo simulations provides a computationally inexpensive approach to probe the average behaviours of a model response under different combinations of input variables.

This technique is often applied to investigate the response of many complex dynamical models—such as those including mechanics [40], electromagnetics [41], acoustics [42]—where treating multiple variables one-at-a-time is not appropriate due to nonlinearity. Different techniques for sensitivity analysis were considered for an AC distribution system by the recent works in [70], [104] to identify and rank critical parameters. In [70] it was identified that variance-based techniques offer the best trade-

off between accuracy and computational practicality for large AC power system stability studies.

VBSA is based on the decomposition of an arbitrary multivariate function into an additive series of many lower-order functions. Firstly, let us consider a function $f(X)$ with output Y, shown in (5.4):

$$Y = f(X) \tag{5.4}$$

where X denotes a vector of n input variables, $X = [X_1, X_2, \dots, X_n]$.

The function $f(X)$ in (5.4) can be decomposed into a finite expansion of $2^n - 1$ additive components (or *terms*) of the following form in (5.5), known as the *high-dimensional model representation* (HDMR) [105]:

$$Y = f_0 + \sum_{s=1}^{n} \sum_{i_1 < \cdots < i_s} f_{i_1 \dots i_s}\left(X_{i_1 \dots i_s}, \dots, X_{i_s}\right) \tag{5.5}$$

and can be equivalently represented as (5.6):

$$\begin{aligned} Y = f_0 &+ \sum_{i=1}^{n} f_i(X_i) + \sum_{1 \le i < j \le n} f_{ij}\left(X_i, X_j\right) \\ &+ \sum_{1 \le i_1 < \cdots < i_l \le n} f_{i_1 i_2 \dots i_l}\left(X_{i_1}, X_{i_2}, \dots, X_{i_l}\right) + \cdots \\ &+ f_{12\dots n}(X_1, X_2, \dots . X_n) \end{aligned} \tag{5.6}$$

where f_0 is a constant value; and all additive component functions (i.e., f_i, f_j, f_{ij}, $\dots, f_{12\dots n}$) contribute to the output Y through unique inputs variables symbolized by subscripts. The first order term $f_i(X_i)$ shows the contribution by the independent variation of the i-th variable X_i; the second-order term $f_{ij}\left(X_i, X_j\right)$ contributes to the output as a result of an interaction between inputs X_i and X_j, where this contribution cannot be modelled by the additive result of the individual variations of X_i and X_j alone. Multi-component contributions of this kind are similarly decomposed for all higher-order terms.

To simplify the following discussion, let us assume that the input X is defined over the n-dimensional unit hypercube $X \in [0,1]^n$, i.e., for all $X_i \in [0,1]$. In practice, all uncertainties can be normalised to this condition.

The HDMR decomposition in (5.5) was proven to be unique in [106] if every additive component has zero mean, therefore each component can be considered to be orthogonal to all others as given by (5.7) and (5.8):

$$\int_0^1 f_u(X_u) dX_u = 0, \qquad \forall u \in \{i_i \dots i_s\}, 1 \le i < s \le n \tag{5.7}$$

$$\langle f_u(X_u), f_v(X_v) \rangle = \int_0^1 f_u(X_u) f_v(X_v) dX_u = 0, \quad \forall u \neq v \in \{i_i \dots i_s\}, 1 \le i < s \le n \tag{5.8}$$

As a consequence of (5.7) and (5.8), the component terms in (5.5) and (5.6) can be derived using the conditional expectation operator applied to the original function $f(X)$ and given input variable(s) in (5.9) [74].

$$\begin{aligned} f_0 &= E[Y] \\ f_i(X_i) &= E[Y|X_i] - f_0 \\ f_j(X_j) &= E[Y|X_j] - f_0 \\ f_{ij}(X_i, X_j) &= E[f(X_i, X_j)] - f_i(X_i) - f_j(X_j) - f_0 \end{aligned} \tag{5.9}$$

and so on for all higher order components.

The expected value (i.e. mean) of the output Y is the integration over all variables in X [74], requiring a total of n integrations as demonstrated in (5.10):

$$\begin{aligned} E[Y] &= \int_0^1 \dots \int_0^1 f(X) dX \\ dX &= \prod_{s=1}^{n} dX_s = dX_1 dX_2 \dots dX_n \end{aligned} \tag{5.10}$$

And the conditional expectations of the output Y given random inputs are in (5.11) [74]:

$$E[Y|X_i] = \int_0^1 \dots \int_0^1 f(X) \prod_{s \neq i}^{n} dX_s$$
$$E[Y|X_j] = \int_0^1 \dots \int_0^1 f(X) \prod_{s \neq j}^{n} dX_s \tag{5.11}$$
$$E[Y|X_i, X_j] = \int_0^1 \dots \int_0^1 f(X) \prod_{s \neq i,j}^{n} dX_s$$

and so on for higher-order conditional expectation terms.

From the equations in (5.4)-(5.11), it can be reasoned that a useful measure of sensitivity can be made by comparing the variation between the expected value of different additive components. For example, if the variation of $E[Y|X_i]$ over all X_i is greater than the variation of $E[Y|X_j]$ over all X_j, it can be concluded that the first-order effects of X_i are more sensitive than the first-order effects of X_j (the output varies greater over changes in X_i compared to X_j). This type of reasoning can be formalised explicitly through *ANOVA*.

The orthogonality property in (5.7)-(5.8) allows for the HDMR in (5.5) to be given in terms of variance, so that the variances of sub-functions add up to the total variance of the function $f(X)$ [74].

$$Var[Y] = \sum_{s=1}^{n} \sum_{i_1 < \dots < i_s} Var\left[f_{i_1 \dots i_s}(X_{i_1 \dots i_s}, \dots, X_{i_s})\right] \tag{5.12}$$

and equivalently expanding equation (5.6):

$$\begin{aligned} Var[Y] = &\sum_i Var[f_i(X_i)] + \sum_{i<j} Var\left[f_{ij}(X_i, X_j)\right] \\ &+ \sum_{1 \le i_1 < \dots < i_l \le n} Var\left[f_{i_1 i_2 \dots i_l}(X_{i_1}, X_{i_2}, \dots, X_{i_l})\right] + \cdots \\ &+ Var[f_{12\dots n}(X_1, X_2, \dots . X_n)] \end{aligned} \tag{5.13}$$

Noting that $Var[f_0] = 0$ as f_0 is a constant offset term.

The total variance of $f(X)$ is defined below in (5.10) [75]:

$$Var[Y] = E[(Y - E[Y])^2] = \int_0^1 \dots \int_0^1 (f(X)dX - f_0)^2 \tag{5.14}$$

And the variances of the first-order components are defined using equations from (5.11) [75] :

$$\begin{aligned} Var[f_i(X_i)] &= Var\big[\, E[Y|X_i]\big] = \int_0^1 \dots \int_0^1 f_i^2(X) \prod_{s \neq i}^{k} dX_s \\ Var\big[f_j(X_j)\big] &= Var\Big[\, E\big[Y|X_j\big]\Big] = \int_0^1 \dots \int_0^1 f_j^2(X) \prod_{s \neq j}^{k} dX_s \end{aligned} \tag{5.15}$$

Where the substitutions from (5.9) have been used.

Given that component $f_{ij}(X_i, X_j)$ is orthogonal to both $f_i(X_i)$ and $f_j(X_j)$, variances may be expanded as (5.16):

$$Var\big[f_{ij}(X_i, X_j)\big] = Var\Big[\, \mathrm{E}\big[\mathrm{Y}|\mathrm{X_j}, \mathrm{X_j}\big]\Big] - Var\big[\mathrm{E}[\mathrm{Y}|\mathrm{X_i}]\big] - Var\Big[\mathrm{E}\big[\mathrm{Y}|\mathrm{X_j}\big]\Big] \tag{5.16}$$

Similar expansions for all the variances for higher-order sub-functions are also performed.

5.2.2 Sensitivity Indices

Previously, in Section 5.2.1, we have shown through the analysis of variance of the HDMR, each term can be expanded into terms of variances of conditional expectations. In the seminal work by Sobol [106], they proposed variance-based sensitivity indices by normalising all terms in equation (5.12) by the total variance $Var[Y]$ resulting in the following equation (5.17):

$$1 = \sum_{i=1}^{n} S_i + \sum_{j>i} S_{ij} + \sum_{k>j>i} S_{ijk} + \dots + S_{12..n} \tag{5.17}$$

Where each S-term ($S_i, S_j, \dots S_{ij}, \dots$) is a unique senstivity index. For example:

$$S_i = \frac{Var\big[E[Y|X_i]\big]}{Var[Y]} \tag{5.18}$$

$$S_{ij} = \frac{Var\left[E\left[Y|X_i, X_j\right]\right]}{Var[Y]} \tag{5.19}$$

and so on for all higher order sensitivity indices.

S_i is a first-order sensitivity index for input X_i,; 2nd-order index S_{ij} describing interactions between input variables X_i and X_j; etc. These indices quantify the relative contribution of the corresponding parameters over their range to the output variance.

Just as the total order of the HDMR in (5.5), a total of $2^n - 1$ sensitivity indices is presented by equation (5.17). This poses a significant computational burden if all indices are to be calculated when a large number of input variables are present. Motivated by this, Homma et al. [107] introduced the *total-effect* sensitivity indices S_{Ti} which quantifies the relative contribution of input X_i including all the higher-order terms that feature the X_i variable on the output variance (e.g. $S_{Ti} = S_i + S_{ij} + S_{ik} + S_{ijk}$ for a 3 input system). They argue that, in practice, the indices S_i and S_{Ti} are most often sufficient for assessing the overall sensitivity of the model response to inputs.

To estimate all higher order terms of variable X_i, all other input variables can be considered together as vector X_{ci} (the ci subscript denotes the complement of variable i). Therefore, the following partition of the input vector can be as follows (5.20):

$$X = [X_i, X_{ci}] \tag{5.20}$$

This allows for the HDMR in (5.5) to be simplified as (5.21):

$$f(X) = f_0 + f_i(X_i) + f_{ci}(\mathrm{X_{ci}}) + f_{i,ci}(X_i, \mathrm{X_{ci}}) \tag{5.21}$$

Rearraging the above, so that all additive components containing the i-th terms are on the left hand side:

$$f_i(X_i) + f_{i,ci}(X_i, \mathrm{X_{ci}}) = f(X) - f_0 - f_{ci}(\mathrm{X_{ci}}) \tag{5.22}$$

The total effect X_i on output can be denoted by $f_{i,total}(X_i, \mathrm{X_{ci}}) = f_i(X_i) + f_{i,ci}(X_i, \mathrm{X_{ci}})$. Taking the variance of the terms in (5.22):

$$Var\left[f_{i,total}(X_i, \mathrm{X_{ci}})\right] = Var[f(X)] - Var\left[E[f(X_{ci})]\right] \tag{5.23}$$

Using (5.23), the total-effect sensitivity indices S_{Ti} can be calculated by dividing by the total variance:

$$\frac{Var\left[f_{i,total}(X_i, \mathrm{X_{ci}})\right]}{Var[f(X)]} = 1 - \frac{Var\left[E[f(X_{ci})]\right]}{Var[f(X)]} \tag{5.24}$$

Where (5.24) is equivalent to (5.25):

$$S_{Ti} = 1 - \frac{Var\left[E[Y|X_{ci}]\right]}{Var[Y]} \tag{5.25}$$

Here it becomes clear that the difference between total effect index (S_{Ti}) and first order index (S_i) accounts for all the interactions between X_i and all other aggregated variables.

Interpreting the different sensitivity indices:

- If S_i is 1, then output Y depends on only the parameter X_i.
- If $S_{Ti} - S_i$ is zero, then no interactions exist between X_i and other input variables.
- If S_{Ti} is zero, then by definition, S_i is also zero, and output Y is not dependent on X_i.
- The sum of the first order sensitivity indices (S_i, S_j, ...) should equal to one by definition (5.17).

5.2.3 Estimation of Sensitivity Indices through Probabilistic Sampling

The sensitivity indices are derived based on the high dimensional integrations, shown in (5.10), (5.11), (5.15), where analytical integration is simply not possible due to no knowledge of the explicit functions in the decomposition. Probabilistic sampling with Monte Carlo simulation, however, can be used to estimate the sensitivity indices [103].

Consider a set of different inputs mapped onto their outputs through the original function $f(X)$ in (5.26):

$$\begin{bmatrix} X_{1,1} & X_{1,2} & \cdots & X_{1,n} \\ X_{2,1} & X_{2,2} & \cdots & X_{2,n} \\ \vdots & \vdots & & \vdots \\ X_{m,1} & X_{m,2} & \cdots & X_{m,n} \end{bmatrix} \overset{f(X)}{\Longrightarrow} \begin{bmatrix} Y_1 \\ Y_2 \\ \vdots \\ Y_m \end{bmatrix} \tag{5.26}$$

Above, each row is considered as a single sample scenario for the function $f(X)$ where n is the number of variables in X. In other words, $f(X_{i,1}, \ldots X_{i,n}) = Y_i$ is a single scenario based on the random sampling of input X. Every column is randomly sampled from the probability distribution for the given input variable. The total number of samples taken is m for each scenario. The total number of Monte-Carlo simulations needed is therefore m.

Several quasi-random sets have been developed to sample more evenly over the multidimensional (*m,n*) input space, often referred to the as low discrepancy sequences. These include Latin hypercube sampling [108] and Sobol sequences [108] that are used to more effectively study the effect of parameter interactions in the function with a lesser number of m compared to conventional random sampling. Efficient multidimensional sampling becomes critical to the fast computation of sensitivity indices in complex power system models. To achieve this, hypercube sampling is recommended when applying VBSA to the small-signal analysis of LVDC DPSs (further details are provided in Section 5.3).

While computing the total variance is simple, estimating the variance of conditional expectations, as shown in equations (5.15) requires additional work. Conditional expectations can be rewritten as covariances [106] (discussed in detail on pg. 124) and a method for sensitivity indices estimation based on resampling input variables from two mutually independent Monte-Carlo sets was developed in [107]. Based on [107], the implementation used in this thesis is summarised in the following paragraphs.

Consider two mutually independent input spaces denoted by superscripts A and B in (5.27):

$$X^{A_i,A_{ci}} = [\mathrm{X}_i^A, \mathrm{X}_{ci}^A] \qquad X^{B_i,B_{ci}} = [\mathrm{X}_i^B, \mathrm{X}_{ci}^B] \tag{5.27}$$

where input vector $X^{A_i,A_{ci}}$ has the i-th variable sampled from A and ci-th vector sampled from set A

With (5.27) the outputs can be denoted as the following equations:

$$Y^{A_i,A_{ci}} = f(X^{A_i,A_{ci}}) \quad Y^{B_i,B_{ci}} = f(X^{B_i,B_{ci}}) \tag{5.28}$$

Such that the following sets from each input spaces, A and B, are sampled m-times to generate m-scenarios (5.29):

$$\begin{bmatrix} X_{1,1}^A & X_{1,2}^A & \cdots & X_{1,i}^A & \cdots & X_{1,n}^A \\ X_{2,1}^A & X_{2,2}^A & \cdots & X_{2,i}^A & \cdots & X_{2,n}^A \\ \vdots & \vdots & & \vdots & & \vdots \\ X_{m,1}^A & X_{m,2}^A & \cdots & X_{m,i}^A & \cdots & X_{m,n}^A \end{bmatrix} \overset{f(X)}{\Longrightarrow} \begin{bmatrix} Y_1^{A_i,A_{ci}} \\ Y_2^{A_i,A_{ci}} \\ \vdots \\ Y_m^{A_i,A_{ci}} \end{bmatrix}$$
$$\begin{bmatrix} X_{1,1}^B & X_{1,2}^B & \cdots & X_{1,i}^B & \cdots & X_{1,n}^B \\ X_{2,1}^B & X_{2,2}^B & \cdots & X_{2,i}^B & \cdots & X_{2,n}^B \\ \vdots & \vdots & & \vdots & & \vdots \\ X_{m,1}^B & X_{m,2}^B & \cdots & X_{m,i}^B & \cdots & X_{m,n}^B \end{bmatrix} \overset{f(X)}{\Longrightarrow} \begin{bmatrix} Y_1^{B_i,B_{ci}} \\ Y_2^{B_i,B_{ci}} \\ \vdots \\ Y_m^{B_i,B_{ci}} \end{bmatrix} \tag{5.29}$$

Samples may be taken from separate input spaces, for example the i-th variable is sampled from B while ci-th vector sampled from A as shown in (5.30):

$$X^{B_i,A_{ci}} = [\mathrm{X}_i^B, \mathrm{X}_{ci}^A] \tag{5.30}$$

$$Y^{B_i,A_{ci}} = f(X^{B_i,A_{ci}}) \tag{5.31}$$

For m-samples this becomes:

$$\begin{bmatrix} X_{1,1}^A & X_{1,2}^A & \cdots & X_{1,i}^B & \cdots & X_{1,n}^A \\ X_{2,1}^A & X_{2,2}^A & \cdots & X_{2,i}^B & \cdots & X_{2,n}^A \\ \vdots & \vdots & & \vdots & & \vdots \\ X_{m,1}^A & X_{m,2}^A & \cdots & X_{m,i}^B & \cdots & X_{m,n}^A \end{bmatrix} \overset{f(X)}{\Longrightarrow} \begin{bmatrix} Y_1^{B_i,A_{ci}} \\ Y_2^{B_i,A_{ci}} \\ \vdots \\ Y_m^{B_i,A_{ci}} \end{bmatrix} \tag{5.32}$$

Covariance, $Cov(\cdot)$, is a measure of the correlation between two sets of variances and can be used for the estimation of conditional variances, with the following property discussed in [109]. As samples X_{ci} are identical between the variable pairs, the covariance calculates the variance with respect to the independent X_i terms, in effect finding the variance when varying X_i:

$$Var\big(E(Y|X_i)\big) = Cov(Y^{A_i,A_{ci}}, Y^{B_i,A_{ci}}) \tag{5.33}$$

Therefore, sensitivity indices can be estimated by calculating the covariances between differently sampled input sets.

$$S_i = \frac{Cov(Y^{A_i,A_{ci}}, Y^{B_i,A_{ci}})}{Var(Y)} \tag{5.34}$$

A possible estimator implementation has been presented in [109], referred to as *a second estimator*, and is shown below in (5.35):

$$S_i = \frac{\frac{1}{m}\sum_1^m Y^{A_i,A_{ci}} Y^{B_i,A_{ci}} - \left(\frac{1}{m}\sum_1^m Y^{A_i,A_{ci}}\right)\left(\frac{1}{m}\sum_1^m Y^{B_i,A_{ci}}\right)}{\frac{1}{m}\sum_1^m (Y^{A_i,A_{ci}})^2 - \left(\frac{1}{m}\sum_1^m Y^{A_i,A_{ci}}\right)^2} \tag{5.35}$$

The estimator in (5.35) has been implemented for calculating the first-order and total-effect sensitivity indices throughout this thesis. This method requires a total $m(n+2)$ model evaluations.

5.3 Application of VBSA for Small-Signal Analysis of LVDC DPSs

This section presents our methodology for applying the method of VBSA to power system models to investigate the small-signal behaviour over all possible operating conditions under uncertainty. VBSA requires the formulation of a model or function in terms of deterministic input-output behaviour. Here we make a distinction between the system model which describes the nonlinear averaged behaviour of the power system states, and the stability model which is the eigenvalue (modal) decomposition of the linearised averaged model. The stability model can be viewed as a function which maps the (uncertain) input variables to the eigenvalues of the linearised system.

The methodology proposed consists of the following steps:

1. Treat variables ($\bar{P}$) as inputs to $F(\bar{X}, \bar{U}, \bar{P}) = 0$ where $\bar{U}$ is known and $\bar{X}$ is unknown.
2. For given inputs, numerically solve for X in $F(\bar{X}, \bar{U}, \bar{P}) = 0$;
3. Substitute values for $\bar{X}, \bar{U}, \bar{P}$ into the linear state-space model $\dot{X} = A(\bar{X}, \bar{U}, \bar{P})X + B(\bar{X}, \bar{U}, \bar{P})U$;
4. Calculate output eigenvalues by solving for λ in $Av = \lambda v$.

The stability of the system can be assessed from the real-part of the eigenvalues $Re(\lambda_i)$, or damping factor ζ_i, of the linearised small-signal model. Due to the parametric uncertainty, the steady-state operating point (x_0) and system eigenvalues are also uncertain. Eigenvalues must be numerically computed and are dependent on the uncertain input variables. This process can be considered as a model input–output mapping denoted by: $f : X \mapsto Y$, where X is the vector of uncertain input parameters and Y is the real-part of the eigenvalue(s). Random sampling from the probability distributions of the uncertain variables generates a unique scenario. For a given scenario m, the system equations are represented by the simplified form: $dx/dt = f_m(x)$. Operating point x_0 is determined when all state variables no longer vary with time, i.e., $f_m(x_0) = 0$, and is calculated using a numerical solver (*fsolve* in MATLAB). For each scenario, an LTI model in state space form is generated via Jacobian linearisation about x_0:

$$\frac{dx}{dt} = A_m x + B_m u \tag{5.36}$$

where,

$$A_m = \left.\frac{\partial f_m(x)}{\partial x}\right|_{x=x_0} \qquad B_m = \left.\frac{\partial f_m(x)}{\partial u}\right|_{x=x_0} \tag{5.37}$$

Matrix A is an $n \times n$ matrix which has a set of n distinct eigenvalues $(\lambda_1, \lambda_2, \dots, \lambda_n)$ representing the modal response of the system, and is used to find the stability margin by assessing the real part of the critical eigenvalues which corresponds to the oscillatory modes with the least damping ratio.

Under uncertainty, a difficulty lies when the right-most (critical) eigenvalues are related to different subsystems. Mode-tracking becomes a necessary step in each model evaluation, and is discussed in detail in Section 6.2.1. For mode-tracking, participation factor analysis is used to associate each eigenvalue to their most dominant state variables where the participation factors quantify the influence of a state variable (i) on a given eigenvalue (j) and are defined in equation (5.38).

$$p_{ij} = \frac{|w_{ij}||v_{ji}|}{\Sigma_{k=1}^{N}(|w_{ik}||v_{ki}|)} \tag{5.38}$$

This allows to reliably identify and group the eigenvalues from disparate model evaluation to the same subsystem.

5.4 Parallel-Connected Input Filters with CPLs fed by an Uncertain Distribution Line: A Case Study

5.4.1 Aim

Traditional approaches focused on the study of nominal models ignore parameter interactions and nonlinearity, two critical characteristics of highly uncertain LVDC DPSs. The aim of this case study is to demonstrate the application of VBSA for small-signal analysis outlined in Section 5.3 to a parallel-connected input filters with CPLs. The methodology is used to identify which parameters, over their uncertainties, exhibit nonlinear effects through their interactions on the small-signal stability. After identification of interacting parameters—the line resistance and input filter resonant frequencies—local derivative-based sensitivity analysis using two-factor-at-a-time variation is used to demonstrate that a drastically different effect of the sensitivity of line resistance on small-signal dynamics depending on operating condition.

5.4.2 System overview

Figure 5.1 shows the configuration of a distribution system with two active loads sharing a common voltage bus. The source is modelled as an ideal voltage source with a finite line resistance (R_{line}). Each active load is modelled as a tightly-regulated synchronous buck converter with an LC low-pass input filter, as shown in Figure 5.2. The buck converter's control loop is implemented as a type-III voltage compensator represented in state-space form (see Section 3.3.3). The state vector $x_{Ci}(t)$, input vector $u_{Ci}(t)$, and output vector $y(t)$ are given in (5.40):

$$\begin{aligned} x_{Ci}(t) &= \left[x_{1,Ci}(t), x_{2,Ci}(t), x_{3,Ci}(t)\right]^T \\ u_{Ci}(t) &= \left[v_{C,Bi}(t) - u_{ref,Ci}(t)\right] \\ y(t) &= D(t) \end{aligned} \tag{5.39}$$

Where $D(t)$ is the buck converter duty cycle.

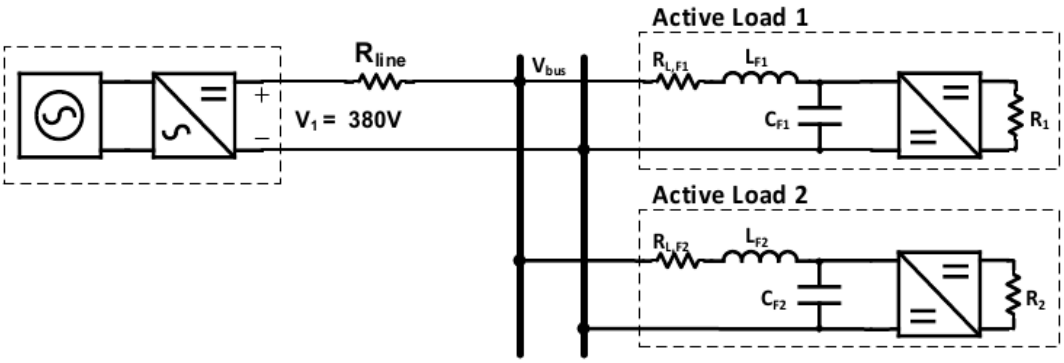

FIGURE 5.1 Studied LVDC DPS with multiple active loads fed by a non-ideal (resistive) line.

A poorly damped input filter may induce instability on the bus voltage ($V_{bus}(t)$) due to the negative input impedance characteristics of the buck converter (see Section 2.3). Stability analysis of each active load subsystem individually becomes inapplicable in the presence of other loads in parallel. R_{line} can provide a damping effect for the system under study [51], but also can contribute to the coupling between the loads, as indicated in [26].

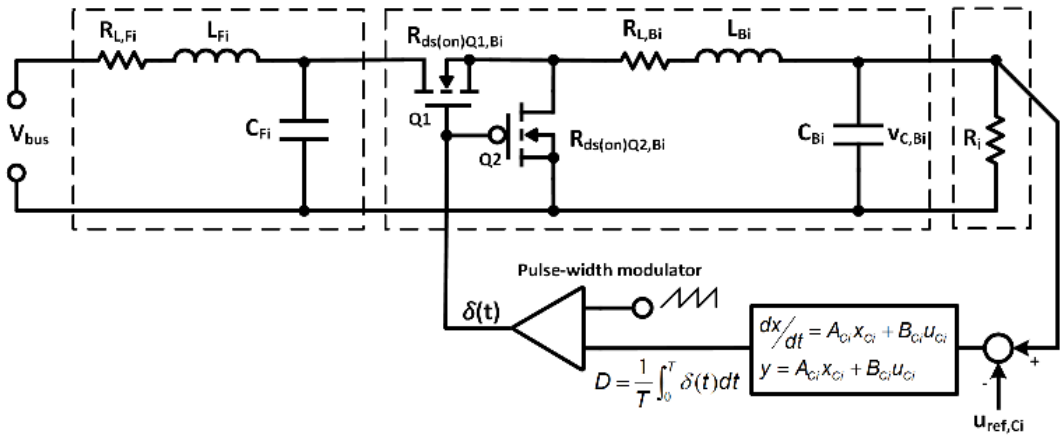

FIGURE 5.2 Circuit diagram of a single active load

5.4.2.1 System Model

The modelling methodology is described in detail in Chapter 2.6. The system in Figure 5.1 is modelled as a nonlinear state-space system of equations. For generality in the system model description, an n-number of parallel-connected active loads fed by the same line resistance can expressed in a single model. Firstly, let the parameters of each

subsystem of an active load be denoted by the subscript i. Active load ALi, is formed by combining the filter Fi, averaged buck converter Bi, controller Ci and load resistor Ri.

By applying the circuit averaging technique and Kirchhoff laws to the dynamic models in Figure 5.1-Figure 5.2, each active load ALi can be expressed by the set of differential equations in (5.40) and bus voltage in (5.41).

$$\frac{dv_{C,Fi}}{dt} = \frac{i_{L,Fi}}{C_{Fi}} - \frac{i_{L,Bi}D_{11,Ci}\left(u_{ref,Ci} - v_{C,Bi}\right)}{C_{Fi}} + \frac{i_{L,Bi}C_{11,Ci}x_{1,Ci}}{C_{Fi}} + \frac{i_{L,Bi}C_{12,Ci}x_{2,Ci}}{C_{Fi}} + \frac{i_{L,Bi}C_{13,Ci}x_{3,Ci}}{C_{Fi}}$$

$$\frac{di_{L,Fi}}{dt} = \left(v_1 - v_{C,Fi} - R_{line}\sum_{i=1}^{n} i_{L,Fi} - i_{L,Fi}R_{L,Fi}\right)/L_{Fi}$$

$$\frac{dv_{C,Bi}}{dt} = \left(i_{L,Bi} - v_{C,Bi}/R_i\right)/C_{Bi}$$

$$\begin{aligned}\frac{di_{L,Bi}}{dt} = -\Big(&v_{C,Bi} \\ &- v_{C,Fi}\left(D_{11,Ci}\left(u_{ref,Ci} - v_{C,Bi}\right) + C_{11,Ci}x_{1,Ci} + C_{12,Ci}x_{2,Ci}\right. \\ &\left. + C_{13,Ci}x_{3,Ci}\right) + i_{L,Bi}\left(R_{ds(on)Q2,Bi} + R_{L,Bi}\right) \\ &+ i_{L,Bi}\left(R_{ds(on)Q1,Bi} - R_{ds(on)Q2,Bi}\right)\left(D_{11,Ci}\left(u_{ref,Ci} - v_{C,Bi}\right)\right. \\ &\left. + C_{11,Ci}x_{1,Ci} + C_{12,Ci}x_{2,Ci} + C_{13,Ci}x_{3,Ci}\right)\Big)/L_{Bi}\end{aligned} \tag{5.40}$$

$$\frac{dx_{1,Ci}}{dt} = B_{11,Ci}\left(u_{ref,Ci} - v_{C,Bi}\right) + A_{11,Ci}x_{1,Ci} + A_{12,Ci}x_{2,Ci} + A_{13,Ci}x_{3,Ci}$$

$$\frac{dx_{2,Ci}}{dt} = B_{21,Ci}\left(u_{ref,Ci} - v_{C,Bi}\right) + A_{21,Ci}x_{1,Ci} + A_{22,Ci}x_{2,Ci} + A_{23,Ci}x_{3,Ci}$$

$$\frac{dx_{3,Ci}}{dt} = B_{31,Ci}\left(u_{ref,Ci} - v_{C,Bi}\right) + A_{31,Ci}x_{1,Ci} + A_{32,Ci}x_{2,Ci} + A_{33,Ci}x_{3,Ci}$$

$$v_{bus}(t) = v_1(t) - R_{line} \sum_{i=1}^{n} i_{L,Fi}(t) \tag{5.41}$$

To note, equation (5.41) above shows the sharing of the common bus through the $i_{L,Fi}(t)$ state variable, i.e., R_{line} contributes to a voltage drop of $V_{bus}(t)$ based on the sum of the currents flowing into each active load.

For the two active load system in Figure 5.1, this results in a state-space model of 14th order with state and input vectors shown below in (5.42) and (5.43):

$$\begin{aligned} &x(t) \\ &= [v_{C,F1}(t), i_{L,F1}(t), v_{C,B1}(t), i_{L,B1}(t), x_{1,C1}(t), x_{2,C1}(t), x_{3,C1}(t), \\ &\ v_{C,F2}(t), i_{L,F2}(t), v_{C,B2}(t), i_{L,B2}(t), x_{1,C2}(t), x_{2,C2}(t), x_{3,C2}(t)]^T \end{aligned} \tag{5.42}$$

$$u(t) = [v_1(t), \quad u_{ref,C1}(t), \quad u_{ref,C2}(t)]^T \tag{5.43}$$

5.4.2.2 System parameters and uncertainties

Two case conditions are considered for the system in Figure 5.1. Case A has matched load input filters such that their nominal resonant frequencies are identical ($f_{r,F1}$ = 114Hz, $f_{r,F2}$ = 114Hz). Case B has well separated input filter resonant frequencies ($f_{r,F1}$ = 114Hz, $f_{r,F2}$ = 60Hz). Both cases have several parameters with uncertainties that are modelled as continuous uniform distributions on the interval given by the percentages around the nominal value. Table 5.1 and Table 5.2 show the system parameters and corresponding uncertainties.

TABLE 5.1 Fixed system parameters

Input/Parameter	Symbol	Nominal Value	Units
Source voltage	v_1	380	V
Command voltages	$u_{ref,C1}, u_{ref,C2}$	100	V
Output filter capacitances	C_{B1}, C_{B2}	1200	µF
Output filter inductances	L_{B1}, L_{B2}	100	µH
DCRs of L_{B1}, L_{B2}	$R_{L,B1}, R_{L,B2}$	10	mΩ
High-side switch (Q1) on state resistances	$R_{DS(on)Q1,B1}, R_{DS(on)Q1,B2}$	5	mΩ
Low-side switch (Q2) on state resistances	$R_{DS(on)Q2,B1}, R_{DS(on)Q2,B2}$	5	mΩ

TABLE 5.2 Uncertain parameters

Parameter	Symbol	Nominal Value	Units	Uncertainty
Line resistance	R_{line}	100	mΩ	± 100 %
Input filter 1 capacitance	C_{F1}	880	µF	± 30 %
Input filter 1 inductance	L_{F1}	2.2	mH	± 30 %
DCR of L_{F1}	$R_{L,F1}$	10	mΩ	± 50 %
Load 1 resistance	R_1	5	Ω	± 50 %
Load 2 resistance	R_2	5	Ω	± 50 %

The controllers used for both synchronous buck converters, shown in Figure 5.2, are identical for both active loads, with parameters shown in equation (5.44). The buck converter has a switching frequency of 50 kHz and under nominal parameters, the regulator voltage loop gain is designed to a 1 kHz crossover frequency.

$$A_{Ci} = \begin{bmatrix} 0 & -1.52e4 & -2.29e4 \\ 0 & -8.75e4 & -1.27e5 \\ 0 & 0 & -9.17e4 \end{bmatrix} \qquad B_{Ci} = \begin{bmatrix} 13.08 \\ 72.7 \\ 109.5 \end{bmatrix}$$
$$C_{Ci} = [-23.65 \quad 131.5 \quad 198] \qquad D_{Ci} = -0.113 \tag{5.44}$$

Table 5.3 gives the parameters for the input filter of active load 2 under the two studied system configurations (denoted as Case A and Case B).

TABLE 5.3 Case A and Case B values for input filter (*F2*) of active load 2

Parameter	Symbol	Nominal Value (Case A)	Nominal Value (Case B)	Units	Uncertainty
Input filter 2 capacitance	C_{F2}	880	1500	µF	± 30 %
Input filter 2 inductance	L_{F2}	2.2	4.7	mH	± 30 %
DCR of L_{F2}	$R_{L,F2}$	50	50	mΩ	± 50 %

5.4.3 Identification of Interaction Effects using VBSA

5.4.3.1 Method

The procedure used to perform VBSA for the system is outlined in the steps below:

1. Sample the probability distribution of all uncertain parameters using pseudo-random sampling to generate 12,000 unique scenarios.
2. For each scenario:
    a. Calculate steady-state operating point of each scenario.
    b. Linearise to obtain the system matrix A and calculate eigenvalues and corresponding participation factors.
    c. Based on participation factors, identify the two critical eigenvalue pairs related to the different input filter modes.
3. Calculating S_i and S_{Ti} on the real part of the eigenvalues from Step 2 using an implementation of the estimator from Section 5.2.3.

The total calculation time was approximately 170 seconds to perform 12,000 unique model evaluations using an Intel Core i7-4790 @ 3.60GHz with 16.0 GB of memory.

5.4.3.2 Results and discussion

VBSA results for the system under study are shown in Figure 5.3 and Figure 5.4. The first-order sensitivity indices Si indicate that in both Case A and Case B, $\lambda_{1,2}$ responds to changes in AL1 parameters ($R_1, C_{F1}, L_{F1}, R_{L,F1}$) whereas $Re(\lambda_{3,4})$ responds mainly to changes in AL2 parameters ($R_2, C_{F2}, L_{F2}, R_{L,F2}$). This is expected as $\lambda_{1,2}$ and $\lambda_{3,4}$ have been classified by their dominant participation factors which associate them either to AL1 or AL2. The results show that the most influential parameter for both $Re(\lambda_{1,2})$ and $Re(\lambda_{3,4})$ is Rline, meaning that reduction in the uncertainty of Rline will reduce the output variance the most. Comparing Case A to Case B, it can be observed that they differ primarily in total effect indices S_{Ti} and interaction effects (S_{Ti}-S_i).

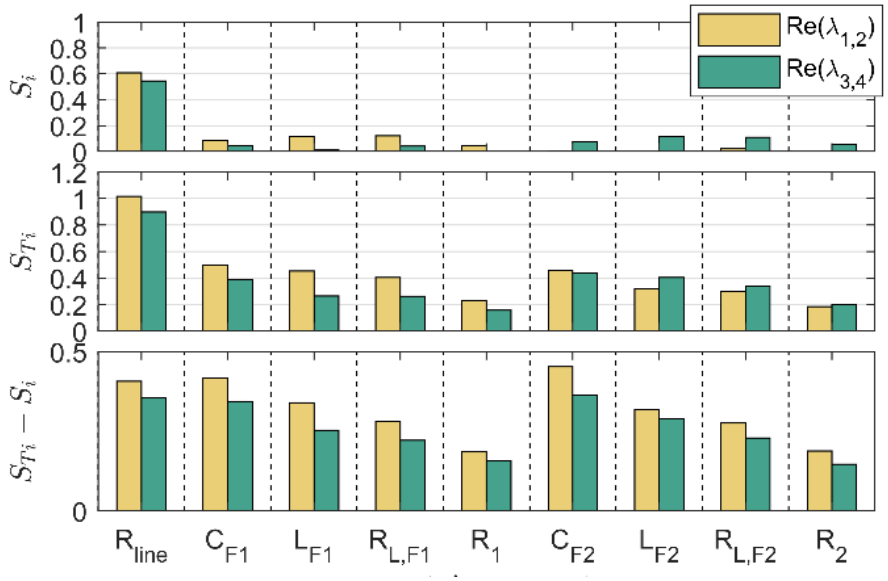

FIGURE 5.3 Estimation of VBSA sensitivity indices under *Case A*.

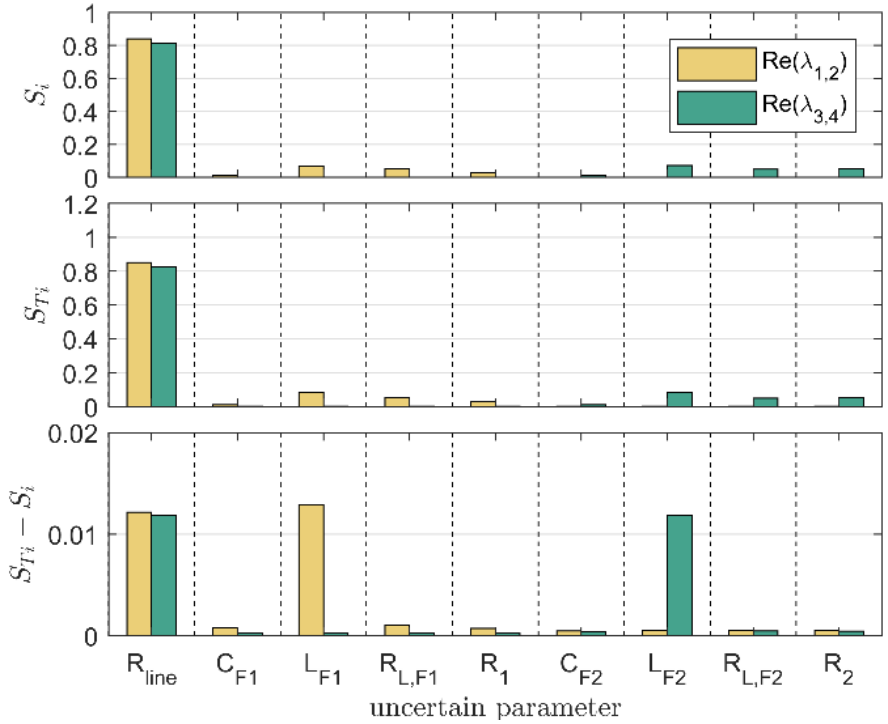

FIGURE 5.4 Estimation of VBSA sensitivity indices under *Case B*.

Under the matching filters case (Case A), the total variances of $Re(\lambda_{1,2})$ respond to changes in both AL1 and AL2 parameters indicating interactions between the

parameters of these two load subsystems, i.e., varying multiple parameters simultaneously produces a non-additive response on the movement of the eigenvalue. Of interest is the significant interaction effect of R_{line} which suggests that the behaviour of R_{line} on $Re(\lambda_{1,2})$ depends on the other interacting variables. This phenomenon is investigated further in the next section.

The results in Figure 5.4 show that Case B exhibits minimal interaction effects and no interaction between AL1 and $\lambda_{3,4}$, and AL2 and $\lambda_{1,2}$; meaning that parameters with zero interaction terms will have no effect on the sensitivity of any other parameter. For example, changes in the value of L_{F2} in the uncertainty range will not affect $Re(\lambda_{1,2})$ associated with AL1.

A limitation of using the total effect sensitivity measure is that it cannot identify which particular parameters are interacting. Modification of the adopted sampling procedure and estimator can be made to accommodate the 2nd-order and higher-order sensitivities [75], at the expense of increased total computation time. Additionally, it is important to note that VBSA indices only show the importance of particular variable(s) and do not quantify whether increasing or decreasing a variable will destabilize or stabilize the system.

5.4.4 Investigation of the effect of source-side resistance via modal analysis

To further investigate the effect of R_{line} on the stability of Case A system, the local sensitivity $\partial Re(\lambda_{1,2})/\partial R_{line}$ is calculated for different values of AL2 input filter resonant frequency. This is achieved by adjusting parameters L_{F2} and C_{F2}. Results presented in Figure 5.5 and Figure 5.6 indicate drastically different behaviours of the system under perturbations in R_{line}.

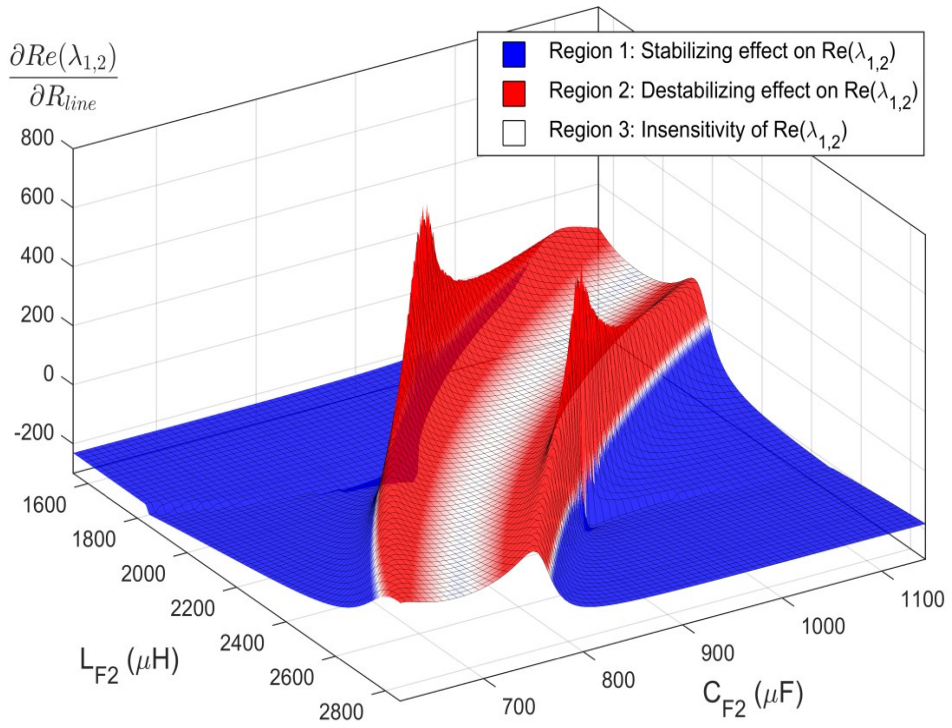

FIGURE 5.5 Effects of 30% parameter uncertainty in C_{F2} and L_{F2} on the derivative sensitivity of the critical eigenvalue to R_{line} perturbations (for *Case 1*). All other parameters remain nominal.

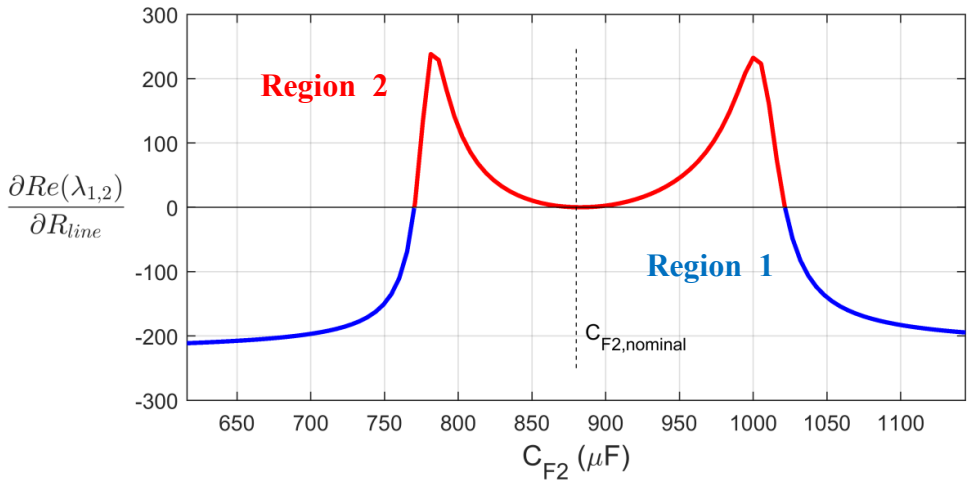

FIGURE 5.6 Critical eigenvalue sensitivity to R_{line} changes vs. capacitance C_{F2} (cross-section of Figure 5.5 at fixed inductance value $L_{F2} = 2.2\text{mF}$)

The results in Figure 5.5 can be classified into 3 regions:

Region 1: Line resistance R_{line} is stabilizing due to equivalent series damping of the filters.

Region 2: Line resistance R_{line} is destabilizing due to increase in filter coupling effects.

Region 3: Critical eigenvalue insensitivity to changes in R_{line} when the two filters are matched.

For clarity, a cross-section view of Figure 5.5 is shown in Figure 5.6 when L_{F2} has nominal value. From this it can be seen that for R_{line} to have a damping effect, the system has to be operating in Region 1. When C_{F2} is near its nominal value, the effect of positive perturbations in R_{line} is destabilising.

5.4.5 Validation of predicted behaviour using time-domain simulation

The detailed switching model of the system shown in Figure 5.1 is simulated using *Simulink/SimPowerSystems*. The effects of changes in R_{line} under different operating conditions, as identified in the previous section, are verified using time domain simulations. To investigate the effect on the stability, the time-domain simulation models are configured to operate in Region 1 (R_{line} stabilizing) and Region 2 (R_{line} destabilizing). Table 5.4 is used to select AL2 input filter parameters. Load resistances R_1 and R_2 are also varied between cases so that the system operates near instability, as given below.

TABLE 5.4 Simulation scenarios under operation in Region 1 and Region 2.

Region	C_{F2}	L_{F2}	Operating load condition ($R_1 = R_2$)	$Re(\lambda_{1,2})$
2	1000 μF	2.2 mH	2 Ω	-4.76
1	1100 μF	2.2 mH	1.4 Ω	-3.7

Referring to the simulation results in Figure 5.7 and Figure 5.8, at $t = 0$ the system operates in steady-state at the nominal line resistance ($R_{line} = 0.1\Omega$). R_{line} is then incrementally varied by ±0.01Ω every 1s to observe the effect on V_{bus}. In Region 2, unstable oscillations occur when R_{line} is increased to 0.14Ω at t = 4 (Figure 5.7(b)), whereas in Region 1 R_{line} can be safely increased to the upper bounded value of 0.2Ω

without exhibiting instability (Figure 5.8(b)). These results confirm the predicted system behaviour in Section 4. Decreasing R_{line} results in the oscillatory behaviour in both Region 1 and Region 2. In Region 2, the instability occurs when R_{line} is decreased to 0.02Ω (Figure 5.7(a)) compared to Region 1 instability at 0.06Ω (Figure 5.8(a)). It can be concluded that R_{line} has both damping and coupling effects on AL1 and AL2 and under certain operating condition it can destabilize the system

In this paper a system with two active loads under parametric uncertainties is analysed. An improved analysis approach has been proposed using VBSA in order to identify system parameter(s) that have a significant impact on the small-signal stability. For the system under study source-side resistance interacts with other uncertain parameters when input filter resonant frequencies of load 1 and load 2 are matched. Further analysis using local sensitivity analysis reveals that source-side resistance can exhibit different effects on the small signal stability: stabilizing (damping), destabilizing, and no impact (insensitivity). The predicted model behaviours are validated through time domain simulation.

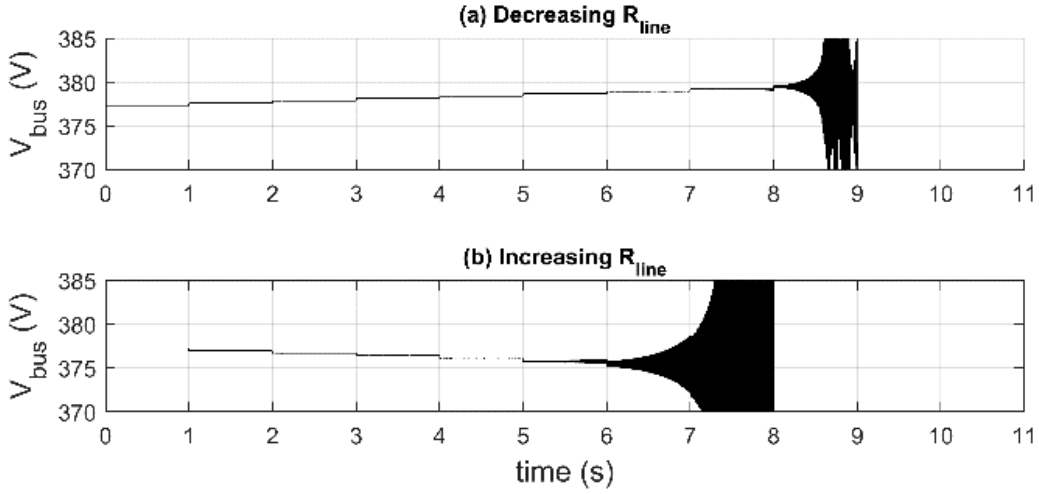

FIGURE 5.7 Region 2, time domain simulations showing the effect on V_{bus} under: **(a)** decreasing R_{line}, **(b)** increasing R_{line}.

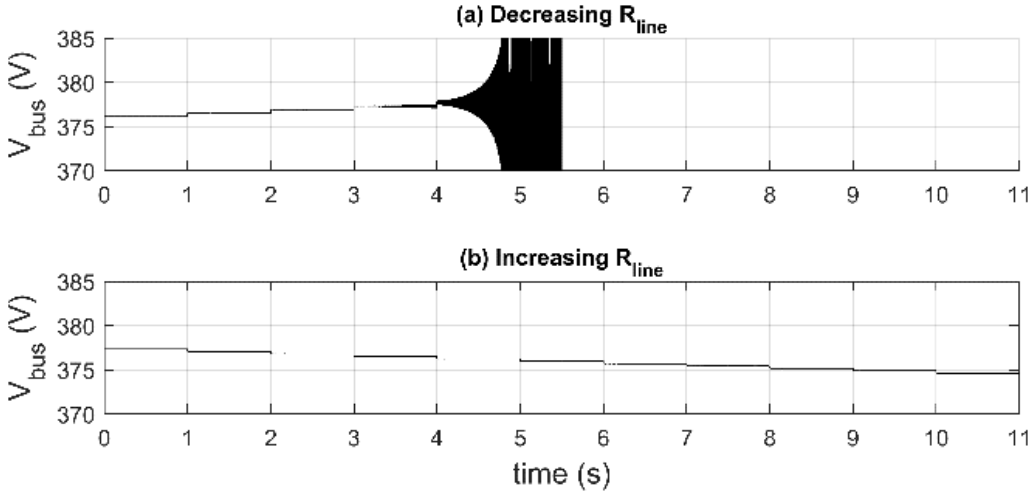

FIGURE 5.8 Region 1, time domain simulations showing the effect on V_{bus} under: **(a)** decreasing R_{line}, **(b)** increasing R_{line}.

5.4.6 Conclusions from the case study

In this case study, VBSA was performed on two systems with identical structure but with a different set of nominal values on input filters. Results indicated that the effectiveness of source-side resistive damping was reduced when resonant frequencies of input filters are nominally matched. VBSA found that interactions are present between parallel loads and source-side resistances, and these results are verified against conventional derivative-based sensitivity analysis and discussed. For the first time, the apparent dichotomy in the effect of source-side line resistance is revealed: line resistance can act as both a stabilizing and destabilizing element on the overall system depending on operating conditions. The predicted model behaviours are validated through time domain simulations.

5.5 Summary

This chapter has introduced and provided the framework for the application of the probabilistic VBSA for identifying and quantifying first- and total-order effects of parameter, as well as their interactions, across all possible operating conditions. A novel procedure for applying VBSA to realistic models of LVDC DPS has been established in order to aid in the analysis of parameter effects on small-signal stability analysis, and as an effective screening tool for assessing the effect of multiple parameter uncertainties. The new procedure has been applied on a case example LVDC DPS with parallel-connected input filters feeding CPLs. It was found that source-side resistance interacts with other uncertain parameters when input filter resonant frequencies of the parallel filters become closely matched, significantly impacting small-signal dynamics due to strong nonlinear interaction phenomena. The next chapter further investigates this phenomenon in terms of source-load interactions and mode coupling.

Chapter 6

Analysis of Mode Coupling Between Parallel-connected Input Filters with Constant Power Loads

ABSTRACT This chapter investigates the resonant coupling phenomenon between parallel loads observed from the interaction analysis from Chapter 5. Stability and derivative sensitivity are influenced by the interaction of source-side resistance and active loads. Here, linear modal coupling theory is extended to analyse this phenomenon. Divergence of eigenvalue loci between the coupled-system model and the equivalent decoupled-system model is used to quantify the effect of the coupling phenomenon, as well as predict the best and worst-case system damping. The apparent dichotomy in the effect of line resistance is finally resolved: line resistance can be apportioned to both subsystem damping and contribute to the coupling between subsystems.

The trajectory of eigenvalues under parametric perturbations is also shown to exhibit a mode swapping behaviour, where continuous eigenvalues exchange modal properties instead of diverging. To address this phenomenon, an algorithm based on participation factor analysis has been developed to ensure the conformity of eigenvalues to given subsystems.

Small-signal stability and sensitivity analysis of the system models are validated through experimental results, and several scenarios are presented demonstrating the practical importance of the mode coupling on small-signal dynamics.

6.1 Introduction

Chapter 6 contains detailed analysis of the effect of the resonant coupling phenomenon between parallel loads reported in the literature (Chapters 1 and 2). Subsequently it was revealed that stability is critically influenced by the interaction of source-side resistance and active loads in Chapter 5. Linear modal coupling theory is extended in this chapter to analyse resonant interaction phenomenon. We show that the difference of eigenvalue loci between the coupled-system model and the equivalent decoupled-system model can be used to quantify the effect of the coupling phenomenon, as well as predict the best and worst-case system damping. Through analysis of the coupled/decoupled-system models, the dichotomy presented in Chapter 5 is resolved: source-side line resistance is shown to contribute to both the damping of individual subsystems (thereby increasing small-signal stability) whilst simultaneously contributing to the coupling between subsystems (thereby decreasing small-signal stability). As a result, the combined effect of the line resistance is destabilizing when the coupling component exceeds that of the damping component.

This chapter makes contributions in the following directions: Firstly, interaction between modes arises due to feedback coupling terms in the linearised system models. An analysis framework based on analysing the decoupled-system model is formulated and used to quantify the effect of mode coupling on stability margin.

Secondly, through parametric sensitivity analysis we resolve the dichotomy of the small-signal dynamic effects of line resistance. Line resistance functions as stabilizing element due to equivalent series damping and can also function as a destabilizing element due to increasing mode coupling. This is demonstrated experimentally in a practical system. When coupling effects begin to dominate, further increasing line resistance reduces stability margins.

The structure of this chapter is as follows. In Section 6.2, the modal coupling phenomenon is investigated through the effect parametric changes on eigenvalues. To cope with the phenomenon of mode swapping, mode tracking based on participation factor analysis is formulated for the first time. We introduce the concept of the decoupled state-space model which predicts the behaviour of eigenvalues assuming no feedback coupling between subsystems. Section 6.3 models the two-coupled filter-load system fed by a line

resistance from Chapters 4 and 5 as a system with ideal CPLs. Section 6.4 analyses the effect of model coupling: stability margins using minimum damping ratio are studied and sensitivity analysis is performed at various operating conditions. This analysis quantifies the effect of source-side resistance: it is both stabilizing through equivalent damping and destabilizing through increasing coupling, and this strongly relates to the resonant frequencies of the parallel-connected LC filters. Section 6.5 verifies behaviour using experimental measurements from the test rig. Finally, Section 6.6 summarises the chapter.

6.1.1 Background

Stability may also be impacted by the dynamic interactions between different subsystems in power distribution networks. Papers [45], [93], [110], [111] provide important insights into the complexity of interactions between sources, loads, network dynamics and controllers.

Through an impedance-based approach, the authors in [45] illustrate a reduction in stability margins due to mutual interaction occurring between parallel-connected converters in the presence of a non-ideal grid. To quantify the effect of these types of interactions, eigenvalue sensitivity and participation factor analysis are often used to assess the impact of parameter variation on stability [19].

Mode coupling is known to occur near resonance when one oscillatory mode coincides with another in terms of frequency and damping. This interaction phenomenon is often observed by studying the behaviour of eigenvalues of a linear system as a function of a parameter. As modes become coupled, they are no longer independent of each other and the eigenvalues appear to diverge on the complex eigenspace and is exhibited as energy transfer between modes and an increase in oscillatory behaviour of the system [112]. Issues surrounding this phenomenon are studied extensively in several applications and are sometimes referred to as mode repulsion, veering, and eigenvalue avoidance.

The impact of mode coupling is an important consideration in the operation of power systems with series-compensated transmission line. Subsynchronous resonance arises from the interaction between the mechanical (torsional dynamic) mode and

electrical damping mode and can lead to instability with sustained oscillations [17], [18], [90]. Similarly, mode coupling can degrade stability margins in AC DPSs due to the resonance interaction between parallel LCL filters [22], [23], [43], [44] and demonstrated by [21] to be the result of coupling via circulating currents between filters.

Evidence of mode coupling phenomenon is exhibited in LVDC DPSs consisting of multiple parallel ALs. The work in [51] implemented a source-side virtual resistance-based compensator capable of stabilizing multiple active loads, however observed that the effectiveness is reduced when input filter resonant frequencies were coincident. Similarly, [26] identifies interaction between ALs and argue that line resistance is a factor responsible for coupling between filters. Chapter 5 revealed that parameter interactions occur between line resistance and filters only when filters are closely matched. Further sensitivity analysis indicted that the line resistance could exhibit either a stabilizing or destabilizing characteristic depending on the parameters of filters.

The behaviour of eigenvalues to parameter changes is crucial in understanding which parameters influence stability at to what degree. The conventional approach is to calculate the derivative of the eigenvalues with respect to a given parameter. Under larger changes in parameters, conclusions drawn from the derivative sensitivity at a single operating point is no longer suitable.

6.2 Mode Tracking and the Decoupled State-space Model

6.2.1 Mode tracking under parameter variation

The trajectories of eigenvalues of a linear system model are known to behave in unexpected ways as parameters are varied. During coupling between two modes, eigenvalue loci tend to diverge or coalesce. Under some conditions, the phenomena of *mode switching* may occur as eigenvalues approach with an exchange in the modal properties of the eigenvalues. This creates a fundamental problem on tracking the trajectories of eigenvalues, what is referred to as *mode tracking* -- the aim is to ensure a consistent relationship between individual eigenvalues to the states that give rise to them.

Using the previous example in Section 2.5.2.1, we first show the phenomena of mode switching and demonstrate the problem of mode tracking. Figure 6.1 shows examples of some of the possible eigenvalue trajectories when varying a parameter.

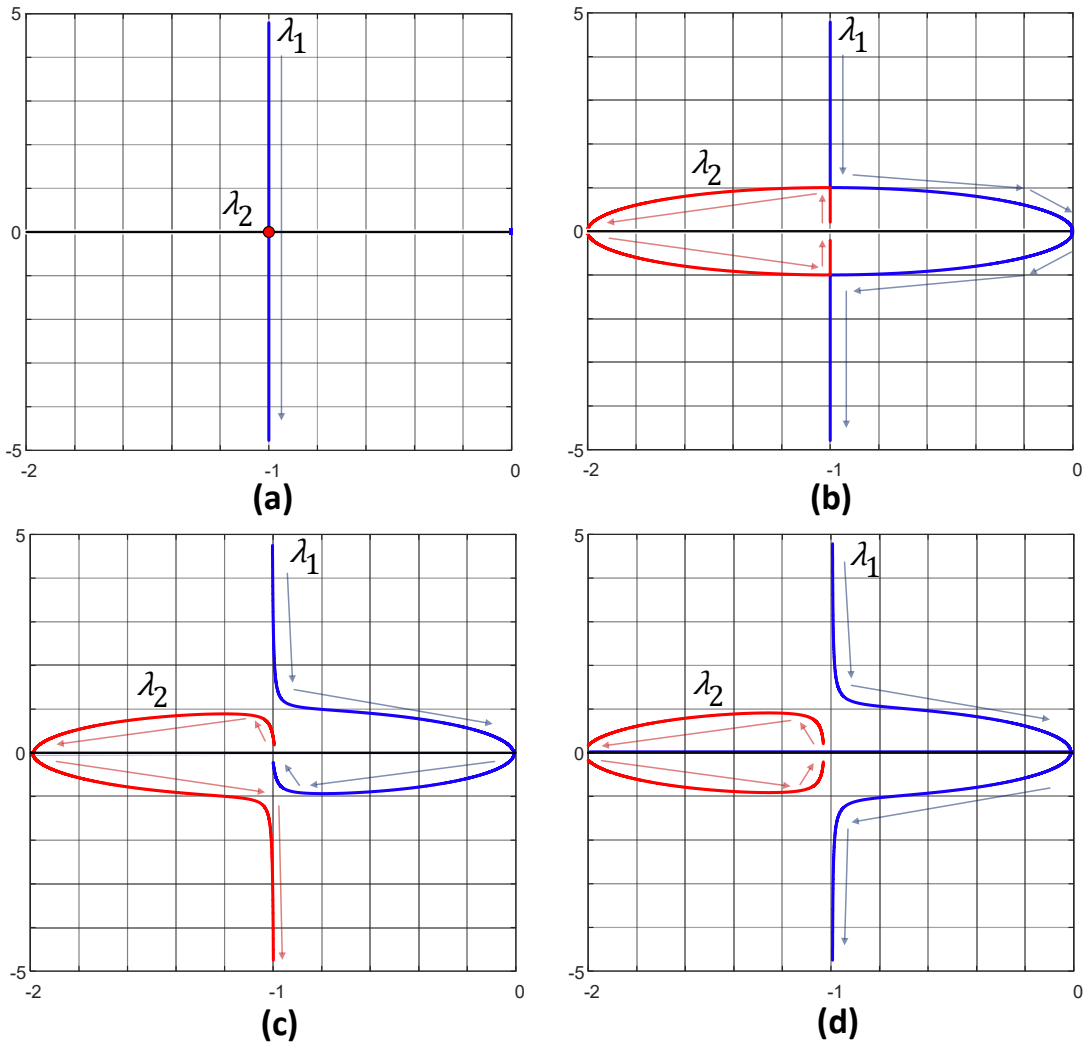

FIGURE 6.1 Possible eigenvalue (λ_1, λ_2) trajectories when varying a single parameter

The matrices that give rise to each of the trajectories in Figure 6.1 are given below in equation (6.1).

$$(\boldsymbol{a}): \begin{bmatrix} -1+j\rho_1 & 0 \\ 0 & -1+j\rho_2 \end{bmatrix}$$
$$(\boldsymbol{b}): \begin{bmatrix} -1+j\rho_1 & 1 \\ 1 & -1+j\rho_2 \end{bmatrix} \tag{6.1}$$

$$(\boldsymbol{c}): \begin{bmatrix} -1 + j\rho_1 & 1 + j0.01 \\ 1 + j0.01 & -1 + j\rho_2 \end{bmatrix}$$

$$(\boldsymbol{d}): \begin{bmatrix} -1 \pm j\rho_1 & 1 + j0.01 \\ 1 - j0.01 & -1 + j\rho_2 \end{bmatrix}$$

Where varied parameter $\rho_1 = [5, -5]$, and fixed parameter $\rho_2 = 0$.

The trajectories presented in Figure 6.1 are briefly discussed. Figure 6.1(a) shows two independent eigenvalues that do not interact. As λ_1 passes λ_2 at point (-1,0) without any deviation. At this point a repeat eigenvalue exists.

Figure 6.1(b) shows that λ_2 becomes attracted to λ_1 up to point (-1,1) where to begin to rapidly diverge in the real axis. Eigenvalues can be seen to couple with frequencies coalescing/being pulled together. A critical point exists when $\rho_1 = \rho_2$ where $\lambda_1 = 0$ indicating that system dynamics have become marginal stable.

Figure 6.1(c) shows the phenomena of mode swapping. Even though the same parameter is varied over the same range in Figures (a)(b)(d), the eigenvalue ordering does not hold consistently over the variation. Therefore, 1 at the start of the trajectory (p=5) assuming the state x_1 corresponded to λ_1), at the end of the trajectory (p=-5) state x_1 is now represented by λ_2.

Figure 6.1(d) shows a very similar trajectory to Figure 6.1(c) but does not exhibit any mode swapping phenomenon.

This mode swapping phenomenon occasionally arises in literature relating to power systems. Paper [91] identifies these two types of eigenvalue interactions types as Type A is and Type B interactions. Type A are characterized by eigenvalue crossing avoidance where eigenvalues transition into each other, with an exchange in mode properties, (as visually represented by Figure 6.1(c)). Type B has eigenvalues veering or crossing behaviour (as visually represented by Figure 6.1(d)). A more comprehensive analysis of this phenomenon may be found in [18].

An often-made assumption in dynamic studies is to order eigenvalues by their magnitude. Tracking the eigenvalue with the largest real-part characterizes the most dominant response in the system [70], [113]. Alternatively, papers [101], [114] perform continuous eigenvalue tracing [68], [115] using the property that eigenvalue loci curves are continuous over iterative perturbations [89], [116]. As shown in the simple example with results

portrayed in Figure 6.1, both approaches are not appropriate for tracking as this may result in inconsistent ordering over (multiple) parameter variations.

To account for the possible occurrence of the mode swapping phenomenon, a procedure is developed in this thesis to track eigenvalues based their maximum contributing states. Here we make a clear distinction between eigenvalues and modes. While eigenvalues are simply the characteristic roots of a system (denoted with numeric subscripts $\lambda_1, \lambda_2, \dots, \lambda_n$), the modes shall be defined and linked to the physical interpretation or structure of the system (denoted with the prefix 'm' in the subscripts $\lambda_{m1}, \lambda_{m2}, \dots, \lambda_{mn}$).

To achieve consistent interpretation following eigenvalue analysis, participation factor analysis is used to track each of the eigenvalues to the modes defined by state participation. The eigenvalue calculated at each iteration must be sorted so that maximal participation is linked to a consistent ordering of the state variables of the system. Participation factors can be calculated as (6.2) [67]:

$$p_{k,i} = \frac{|v_{i,k}||w_{k,i}|}{\sum_{k=1}^{n}|v_{i,k}||w_{k,i}|} \tag{6.2}$$

Here, i^{th} eigenvalue relates to the k^{th} state variable. However, it is important to emphasise that i is in no particular order.

Representing all participation factors as a single matrix in (6.3):

$$\mathrm{P} = \begin{array}{c} \\ \lambda_1 \\ \lambda_i \\ \lambda_n \end{array} \begin{array}{c} \begin{array}{ccccc} x_1 & & x_j & & x_n \end{array} \\ \begin{bmatrix} p_{1,1} & \cdots & p_{1,j} & \cdots & p_{1,n} \\ \vdots & \ddots & \vdots & \ddots & \vdots \\ p_{i,1} & \cdots & p_{i,j} & \cdots & p_{i,n} \\ \vdots & \ddots & \vdots & \ddots & \vdots \\ p_{n,1} & \cdots & p_{n,j} & \cdots & p_{n,n} \end{bmatrix} \end{array} \tag{6.3}$$

The matrix above can be rearranged so that the maximum participation factor is at the diagonal, as indicated in (6.4). Following this, each eigenvalue is now ordered consistent manner as modes—λ_{m1} corresponds to x_1, λ_{m2} corresponds to x_2, etc.

$$\mathrm{P} = \begin{array}{c} \\ \lambda_{\mathrm{m}1} \\ \\ \lambda_{mi} \\ \\ \lambda_{mn} \end{array} \begin{array}{c} \begin{array}{cccccc} x_1 & & x_j & & x_n \end{array} \\ \begin{bmatrix} \boxed{p_{1,1}} & \cdots & p_{1,j} & \cdots & p_{1,n} \\ \vdots & \boxed{\ddots} & \vdots & \ddots & \vdots \\ p_{i,1} & \cdots & \boxed{p_{i,j}} & \cdots & p_{i,n} \\ \vdots & \ddots & \vdots & \boxed{\ddots} & \vdots \\ p_{n,1} & \cdots & p_{n,j} & \cdots & \boxed{p_{n,n}} \end{bmatrix} \end{array} \tag{6.4}$$

Applying this mode tracking approach to the trajectories generated in Figure 6.1(c) results in the corrected graph in Figure 6.2, below. Eigenvalue movements now feature a discontinuity or jump in loci over a continual change in parameter.

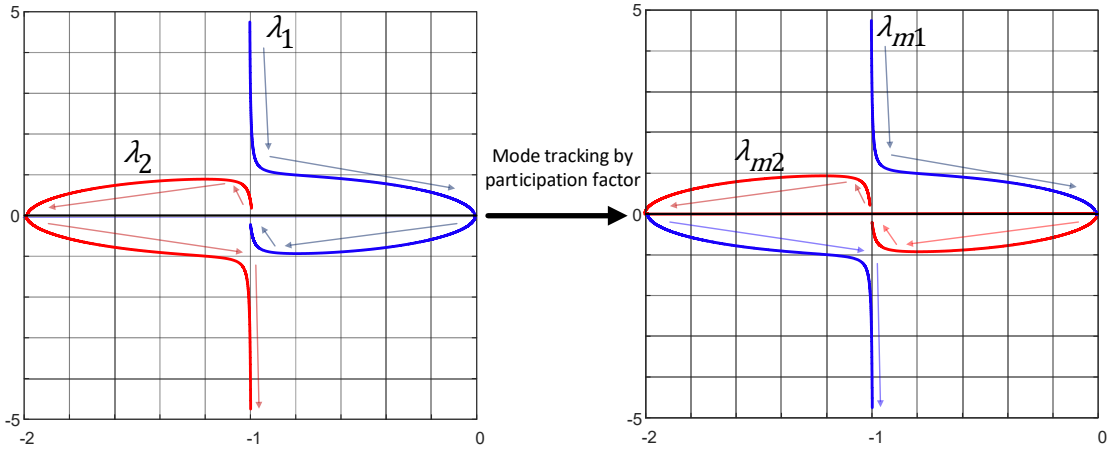

FIGURE 6.2 Eigenvalue mode tracking via participation factor analysis.

6.2.2 Decoupled State-Matrix Model

Referring back to the modelling approach in Chapter 3, complete power system models can be viewed as the interconnection of a number of subsystem models where each subsystem can be modelled independently. Here, we refer to the complete power system model as the interconnected state-space model. Interconnection introduces feedback dynamics between the different subsystems. This feedback may result in modal coupling between subsystems that may have a significant impact the dynamics of the fully interconnected system.

A new *decoupled state-space model* (DSSM) is defined by removing all coupling terms from the fully *interconnected state-space model (*ISSM). These coupling terms appear as terms in the off-diagonal of the state-matrix (A) in the ISSM and can be subtracted to generate the DSSM. For the purposes of small-signal stability analysis, only the characteristics of the state matrix A are relevant here.

The state matrix of DSSM (A_{DSSM}) can be found by subtracting a newly defined matrix A_C containing only coupling terms (6.5):

$$\underbrace{\begin{bmatrix} \boldsymbol{A_1} & 0 & \cdots & 0 \\ 0 & \boldsymbol{A_2} & 0 & \vdots \\ \vdots & 0 & \ddots & 0 \\ 0 & \cdots & 0 & \boldsymbol{A_N} \end{bmatrix}}_{A_{DSSM}} = \underbrace{\begin{bmatrix} \boldsymbol{A_1} & \sigma_{12} & \cdots & \sigma_{1N} \\ \sigma_{21} & \boldsymbol{A_2} & \ddots & \vdots \\ \vdots & \ddots & \ddots & \sigma_{\dots} \\ \sigma_{N1} & \cdots & \sigma_{\dots} & \boldsymbol{A_N} \end{bmatrix}}_{A_{ISSM}} - \underbrace{\begin{bmatrix} 0 & \sigma_{12} & \cdots & \sigma_{1N} \\ \sigma_{21} & 0 & \ddots & \vdots \\ \vdots & \ddots & \ddots & \sigma_{\dots} \\ \sigma_{N1} & \cdots & \sigma_{\dots} & 0 \end{bmatrix}}_{A_C} \tag{6.5}$$

$$A_{DSSM} = A_{ISSM} - A_C$$

Where A_{ISSM} is the state-matrix of the ISSM that is equal to the conventional A matrix derived using the full-system description.

It is important to note that the subsystem state-matrices ($A_1, A_2, \dots, A_N$) are not necessarily identical to the state-matrices of the separately modelled subsystems (denoted as $A_i{}'$) and therefore should be treated as semi-interconnected subsystem models. Feedback terms that are not coupling factors may appear in A_i. Thus, in general, $A_i{}' \neq A_i$.

Considering only two subsystems, the combined system matrix A_{ISSM} can be separated out as the sum of uncoupled subsystems A_{DSSM} and coupling terms A_C. The individual subsystems A_1 and A_2 are block-diagonal in A_{DSSM} with coupling terms σ in

the off-diagonal. In effect, the coupling terms are *blocked* in A_{DSSM} ($A_{DSSM} = \mathrm{diag}(A_1, A_2)$).

This modelling methodology forms the basis of studying modal interactions by comparing the eigenvalues calculated between coupled and uncoupled systems. The decoupled system A_{DSSM} can be used to generate a trajectory of eigenvalues assuming no modal coupling. Therefore, any deviation of eigenvalues in the combined interconnected system is attributable only to mode coupling phenomena.

From equation (6.5), it is interesting to note that the trace of A_{ISSM} is identical to the trace of A_{DSSM} (diagonal terms are identical indicating that the sum of the eigenvalues must also be identical between the total system and uncoupled equivalent). This suggests that mode coupling results in a complementary effect on different eigenvalues (as one eigenvalue is pushed further positive, another must be pushed leftwards). Even though the damping of a single mode is reduced, the sum or total damping of all modes in the system remains constant.

Modal decomposition can be performed on the ISSM, given by (6.6):

$$W^T V \Lambda = W^T A_{ISSM} V \tag{6.6}$$

Where eigenvectors are normalised $W^T V = V W^T = I$.

Expanding A_{ISSM} into the sum of A_{DSSM} and A_C is given in (6.7):

$$\begin{aligned} W^T A_{ISSM} V &= W^T (A_{DSSM} + A_C) V \\ &= W^T A_{DSSM} V + W^T A_C V \\ &= \begin{bmatrix} diag\{\Lambda_1\} & 0 \\ 0 & diag\{\Lambda_2\} \end{bmatrix} + W^T A_C V \end{aligned} \tag{6.7}$$

Where Λ_1, Λ_2 are the diagonal matrices of eigenvalues of A_1, A_2.

If the above transformation for the coupling matrix A_C is zero, then the coupling effects between subsystems can be neglected. The eigenvalues of the DSSM form a template of trajectories assuming a decoupled system, which provides both a qualitative and quantitatively way to investigate the effect of modal coupling phenomenon. This is demonstrated by the practical example in Section 6.3.

6.3 Mode Coupling Between Parallel-connected Input Filters with Constant Power Loads

6.3.1 System Overview

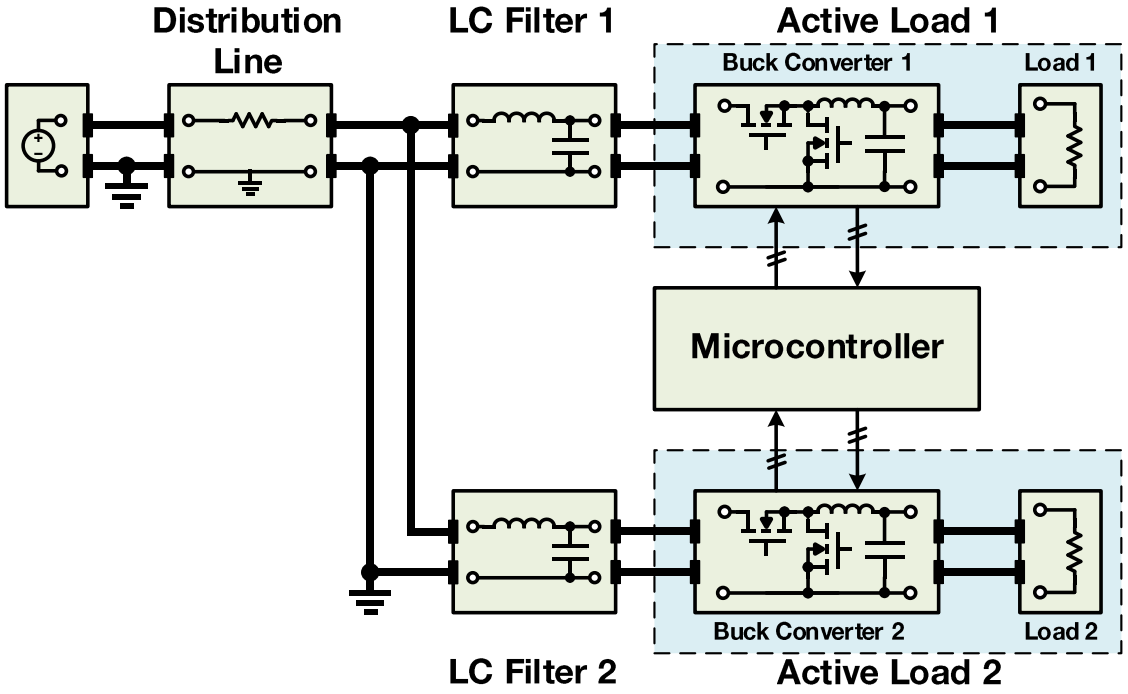

FIGURE 6.3 Block diagram overview of the LVDC power system with two parallel-connected filter-load subsystems on the same distribution bus fed by a resistive line

Figure 6.3 shows a LVDC DPS with two input-filtered active loads (AL) connected to a common bus. Each AL is comprised of a tightly-controlled buck converter providing a regulated output voltage to resistive loads. ALs therefore act as CPLs at their input provided within the closed-loop bandwidths. The switching nature necessitates that these active loads must feature LC power line filters at the input to attenuate EMI. In many practical LVDC DPS applications, the power sources servicing loads are often located at a distance. Here, the distribution lines between the source and loads are assumed to be long cables that are primarily characterized by their resistance R_{line}, which is a valid assumption for when investigating low-frequency dynamic phenomena.

6.3.2 Detailed model description with active loads

This section provides a brief summary the detailed model of the two input-filtered active load system. A single input-filtered active load system has previously been modelled and experimentally verified in Chapter 4. Chapter 5 had investigated a similar system structure (albeit as a 380V DC system with different parameters) featuring two active loads, modelled as a 14th order system with a state-space representation.

Chapter 5 had shown that the effectiveness of source-side resistive damping is reduced when resonant frequencies of the input filters are similar. Parameter interactions were shown to be present not only between the parallel loads, but also on source-side resistances. Evidence indicated that line resistance can act as both a stabilizing and destabilizing element on the overall system dependent on operating conditions.

The next section (Section 6.4) provides a reduced-order model based on ideal CPLs of the system described in Section 5.4.2.1.

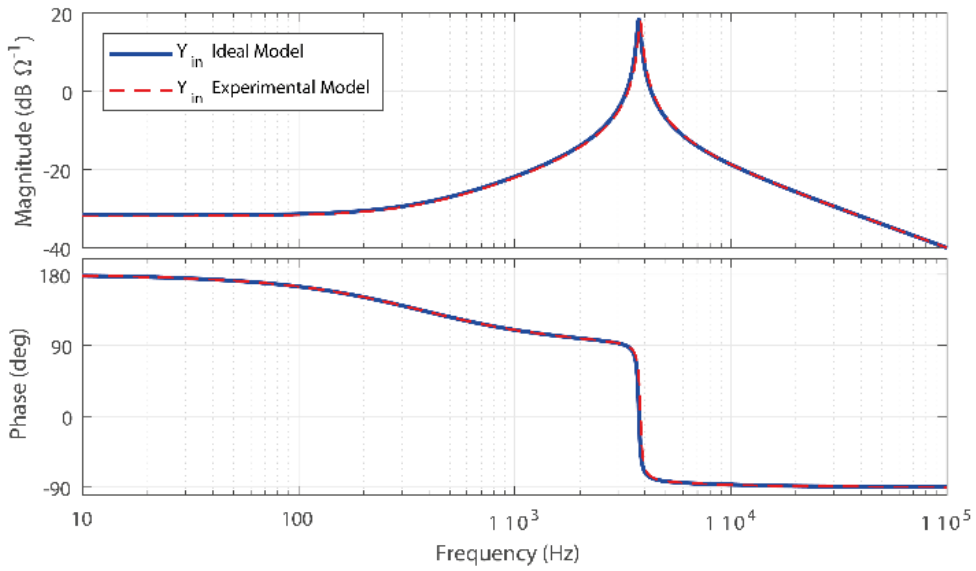

FIGURE 6.4 Comparison of the input impedance Bode diagrams of the detailed model (based on active loads with controller dynamics) and simplified model (based on ideal CPLs).

6.3.3 Simplified model description with ideal CPLs

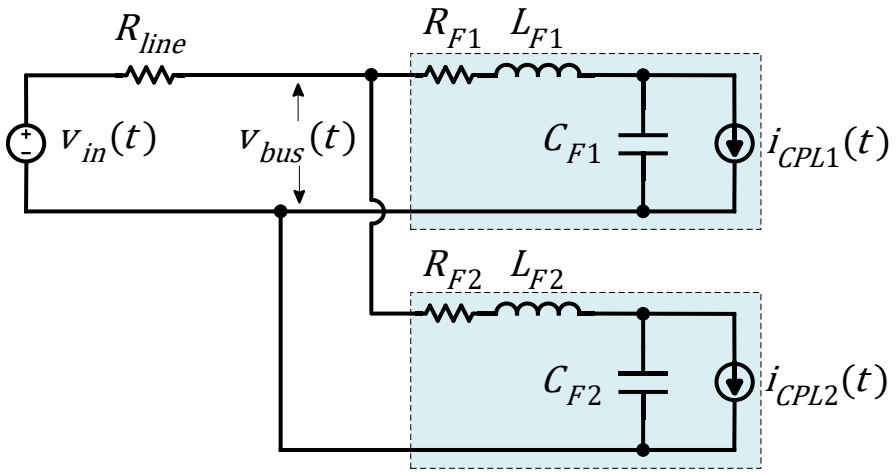

FIGURE 6.5 Ideal circuit model of the system in Figure 6.3.

The system represented in Figure 6.3 may be modelled with a simplified reduced order 4-state system with circuit diagram given in Figure 6.5. Each AL has been simplified to an equivalent CPL model. LC filter models have omitted capacitor ESR (inductor DCR remans to represent the total filter damping). The distribution line is a resistive cable modelled as a resistor R_{line}.

While the model equations may be generated using the framework outlined in Chapter 3, the circuit model is sufficiently simple for a straightforward application of Kirchhoff's laws to derive the governing differential and output equations (6.8)-(6.13). In the equations below, the subscript i indexes an individual parallel-connected filter-load system where R_{line} can be seen to couple these subsystems together in differential equation (6.9).

$$\frac{dv_{C,Fi}(t)}{dt} = \frac{i_{L,Fi}(t) - i_{CPLi}(t)}{C_{Fi}} \tag{6.8}$$

Where $i_{CPL,i} = P_{CPL,i}/v_{C,Fi}$.

$$\frac{di_{L,Fi}(t)}{dt} = \frac{v_{in}(t) - v_{C,Fi}(t) - i_{L,Fi}(t)R_{L,Fi} - R_{line}\sum_{j=1}^{n} i_{L,Fj}(t)}{L_{Fi}} \tag{6.9}$$

This system features two ALs, therefore $n = 2$.

The bus voltage $v_{bus}(t)$ can be derived the terms of the state and input variables:

$$v_{bus}(t) = v_{in}(t) - R_{line} \sum_{j=1}^{n} i_{L,Fj}\,(t) \tag{6.10}$$

For the combined system, the vector of state variables and input variables are given in (6.11)-(6.13):

$$x(t) = [v_{C,F1}(t), \quad i_{L,F1}(t), \quad v_{C,F2}(t), \quad i_{L,F2}(t)]^T \tag{6.11}$$

$$u(t) = [v_{in}(t), \quad P_{CPL1}(t), \quad P_{CPL2}(t)]^T \tag{6.12}$$

$$y(t) = v_{bus}(t) \tag{6.13}$$

The linearised system model, given by state-space matrices in (6.14)-(6.17), are used to examine the small-signal behaviour. From the linearisation procedure, the parameters $\bar{v}_{C,F1}$ and $\bar{v}_{C,F2}$ have been introduced to represent the operating point of the input voltage of the nonlinear CPLs. Given that the resistances are small, it becomes reasonable to approximate CPL input voltage to that of the source voltage, i.e., $v_{in}(t) \cong \bar{v}_{C,F1} \cong \bar{v}_{C,F2}$.

The symbolic linear state-space model of the system in Figure 6.5 is described fully by (6.14)-(6.17):

$$A = \begin{bmatrix} -\dfrac{1}{C_{F1}R_{CPL,1}} & \dfrac{1}{C_{F1}} & 0 & 0 \\ -\dfrac{1}{L_{F1}} & -\dfrac{R_{L,F1}+R_{line}}{L_{F1}} & 0 & -\dfrac{R_{line}}{L_{F1}} \\ 0 & 0 & \dfrac{1}{C_{F2}R_{CPL,2}} & \dfrac{1}{C_{F2}} \\ 0 & -\dfrac{R_{line}}{L_{F2}} & -\dfrac{1}{L_{F2}} & -\dfrac{R_{L,F2}+R_{line}}{L_{F2}} \end{bmatrix} \tag{6.14}$$

$$B = \begin{bmatrix} 0 & \dfrac{1}{C_{F1}\bar{v}_{C,F1}} & 0 \\ \dfrac{1}{L_{F1}} & 0 & 0 \\ 0 & 0 & 0 \\ \dfrac{1}{L_{F2}} & 0 & \dfrac{1}{C_{F2}\bar{v}_{C,F2}} \end{bmatrix} \tag{6.15}$$

$$C = [0 \quad -R_{line} \quad 0 \quad -R_{line}] \tag{6.16}$$

$$D = [1 \quad 0 \quad 0] \tag{6.17}$$

The nominal parameters of the model described above are shown in Table 6.1. In practice, the actual values differ from the nominal values due to uncertainties and will deviate over time due aleatoric variability. In Section 6.4, line resistance (R_{line}), filter parameters, and load power are varied to investigate the effect of mode coupling over differing conditions.

TABLE 6.1 System parameters of the reduced-order circuit model

Symbol	Nominal Value	Unit	Description
v_{in}	48	V	Input voltage
R_{line}	0.25	Ω	Line resistance
C_{F1}, C_{F2}	40	μF	Capacitance of Filter 1 and 2
L_{F1}, L_{F2}	1000	μH	Inductance of Filter 1 and 2
$R_{L,F1}$, $R_{L,F2}$	0.5	Ω	DCR of L_{F1}, L_{F2}
P_{CPL1}, P_{CPL2}	50	W	Power of Load 1 and 2

6.4 Small-signal Stability Analysis of the LVDC DPS Affected by Mode Coupling

6.4.1 Effect of filter parameter changes on mode coupling and small-signal stability

We begin by studying the eigenvalue modes of the model presented in the previous section over stepwise perturbations in the resonant frequency of a single filter ($\omega_{n,F1} = 1/\sqrt{C_{F1}L_{F1}}$) while all other system parameters are assumed to be constant as defined in Table 6.1. C_{F1} and L_{F1} are varied proportionally to ensure the damping factor of the filter ($\zeta_{F1} = R_{L,F1}/(2\sqrt{\frac{C_{F1}}{L_{F1}}})$) remains constant. Mode tracking of eigenvalues is achieved by associating them to the dominant filter states using the maximum participation factors, as given definitions in the Table 6.2, below, based on the procedure outlined in Section 6.2.

TABLE 6.2 Mode tracking based on dominant states

Subsystem	Mode	Dominant States (maximum participation)	Eigenvalues
Filter 1 (F1)	'Mode 1'	$I_{L,F1}$, $V_{C,F1}$	$\lambda_{1,2}$
Filter 2 (F2)	'Mode 2'	$I_{L,F2}$, $V_{C,F2}$	$\lambda_{3,4}$

Figure 6.6 and Figure 6.7 show the eigenvalue modes and participation factors as a function of changes in filter 1 resonant frequency from 3850 rad/s to 7150 rad/s while keeping constant filter damping ratios $\zeta_{F1} = \zeta_{F2} = 0.0028$ and holding filter 2 constant $\omega_{n,F2}$ = 5000 rad/s.

The presence of other circuit elements in the network (e.g., CPLs, R_{line}) modifies the overall damping of the modes of the system, denoted as $\zeta_{ISSM,1}$ and $\zeta_{ISSM,2}$. Due to the complexity, explicit analytical expressions cannot be obtained for $\zeta_{ISSM,1}$ and $\zeta_{ISSM,2}$, and are calculated numerically from eigenvalues.

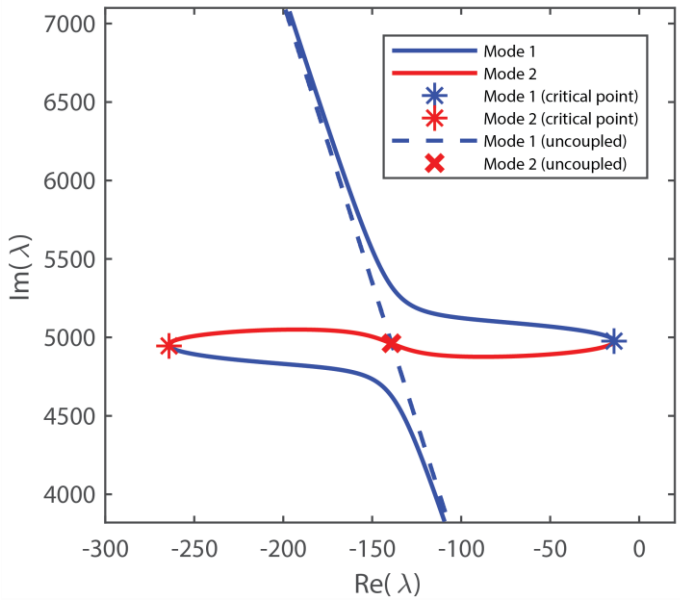

FIGURE 6.6 Trajectory of eigenvalues '*Mode 1'* and '*Mode 2*' over varying resonant frequency of *filter 1* ($3850 < \omega_{n,F1} < 7150$ rad/s). Filter damping ratios held constant ($\zeta_{F1} = \zeta_{F2} = 0.0028$)*;* $R_{line} = 0.25\Omega$.

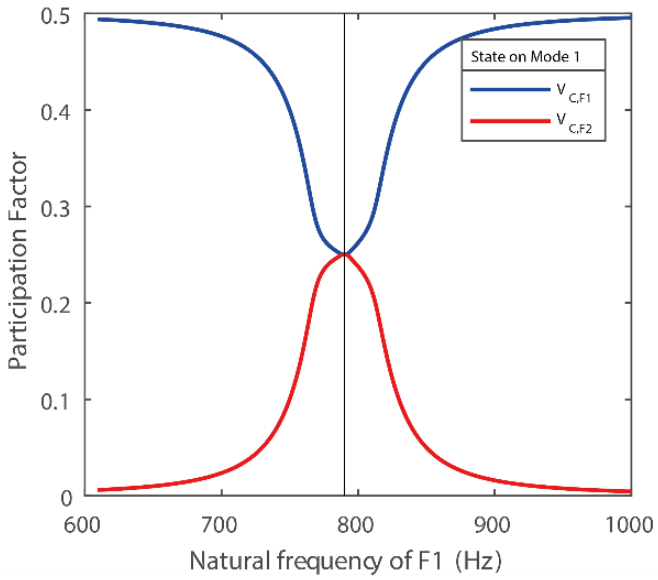

FIGURE 6.7 Trajectory of participation factors '*State* $V_{C,F1}$ to *Mode 1'* and '*State* $V_{C,F2}$ to *Mode 1*' over varying resonant frequency of *filter 1* ($3850 < \omega_{n,F1} < 7150$ rad/s). Filter damping ratios held constant ($\zeta_{F1} = \zeta_{F2} = 0.0028$)*;* $R_{line} = 0.25\Omega$.

Figure 6.8 depicts the trajectories of Mode 1 and Mode 2 in the system A_{ISSM} (solid lines) and the decoupled template A_{DSSM} (dashed line). Starting at well separated filter frequencies ($\omega_{n,F1}$ = 3850 rad/s, $\omega_{n,F2}$ = 5000 rad/s) the modes of A_{ISSM} nearly coincide with the modes of A_{DSSM}. As $\omega_{n,F1}$ is increased and approaches $\omega_{n,F2}$, it is observed that the modes of A_{ISSM} rapidly change and deviate away from each other and away from the A_{DSSM} template.

The participation factors in Figure 6.9 indicate that this occurs when filter states begin to couple to an extent. Minimum damping occurs when filters are matched ($\omega_{n,F1} = \omega_{n,F2}$) and is denoted as the critical point in the graphs. As noted in the theory in Section 6.3, the total sum of the damping in A_{ISSM} and A_{DSSM} are constant; however, during the coupling phenomenon modes appear to repel each other resulting in one of the modes being pushed towards the real-axis, indicating a degradation of the overall stability margin of the system. As filter frequencies separate away from the critical point towards extrema, coupling reduces and the eigenvalues of A_{ISSM} approaches the eigenvalues of A_{ISSM} asymptotically.

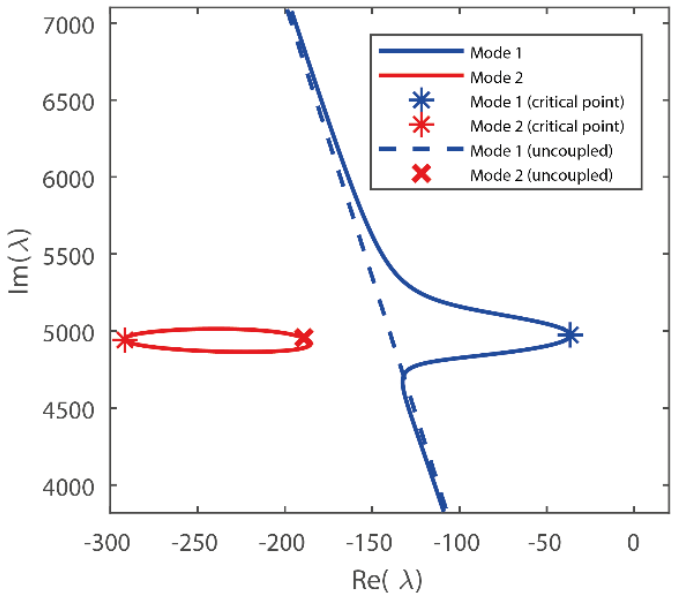

FIGURE 6.8 Trajectory of eigenvalues '*Mode 1'* and '*Mode 2*' over varying resonant frequency of *filter 1* ($3850 < \omega_{n,F1} < 7150$ rad/s). Filter damping ratios, $\zeta_{F1}=0.0028$, $\zeta_{F2}=0.0038$; $R_{line} = 0.25\Omega$.

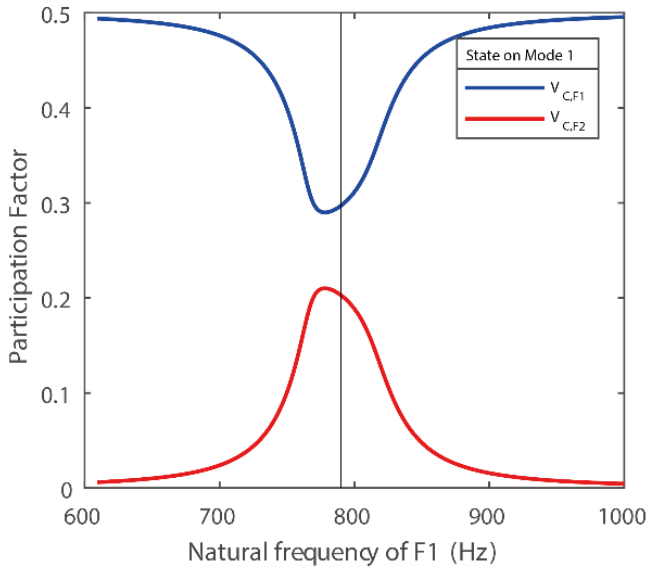

FIGURE 6.9 Trajectory of participation factors '*State $V_{C,F1}$* to *Mode 1'* and '*State $V_{C,F2}$* to *Mode 1*' over varying resonant frequency of *filter 1* ($3850 < \omega_{n,F1} < 7150$ rad/s). Filter damping ratios, $\zeta_{F1}=0.0028$, $\zeta_{F2}=0.0038$; $R_{line} = 0.25\Omega$.

The behaviours of modes during coupling do not have consistent properties. Figure 6.6 shows that the two modes exchange location after crossing the critical point, resulting in a discontinuity of modes as a function of resonant frequency. This is due to an exchange in participation factors associated with each eigenvalue. This shows the behaviour of modes when filter 2 has an increased filter damping ($R_{L,F2} = 0.6, \zeta_{F2} = 0.0038$) compared to filter 1. In this instance, the filter modes are not exchanged during coupling and remain continuous. This inconsistent behaviour of eigenvalues corroborates the need for mode-tracking. The proposed technique based on participation factors addresses this adequately. The total amount of deviation away the A_{DSSM} template during interaction also differs compared to between the cases.

6.4.2 Effect of source-side line resistance variability on mode coupling and small-signal stability

This section investigates the changes in coupling phenomena as a function of R_{line}. As mentioned previously, R_{line} can interact strongly with filter parameters when filter resonances are similar and can exhibit drastically different effects on stability depending on operating conditions [26], [51], [76]. R_{line} appears as a feedback coupling term and is considered as a coupling parameter, and also noting that when $R_{line} = 0$ the filters will be completely uncoupled as the eigenvalues of A_{ISSM} equal the eigenvalues of A_{DSSM}.

In stability analysis it is often pertinent to study the response of the mode with the most critical stability margin irrespective of the mode participating states. To simplify, equations (6.18)-(6.20) are used to transform system modes into a single worst-case damping ratio ($\zeta_{\min}$).

The damping ratio corresponding to mode λ_i is defined as (6.18):

$$\zeta_i = -\cos\left(\left(\arctan\left(\omega_i/\sigma_i\right)\right)\right) \tag{6.18}$$

where σ_I and ω_I are the real and imaginary components of eigenvalue $\lambda_i = \sigma_i \pm j\omega_i$.

The minimum damping is defined as (6.19):

$$\zeta_{min} \triangleq \min_k\{-\cos\left(\arctan\left(\frac{\omega_i}{\sigma_i}\right)\right)\} \tag{6.19}$$

The sensitivity of the critical damping is used to determine the effect of perturbations of parameter p on the small-signal stability of the mode.

$$\frac{\partial \zeta_{min}}{\partial p} = \sin\left(\arctan\left(\frac{\omega}{\sigma}\right)\right)\left(\frac{\sigma\frac{\partial \omega}{\partial p} - \omega\frac{\partial \sigma}{\partial p}}{\sqrt{\sigma^2+\omega^2}}\right) \tag{6.20}$$

The same procedure of varying the resonant frequency of a single filter, as done in the previous section, is performed at different values of R_{line}. depicts the changes in system damping over filter frequency. depicts the sensitivity of damping to R_{line} over filter frequency. To aid discussion, two different cases for filter 1 are highlighted below:

Case A: ($\omega_{n,F1}$ = 770 Hz, $\omega_{n,F2}$ = 790Hz, $\zeta_{n,F1} = \zeta_{n,F2} = 0.0028$).

Case B: ($\omega_{n,F1}$ = 707 Hz, $\omega_{n,F2}$ = 790Hz, $\zeta_{n,F1} = \zeta_{n,F2} = 0.0028$).

TABLE 6.3 summarizes the values of damping and sensitivity at the different values of R_{line} for Cases A and B.

TABLE 6.3 Summary of damping and sensitivity under different values of R_{line}.

	Case A		Case B	
R_{line} (Ω)	ζ_{min}	$\partial\zeta_{min}/\partial R_{line}$	ζ_{min}	$\partial\zeta_{min}/\partial R_{line}$
0	0.0028	0.1005	0.0028	0.1005
0.1	0.0120	0.0753	0.0127	0.0974
0.25	0.0090	-0.0431	0.0223	0.0935
0.5	0.0050	-0.0045	0.0446	0.0122

Plots in Figure 6.10 and Figure 6.11 give the system damping ratio and sensitivity over a change in resonant frequency. From this, the following observations are made:

Two conditions result in a minimum system damping (ζ_{min}=0.0028). Firstly, when R_{line} = 0 signifying absence of any additional filter damping. Secondly when both filters are perfectly matched ($\omega_{n,F1} = \omega_{n,F2}$) under any values of R_{line} indicating that damping via R_{line} is negligible/ineffective.

As filter resonant frequencies become well-separated, the damping ratios approach the values under A_{ISSM} uncoupled-system template. Different behaviours of R_{line} can be observed depending of filter frequency separation. Considering Case A, it is seen that at

beyond some value of R_{line}, the system's minimum damping degrades. R_{line} values of 0.25 and 0.1 result in a wider stability margin than R_{line} of 0.5. Case B does not suffer from this as the damping ratio sensitivity to R_{line} is always positive.

Figure 6.11 shows that R_{line} can be both stabilizing and destabilizing depending on values of R_{line} and the filter frequency separation. The frequency range between filters at which stability degrades due to coupling effects increases with R_{line}.

Complex nonlinear relationship as a function of both R_{line} and filter frequencies. As R_{line} increases the frequencies between filter range of which R_{line} coupling effects dominate increases.

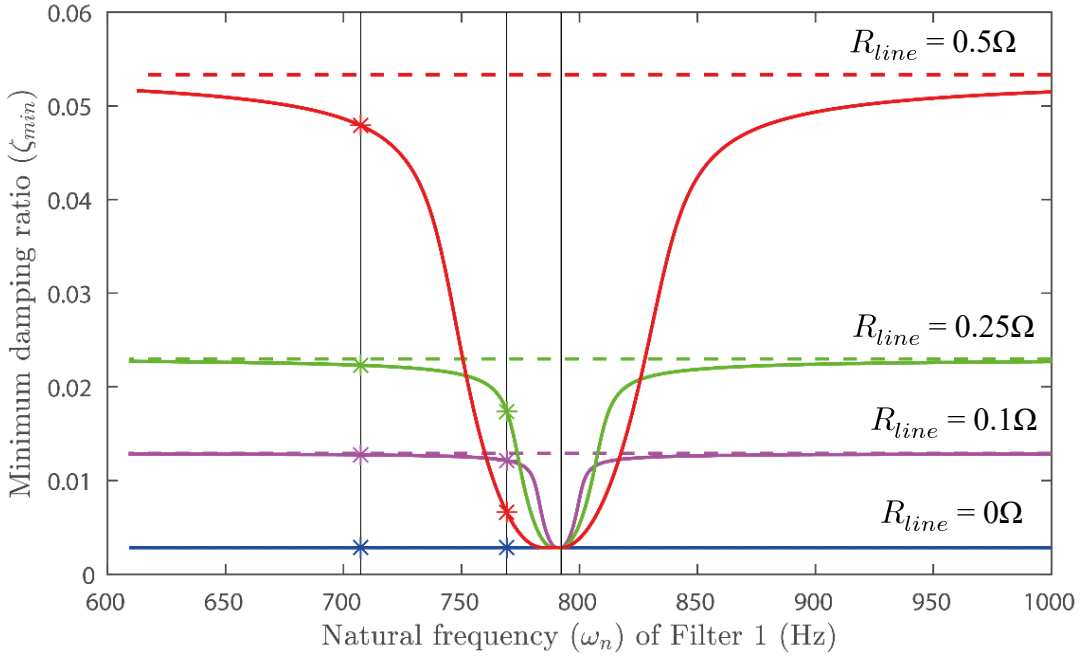

FIGURE 6.10 System minimum damping ratio (ζ_{min}) as a function of the resonant frequency of filter 1 ($3850 < \omega_{n,F1} < 7150$ rad/s) at different values of line resistance $R_{line} = \{0, 0.1, 0.25, 0.5\}$.

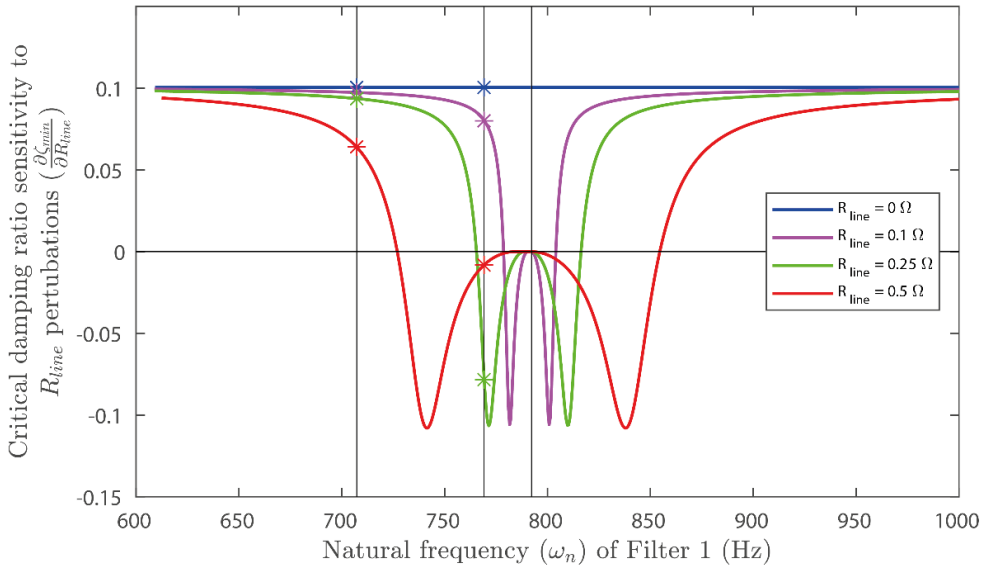

FIGURE 6.11 Sensitivity of minimum damping ratio (ζ_{min}) to R_{line} perturbations as a function of the resonant frequency of filter 1 ($3850 < \omega_{n,F1} < 7150$ rad/s) at different values of line resistance $R_{line} = \{0,0.1,0.25,0.5\}$.

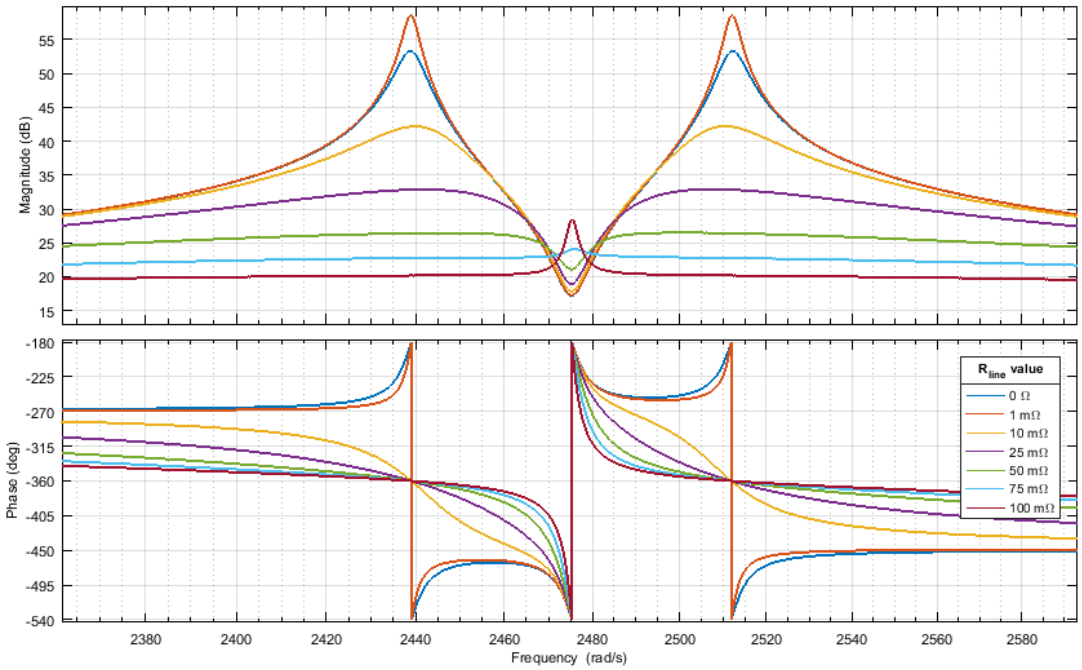

FIGURE 6.12 Input impedance of the system under different R_{line} values.

Figure 6.12 shows the behaviour of the input impedance at different R_{line} values. At low values of R_{line}, the system is considered uncoupled and shows 2 distinct peaks in the input admittance magnitude plot. These peaks can be damped by increasing R_{line} up until some crossover point where a new centre-peak begins to appear when the filters become sufficiently coupled due to the R_{line} increase. Further increasing R_{line} beyond this point increases the magnitude of this peak which has an overall destabilizing effect.

6.5 Experimental Results

To investigate the effect of uncertain line resistance on the stability, an experimental LVDC DPS consisting of two active loads operating in parallel was developed, presented in Chapter 4. The critical value of the power delivered to the loads at the onset of instability serves as an indicator of the damping in the system:

$$P_{max} \propto \frac{1}{\zeta_{min}} \tag{6.21}$$

Each active load is realized using a synchronous buck converter with a tightly regulated output and an input LC filter. Under nominal operating conditions, each buck converter designed to step-down a 48V DC input to 24V DC output for a 10Ω load. Voltage mode control is achieved using a 3-pole 3-zero compensator implemented digitally on a TMS320F28379D microcontroller with a control bandwidth of approximately 5 kHz and a switching frequency of 100 kHz.

An active load based on tightly regulated converters is well modelled using the active load using an ideal CPL presented in Chapter 3. The Bode plot in Figure 6.4 show the comparison between the input impedance of the ideal CPL-based active load model and the practical active load in model. Higher order dynamics in the converter model can be neglected as the controller bandwidth is sufficiently higher than that of the LC filter resonant frequency. Similarly, sensor noise and discretization effects can be neglected. Matching the DC gains shows that the active load present CPL behaviour of approximately 47 W to the source interface.

Considered are two different experimental systems that differ in the values of the input filters of the active loads. Experimentally measured values are provided in Table

6.4. System 1 has nominally matched filters (40uF, 1000uH), however it is crucial to note that the parametric uncertainty in practical systems will result frequency mismatch between filters ($\Delta\omega_r$). System 2 has increased input filter capacitance of one of active loads so that $\Delta\omega_r$= 40 rad/s.

TABLE 6.4 Measured filter parameters in the experimental system.

	System 1		System 2	
Parameter	Active Load 1	Active Load 2	Active Load 1	Active Load 2
C_{Fi} (μF)	39.543	37.7	51.2	37.7
L_{Fi} (μH)	992.67	955.11	992.67	955.11
$R_{\mathrm{L,Fi}}$ (mΩ)	574	583.24	574	583.24

Figure 6.13 shows the total power ($P_T = P_1 + P_2$) that can be delivered to both active loads before instability occurs over different values of R_{line}, assuming each active load delivers the same power ($P_1 = P_2$). These plots are generated by iteratively finding the critical destabilizing power at different values of R_{line} using the small-signal model.

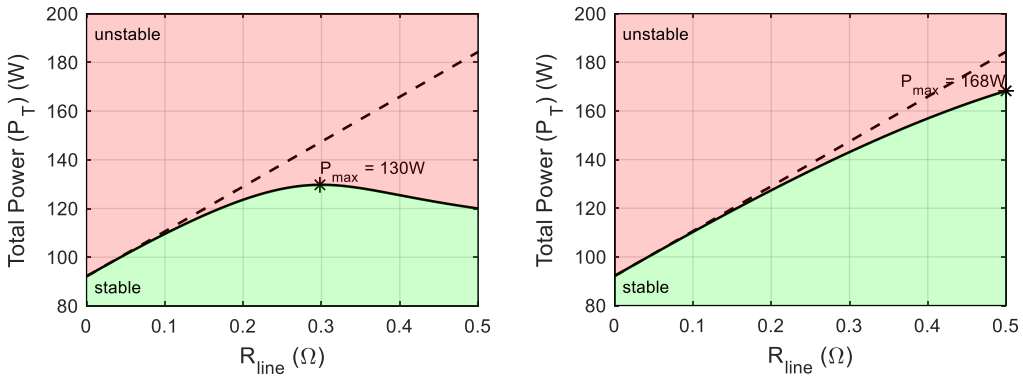

(a) (b)

FIGURE 6.13 Power stability boundaries at different values of R_{line} values: (a) System 1; (b) System 2.

Figure 6.13(a) shows System 1 (coupled system) results. Considering the operating point $P_T = 60W$, there exists an upper and lower limit of R_{line} for system stability ($R_{line} = [0.17, 0.5]$). Maximum power (P_{max}) occurs when $\partial\zeta_{\min}/\partial R_{line} = 0$ at R_{line} = 0.3. The reduction in stability margin occurs when R_{line} increases beyond this point resulting in a negative $\partial\zeta_{\min}/\partial R_{line}$ indicating that coupling effects begin to dominate.

Limiting R_{line} to 0.3 ensures that positive perturbations in R_{line} always exhibit a stabilizing effect.

System 2 results are shown in Figure 6.13(b). R_{line} acts as stabilizing element due to equivalent series damping. The stability boundary generally follows the predicted power of the uncoupled template, however at high values of R_{line} some discrepancy is observed. This indicates a reduced effectiveness R_{line} and is attributable to some modal coupling.

The objective is now to verify the effects of mode coupling on the stability boundaries identified. The experimental setup of the studied LVDC DPSs is presented in Figure 6.14.

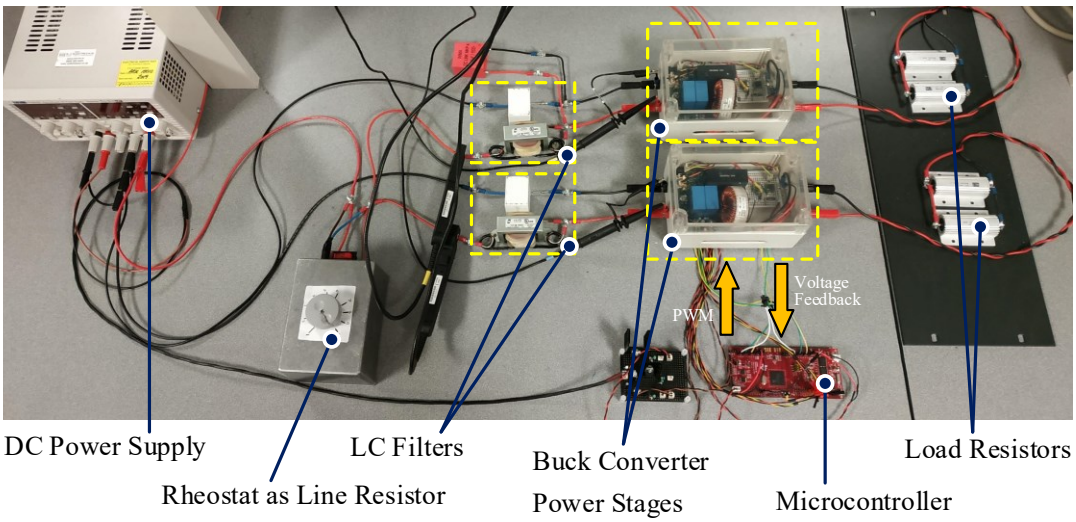

FIGURE 6.14 Test-bench of the experimental two-parallel connected cascaded power system.

During operation, each active load delivers equal power, controlled by adjusting reference voltage while keeping load resistance constant. A rheostat is located at the source-side and is used to mimic the effect of an uncertain line resistance.

The procedure used to verify the effect of R_{line} changes on stability of both systems is as follows. By varying power level, each system is initially set to operate near instability (within 5W) at a nominal value of R_{line} (0.25Ω). Subsequently, positive increments of R_{line} was done observe the effect on stability. Similarly, the same procedure was performed with decrements of R_{line}.

Experimental results using System 1 - closely matched input filters.

As shown in Figure 6.15, below, an increase in line resistance R_{line} from 0.25 to 0.5Ω causes instability. Voltage and current oscillations begin to occur in both of filters and indicate a circulating current exists between the two filters. This behaviour was predicted, and this is the effect of R_{line} contributing to coupling between filters.

Participation factor analysis confirms that the eigenvalue modes have contribution from the states of both filters, therefore an exchange of energy occurs between filters as indicated by Figure 6.16.

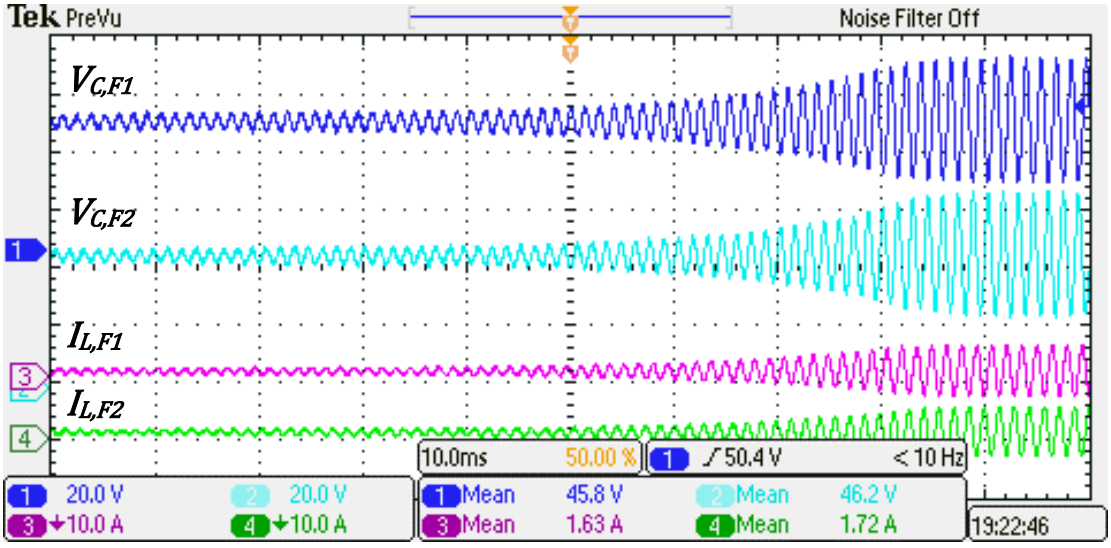

FIGURE 6.15 Filter waveforms of active loads in parallel connected to a resistive distribution line after increasing line resistance from 0.25Ω to 0.5Ω showing unstable oscillations. Operation under closely matched input filters (*System 1*).

This is in contrast to the instability occurring when decreasing R_{line} from 0.25 to 0.17Ω in Figure 6.17. Mode coupling does not occur as only one of the filters (filter 1) becomes unstable. Some ringing occurs in filter 2 (indicating some coupling) but quickly dissipates to a steady-state constant values as prior to the onset of instability, albeit with minor noise. Only source-load interaction instability of active load 1 occurs.

With closely matched filters, experimental results show and confirm the theory that instability occurs due to an increase in mode coupling and from conventional source-load interaction (CPL problem) without mode coupling. Caution is therefore warranted in uncertain LVDC DPSs as instability can occur with an increasing line resistance, dependent

on operating conditions and filter parameters. The coupling phenomenon can be responsible for a significant degradation of system stability margin.

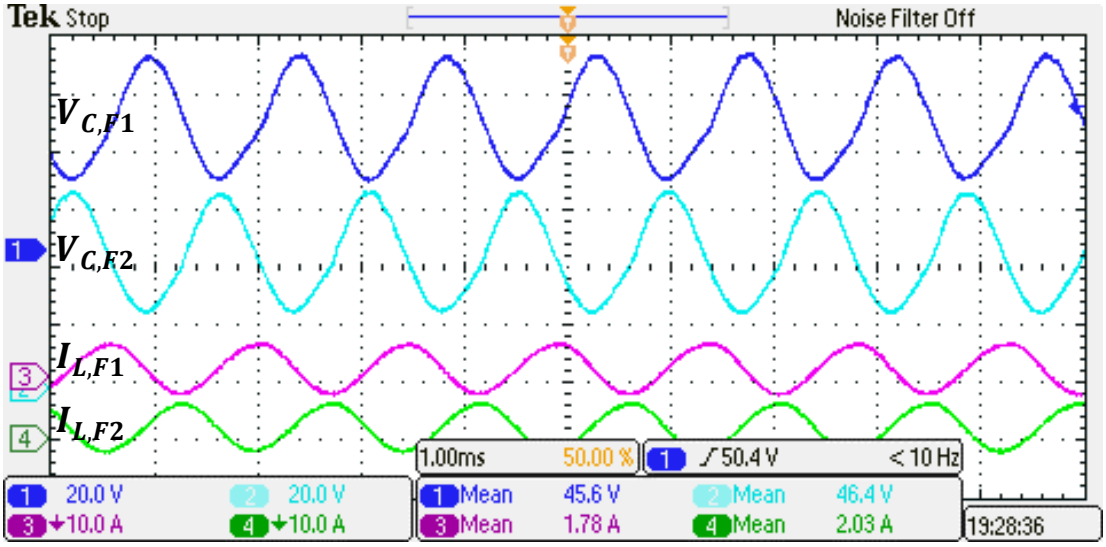

FIGURE 6.16 Zoomed snapshot of oscillations in Figure 6.15 indicating a coupling between filters and exchange of energy (i.e., as voltage of F_1 rises, the voltage in F_1 falls).

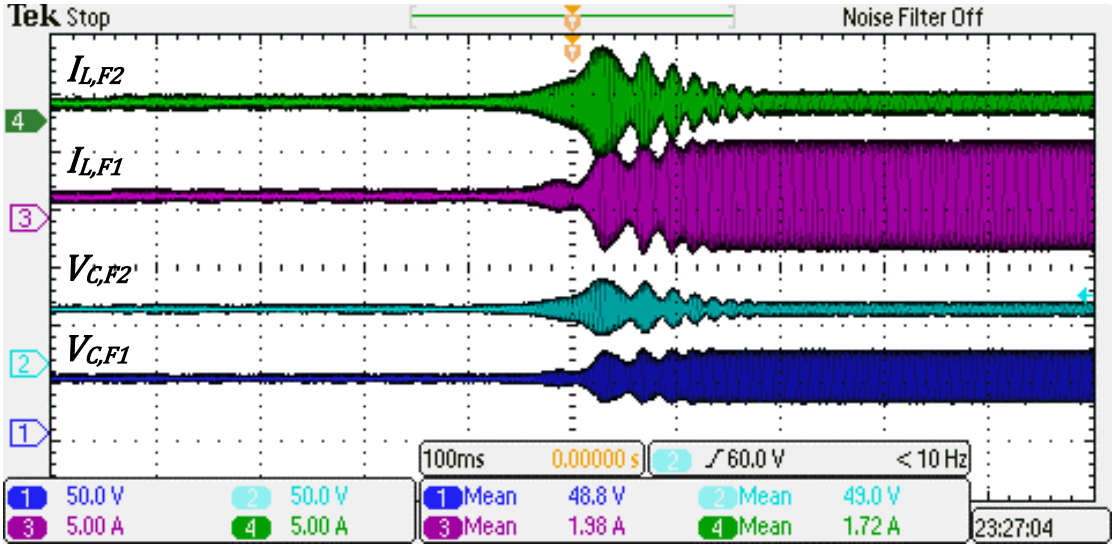

FIGURE 6.17 Filter waveforms of active loads in parallel connected to a resistive distribution line after decreasing line resistance from 0.25Ω to 0.17Ω showing unstable oscillations. Operation under closely matched input filters (*System 1*).

Experimental results using System 2 - well-separated input filters.

Figure 6.18 shows a decrease in in line resistance R_{line} from 0.25 to 0.1Ω resulting in instability of a single filter. The voltage and current waveforms of filter 1 begin to oscillate, while the voltage and current waveforms of filter 2 are unaffected.

As predicted by the analysis of the theoretical model in Figure 6.13(b), an increasing line resistance does not destabilise the system under the well-separated filter case. Observations showed no change in dynamics of the filter waveforms after increasing R_{line} from 0.25 to 0.55Ω. Therefore the line resistance can be used to stabilise the CPL instability phenomena of multiple parallel active loads, as shown by Wu et al. [51].

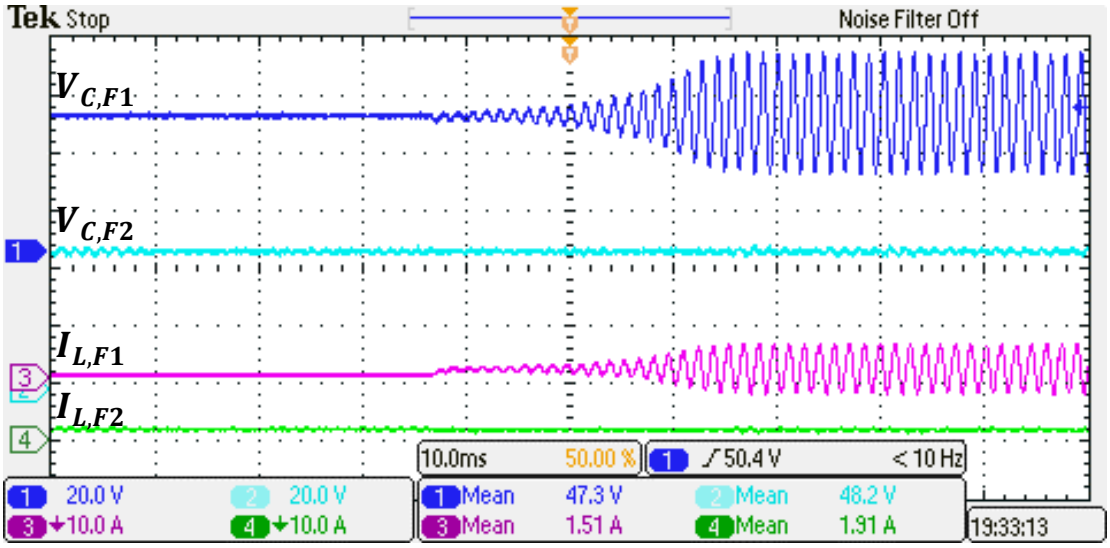

FIGURE 6.18 Filter waveforms of active loads in parallel connected to a resistive distribution line after decreasing line resistance from 0.25Ω to 0.1Ω. Unstable oscillations only occur in a single filter. Operation under well-separated input filters (*System 2*).

6.6 Summary

This chapter has investigated the resonant coupling phenomenon between parallel loads observed from the interaction analysis from Chapter 5. Linear modal coupling theory has been used to analyse this phenomenon. Divergence of eigenvalue loci between the complete system, the interconnected state-matrix model (ISSM), and the newly developed decoupled state-matrix model (DSSM) are used to quantify the effect of the coupling phenomenon, as well as predict the best and worst-case system damping. The apparent dichotomy in the effect of line resistance is finally resolved for the first time: line resistance can be apportioned to both subsystem damping and contribute to the coupling between subsystems.

The trajectory of eigenvalues under parametric perturbations is also shown to exhibit a mode swapping behaviour, where continuous eigenvalues exchange modal properties instead of diverging. To address this phenomenon, a mode-tracking approach based on participation factor analysis has been developed to ensure the conformity of eigenvalues to given subsystems.

Small-signal dynamics and sensitivity analysis of the system models are validated through experimental results, and several scenarios are presented demonstrating the impact of the mode coupling on small-signal stability boundaries. Caution is needed when line resistance is subject to uncertainty in systems with multiple parallel active loads. Finally, the dichotomy in the effect of line resistance is resolved experimentally: line resistance can influence both subsystem damping and contribution to coupling between subsystems.

Chapter 7

Conclusion

This chapter concludes the thesis with a summary of the research and discusses the original contributions and other key results. Recommendations on potential future research that extend this work is provided.

7.1 Thesis Summary

Power electronic converters play a vital role in the transition towards low voltage (LV)DC distributed power systems (DPSs) with the proliferation of renewables and end-use electrification. These systems are prone to oscillations from small disturbances due to interactions occurring between sources and loads—power electronic converters, with their tight regulation, introduce a negative impedance characteristic that may destabilize poorly damped oscillatory modes of the network. Recent evidence of the existence of modal interactions that may occur between loads gives rise to additional complexity in dynamic behaviour. As DPSs are subject to many inherent uncertainties and a wide range of operating conditions, different interaction phenomena may influence the small-signal dynamics in a nonlinear manner. Hence, with highly uncertain systems, extrapolating behaviour based on ideal and nominal models is shown to lead to a serious qualitative error.

Modelling and small-signal analysis of LVDC DPSs with uncertainties arising from parameter variability. A new automated tool, SymMIAL, has been developed to help synthesise high-fidelity state-space system models based on a modular approach. Symbolic linearisation is performed to ensure models represent small-signal dynamics

over all possible operating points. Probabilistic VBSA is presented as a useful technique to quantify the influence of parameters and their interactions over the full-range of uncertainties.

With this probabilistic sensitivity analysis technique and the newly developed modelling tools, the impact of uncertain parameters on the small-signal dynamics of LVDC DPSs has been comprehensively investigated on an example DC power system featuring two parallel filter-converter subsystems fed from a common point through a resistive line. For the first time, an apparent dichotomy in the effect of source-side line resistance is revealed through small-signal sensitivity analysis over multiple parameter variations—line resistance is shown to contribute to both positive and negative damping to filter modes, depending on precise operating conditions.

To resolve this contention, linear mode coupling theory was applied to the system state-space models. Contribution of line resistance to damping of modes is quantified and apportioned to the different interaction phenomena identified. Positive damping occurs through source-load interaction; and negative damping occurs through modal interaction. Our analytical results based on the theoretical models are validated against measured data from built experimental hardware LVDC DPSs and simulations.

7.2 Research Outcomes

The thesis has focused on the small-signal stability of power electronics dominated LVDC DPS and the analysis of interactions between system components. Compared to traditional power systems, DPSs are increasingly prone to small-signal instability risks with the introduction of fast control loop dynamics of power electronic interfaces interacting with poorly damped oscillatory modes of the distribution network. These systems are known to be subjected to many inherent uncertainties and a wide range of operating conditions. Interactions occurring between components may influence the small-signal stability in a nonlinear manner, therefore extrapolating behaviour based on nominal models in no longer sufficient for highly uncertain systems. Two types of interaction phenomena have been discussed in detail within the thesis: source-load interactions and modal interactions. Procedures to assess the impact of these interactions on stability have

been presented. In particular, modal coupling has been often neglected in literature, and this work furthers the understanding the nature of coupling in LVDC DPSs.

7.2.1 Original contributions

As part of this thesis the following journal paper was published, 'Influence of parametric uncertainties and their interactions on small-signal stability: A case example of parallel-connected active loads in a DC microgrid' [76] relating to the research further expanded upon in Chapter 5. This work was also presented at the 9th IET International Conference on Power Electronics, Machines and Drives (PEMD 2018).

The following list summarises the key original contributions of this thesis:

1. We have established a practical methodology for the analysis of parameter interactions and set of practical tools (SymMIAL) for fast and accurate probabilistic small-signal analysis of LVDC DPSs (Chapter 3 and Chapter 5). VBSA can now be applied to LVDC DPSs, with minimal effort in model development by the user, to study the influence of parametric uncertainties on small-signal system dynamics.
    a. The SymMIAL MATLAB toolbox was developed to automate the generation of nonlinear symbolic system models based on the input-output interconnection of different components. A library of component models was programmed to accurately describe the internal dynamics of power electronics interfaces with detailed circuit representation and feedback controllers.
    b. VBSA was selected based on a detailed review of the adjacent literature. Here we have implemented computation of sensitivity indices as part of SymMIAL toolbox to determine the most influential parameters and their interactions over specified uncertainty range.
2. We have firstly identified an apparent dichotomy in the effect of source-side resistance on small-signal stability in DC-based parallel-filter-converter systems. Source resistance has drastically different effect on small-

signal stability depending on operating condition: it can both increase stability margin or decrease stability margin.

3. This apparent dichotomy in the effect of line resistance is finally resolved: line resistance can be apportioned to both subsystem damping and contribute to the coupling between subsystems based on linear modal coupling theory presented in Chapter 6. Analytical results based on theoretical models have been validated against measured data from experimental hardware LVDC DPSs and simulations.
4. Based on this work, it was revealed that a mode-swapping phenomenon can occur when varying parameters of LVDC DPSs models due to modal coupling. This presented a challenge for tracking the relevant mode under investigation over parameter perturbation. To address this, a procedure based on sorting calculated eigenvalues to modes defined by participation factors is developed. Blindly selecting the right-most eigenvalue when calculating sensitivity indices as commonly done in literature is shown to be inappropriate when modal coupling is known to occur.

7.3 Suggestions for Future Research

The following list is intended to guide potential future research relating to the thesis themes of modelling, stability analysis, and parameter interactions under uncertainty in LVDC distributed power systems:

- Chapter 5 applied VBSA to power system models. Nevertheless, alternative global sensitivity analysis methods may provide certain advantages that have been not been fully considered in this thesis.

  VBSA may be inapplicable if the variances are shown not to be the most appropriate measure of the variability of the distribution of the input parameter. Other techniques, notability distribution-based sensitivity indices (e.g. [117]) provide sensitivity measures on the probability distribution themselves—i.e. quantifying the effect of the input's distribution on output's distribution. Likewise, computational considerations are of major concern when the number of uncertainties considered is

large. In the recent works related to bulk AC power systems, [118] introduce game theoretic approaches to the identification of influential parameters, and [119] apply a fast Gaussian process regression to learn and analyse the critical eigenvalue behaviours over uncertainties.

It is proposed that a comprehensive review and comparative evaluation of global sensitivity methods, as applied to highly uncertain LVDC DPSs models, is required to provide further justification for use of a specific technique (based on the review of literature we had concluded VBSA is highly suitable, however alternative method(s) may, in fact, be more appropriate for DC DPSs). Further emphasis could be made on specific metrics/criteria by which all these methods can be compared.

- In this work, VBSA was applied directly on the real-part of calculated model eigenvalues ($X \mapsto Re(\lambda)$). In VBSA, since it is a general method for studying any input-output relationship over uncertainty, the choice of output variable to be investigated is up to the user's discretion. Calculation of sensitivity indices on alternative outputs such as eigenvectors, participation factors, state variables, or derivative sensitivities is worth consideration for investigating the effects of interactions. Repeated Monte-Carlo simulation here would not be needed as the modal decomposition has already been done when computing the eigenvalues in our developed approach (see: Chapter 5).

  The focus of this work was strictly on parametric uncertainties under assumption of continuous uniform distributions. Firstly, parameter uncertainties may be correlated with each other, and more correctly characterised by other probability distribution functions (e.g. Gaussian) [120]. Secondly, DPSs are known to have significant input variability due to stochastic nature of renewables and is often increasingly studied in literature [113]. Further stability assessment under these types of uncertainties is becoming a crucial issue with the proliferation of renewables and probabilistic nature of (load) demands.

- Active damping techniques are based on implementing additional controller dynamics to mitigate instability phenomena without adding extra losses. Active damping methods are more selective in their action, they do not produce losses, but they are

also more sensitive to parameter uncertainties. The best placement of controller has so far not been established in literature, with different implementations on the source-side or the load-side when considering a simple cascaded system. Future work can focus on optimal placement in terms of observability/controllability, effectiveness of method under uncertainty, and the development of design-oriented procedures. Furthermore, given the unpredictable nature of parameter sensitivities during mode coupling, mitigation of mode coupling phenomena should be made a priority.

- Behaviour of mode coupling should be investigated in detail in the frequency domain to further understand complex dynamic behaviour. Parallel active loads may be represented as a reshaping of impedances, as shown below in Figure 7.1 with transfer functions in (7.1):

$$v_2(s) = v_1(s)/(1 + (Y_{in,1}(s)||Y_{in,2}(s))R_S(s)) \tag{7.1}$$

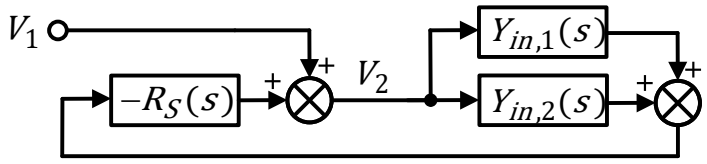

FIGURE 7.1 Frequency domain feedback with two parallel loads, $Y_{in,1}(s)$ and $Y_{in,2}(s)$, reshaped by source-side resistance, $R_S(s)$.

- The developed toolbox, SymMIAL, was developed for modelling only DC DPSs with common DC-DC converter topologies. In practical DPSs, more complex topologies will exist, such as double-ended push-pull, half-bridge (LLC-type) and full-bridge converters (resonant-type) [33]. These typically have elaborate control schemes including current-mode regulation, variable frequency, synchronous rectification, additional inner loop controllers [94], etc. When the LVDC DPS requires bidirectional power flows, dual active bridge converters (DAB) are often implemented [121] and could be studied. Tian et al. [121] investigated source-load

interaction of cascaded DAB with VSI under bidirectional conditions—forward and reverse power flow—showing that the stability margin differs between the conditions due to impedance interaction. Similarly, droop controllers are required for load current sharing in LVDC microgrid applications. These inherently modify impedances of converters which are already known to influence interaction phenomena [122].

LVDC DPSs often interface to conventional AC bulk systems or AC DPSs. One particular challenge is modelling these systems back to a common DC reference frame (i.e., dq-frame), especially when multiple system frequencies exist. A large proportion of active load are also DC-AC inverters for motor drives—induction or PMSM motor loads. This thesis could be extended by including modelling the AC-side for interaction and stability analysis. A number of existing works provide a foundation towards this effort [19], [94].

For future work, the SymMIAL toolbox could be extended towards a more comprehensive and scalable library of analytical models for source, load and network dynamics. This would enable identification of interaction effects for stability analysis using VBSA of a larger variety of future DPSs.

References

[1] IRENA (2019), "Innovation landscape for a renewable-powered future: Solutions to integrate variable renewables," 2019 [Online]. Available: https://www.irena.org/-/media/Files/IRENA/Agency/Publication/2019/Feb/IRENA_Innovation_Landscape_2019_report.pdf. [Accessed: 29-Nov-2019]

[2] IRENA (2019), "Global energy transformation: A roadmap to 2050," 2019 [Online]. Available: https://www.irena.org/-/media/Files/IRENA/Agency/Publication/2019/Apr/IRENA_Global_Energy_Transformation_2019.pdf. [Accessed: 04-Jan-2020]

[3] IET (2013), "Electricity Networks Handling a Shock to the System," 2013 [Online]. Available: https://www.theiet.org/media/2785/elec-shock-tech.pdf. [Accessed: 27-May-2018]

[4] T. Dragičević, J. C. Vasquez, J. M. Guerrero, and D. Škrlec, "Advanced LVDC Electrical Power Architectures and Microgrids: A step toward a new generation of power distribution networks," *IEEE Electrification Magazine*, vol. 2, no. 1, pp. 54–65, 2014.

[5] IEC (2017), "LVDC: electricity for the 21st century," 2017 [Online]. Available: https://www.iec.ch/technologyreport/pdf/IEC_TR-LVDC.pdf. [Accessed: 18-Nov-2019]

[6] International Energy Agency, *World Energy Outlook 2018*. 2018, p. 661 [Online]. Available: https://www.oecd-ilibrary.org/content/publication/weo-2018-en. [Accessed: 10-Jan-2020]

[7] World Commission on Environment and Development, *Our Common Future*. Oxford University Press, 1987 [Online]. Available: https://sustainabledevelopment.un.org/content/documents/5987our-common-future.pdf. [Accessed: 29-Nov-2020]

[8] Department for Business, Energy & Industrial Strategy, "Digest of United Kingdom Energy Statistics (DUKES)," 2018 [Online]. Available: https://www.gov.uk/government/statistics/digest-of-uk-energy-statistics-dukes-

2018-main-report. [Accessed: 04-Jan-2020]

[9] R. H. Lasseter, "MicroGrids," in *2002 IEEE Power Engineering Society Winter Meeting. Conference Proceedings (Cat. No.02CH37309)*, 2002, vol. 1, pp. 305–308 vol.1.

[10] S. Chowdhury and P. Crossley, *Microgrids and Active Distribution Networks*. London: Institution of Engineering and Technology, 2009.

[11] T. Dragičević, X. Lu, J. C. Vasquez, and J. M. Guerrero, "DC Microgrids—Part II: A Review of Power Architectures, Applications, and Standardization Issues," *IEEE Transactions on Power Electronics*, vol. 31, no. 5, pp. 3528–3549, 2016.

[12] S. Parhizi, H. Lotfi, A. Khodaei, and S. Bahramirad, "State of the Art in Research on Microgrids: A Review," *IEEE Access*, vol. 3, pp. 890–925, 2015.

[13] P. Karlsson and J. Svensson, "DC bus voltage control for a distributed power system," *IEEE Transactions on Power Electronics*, vol. 18, no. 6, pp. 1405–1412, 2003.

[14] P. Kundur, J. Paserba, and S. Vitet, "Overview on definition and classification of power system stability," in *CIGRE/IEEE PES International Symposium Quality and Security of Electric Power Delivery Systems, 2003. CIGRE/PES 2003.*, 2003, pp. 1–4.

[15] U. Markovic, O. Stanojev, E. Vrettos, P. Aristidou, and G. Hug, "Understanding Stability of Low-Inertia Systems," 2019 [Online]. Available: engrxiv.org/jwzrq. [Accessed: 10-Jan-2020]

[16] W. Du, X. Chen, and H. F. Wang, "Power System Electromechanical Oscillation Modes as Affected by Dynamic Interactions From Grid-Connected PMSGs for Wind Power Generation," *IEEE Transactions on Sustainable Energy*, vol. 8, no. 3, pp. 1301–1312, 2017.

[17] K. R. Padiyar, *Analysis of Subsynchronous Resonance in Power Systems*. Springer US, 1999 [Online]. Available: https://doi.org/10.1007%2F978-1-4615-5633-6. [Accessed: 10-May-2018]

[18] I. Dobson and E. Barocio, "Perturbations of weakly resonant power system electromechanical modes," *IEEE Transactions on Power Systems*, vol. 20, no. 1, pp. 330–337, 2005.

[19] N. Bottrell, M. Prodanovic, and T. C. Green, "Dynamic Stability of a Microgrid With an Active Load," *IEEE Transactions on Power Electronics*, vol. 28, no. 11, pp. 5107–5119, 2013.

[20] Z. Shuai, Y. Hu, Y. Peng, C. Tu, and Z. J. Shen, "Dynamic Stability Analysis of Synchronverter-Dominated Microgrid Based on Bifurcation Theory," *IEEE*

Transactions on Industrial Electronics, vol. 64, no. 9, pp. 7467–7477, 2017.

[21] M. Lu, X. Wang, P. C. Loh, and F. Blaabjerg, "Resonance Interaction of Multi-parallel Grid-Connected Inverters With LCL Filter," *IEEE Transactions on Power Electronics*, vol. 32, no. 2, pp. 894–899, 2017.

[22] H. Tao, Y. Zhou, G. Zhang, and Z. Zheng, "Parallel Resonance Mechanism Analysis and Suppression of Inductance-Capacitance-Inductance Grid-Connected Inverters," *Energies*, vol. 12, no. 9, p. 1656, 2019 [Online]. Available: http://dx.doi.org/10.3390/en12091656

[23] J. L. Agorreta, M. Borrega, J. López, and L. Marroyo, "Modeling and Control of N-Paralleled Grid-Connected Inverters With LCL Filter Coupled Due to Grid Impedance in PV Plants," *IEEE Transactions on Power Electronics*, vol. 26, no. 3, pp. 770–785, 2011.

[24] S. Whaite, B. Grainger, and A. Kwasinski, "Power Quality in DC Power Distribution Systems and Microgrids," *Energies*, vol. 8, no. 5, pp. 4378–4399, 2015 [Online]. Available: http://dx.doi.org/10.3390/en8054378

[25] D. M. Mitchell, "Power line filter design considerations for DC-DC converters," *IEEE Industry Applications Magazine*, vol. 5, no. 6, pp. 16–26, 1999.

[26] S. R. Huddy and J. D. Skufca, "Amplitude Death Solutions for Stabilization of DC Microgrids With Instantaneous Constant-Power Loads," *IEEE Transactions on Power Electronics*, vol. 28, no. 1, pp. 247–253, 2013.

[27] M. Wu and D. D. Lu, "Active stabilization methods of electric power systems with constant power loads: a review," *Journal of Modern Power Systems and Clean Energy*, vol. 2, no. 3, pp. 233–243, 2014.

[28] R. W. Erickson, "Optimal single resistors damping of input filters," in *APEC '99. Fourteenth Annual Applied Power Electronics Conference and Exposition*, 1999, vol. 2, pp. 1073–1079 vol.2.

[29] M. K. AL-Nussairi, R. Bayindir, P. Sanjeevikumar, L. Mihet-Popa, and P. Siano, "Constant power loads (CPL) with microgrids: problem definition, stability analysis and compensation techniques," *Energies*, vol. 10, no. 10, p. 1656, 2017.

[30] A. Emadi, A. Khaligh, C. H. Rivetta, and G. A. Williamson, "Constant power loads and negative impedance instability in automotive systems: definition, modeling, stability, and control of power electronic converters and motor drives," *IEEE Transactions on Vehicular Technology*, vol. 55, no. 4, pp. 1112–1125, 2006.

[31] S. Singh, A. R. Gautam, and D. Fulwani, "Constant power loads and their effects in DC distributed power systems: A review," *Renewable and Sustainable Energy Reviews*, vol. 72, pp. 407 – 421, 2017 [Online]. Available:

http://www.sciencedirect.com/science/article/pii/S1364032117300412

[32] R. D. Middlebrook, “Small-signal modeling of pulse-width modulated switched-mode power converters,” *Proceedings of the IEEE*, vol. 76, no. 4, pp. 343–354, 1988.

[33] R. W. Erickson and D. Maksimovic, *Fundamentals of Power Electronics*, 2ed ed. Springer, 2001.

[34] M. Cupelli, L. Zhu, and A. Monti, “Why Ideal Constant Power Loads Are Not the Worst Case Condition From a Control Standpoint,” *IEEE Transactions on Smart Grid*, vol. 6, no. 6, pp. 2596–2606, 2015.

[35] N. O. Sokal, “System oscillations from negative input resistance at power input port of switching-mode regulator, amplifier, DC/DC converter, or DC/DC inverter,” in *1973 IEEE Power Electronics Specialists Conference*, 1973, pp. 138–140.

[36] R. D. Middlebrook, “Input Filter Considerations in Design and Application of Switching Regulators,” in *IEEE Industry Applications Society Annual Meeting, October 11-14*, 1976.

[37] R. D. Middlebrook, “Design Techniques for Preventing Input-Filter Oscillations in Switched-Mode Regulators,” in *Proceedings of Powercon 5, The Fifth National Solid-State Power Conversion Conference*, 1978.

[38] I. Dobson and E. Barocio, “Perturbations of weakly resonant power system electromechanical modes,” in *2003 IEEE Bologna PowerTech Conference Proceedings*, 2003.

[39] W. Du, Q. Fu, H. Wang, and Y. Wang, “Concept of Modal Repulsion for Examining the Subsynchronous Oscillations Caused by Wind Farms in Power Systems,” *IEEE Transactions on Power Systems*, vol. 34, no. 1, pp. 518–526, 2019.

[40] A. W. Leissa, “On a curve veering aberration,” *Zeitschrift für angewandte Mathematik und Physik ZAMP*, vol. 25, no. 1, pp. 99–111, 1974 [Online]. Available: https://doi.org/10.1007%2Fbf01602113

[41] K. R. Schab, J. M. Outwater, M. W. Young, and J. T. Bernhard, “Eigenvalue Crossing Avoidance in Characteristic Modes,” *IEEE Transactions on Antennas and Propagation*, vol. 64, no. 7, pp. 2617–2627, 2016.

[42] N. C. Perkins and C. D. Mote, “Comments on curve veering in eigenvalue problems,” *Journal of Sound and Vibration*, vol. 106, no. 3, pp. 451–463, 1986 [Online]. Available: https://doi.org/10.1016%2F0022-460x%2886%2990191-4

[43] J. He, Y. W. Li, D. Bosnjak, and B. Harris, "Investigation and Active Damping of Multiple Resonances in a Parallel-Inverter-Based Microgrid," *IEEE Transactions on Power Electronics*, vol. 28, no. 1, pp. 234–246, 2013.

[44] Q. Qian, S. Xie, L. Huang, J. Xu, Z. Zhang, and B. Zhang, "Harmonic Suppression and Stability Enhancement for Parallel Multiple Grid-Connected Inverters Based on Passive Inverter Output Impedance," *IEEE Transactions on Industrial Electronics*, vol. 64, no. 9, pp. 7587–7598, 2017.

[45] C. Wan, M. Huang, C. K. Tse, and X. Ruan, "Effects of Interaction of Power Converters Coupled via Power Grid: A Design-Oriented Study," *IEEE Transactions on Power Electronics*, vol. 30, no. 7, pp. 3589–3600, 2015.

[46] W. Du, X. Chen, and H. F. Wang, "Strong Dynamic Interactions of Grid-Connected DFIGs With Power Systems Caused by Modal Coupling," *IEEE Transactions on Power Systems*, vol. 32, no. 6, pp. 4386–4397, 2017.

[47] C. Yu *et al.*, "Modeling and Resonance Analysis of Multiparallel Inverters System Under Asynchronous Carriers Conditions," *IEEE Transactions on Power Electronics*, vol. 32, no. 4, pp. 3192–3205, 2017.

[48] I. Dobson, "Strong resonance effects in normal form analysis and subsynchronous resonance," in *Bulk Power System Dynamics and Control V, August 26-31*, 2001.

[49] M. Klein, G. J. Rogers, and P. Kundur, "A fundamental study of inter-area oscillations in power systems," *IEEE Transactions on Power Systems*, vol. 6, no. 3, pp. 914–921, 1991.

[50] I. Dobson, J. Zhang, S. Greene, H. Engdahl, and P. W. Sauer, "Is strong modal resonance a precursor to power system oscillations?," *IEEE Transactions on Circuits and Systems I: Fundamental Theory and Applications*, vol. 48, no. 3, pp. 340–349, 2001.

[51] M. Wu and D. D. Lu, "A Novel Stabilization Method of LC Input Filter With Constant Power Loads Without Load Performance Compromise in DC Microgrids," *IEEE Transactions on Industrial Electronics*, vol. 62, no. 7, pp. 4552–4562, 2015.

[52] A. A. A. Radwan and Y. A. I. Mohamed, "Linear Active Stabilization of Converter-Dominated DC Microgrids," *IEEE Transactions on Smart Grid*, vol. 3, no. 1, pp. 203–216, 2012.

[53] S. Sumsurooah, M. Odavic, S. Bozhko, and D. Boroyevich, "Robust Stability Analysis of a DC/DC Buck Converter Under Multiple Parametric Uncertainties," *IEEE Transactions on Power Electronics*, vol. 33, no. 6, pp. 5426–5441, 2018.

[54] J. Elizondo, R. Y. Zhang, J. K. White, and J. L. Kirtley, "Robust small signal stability for microgrids under uncertainty," in *2015 IEEE 6th International Symposium on Power Electronics for Distributed Generation Systems (PEDG)*, 2015, pp. 1–8.

[55] D. Marx, P. Magne, B. Nahid-Mobarakeh, S. Pierfederici, and B. Davat, "Large Signal Stability Analysis Tools in DC Power Systems With Constant Power Loads and Variable Power Loads—A Review," *IEEE Transactions on Power Electronics*, vol. 27, no. 4, pp. 1773–1787, 2012.

[56] M. Belkhayat, "Stability criteria for AC power systems with regulated loads," 1997 [Online]. Available: https://docs.lib.purdue.edu/dissertations/AAI9821703/

[57] A. Griffo and J. Wang, "Large Signal Stability Analysis of 'More Electric' Aircraft Power Systems with Constant Power Loads," *IEEE Transactions on Aerospace and Electronic Systems*, vol. 48, no. 1, pp. 477–489, 2012.

[58] A. B. Iskakov and I. B. Yadykin, "Lyapunov modal analysis and participation factors with applications to small-signal stability of power systems," 2019.

[59] S. Sumsurooah, M. Odavic, and D. Boroyevich, "Modelling and Robust Stability Analysis of Uncertain Systems," in *Proceedings of the 2013 Grand Challenges on Modeling and Simulation Conference*, 2013.

[60] S. Sumsurooah, M. Odavic, and S. Bozhko, "μ Approach to Robust Stability Domains in the Space of Parametric Uncertainties for a Power System With Ideal CPL," *IEEE Transactions on Power Electronics*, vol. 33, no. 1, pp. 833–844, 2018.

[61] S. Sumsurooah, M. Odavic, and S. Bozhko, "A Modeling Methodology for Robust Stability Analysis of Nonlinear Electrical Power Systems Under Parameter Uncertainties," *IEEE Transactions on Industry Applications*, vol. 52, no. 5, pp. 4416–4425, 2016.

[62] T. Pavlovic, T. Bjazic, and Z. Ban, "Simplified Averaged Models of DC–DC Power Converters Suitable for Controller Design and Microgrid Simulation," *IEEE Transactions on Power Electronics*, vol. 28, no. 7, pp. 3266–3275, 2013.

[63] S. D. Sudhoff, S. F. Glover, P. T. Lamm, D. H. Schmucker, and D. E. Delisle, "Admittance space stability analysis of power electronic systems," *IEEE Transactions on Aerospace and Electronic Systems*, vol. 36, no. 3, pp. 965–973, 2000.

[64] A. Riccobono and E. Santi, "Comprehensive Review of Stability Criteria for DC Power Distribution Systems," *IEEE Transactions on Industry Applications*, vol. 50, no. 5, pp. 3525–3535, 2014.

[65] X. Zhang, X. Ruan, and C. K. Tse, "Impedance-Based Local Stability Criterion for DC Distributed Power Systems," *IEEE Transactions on Circuits and Systems*

I: Regular Papers, vol. 62, no. 3, pp. 916–925, 2015.

[66] T. Dragičević, X. Lu, J. C. Vasquez, and J. M. Guerrero, "DC Microgrids—Part I: A Review of Control Strategies and Stabilization Techniques," *IEEE Transactions on Power Electronics*, vol. 31, no. 7, pp. 4876–4891, 2016.

[67] P. W. Sauer and M. A. Pai, *Power System Dynamics and Stability*. Upper Saddle River, N.J.: Prentice Hall, 1998.

[68] X. Wen and V. Ajjarapu, "Application of a novel eigenvalue trajectory tracing method to identify both oscillatory stability margin and damping margin," *IEEE Transactions on Power Systems*, vol. 21, no. 2, pp. 817–824, 2006.

[69] C. I. Hill, K. Areerak, T. Yang, S. Bozhko, and M. Odavic, "Automated stability assessment of more electric aircraft electrical power systems," in *2015 International Conference on Electrical Systems for Aircraft, Railway, Ship Propulsion and Road Vehicles (ESARS)*, 2015, pp. 1–6.

[70] R. Preece and J. V. Milanović, "Assessing the Applicability of Uncertainty Importance Measures for Power System Studies," *IEEE Transactions on Power Systems*, vol. 31, no. 3, pp. 2076–2084, 2016.

[71] R. Preece and J. V. Milanović, "Efficient Estimation of the Probability of Small-Disturbance Instability of Large Uncertain Power Systems," *IEEE Transactions on Power Systems*, vol. 31, no. 2, pp. 1063–1072, 2016.

[72] F. Gao, X. Zheng, S. Bozhko, C. I. Hill, and G. Asher, "Modal Analysis of a PMSG-Based DC Electrical Power System in the More Electric Aircraft Using Eigenvalues Sensitivity," *IEEE Transactions on Transportation Electrification*, vol. 1, no. 1, pp. 65–76, 2015.

[73] A. Saltelli, S. Tarantola, F. Campolongo, and M. Ratto, *Sensitivity Analysis in Practice: A Guide to Assessing Scientific Models*. USA: Halsted Press, 2004.

[74] A. Saltelli, P. Annoni, I. Azzini, F. Campolongo, M. Ratto, and S. Tarantola, "Variance based sensitivity analysis of model output. Design and estimator for the total sensitivity index," *Computer Physics Communications*, vol. 181, no. 2, pp. 259 – 270, 2010 [Online]. Available: http://www.sciencedirect.com/science/article/pii/S0010465509003087

[75] A. Saltelli, "Making best use of model evaluations to compute sensitivity indices," *Computer Physics Communications*, vol. 145, no. 2, pp. 280 – 297, 2002 [Online]. Available: http://www.sciencedirect.com/science/article/pii/S0010465502002801

[76] N. Nesterov and M. Odavic, "Influence of parametric uncertainties and their interactions on small-signal stability: A case example of parallel-connected active loads in a DC microgrid," *The Journal of Engineering*, vol. 2019, no. 17, pp.

4315–4320, 2019.

[77] T. Williams, *EMC for Product Designers (Fifth Edition)*, Fifth Edition. Newnes, 2017.

[78] R. D. Middlebrook and S. Cuk, "A general unified approach to modelling switching-converter power stages," in *1976 IEEE Power Electronics Specialists Conference*, 1976, pp. 18–34.

[79] D. F. D. Tan, "A Review of Immediate Bus Architecture: A System Perspective," *IEEE Journal of Emerging and Selected Topics in Power Electronics*, vol. 2, no. 3, pp. 363–373, 2014.

[80] J. C. Doyle, B. A. Francis, and A. R. Tannenbaum, *Feedback Control Theory*. Prentice Hall Professional Technical Reference, 1991.

[81] A. Kwasinski and C. N. Onwuchekwa, "Dynamic Behavior and Stabilization of DC Microgrids With Instantaneous Constant-Power Loads," *IEEE Transactions on Power Electronics*, vol. 26, no. 3, pp. 822–834, 2011.

[82] L. Corradini, P. Mattavelli, M. Corradin, and F. Polo, "Analysis of Parallel Operation of Uninterruptible Power Supplies Loaded Through Long Wiring Cables," *IEEE Transactions on Power Electronics*, vol. 25, no. 4, pp. 1046–1054, 2010.

[83] J. Sun, "Impedance-Based Stability Criterion for Grid-Connected Inverters," *IEEE Transactions on Power Electronics*, vol. 26, no. 11, pp. 3075–3078, 2011.

[84] A. M. Rahimi and A. Emadi, "An Analytical Investigation of DC/DC Power Electronic Converters With Constant Power Loads in Vehicular Power Systems," *IEEE Transactions on Vehicular Technology*, vol. 58, no. 6, pp. 2689–2702, 2009.

[85] H. Mosskull, M. Jansson, and T. Trostén, "Optimal line current limitation of CPLs fed through input LC-filters," *Control Engineering Practice*, vol. 89, pp. 43 – 55, 2019 [Online]. Available: http://www.sciencedirect.com/science/article/pii/S0967066118304799

[86] V. Sanna, "Methodology for Dynamic Stability and Robustness Analysis of Commercial-Power-Module-Based DC-Distributed Systems," 2015 [Online]. Available: https://trepo.tuni.fi//handle/10024/115139. [Accessed: 01-Dec-2017]

[87] A. E. Aroudi, D. Giaouris, H. H. Iu, and I. A. Hiskens, "A Review on Stability Analysis Methods for Switching Mode Power Converters," *IEEE Journal on Emerging and Selected Topics in Circuits and Systems*, vol. 5, no. 3, pp. 302–315, 2015.

[88] W. Du, Y. Wang, H. Wang, and Q. Fu, "Concept of Modal Repulsion for Examining the Sub-Synchronous Oscillations in Power Systems," *IEEE Transactions on Power Systems*, vol. 33, no. 4, pp. 4614–4624, 2018.

[89] A. P. Seyranian and A. A. Mailybaev, *Multiparameter Stability Theory with Mechanical Applications*. World Scientific, 2003.

[90] W. Du, Q. Fu, and H. Wang, "Method of Open-Loop Modal Analysis for Examining the Subsynchronous Interactions Introduced by VSC Control in an MTDC/AC System," *IEEE Transactions on Power Delivery*, vol. 33, no. 2, pp. 840–850, 2018.

[91] V. Auvray, I. Dobson, and L. Wehenkel, "Modifying eigenvalue interactions near weak resonance," in *2004 IEEE International Symposium on Circuits and Systems (IEEE Cat. No.04CH37512)*, 2004, vol. 5, pp. V–V.

[92] X. Wang, F. Blaabjerg, and P. C. Loh, "Passivity-Based Stability Analysis and Damping Injection for Multiparalleled VSCs with LCL Filters," *IEEE Transactions on Power Electronics*, vol. 32, no. 11, pp. 8922–8935, 2017.

[93] N. Bottrell, "Small-signal Analysis of Active Loads and Large-signal Analysis of Faults in Inverter Interfaced Microgrid Applications," 2014.

[94] N. Pogaku, M. Prodanovic, and T. C. Green, "Modeling, Analysis and Testing of Autonomous Operation of an Inverter-Based Microgrid," *IEEE Transactions on Power Electronics*, vol. 22, no. 2, pp. 613–625, 2007.

[95] M. Wu, D. D. Lu, and C. K. Tse, "Direct and Optimal Linear Active Methods for Stabilization of LC Input Filters and DC/DC Converters Under Voltage Mode Control," *IEEE Journal on Emerging and Selected Topics in Circuits and Systems*, vol. 5, no. 3, pp. 402–412, 2015.

[96] G. Herbst, "A Building-Block Approach to State-Space Modeling of DC-DC Converter Systems," *J — Multidisciplinary Scientific Journal*, vol. 2, no. 3, pp. 247–267, 2019 [Online]. Available: https://www.mdpi.com/2571-8800/2/3/18

[97] R. L. Williams and D. A. Lawrence, *Linear State-Space Control Systems*. John Wiley & Sons, Ltd, 2007 [Online]. Available: https://onlinelibrary.wiley.com/doi/abs/10.1002/9780470117873

[98] A. M. I. Mohamad and Y. A. I. Mohamed, "Analysis and Mitigation of Interaction Dynamics in Active DC Distribution Systems With Positive Feedback Islanding Detection Schemes," *IEEE Transactions on Power Electronics*, vol. 33, no. 3, pp. 2751–2773, 2018.

[99] A. Emadi, "Modeling of power electronic loads in AC distribution systems using the generalized State-space averaging method," *IEEE Transactions on Industrial*

Electronics, vol. 51, no. 5, pp. 992–1000, 2004.

[100] S. Lee, "Demystifying Type II and Type III Compensators Using OpAmp and OTA for DC/DC Converters," *Texas Instruments Application Report*, 2014 [Online]. Available: https://www.ti.com/lit/an/slva662/slva662.pdf. [Accessed: 01-Jun-2017]

[101] S.-H. Tsai, Y.-K. Wu, and C.-Y. Lee, "A Critical Eigenvalues Tracing Method for the Small Signal Stability Analysis of Power Systems," *Energy and Power Engineering*, vol. 05, pp. 677–682, 2013.

[102] B. Iooss and P. Lemaître, "A review on global sensitivity analysis methods," in *Uncertainty management in Simulation-Optimization of Complex Systems: Algorithms and Applications*, C. Meloni and G. Dellino, Ed. Springer, 2015 [Online]. Available: https://hal.archives-ouvertes.fr/hal-00975701

[103] I. M. Sobol′, "Global sensitivity indices for nonlinear mathematical models and their Monte Carlo estimates," *Mathematics and Computers in Simulation*, vol. 55, no. 1, pp. 271 – 280, 2001 [Online]. Available: http://www.sciencedirect.com/science/article/pii/S0378475400002706

[104] K. N. Hasan, R. Preece, and J. V. Milanović, "Priority Ranking of Critical Uncertainties Affecting Small-Disturbance Stability Using Sensitivity Analysis Techniques," *IEEE Transactions on Power Systems*, vol. 32, no. 4, pp. 2629–2639, 2017.

[105] I. M. Sobol', "Theorems and examples on high dimensional model representation," *Reliability Engineering & System Safety*, vol. 79, no. 2, pp. 187 – 193, 2003 [Online]. Available: http://www.sciencedirect.com/science/article/pii/S0951832002002296

[106] I. M. Sobol, "Sensitivity Estimates for Nonlinear Mathematical Models," 1993.

[107] T. Homma and A. Saltelli, "Importance measures in global sensitivity analysis of nonlinear models," *Reliability Engineering & System Safety*, vol. 52, no. 1, pp. 1 – 17, 1996 [Online]. Available: http://www.sciencedirect.com/science/article/pii/0951832096000026

[108] S. Kucherenko, D. Albrecht, and A. Saltelli, "Exploring multi-dimensional spaces: a Comparison of Latin Hypercube and Quasi Monte Carlo Sampling Techniques," 2015.

[109] A. Janon, T. Klein, A. Lagnoux, M. Nodet, and C. Prieur, "Asymptotic normality and efficiency of two Sobol index estimators," *ESAIM: Probability and Statistics*, vol. 18, pp. 342–364, 2014 [Online]. Available: http://dx.doi.org/10.1051/PS/2013040

[110] W. Du, J. Bi, J. Cao, and H. F. Wang, "A Method to Examine the Impact of Grid Connection of the DFIGs on Power System Electromechanical Oscillation Modes," *IEEE Transactions on Power Systems*, vol. 31, no. 5, pp. 3775–3784, 2016.

[111] C. Luo and V. Ajjarapu, "Identification of interacting power system dynamic phenomena via continuation of invariant subspaces," *16th Power Systems Computation Conference, PSCC 2008*, 2008.

[112] D. Afolabi, "Modal Interaction in Linear Dynamic Systems Near Degenerate Modes," 1991.

[113] S. Q. Bu, W. Du, H. F. Wang, Z. Chen, L. Y. Xiao, and H. F. Li, "Probabilistic Analysis of Small-Signal Stability of Large-Scale Power Systems as Affected by Penetration of Wind Generation," *IEEE Transactions on Power Systems*, vol. 27, no. 2, pp. 762–770, 2012.

[114] D. Yang and V. Ajjarapu, "Tracing of critical eigenvalues for power system analysis via continuation of invariant subspaces and projected Arnoldi method," in *IEEE Power Engineering Society General Meeting, 2005*, 2005, pp. 1630–1636 Vol. 2.

[115] C. Luo and V. Ajjarapu, "A New Method of Eigenvalue Sensitivity Calculation Using Continuation of Invariant Subspaces," *IEEE Transactions on Power Systems*, vol. 26, no. 1, pp. 479–480, 2011.

[116] H. K. Khalil, *Nonlinear systems; 3rd ed.* Upper Saddle River, NJ: Prentice-Hall, 2002.

[117] E. Borgonovo, "A new uncertainty importance measure," *Reliability Engineering & System Safety*, vol. 92, no. 6, pp. 771 – 784, 2007 [Online]. Available: http://www.sciencedirect.com/science/article/pii/S0951832006000883

[118] K. N. Hasan, R. Preece, and J. V. Milanović, "Application of game theoretic approaches for identification of critical parameters affecting power system small-disturbance stability," *International Journal of Electrical Power & Energy Systems*, vol. 97, pp. 344 – 352, 2018 [Online]. Available: http://www.sciencedirect.com/science/article/pii/S014206151732080X

[119] P. Pareek and H. D. Nguyen, "Probabilistic Robust Small-Signal Stability Framework using Gaussian Process Learning," 2019.

[120] S. Banerjee and G. C. Verghese, *Nonlinear Phenomena in Power Electronics: Bifurcations, Chaos, Control, and Applications*. Wiley, 2001.

[121] Y. Tian, F. Deng, Z. Chen, X. Sun, and Y. Hu, "Impedance interaction modeling and analysis for bidirectional cascaded converters," in *2015 9th International Conference on Power Electronics and ECCE Asia (ICPE-ECCE Asia)*, 2015, pp.

2064–2071.

[122] F. Gao *et al.*, “Comparative Stability Analysis of Droop Control Approaches in Voltage-Source-Converter-Based DC Microgrids,” *IEEE Transactions on Power Electronics*, vol. 32, no. 3, pp. 2395–2415, 2017.

[123] IEC (2009), “IEC 60038:2009, IEC standard voltages,” Geneva, Switzerland, 2009.

Appendix A – Source Code Blocks for the SymMIAL Toolbox

A.1 Source Code Overview

This Appendix provides an overview of the MATLAB implementation of the Sym-MIAL toolbox. Code snippets are included here to describe the automated model generation and merging procedures.

Table A.1 provides details of the publicly available repository for the source code and examples for the developed *SymMIAL* MATLAB toolbox.

Table A.1 SymMIAL code repository summary

Title	**Symbolic Model Interconnection and Linearisation**
Code version	SymMIAL v0.8
License	MIT
Repository link	https://github.com/nestn-shf/SymMIAL
Software code languages	Verified under version MATLAB 9.7 R2019b
Requirements & dependencies	MATLAB, Symbolic Math Toolbox, Control System Toolbox, System Identification Toolbox
Developer documentation	https://github.com/nestn-shf/SymMIAL/wiki

A.2 DEFINING SYMBOLIC SUBSYSTEM MODELS

subsystem_SynchronousBuck.m

```
function newSynchronousBuck = subsystem_SynchronousBuck(index)

%% Generate identifiers:
% identifiers
s.ident.base = 'SBUCK';
s.ident.index = index;
s.ident.name = sprintf('%s_%d', s.ident.base, s.ident.index);

% Helper fields
s.numberof.states = 2;
s.numberof.inputs = 3;
s.numberof.outputs = 2;
s.numberof.elements = 6;

%% Generate symbolic identifiers for states inputs outputs elements

% states:
s.ident.state{1,1} = sprintf('VC_%s', s.ident.name);
s.ident.state{1,2} = 'real';
s.ident.state{2,1} = sprintf('IL_%s', s.ident.name);
s.ident.state{2,2} = 'real';

s.ident.diffstate{1,1} = sprintf('diffVC_%s', s.ident.name);
s.ident.diffstate{1,2} = 'real';
s.ident.diffstate{2,1} = sprintf('diffIL_%s', s.ident.name);
s.ident.diffstate{2,2} = 'real';

% inputs:
s.ident.input{1,1} = sprintf('V1_%s', s.ident.name);
s.ident.input{1,2} = 'real';
s.ident.input{2,1} = sprintf('I2_%s', s.ident.name);
s.ident.input{2,2} = 'real';
s.ident.input{3,1} = sprintf('D_%s', s.ident.name);
s.ident.input{3,2} = 'positive';

% output:
s.ident.output{1,1} = sprintf('V2_%s', s.ident.name);
s.ident.output{1,2} = 'real';
s.ident.output{2,1} = sprintf('I1_%s', s.ident.name);
s.ident.output{2,2} = 'real';

% elements:
s.ident.element{1,1} = sprintf('C_%s', s.ident.name);
s.ident.element{2,1} = sprintf('L_%s', s.ident.name);
s.ident.element{3,1} = sprintf('RL_%s', s.ident.name);
s.ident.element{4,1} = sprintf('RC_%s', s.ident.name);
s.ident.element{5,1} = sprintf('RDSONQ1_%s', s.ident.name);
s.ident.element{6,1} = sprintf('RDSONQ2_%s', s.ident.name);

for i = 1:(s.numberof.elements)
   s.ident.element{i,2} = 'positive';

end
```

```
%% Generate symbolic workspace variables
for i = 1:(s.numberof.states)
   eval(sprintf('syms %s %s', s.ident.state{i,1}, s.ident.state{i,2}));
   eval(sprintf('syms %s %s', s.ident.diffstate{i,1}, s.ident.diffstate{i,2}));
end

for i = 1:(s.numberof.inputs)
   eval(sprintf('syms %s %s', s.ident.input{i,1}, s.ident.input{i,2}));
end

for i = 1:(s.numberof.outputs)
   eval(sprintf('syms %s %s', s.ident.output{i,1}, s.ident.output{i,2}));
end

for i = 1:(s.numberof.elements)
   eval(sprintf('syms %s %s', s.ident.element{i,1}, s.ident.element{i,2}));
end

%% Symbolic vectors
s.vector.state{1,1} = eval(sprintf(s.ident.state{1,1}));
s.vector.state{2,1} = eval(sprintf(s.ident.state{2,1}));

s.vector.diffstate{1,1} = eval(sprintf(s.ident.diffstate{1,1}));
s.vector.diffstate{2,1} = eval(sprintf(s.ident.diffstate{2,1}));

s.vector.input{1,1} = eval(sprintf(s.ident.input{1,1}));
s.vector.input{2,1} = eval(sprintf(s.ident.input{2,1}));
s.vector.input{3,1} = eval(sprintf(s.ident.input{3,1}));

s.vector.output{1,1} = eval(sprintf(s.ident.output{1,1}));
s.vector.output{2,1} = eval(sprintf(s.ident.output{2,1}));

for i = 1:(s.numberof.elements)
   s.vector.elements{i,1} = eval(sprintf(s.ident.element{i,1}));
end

%% Governing Equations:
   %% Differential Equation 1:
str = sprintf('%s == (%s - %s)/(%s)', ...
            s.ident.diffstate{1,1}, ...
            s.ident.state{2,1}, ...
            s.ident.input{2,1}, ...
            s.ident.element{1,1});

s.equation.differential{1,1} = eval(str);

if((exist('debug','var') == 1) && (debug == true))
   fprintf('%s system differential equation 1:   %s\n', s.ident.name, char(s.equation.differential{1,1}));
end

   %% Differential Equation 2:
str = sprintf('%s == (-%s - %s*(%s+%s+%s) + %s*%s + %s*%s + %s*%s*(%s-%s))/(%s)', ...
            s.ident.diffstate{2,1}, ...
            s.ident.state{1,1}, ...
            s.ident.state{2,1}, ...
              s.ident.element{6,1}, ...
              s.ident.element{3,1}, ...
              s.ident.element{4,1}, ...
            s.ident.input{1,1}, ...
              s.ident.input{3,1}, ...
            s.ident.input{2,1}, ...
              s.ident.element{4,1}, ...
            s.ident.state{2,1}, ...
```

```
            s.ident.input{3,1}, ...
            s.ident.element{6,1}, ...
            s.ident.element{5,1}, ...
          s.ident.element{2,1});

s.equation.differential{2,1} = eval(str);

if((exist('debug','var') == 1) && (debug == true))
   fprintf('%s system differential equation 2:   %s\n', s.ident.name, char(s.equation.differential{2,1}));
end

   %% Output Equation 1:
str = sprintf('%s == (%s + %s*%s - %s*%s)', ...
          s.ident.output{1,1}, ...
          s.ident.state{1,1}, ...
          s.ident.state{2,1}, ...
            s.ident.element{4,1}, ...
          s.ident.input{2,1}, ...
            s.ident.element{4,1});

s.equation.output{1,1} = eval(str);

if((exist('debug','var') == 1) && (debug == true))
   fprintf('%s system output equation 1:   %s\n', s.ident.name, char(s.equation.output{1,1}));
end

   %% Output Equation 2:
str = sprintf('%s == %s*%s', ...
          s.ident.output{2,1}, ...
          s.ident.state{2,1}, ...
          s.ident.input{3,1});

s.equation.output{2,1} = eval(str);

if((exist('debug','var') == 1) && (debug == true))
   fprintf('%s system output equation 2:   %s\n', s.ident.name, char(s.equation.output{2,1}));
end

%% Return structure containing new subsystem
newSynchronousBuck = s;
```

subsystem_3StateController.m

```
function new3StateControl = subsystem_3StateController(index)

%% Generate identifiers:
% identifiers
s.ident.base = 'BUCKCTRL';
s.ident.index = index;
s.ident.name = sprintf('%s_%d', s.ident.base, s.ident.index);

% Helper fields
s.numberof.states = 3;
s.numberof.inputs = 2;
s.numberof.outputs = 1;
s.numberof.elements = 16;

%% Generate symbolic identifiers for states inputs outputs elements

% states:
s.ident.state{1,1} = sprintf('X1_%s', s.ident.name);
s.ident.state{1,2} = 'real';
```

```
s.ident.state{2,1} = sprintf('X2_%s', s.ident.name);
s.ident.state{2,2} = 'real';
s.ident.state{3,1} = sprintf('X3_%s', s.ident.name);
s.ident.state{3,2} = 'real';

s.ident.diffstate{1,1} = sprintf('diffX1_%s', s.ident.name);
s.ident.diffstate{1,2} = 'real';
s.ident.diffstate{2,1} = sprintf('diffX2_%s', s.ident.name);
s.ident.diffstate{2,2} = 'real';
s.ident.diffstate{3,1} = sprintf('diffX3_%s', s.ident.name);
s.ident.diffstate{3,2} = 'real';

% inputs:
s.ident.input{1,1} = sprintf('Um_%s', s.ident.name);
s.ident.input{1,2} = 'real';
s.ident.input{2,1} = sprintf('Uref_%s', s.ident.name);
s.ident.input{2,2} = 'real';

% output:
s.ident.output{1,1} = sprintf('Y_%s', s.ident.name);
s.ident.output{1,2} = 'real';

% elements:
s.ident.element{1,1} = sprintf('A11_%s', s.ident.name);
s.ident.element{2,1} = sprintf('A12_%s', s.ident.name);
s.ident.element{3,1} = sprintf('A13_%s', s.ident.name);
s.ident.element{4,1} = sprintf('A21_%s', s.ident.name);
s.ident.element{5,1} = sprintf('A22_%s', s.ident.name);
s.ident.element{6,1} = sprintf('A23_%s', s.ident.name);
s.ident.element{7,1} = sprintf('A31_%s', s.ident.name);
s.ident.element{8,1} = sprintf('A32_%s', s.ident.name);
s.ident.element{9,1} = sprintf('A33_%s', s.ident.name);

s.ident.element{10,1} = sprintf('B11_%s', s.ident.name);
s.ident.element{11,1} = sprintf('B21_%s', s.ident.name);
s.ident.element{12,1} = sprintf('B31_%s', s.ident.name);

s.ident.element{13,1} = sprintf('C11_%s', s.ident.name);
s.ident.element{14,1} = sprintf('C12_%s', s.ident.name);
s.ident.element{15,1} = sprintf('C13_%s', s.ident.name);

s.ident.element{16,1} = sprintf('D11_%s', s.ident.name);

for i = 1:(s.numberof.elements)
   s.ident.element{i,2} = 'positive';
end

%% Generate symbolic workspace variables
for i = 1:(s.numberof.states)
   eval(sprintf('syms %s %s', s.ident.state{i,1}, s.ident.state{i,2}));
   eval(sprintf('syms %s %s', s.ident.diffstate{i,1}, s.ident.diffstate{i,2}));
end

for i = 1:(s.numberof.inputs)
   eval(sprintf('syms %s %s', s.ident.input{i,1}, s.ident.input{i,2}));
end

for i = 1:(s.numberof.outputs)
   eval(sprintf('syms %s %s', s.ident.output{i,1}, s.ident.output{i,2}));
end

for i = 1:(s.numberof.elements)
   eval(sprintf('syms %s %s', s.ident.element{i,1}, s.ident.element{i,2}));
```

```
end

%% Symbolic vectors
s.vector.state{1,1} = eval(sprintf(s.ident.state{1,1}));
s.vector.state{2,1} = eval(sprintf(s.ident.state{2,1}));
s.vector.state{3,1} = eval(sprintf(s.ident.state{3,1}));

s.vector.diffstate{1,1} = eval(sprintf(s.ident.diffstate{1,1}));
s.vector.diffstate{2,1} = eval(sprintf(s.ident.diffstate{2,1}));
s.vector.diffstate{3,1} = eval(sprintf(s.ident.diffstate{3,1}));

s.vector.input{1,1} = eval(sprintf(s.ident.input{1,1}));
s.vector.input{2,1} = eval(sprintf(s.ident.input{2,1}));

s.vector.output{1,1} = eval(sprintf(s.ident.output{1,1}));

for i = 1:(s.numberof.elements)
   s.vector.elements{i,1} = eval(sprintf(s.ident.element{i,1}));
end

%% Governing Equations:
   %% Differential Equation 1:
str = sprintf('%s == %s*%s + %s*%s + %s*%s + %s*(-%s+%s)', ...
            s.ident.diffstate{1,1}, ...
            s.ident.element{1,1}, ...
            s.ident.state{1,1}, ...
            s.ident.element{2,1}, ...
            s.ident.state{2,1}, ...
            s.ident.element{3,1}, ...
            s.ident.state{3,1}, ...
            s.ident.element{10,1}, ...
            s.ident.input{1,1}, ...
            s.ident.input{2,1});

s.equation.differential{1,1} = eval(str);

if((exist('debug','var') == 1) && (debug == true))
   fprintf('%s system differential equation 1:   %s\n', s.ident.name, char(s.equation.differential{1,1}));
end

   %% Differential Equation 2:
str = sprintf('%s == %s*%s + %s*%s + %s*%s + %s*(-%s+%s)', ...
            s.ident.diffstate{2,1}, ...
            s.ident.element{4,1}, ...
            s.ident.state{1,1}, ...
            s.ident.element{5,1}, ...
            s.ident.state{2,1}, ...
            s.ident.element{6,1}, ...
            s.ident.state{3,1}, ...
            s.ident.element{11,1}, ...
            s.ident.input{1,1}, ...
            s.ident.input{2,1});

s.equation.differential{2,1} = eval(str);

if((exist('debug','var') == 1) && (debug == true))
   fprintf('%s system differential equation 2:   %s\n', s.ident.name, char(s.equation.differential{2,1}));
end

   %% Differential Equation 3:
str = sprintf('%s == %s*%s + %s*%s + %s*%s + %s*(-%s+%s)', ...
            s.ident.diffstate{3,1}, ...
            s.ident.element{7,1}, ...
```

```
            s.ident.state{1,1}, ...
            s.ident.element{8,1}, ...
            s.ident.state{2,1}, ...
            s.ident.element{9,1}, ...
            s.ident.state{3,1}, ...
            s.ident.element{12,1}, ...
            s.ident.input{1,1}, ...
            s.ident.input{2,1});

s.equation.differential{3,1} = eval(str);

if((exist('debug','var') == 1) && (debug == true))
   fprintf('%s system differential equation 3:   %s\n', s.ident.name, char(s.equation.differential{3,1}));
end

   %% Output Equation 1:
str = sprintf('%s == %s*%s + %s*%s + %s*%s + %s*(-%s+%s)', ...
            s.ident.output{1,1}, ...
            s.ident.element{13,1}, ...
            s.ident.state{1,1}, ...
            s.ident.element{14,1}, ...
            s.ident.state{2,1}, ...
            s.ident.element{15,1}, ...
            s.ident.state{3,1}, ...
            s.ident.element{16,1}, ...
            s.ident.input{1,1}, ...
            s.ident.input{2,1});

s.equation.output{1,1} = eval(str);

if((exist('debug','var') == 1) && (debug == true))
   fprintf('%s system output equation 1:   %s\n', s.ident.name, char(s.equation.output{1,1}));
end

%% Return structure containing new subsystem
new3StateControl = s;
```

A.3 SYSTEM MODEL DEFINITION FROM INTERCONNECTED SUBSYSTEMS

system_Line_2LC_CLBuck.m

```
function [subsystems, netlist, input] = system_Line_2LC_CLBuck()

%% Generate subsystems:
RLINE = subsystem_Resistor(1);
subsystems(1) = RLINE;

LC1 = subsystem_LCFilter(1);
subsystems(2) = LC1;
BUCK1 = subsystem_SynchronousBuck(1);
subsystems(3) = BUCK1;
CTRL1 = subsystem_3StateController(1);
subsystems(4) = CTRL1;
R1 = subsystem_ResistorLoad(1);
subsystems(5) = R1;

LC2 = subsystem_LCFilter(2);
subsystems(6) = LC2;
BUCK2 = subsystem_SynchronousBuck(2);
subsystems(7) = BUCK2;
CTRL2 = subsystem_3StateController(2);
subsystems(8) = CTRL2;
R2 = subsystem_ResistorLoad(2);
subsystems(9) = R2;

%% Generate netlist

netlist{1,1} = ( RLINE.vector.input{2,1} == ...
                 (LC1.vector.output{2,1} + ...
                  LC2.vector.output{2,1}));

netlist{2,1} = (LC1.vector.input{1,1} == RLINE.vector.output{1,1});
netlist{3,1} = (LC2.vector.input{1,1} == RLINE.vector.output{1,1});

netlist{4,1} = (BUCK1.vector.input{1,1} == LC1.vector.output{1,1});
netlist{5,1} = (LC1.vector.input{2,1} == BUCK1.vector.output{2,1});
netlist{6,1} = (CTRL1.vector.input{1,1} == BUCK1.vector.output{1,1});
netlist{7,1} = (BUCK1.vector.input{3,1} == CTRL1.vector.output{1,1});
netlist{8,1} = (R1.vector.input{1,1} == BUCK1.vector.output{1,1});
netlist{9,1} = (BUCK1.vector.input{2,1} == R1.vector.output{1,1});

netlist{10,1} = (BUCK2.vector.input{1,1} == LC2.vector.output{1,1});
netlist{11,1} = (LC2.vector.input{2,1} == BUCK2.vector.output{2,1});
netlist{12,1} = (CTRL2.vector.input{1,1} == BUCK2.vector.output{1,1});
netlist{13,1} = (BUCK2.vector.input{3,1} == CTRL2.vector.output{1,1});
netlist{14,1} = (R2.vector.input{1,1} == BUCK2.vector.output{1,1});
netlist{15,1} = (BUCK2.vector.input{2,1} == R2.vector.output{1,1});

%% Specify the inputs

input{1,1} = RLINE.vector.input{1,1};
```

```
input{2,1} = CTRL1.vector.input{2,1};
input{3,1} = CTRL2.vector.input{2,1};

end
```

generateSystems.m

```
function system = generateSystems(strName)

  %% Define subsystems and connections
  eval(sprintf('[akk, bkk, ckk] = %s();', strName));

  subsystems = akk;
  netlist = bkk;
  input = ckk;

  %% Combine subsystems with netlist rules
  system = combineSymbolically(subsystems, netlist, input);
  clear subsystems netlist input;

  %%
  system = createSystemSteadyStateAnonFunctions(system);
  system = createOutputAnonFunctions(system);

  %% Find Analytic expressions for steady-state
  %{
  system = findSteadyStateAnalytically(system);
  system = createSteadyStateAnalyticFunction(system);

  system = findSteadyStateOutputsAnalytically(system);
  system = createSteadyStateOutputAnalyticFunction(system);
  %}

  %% Linearize via first-order partial derivatives
  system = addJacobian(system);
  system = createJacobianMatrixFunctions(system);

  %% Evaluate transfer functions
  %{
  syms s;
  system = addTransferFunctions(system);
  clear s;
  %}

  %%
  %syms s;
  %lengthOfA = size(system.statespace.A,1);
  %mI = eye(lengthOfA);

  %ans = inv(s*mI-system.statespace.A);

  %% Add partial derivatives in symbolic and function form
```

```
  for ii = 1:length(system.vector.elements)
    pd_matA_sym = diff(system.statespace.A, system.vector.elements{ii});
    system.pd.pd_matA_sym{ii} = pd_matA_sym;
    system.pd.pd_matA_function{ii} = matlabFunction(pd_matA_sym, 'Optimize',false, 'Vars',[system.vector.systemIn-
put{:,1},system.vector.elements{:,1},system.vector.state{:,1}]);
  end

end
```

A.4 DEFINE SYSTEM PARAMETERS AND INPUT DATA

data_Line_2LC_CLBuck_SAME.m

```
function param = data_Line_2LC_CLBuck_SAME()

var_frac = 0.2;

       V1_R_1 = 380;
Uref_BUCKCTRL_1 = 100;
Uref_BUCKCTRL_2 = 100;

     VC_LC_1 = 0;
     IL_LC_1 = 0;
  VC_SBUCK_1 = 0;
  IL_SBUCK_1 = 0;
X1_BUCKCTRL_1 = 0;
X2_BUCKCTRL_1 = 0;
X3_BUCKCTRL_1 = 0;
     VC_LC_2 = 0;
     IL_LC_2 = 0;
  VC_SBUCK_2 = 0;
  IL_SBUCK_2 = 0;
X1_BUCKCTRL_2 = 0;
X2_BUCKCTRL_2 = 0;
X3_BUCKCTRL_2 = 0;

     VC_LC_1_guess = 380;
     IL_LC_1_guess = 2;
  VC_SBUCK_1_guess = 100;
  IL_SBUCK_1_guess = 50;
X1_BUCKCTRL_1_guess = 0;
X2_BUCKCTRL_1_guess = 0;
X3_BUCKCTRL_1_guess = 0;
     VC_LC_2_guess = 380;
     IL_LC_2_guess = 2;
  VC_SBUCK_2_guess = 100;
  IL_SBUCK_2_guess = 50;
X1_BUCKCTRL_2_guess = 0;
X2_BUCKCTRL_2_guess = 0;
X3_BUCKCTRL_2_guess = 0;
```

```
          R_1 = 0.1;

        C_LC_1 = 880e-6;
        L_LC_1 = 2.2e-3;
       RL_LC_1 = 50e-3;
       RC_LC_1 = 1e-9;
     C_SBUCK_1 = 1200e-6;
     L_SBUCK_1 = 100e-6;
    RL_SBUCK_1 = 10e-3;
    RC_SBUCK_1 = 1e-9;
RDSONQ1_SBUCK_1 = 5e-3;
RDSONQ2_SBUCK_1 = 5e-3;
A11_BUCKCTRL_1 = 0;
A12_BUCKCTRL_1 = -1.521e+04;
A13_BUCKCTRL_1 = -2.29e+04;
A21_BUCKCTRL_1 = 0;
A22_BUCKCTRL_1 = -8.749e+04;
A23_BUCKCTRL_1 = -1.273e+05;
A31_BUCKCTRL_1 = 0;
A32_BUCKCTRL_1 = 0;
A33_BUCKCTRL_1 = -9.172e+04;
B11_BUCKCTRL_1 = 13.08;
B21_BUCKCTRL_1 = 72.7;
B31_BUCKCTRL_1 = 109.5;
C11_BUCKCTRL_1 = -23.65;
C12_BUCKCTRL_1 = 131.5;
C13_BUCKCTRL_1 = 198;
D11_BUCKCTRL_1 = -0.113;
    R_RLOAD_1 = 5;

        C_LC_2 = 880e-6;
        L_LC_2 = 2.2e-3;
       RL_LC_2 = 50e-3;
       RC_LC_2 = 1e-9;
     C_SBUCK_2 = 1200e-6;
     L_SBUCK_2 = 100e-6;
    RL_SBUCK_2 = 10e-3;
    RC_SBUCK_2 = 1e-9;
RDSONQ1_SBUCK_2 = 5e-3;
RDSONQ2_SBUCK_2 = 5e-3;
A11_BUCKCTRL_2 = 0;
A12_BUCKCTRL_2 = -1.521e+04;
A13_BUCKCTRL_2 = -2.29e+04;
A21_BUCKCTRL_2 = 0;
A22_BUCKCTRL_2 = -8.749e+04;
A23_BUCKCTRL_2 = -1.273e+05;
A31_BUCKCTRL_2 = 0;
A32_BUCKCTRL_2 = 0;
A33_BUCKCTRL_2 = -9.172e+04;
B11_BUCKCTRL_2 = 13.08;
B21_BUCKCTRL_2 = 72.7;
B31_BUCKCTRL_2 = 109.5;
C11_BUCKCTRL_2 = -23.65;
C12_BUCKCTRL_2 = 131.5;
C13_BUCKCTRL_2 = 198;
D11_BUCKCTRL_2 = -0.113;
    R_RLOAD_2 = 5;


index = 1;
param.u(index).name = getName(V1_R_1);
```

```
param.u(index).val = V1_R_1;
param.u(index).lowerbound = (1-var_frac)*param.u(index).val;
param.u(index).upperbound = (1+var_frac)*param.u(index).val;
param.u(index).pdf = makedist('Uniform', 'lower', param.u(index).lowerbound, 'upper', param.u(index).upperbound);

……

index = 3;
param.u(index).name = getName(Uref_BUCKCTRL_2);
param.u(index).val = Uref_BUCKCTRL_2;
param.u(index).lowerbound = (1-var_frac)*param.u(index).val;
param.u(index).upperbound = (1+var_frac)*param.u(index).val;
param.u(index).pdf = makedist('Uniform', 'lower', param.u(index).lowerbound, 'upper', param.u(index).upperbound);

index = 1;
param.el(index).name = getName(R_1);
param.el(index).val = R_1;
param.el(index).lowerbound = 1e-9;%(1-var_frac)*param.el(index).val;
param.el(index).upperbound = (1+1)*param.el(index).val;
param.el(index).pdf = makedist('Uniform', 'lower', param.el(index).lowerbound, 'upper', param.el(index).upperbound);

……

index = 55;
param.el(index).name = getName(R_RLOAD_2);
param.el(index).val = R_RLOAD_2;
param.el(index).lowerbound = (1-0.5)*param.el(index).val;
param.el(index).upperbound = (1+0.5)*param.el(index).val;
param.el(index).pdf = makedist('Uniform', 'lower', param.el(index).lowerbound, 'upper', param.el(index).upperbound);

index = 1;
param.x(index).name = getName(VC_LC_1);
param.x(index).val = 0;
param.x(index).guess = VC_LC_1_guess;

……

index = 14;
param.x(index).name = getName(X3_BUCKCTRL_2);
param.x(index).val = 0;
param.x(index).guess = X3_BUCKCTRL_2_guess;

end
```

A.5 COMBINING SYMBOLIC SUBSYSTEM MODELS

MAIN.m (1)

```
%% Generate/load system model ----------------------------------------
system_name = 'system_Line_2LC_CLBuck';

currentFolder = pwd;
pathname = strcat(currentFolder,'\data');
dotmat = '.mat';
s = strcat(system_name,dotmat);
systemfile = fullfile(pathname, s);
if (~exist(systemfile))
```

```
  eval(sprintf('%s = generateSystems(system_name);', system_name));
  save(systemfile,system_name);
else
  load(systemfile);
end
clear systemfile pathname currentFolder dotmat s system_name;

%% Generate/load system parameters ---------------------------------------
data_name = 'data_Line_2LC_CLBuck_SEP';

currentFolder = pwd;
pathname = strcat(currentFolder,'\data');
dotmat = '.mat';
s = strcat(data_name ,dotmat);
paramfile = fullfile(pathname, s);
if (~exist(paramfile))
  eval(sprintf('%s = %s();', data_name , data_name ));
  save(paramfile,data_name);
else
  load(paramfile);
end
clear paramfile pathname currentFolder dotmat s data_name;


%% set to working data ---------------------------------------------------

system = system_Line_2LC_CLBuck;
param = data_Line_2LC_CLBuck_SEP;

%[system.vector.systemInput{:,1}]'
%[system.vector.state{:,1}]'
%[system.vector.elements{:,1}]'

[1:length(system.vector.systemInput); [system.vector.systemInput{:,1}]; vpa([param.u(:).val])]'
[1:length(system.vector.state); [system.vector.state{:,1}]]'
[1:length(system.vector.elements); [system.vector.elements{:,1}]; vpa([param.el(:).val])]'

%% check nominal stability -----------------------------------------------

systemFunction = system.equation.anonDifferential;
matrixAFunction = system.equation.analyticMatrixA;
options = optimoptions('fsolve','Display','none');
reducedFunction = @(y) systemFunction(y, [param.u(:).val], [param.el(:).val]);

[x_ss,~,exitflag,~] = fsolve(reducedFunction, [param.x.guess], options);
if (exitflag < 1)
  disp('!!!!! no solution !!!!!!!!');
end
x_ss = x_ss';
outputFunction = system.equation.anonOutput;
y_ss = outputFunction(x_ss, [param.u(:).val], [param.el(:).val]);

C = num2cell([[param.u(:).val]'; [param.el(:).val]'; x_ss]);
matA = matrixAFunction(C{:});
eigenvals = sort(eig(matA));
ii = find(real(eigenvals)>=0);
eigenvals2 = sort(eigenvals);
isUnstable = any(real(eigenvals2(:)) > 0);

%----continued----
```

A.6 VBSA

MAIN.m (2)

```
%% Specify Unknown Variables for SA -------------------------------------

elements_to_test = [1,2,3,4,28,29,30,31,55];
inputs_to_test = [];


%% Setup for VBSA ---------------------------------------------------------
paths.currentFolder = pwd;
paths.sRscript = 'C:/Tools/R/R-3.6.2/bin/Rscript.exe';

N = 10000;

[X1, X2, X] = generateSetForVBSA(elements_to_test, inputs_to_test, N, paths);

num_scenarios = length(X)

X_val_mc = mappingUnitToReal(X, elements_to_test, inputs_to_test, param);

%% Run MC simulations ----------------------------------------------------
tic
  monteScenario = runMonteCarloWithPD(system, param, X_val_mc, inputs_to_test, elements_to_test);
toc

%% SORT EIGENVALUE BY CRITERIA (BELOW) ----------------------------------
%% select most critical eigenvalue, right-most --------------------------
clear y_crit y_real y_imag;
y_crit = zeros(num_scenarios,1);
y_real = zeros(num_scenarios,1);
y_imag = zeros(num_scenarios,1);

for ii = 1:num_scenarios
  eigenvalues = monteScenario.eigs(ii,:);
  [~, ind] = max(real(eigenvalues));
  y_crit(ii,1) = eigenvalues(ind);
  y_real(ii,1) = real(eigenvalues(ind));
  y_imag(ii,1) = imag(eigenvalues(ind));
end
y_avg = mean(y_real)+1i*mean(y_imag);
clear ii ind

%% select by X/Y-axis region, rectangle ---------------------------------
newEigenset1 = selectWindowEigenvalues(monteScenario.eigs, -60, 40, 200, 500);
newEigenset2 = selectWindowEigenvalues(monteScenario.eigs, -80, 40, 500, 1000);

scatter(real(newEigenset2(:,1)),imag(newEigenset2(:,1)))

%% select by participation ----------------------------------------------

modifiedMonteScenario = selectByParticipation(monteScenario,1,1);


%%
%{
figure(1)
hold on;
scatter(real(modifiedMonteScenario.eigs(:,14)), imag(modifiedMonteScenario.eigs(:,14)),'.r')
```

```
scatter(real(modifiedMonteScenario.eigs(:,12)), imag(modifiedMonteScenario.eigs(:,12)),'.b')
%scatter(real(y_crit(:,1)),imag(y_crit(:,1)))
%}

%% Run VBSA ----------------------------------------------------------------

Y = real(modifiedMonteScenario.eigs(:,14));
[S1, T1, V1] = runVBSA(X1, X2, Y, elements_to_test, paths);

Y2 = real(modifiedMonteScenario.eigs(:,12));
[S2, T2, V2] = runVBSA(X1, X2, Y2, elements_to_test, paths);

%----continued----
```

selectByParticipation.m

```
function modifiedMonteScenario = selectByParticipation(monteScenario, whichStates, whichEigs)

%%
whichEigs = [11,12,13,14];
whichStates = [1,2,8,9];

modifiedMonteScenario = monteScenario;

for ii = 1:length(monteScenario.scn_u)
%%
  currentOrder = 1:1:14;

  currEigs = monteScenario.eigs(ii,:);
  currP = monteScenario.P(ii).participation;

  %if(p2 < p4)
  if( (currP(1,whichEigs(2)) + currP(2,whichEigs(2))) < (currP(8,whichEigs(2)) + currP(9,whichEigs(2))) )
    temp1 = currentOrder(14);
    temp2 = currentOrder(13);

    currentOrder(14) = currentOrder(12);
    currentOrder(13) = currentOrder(11);

    currentOrder(12) = temp1;
    currentOrder(11) = temp2;
  else
    % do nothing
  end


  for nn = 1:length(currentOrder)
    newIndex = currentOrder(nn);
    newEigs(nn) = currEigs(newIndex);
    newParticipation(:,nn) = currP(:,newIndex);
  end
  modifiedMonteScenario.eigs(ii,:) = newEigs;
  modifiedMonteScenario.P(ii).participation = newParticipation;
%%
end
%%

end
```

generateSetForVBSA.m

```
function [X1, X2, X] = generateSetForVBSA(elements_to_test, ...
                    inputs_to_test, N, paths)

variables = length(elements_to_test);

set = sobolset(2*variables);
totaldata_unit = net(set,N);

X1 = totaldata_unit(:,1:variables);
X2 = totaldata_unit(:,(variables+1):(2*variables));

currentFolder = paths.currentFolder;
subfolder_data = 'r_data';
subfolder_function = 'r_functions';
sRscript = paths.sRscript;

file = 'X.csv';
sx = sprintf('%s\\%s\\%s', currentFolder, subfolder_data, file);
file = 'X1.csv';
sx1 = sprintf('%s\\%s\\%s', currentFolder, subfolder_data, file);
csvwrite(sx1,X1);
file = 'X2.csv';
sx2 = sprintf('%s\\%s\\%s', currentFolder, subfolder_data, file);
csvwrite(sx2,X2);

file = 'generateScenariosA.R';
data_location = sprintf('%s\\%s', currentFolder, subfolder_data);
data_location = strrep(data_location,'\','/');

toeval = sprintf('!"%s" "%s\\%s\\%s" "%s"',sRscript, currentFolder, ...
        subfolder_function, file, data_location);
eval(toeval);

fileID = fopen('X.csv','r');
formatSpec = '%f';
X = fscanf(fileID, formatSpec, [variables,inf])';
fclose('all');

delete(sx1);
delete(sx2);
delete(sx);

end
```

mappingUnitToReal.m

```
function X_actual = mappingUnitToReal(X, elements_to_test, ...
                    inputs_to_test, param)

% map values [0,1] to required range
  variables = length(elements_to_test);
  num_scenarios = length(X);

  tt = 1e-6;
  y_val = (0: tt: 1-tt);
  X_actual = zeros(num_scenarios, variables);
  for kk = 1:variables
    whichEl = elements_to_test(kk);
    currcdf = icdf(param.el(whichEl).pdf , y_val)';
    for ii = 1:num_scenarios
      index = floor((X(ii,kk)/tt))+1;
      X_actual(ii, kk) = currcdf(index);
      if (X_actual(ii, kk) == 0)
        X_actual(ii, kk) = 1e-9;
      end
    end
  end

end
```

runVBSA.m

```
function [S, T, V] = runVBSA(X1, X2, Y, elements_to_test, paths)

variables = length(elements_to_test);

currentFolder = paths.currentFolder;
subfolder_data = 'r_data';
subfolder_function = 'r_functions';
sRscript = paths.sRscript;

file = 'X1.csv';
sx1 = sprintf('%s\\%s\\%s', currentFolder, subfolder_data, file);
csvwrite(sx1,X1);

file = 'X2.csv';
sx2 = sprintf('%s\\%s\\%s', currentFolder, subfolder_data, file);
csvwrite(sx2,X2);

file = 'Y.csv';
sy = sprintf('%s\\%s\\%s', currentFolder, subfolder_data, file);
csvwrite(sy,Y);

file = 'sobolSaltA.R';
data_location = sprintf('%s\\%s', currentFolder, subfolder_data);
data_location = strrep(data_location,'\','/');

toeval = sprintf('!"%s" "%s\\%s\\%s" "%s"', sRscript, currentFolder, ...
                 subfolder_function, file, data_location);
eval(toeval);

fileID = fopen('S.csv','r');
formatSpec = '%f';
```

```
S = fscanf(fileID, formatSpec, [variables,inf])';
fileID = fopen('T.csv','r');
formatSpec = '%f';
T = fscanf(fileID, formatSpec, [variables,inf])';
fileID = fopen('V.csv','r');
formatSpec = '%f';
V = fscanf(fileID, formatSpec, [variables,inf])';
fclose('all');

end
```

sobolSaltA.R

```
options(echo=TRUE)
args <- commandArgs(trailingOnly = TRUE)
print(args)
name <- args[1]
print(name)

setwd(name)
library(sensitivity)
library(boot)

X1 <- read.csv('X1.csv',header=FALSE)
X2 <- read.csv('X2.csv',header=FALSE)

X1 <- data.frame(X1)
X2 <- data.frame(X2)

x <- sobolSalt(model = NULL, X1, X2, scheme="A", nboot = 0)

y <- read.csv('y.csv',header=FALSE)
y <- as.numeric(unlist(data.frame(y)))
tell(x,y)

write.table(getElement(x, "V"), file = "V.csv", append = FALSE, quote = TRUE,
        sep = " ", eol = "\n", na = "NA", dec = ".", row.names = FALSE,
        col.names = FALSE, qmethod = c("escape", "double"), fileEncoding = "")

write.table(getElement(x, "S"), file = "S.csv",      append = FALSE, quote = TRUE,
        sep = " ", eol = "\n", na = "NA", dec = ".", row.names = FALSE,
        col.names = FALSE, qmethod = c("escape", "double"), fileEncoding = "")

write.table(getElement(x, "T"), file = "T.csv", append = FALSE, quote = TRUE,
        sep = " ", eol = "\n", na = "NA", dec = ".", row.names = FALSE,
        col.names = FALSE, qmethod = c("escape", "double"), fileEncoding = "")

print("VBSA SUCCESS!")
```

generateScenariosA.R

```
options(echo=TRUE)
args <- commandArgs(trailingOnly = TRUE)
print(args)
name <- args[1]
print(name)

setwd(name)
library(sensitivity)
library(boot)

X1 <- read.csv('X1.csv',header=FALSE)
X2 <- read.csv('X2.csv',header=FALSE)

X1 <- data.frame(X1)
```

```
X2 <- data.frame(X2)

x <- sobolSalt(model = NULL, X1, X2, order = 1, nboot = 0)

data <- getElement(x, "X")

write.table(getElement(x, "X"), file = "X.csv", append = FALSE, quote = TRUE,
        sep = " ", eol = "\n", na = "NA", dec = ".", row.names = FALSE,
        col.names = FALSE, qmethod = c("escape", "double"), fileEncoding = "")

print("GENERATED SAMPLES SUCCESS!")
```

Appendix B – Component Parameter Measurement and Estimation

B.1 Input LC Filters

Frequency response analysis is used for the characterisation of the low-pass input filters. The filter models used in theoretical analysis must match the output impedance characteristics derived from experimental measurements. The filters used in test-bench setup are comprised of different discrete capacitors and inductors connected together. The frequency response of each component ($Z_x(j\omega)$) is first measured in order to obtain the combined output impedance of the filter ($Z_{out}(j\omega)$), as illustrated in Figure B.1. Practical components are subject to wide tolerances and changes over their lifetime, therefore individually measured components enable different connection configurations to ensure that the filter-under-test meets the required characteristics (i.e., to resonant frequency and magnitude). Furthermore, frequency response measurements are used to confirm that the lumped parameter model with parasitic elements is sufficient to accurately represent the filter's response for the purposes of small-signal stability analysis.

An LCR meter (*Hioki IM3533-01*) with automatic frequency sweep functionality was used to measure the frequency response of each component.

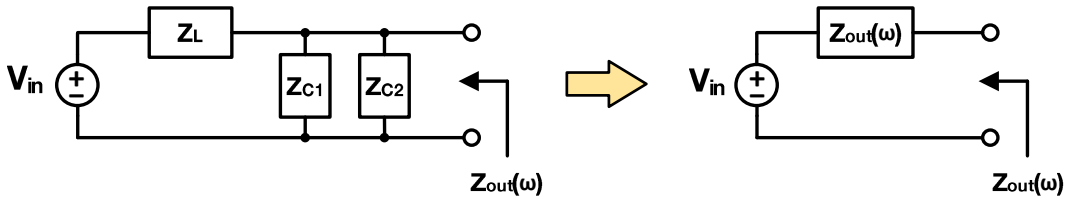

FIGURE B.1 (a) Output impedance Z_{out} low-pass filter design using frequency response data of individual elements Z_L, Z_{C1}, Z_{C2}, **(b)** Representation of the combined frequency response for Z_{out} (where source input V_{in} replaced by a short circuit).

$$Z_{out} = (Z_L^{-1} + Z_{C1}^{-1} + Z_{C2}^{-1})^{-1} \quad \text{(B.1)}$$

Z_{L1} is the impedance of the external LC filter inductor.

Z_{C1} is the impedance of the external LC filter capacitor.

Z_{C2} is the impedance of the input capacitor of the buck converter.

The TDHBG2500P100 converter prototype has between the input terminals a 10µF film capacitor (TDK B32794D2106K) for decoupling and, being in parallel, is considered as part of the input filter.

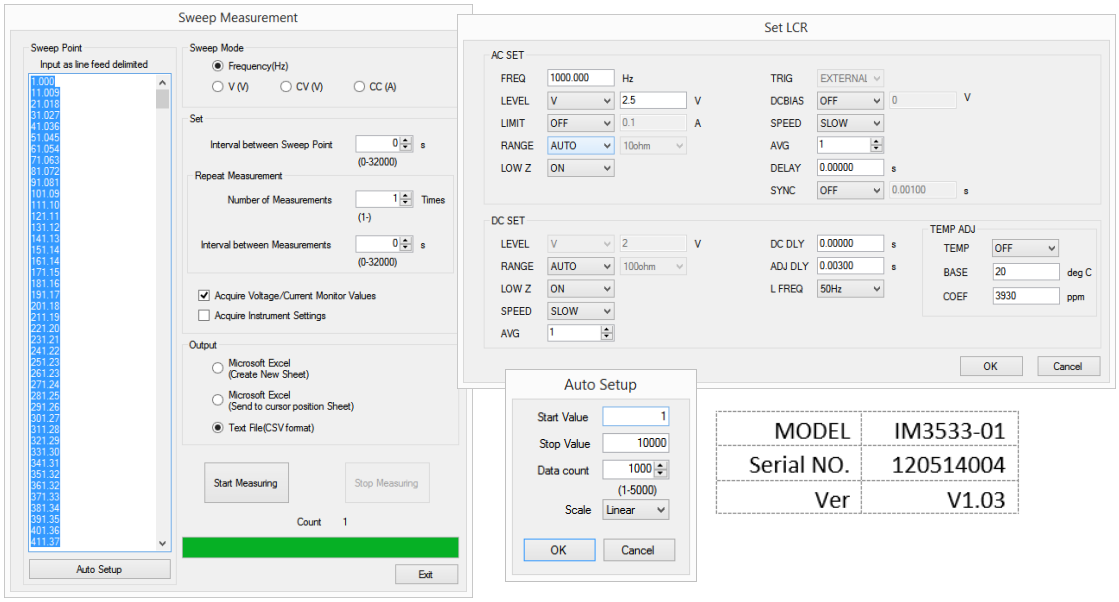

FIGURE B.2 Frequency sweep measurement settings, LCR Meter *Hioki IM3533-01*

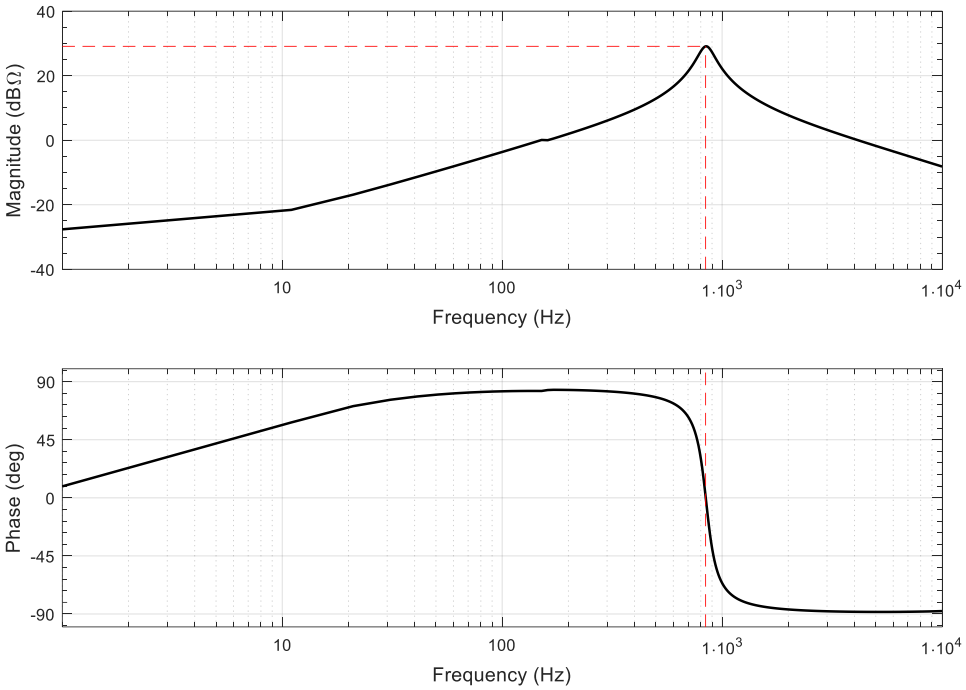

FIGURE B.3 Output impedance Z_{out} of input filter 1 based on parameter measurements.

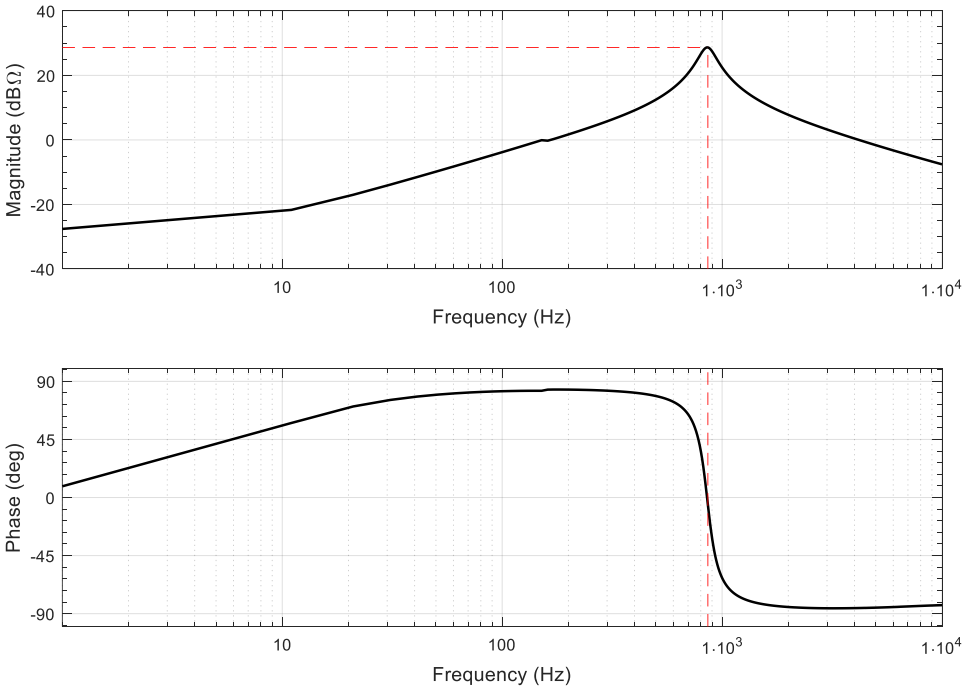

FIGURE B.4 Output impedance Z_{out} of input filter 2 based on parameter measurements.

In order to get an experimentally based model, the MATLAB system identification was used to fit the experimentally measured frequency response data (*FRD*) to grey box model using the MATLAB command *'greyest'*.

The second order model for the input filter in Figure B.5 was fitted to the FRD. The equations in (B.3) shows the parametric state-space model of the filter in Figure B.5 used for parameter estimation. Equivalent transfer function model is presented in (B.2). This is measured from the output terminals of the filter with the voltage source replaced by a short circuit to ground.

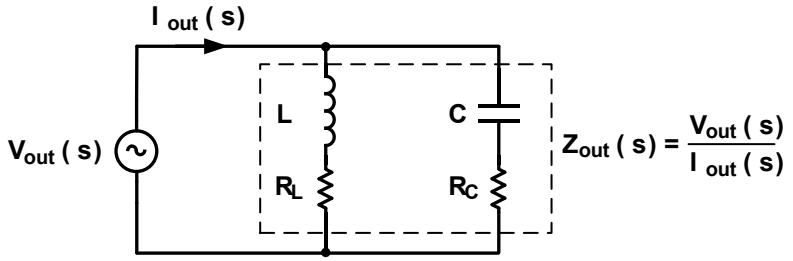

FIGURE B.5 Filter model used to fit experimental *FRD* (impedance data) for parameter estimation.

$$Z_{out}(s) = \frac{(sCR_C + 1)(sL + R_L)}{s^2LC + sC(R_C + R_L) + 1} \tag{B.2}$$

$$\frac{d}{dt}\begin{bmatrix} I_L \\ V_C \end{bmatrix} = \begin{bmatrix} -\frac{R_L}{L} & 0 \\ 0 & -\frac{1}{CR_C} \end{bmatrix}\begin{bmatrix} I_L \\ V_C \end{bmatrix} + \begin{bmatrix} \frac{1}{L} \\ \frac{1}{CR_C} \end{bmatrix} V_{out} \tag{B.3}$$

$$I_{out} = \begin{bmatrix} 1 & -\frac{1}{R_C} \end{bmatrix}\begin{bmatrix} I_L \\ V_C \end{bmatrix} + (\frac{1}{R_C})V_{out}$$

A passband weighting prefilter on frequencies above 300Hz was applied during grey box model estimation to better match the impedance data at the resonant frequency. This was done in order to ensure the fitted filter model closely represents the behaviour of the real filter connected with a CPL, where the minor loop gain frequencies are closest to the boundary of instability.

This fitted model has minor discrepancies near DC and low frequencies. This is likely due to the non-ideal (nonlinear) behaviour of the inductors and capacitors that is not accounted for in the lumped element model. The use of a more detailed filter model that includes parasitic elements was not required to the overall study. The 2nd order model matches the measured data around the resonant peak and is therefore able to predict small-signal instability with sufficient accuracy.

TABLE B.1 Parameters for different filter designs

Filter	Nominal values		Refined values				Derived measures	
	Induct-ance (µH)	Capacit-ance (µF)	Inductance (µH)	Capacit-ance (µF)	DCR (mΩ)	ESR (mΩ)	Natural frequency, f_n (Hz)	Damp-ing ratio, ζ
F1	1000	40	879.46	39.72	656.8	106.0	851.5	0.0811
F2	1000	40	853.66	39.92	614.4	154.3	862.1	0.0831
F1-II	1000	42.5	879.58	42.18	657.0	94.0	826.3	0.0822
F1-III	1000	45	879.69	44.61	657.2	84.0	803.4	0.0835
F1-IV	1000	47.5	879.78	47.04	657.4	75.6	782.3	0.0847
F1-V	1000	50	879.84	49.58	657.5	68.1	762.0	0.0861
F1-VI	1000	55	880.00	54.48	657.8	56.4	726.9	0.0889
F1-VII	1000	60	879.69	59.17	657.0	48.0	697.6	0.0914
F1-VIII	1000	190	909.84	188.02	282.8	38.4	384.8	0.0730

TABLE B.2 Filter designs (*F1-II* to *F1-VIII*) by auxiliary capacitor(s) selection

Filter	Auxiliary capacitance	Auxiliary capacitor parallel combination
F1-II	+2.5 µF	CAUX1
F1-III	+5 µF	CAUX1, CAUX3
F1-IV	+7.5 µF	CAUX1, CAUX2, CAUX3
F1-V	+10 µF	CAUX5
F1-VI	+15 µF	CAUX1, CAUX3, CAUX5
F1-VII	+20 µF	CAUX6
F1-VIII	+150 µF	CAUX8 + CAUX10

TABLE B.3 Auxiliary capacitor values and part numbers

Auxiliary Capacitor	Value	Description	Manufacturer	Manufacturer Part Number
CAUX1	2.5 µF	2.5µF Film Capacitor 400V Polypropylene (PP), Metallized Radial	KEMET	C4AF3BU4250A12K
CAUX2	2.5 µF	2.5µF Film Capacitor 400V Polypropylene (PP), Metallized Radial	KEMET	C4AF3BU4250A12K
CAUX3	2.5 µF	2.5µF Film Capacitor 400V Polypropylene (PP), Metallized Radial	KEMET	C4AF3BU4250A12K
CAUX5	10 µF	10µF Film Capacitor 1100V (1.1kV) Polypropylene (PP), Metallized Radial - 4 Leads	WIMA	DCP4P051007GD4KSC9
CAUX6	20 µF	20µF Film Capacitor 1100V (1.1kV) Polypropylene (PP), Metallized Radial	WIMA	DCP4P052007ID2JSSD
CAUX8	50 µF	50µF Film Capacitor 600V Polypropylene (PP), Metallized Radial - 4 Leads	WIMA	DCP4I055007JD4KSSD
CAUX10	100 µF	100µF Film Capacitor 500V Polypropylene (PP), Metallized Radial - 4 Leads	Vishay BC Components	MKP1848C71050JY5

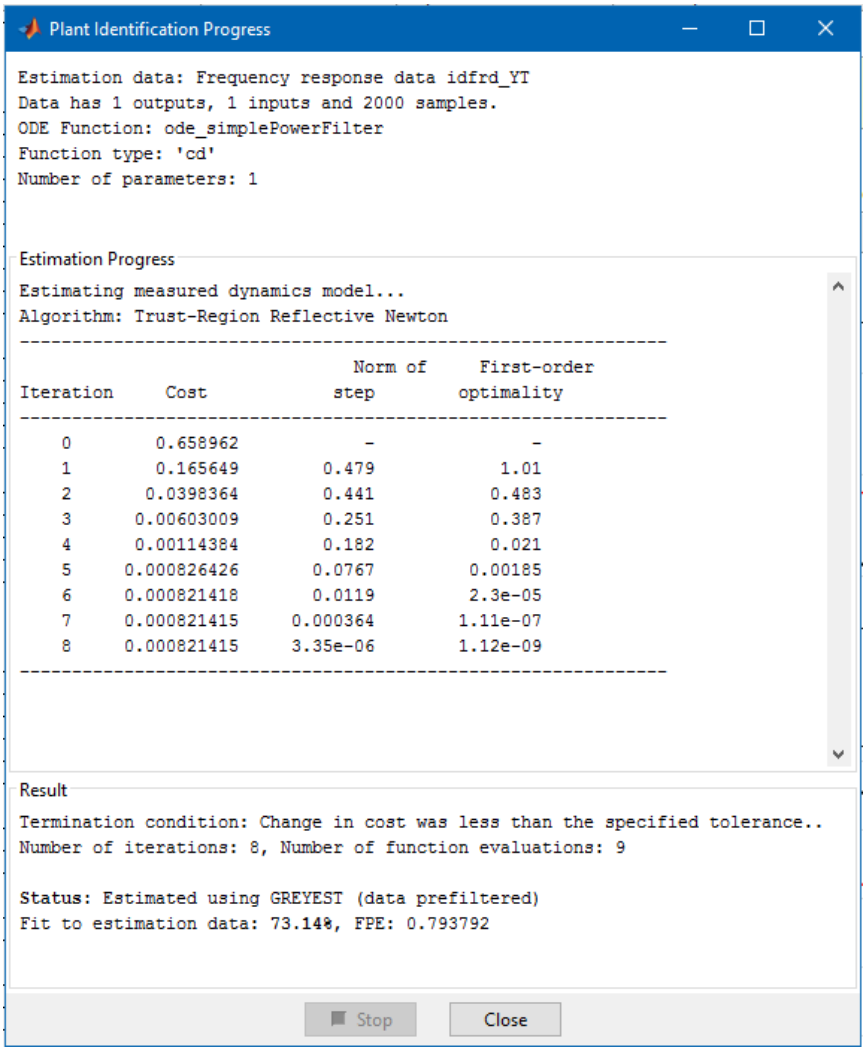

FIGURE B.6 Example process for parameter estimation by fitting to a greybox plant model using experimentally measured *FRD*

B.2 RESISTOR AS LVDC DISTRIBUTION LINE

In a practical system, cables are used to connect generators to loads often over a long distance and in environments with varying temperature. Therefore, the characteristics of the distribution lines are subject to uncertainty. A purely resistive model was used to emulate the characteristics of long cables in the lab. Resistance is dominant at the low frequencies relevant for small-signal stability therefore omitting reactance is justified. Equation (B.4), below, shows how line resistance R_{line} can be calculated as a function of length and temperature.

$$R_{line}(\Omega) = \frac{\rho_0\big(1 + \alpha(T - T_0)\big)L}{S} \tag{B.4}$$

Where,

ρ_0 ($\Omega.mm^2/m$) is the resistivity of the material ($\rho_{0,Al}$ = 0.0294, $\rho_{0,Cu}$ = 0.0171),

S (mm^2) is the nominal cross-sectional area of the conductor in mm^2

L (m) is the cable length

α (K^{-1}) is the temperature coefficient of resistance referenced to initial temperature T_0 (α_{Al} = 0.00429, α_{Cu} 0.00386)

T (°C) conductor temperature

T_0 (°C) initial temperature reference (typically 20°C)

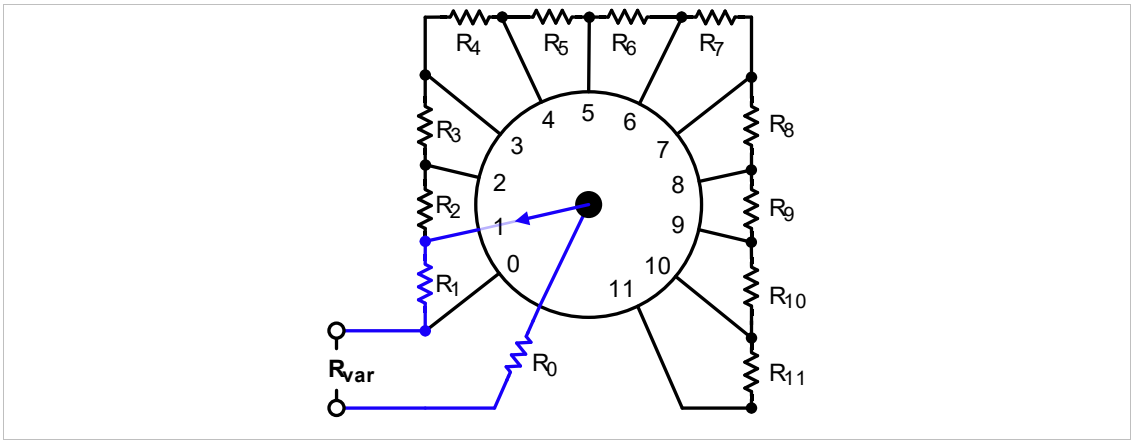

FIGURE B.7 Variable resistor model used in test-bench experiments with parameter values given in Table B.4.

The use of a large cross-sectional area for conductors can be used to minimise resistive losses (I^2R) at the expense of weight and cost. However, a trade-off between

these factors often results in cross-section being compromised, therefore yielding a higher resistance per unit length. Assuming a copper cable of 2.5mm^2 (14 AWG) with a cable length up to 100m in an operating environment between −40 °C to 50 °C results in a resistance (R_{line}) value ranging from 0 to 700mΩ.

To vary resistance during experiments, a high current rheostat was used to emulate a LVDC distribution line. A rotary wire wound rheostat (Ohmite RJSR50E, 0.5Ohm 50W) was used with resistance measured at marked positions enabling precise changes during experimentation.

TABLE B.4 Rheostat (*Ohmite RJSR50E*) resistance–position values, experimentally measured.

Notch Position	Incremental Resistance, R_{pos} (mΩ)	Terminal Resistance, R_{rheo} (mΩ)	Notch Position	Incremental Resistance, R_{pos} (mΩ)	Terminal Resistance, R_{rheo} (mΩ)
0	17.2	17.2	6	45.5	303.5
1	43	60.2	7	64	367.5
2	45.3	105.5	8	38.5	406
3	44	149.5	9	54	460
4	46.7	196.2	10	50	510
5	61.8	258	11	40	550